

Papers presented at
the 6th International Seminar on

LOCAL MECHANICAL PROPERTIES 2009

LOKÁLNÍ MECHANICKÉ VLASTNOSTI 2009

November 11th to 13th, 2009

Telč, Czech Republic



Organized by the Czech Technical University in Prague
in cooperation with
Technical University of Košice
and West Bohemian University in Plzeň

2009

s263

Preface

Following the progress in the development of the nano/micro-level experimental equipment local mechanical properties have become a very attractive subject for many researchers. It is well documented also by the growing attendance of already 6th international seminar on **Local Mechanical Properties**. The seminar was held on November 11th-13th, 2009 in Telč, South Bohemia.

The 2009 year was organized by Dr. Jiří Němeček and his team from the Department of Mechanics, Faculty of Civil Engineering, Czech Technical University in Prague in cooperation with Technical University of Košice and West Bohemian University (ZČU Plzeň). It was attended by around 50 participants from both academia and industry covering several European countries (the Czech Republic, Slovakia, Poland, Switzerland, Germany, Bulgaria and Ukraine). The seminar followed well established traditions found in previous years in Košice 2004 and 2005, Plzeň – Nečtiny 2006, Brno – Šlapanice 2007, Herlany near Košice 2008.

The scope of the seminar was focused on the presentation of research results in the field of experimental methods, material engineering, computations and modeling of material behavior and the assessment of its local mechanical properties at nano/micro-scale. Contributions on nanoindentation and other methods for hardness assessment, measurement of deformations and stresses, time-dependent properties and related microstructure analyses (ESEM, AFM, XRD, etc.) are included in the contributions.

EDITORS

doc. Ing. Jiří Němeček, Ph.D. (ČVUT Praha)
prof. Ing. Ladislav Pešek, CSc. (TU Košice)
doc. Ing. Olga Bláhová, Ph.D. (ZČU Plzeň)

LOCAL ORGANIZING COMMITTEE

doc. Ing. Jiří Němeček, Ph.D. (ČVUT Praha)
Ing. Pavla Pečová (ČVUT Praha)
Ing. Jaroslav Lukeš (ČVUT Praha)

SEMINAR CO-CHAIRMEN

prof. Ing. Ladislav Pešek, CSc. (TU Košice)
doc. Ing. Olga Bláhová, Ph.D. (ZČU Plzeň)

SCIENTIFIC COMMITTEE

doc. Ing. Olga Bláhová, Ph.D. (ZČU Plzeň)
Dr. Eng. Małgorzata Garbiak (WPUT, Szczecin)
RNDr. František Lofaj, DrSc. (IMV AV, Košice)
prof. Ing. Jaroslav Menčík, CSc. (Univ. Pardubice)
doc. Ing. Jiří Němeček, Ph.D. (ČVUT Praha)
prof. Ing. Ladislav Pešek, CSc. (TU Košice)
Ing. Pavol Zubko, Ph.D. (TU Košice)

Declaration

All contributions included in this journal special issue were reviewed before publication by members of the scientific committee.

SUPPORTERS



Content

Invited papers

<i>Malgorzata Garbiak</i>	Applying microhardness to microstructure analysis	s267
<i>František Lofaj, Jiří Němeček, Olga Bláhová</i>	A comparative study of the nanoindentation measurements on thin coatings	s271
<i>Jaroslav Menčík</i>	Determination of parameters of visco-elastic materials by instrumented indentation. Part3: rheological model and other characteristics	s275
<i>Jiří Němeček, Jaroslav Lukeš</i>	On the evaluation of elastic properties from nanoindentation of heterogeneous systems	s279
<i>Galina Zamfirova, V. Gaydarov, T. Zaharescu, L.G.A. Silva</i>	Microindentation study of electron beam irradiated polyamide samples	s283

Regular papers

<i>Lubomír Ambriško, Ladislav Pešek, Stanislava Hlebová</i>	Determination of plastic zone by UCI technique on thin steel sheets	s287
<i>Olga Bláhová</i>	The influence of preoxidation on local mechanical properties of Zr-alloys	s291
<i>Petr Bohac, Radim Ctvrtlik, Martin Stranyanek</i>	Potential utilisations for nanotesters	s295
<i>Jan Brumek, Bohumír Strnadel, Ivo Dlouhý</i>	Use of genetic algorithm for identification of nonlinear constitutive material models	s299
<i>Renata Dvořáková, Emil Svoboda, Karel Maňas</i>	Application of the surface roughness spectrum analysis at diagnosing functional performance of armament components	s303
<i>Renata Eichlerová, Jaroslav Lukeš, Svatava Konvičková, Pavel Bradna</i>	Effect of time on nanoindentation elastic modulus of three different dental restorative composites	s307
<i>Petra Gavendová, Pavol Zubko, Ladislav Pešek And Olga Bláhová</i>	Determining the stress – strain relationship by depth sensing indentation on two construction materials	s310
<i>Libor Holáň, Jaroslav Pokluda, Karel Slámečka,</i>	Local aspects of shear-mode crack propagation in austenitic steel	s314
<i>Šárka Houdková, Olga Bláhová, František Zahálka</i>	Evaluation of mechanical properties of hvof sprayed coatings by the CSM indentation method	s318
<i>Zdeněk Joska, Miroslav Pospíchal, Jaromír Kadlec, Jiří Sukáč</i>	Mechanical properties of duplex system: zrn coating on plasma nitrided stainless steel	s322
<i>Michaela Kašparová, Šárka Houdková, František Zahálka</i>	Adhesive-cohesive strength of Cr ₃ C ₂ -NiCr HVOF sprayed coatings	s326

<i>Róbert Kočiško, Pavol Zubko, Juraj Ďurišin, Mária Molnárová, Andrea Kováčová, Michal Kvačkaj, Július Bacsó</i>	The mechanical properties of OFHC copper after ECAP processing	s330
<i>Antonín Kříž, Petr Beneš, Jiří Šimeček</i>	Impact test of surface	s334
<i>Jaroslav Lukeš, Josef Šepitka, Jiří Němeček</i>	Dynamic nanoindentation of bovine intervertebral end plate	s338
<i>Joanna Maszybrocka, Jerzy Cybo, Adrian Barylski</i>	Changes of micromechanical properties of ultra high molecular weight polyethylene after electron beam irradiation and uniaxial compression	s342
<i>Rostislav Medlín, Olga Bláhová, Václav Švorčík</i>	Evaluation of Au thin film on polyethylene and glass	s346
<i>Mária Mihalíková, Lubomír Ambriško, Ladislav Pešek</i>	The hardness analysis of the if steel sheet after a plastic deformation	s350
<i>Mária Molnárová, Tibor Kvačkaj, Róbert Kočiško, Lenka Némethová</i>	Evaluation of carbon content in austenite by indirect method	s353
<i>Martin Négyesi, Olga Bláhová, Jaroslav Burda, Věra Vrtílková</i>	Experimental background for diffusion models of Zr1Nb-O system	s356
<i>Jiří Nohava, Petr Haušild</i>	New grid indentation method for multiphase materials	s360
<i>Jan Řiha, Olga Bláhová, Pavol Šutta</i>	Mechanical properties and structure of Zr-Nb alloy after high-temperature transformations	s364
<i>Libor Severa, Jaroslav Buchar, Jiří Němeček, Šárka Nedomová</i>	Nanoindentation as a new tool for evaluation of hen's eggshell local mechanical properties	s368
<i>Hanna Smolenska</i>	Effect of temperature and gaseous medium on the structure and microhardness of the cobalt base clad layers	s371
<i>Jaroslav Sobota, Jan Grossman, Jiří Vyskočil, Rudolf Novák, Tomáš Fořt, Tomáš Vitů, Libor Dupák</i>	Could humidity affect the mechanical properties of carbon based coatings?	s375
<i>Marie Válová, Jan Suchánek, Olga Bláhová</i>	Characteristics of duplex coating steels	s378
<i>Václav Veselý, Zbyněk Keršner, Jiří Němeček, Petr Frantík, Ladislav Řoutil, Barbara Kucharczyková</i>	Estimation of fracture process zone extent in cementitious composites	s382
<i>Josef Volák, Václav Mentl</i>	Testing of small local zones by means of small punch test at room and creep temperatures	s386
<i>Pavol Zubko, Ladislav Pešek, Ivana Zajacová, Olga Bláhová</i>	Mechanical properties of thermoplastic composites	s390

APPLYING MICROHARDNESS TO MICROSTRUCTURE ANALYSIS

MALGORZATA GARBIAK *

*West Pomeranian University of Technology, Al. Piastów 17
70-310 Szczecin
Malgorzata.Garbiak@zut.edu.pl*

Keywords: microhardness, microstructure, histogram

1. Introduction

Along with conventional characterisation methods (chemical or phase composition, macrohardness, grain size distribution etc), the microhardness distribution pattern might be the quantitative metallography analysis tool to uniquely characterise the microstructure and quantify material properties¹.

Microhardness testing is widely employed to conduct the study on individual phases, diffusion gradients, aging phenomenon, etc. The sensitivity of hardness measurements (the ability to distinguish changes and thus structural components of the material) depends on many factors. One of them is the loading force which has to be selected for a given microstructure.

The main potential difficulty in microhardness measurements concerns the possible dependence of microhardness values on the test load. As the test load is reduced below a certain threshold, the measured microhardness value may tend to decrease or increase depending on the material². The general principle is that the microhardness tests carried out on individual phases need to use as large a load as possible to ensure the repetitiveness of measurements. However, for simple comparison of relative microhardness, the values obtained at a fixed load can be used without the need to allow for a load dependence. Assuming the above, the random microhardness measurements conducted under a small load can be applied to characterise and compare the changes in microstructure of alloys with different thermal history.

The aim of this work is to use a microhardness indentation technique to detect the effect of annealing process on microstructure evolution in creep resistant 0.3C-30Ni-18Cr cast steel.

2. Material and Tests

The austenitic 0.3C-30Ni-18Cr cast steel with varying content of Nb, Ti and Si was used for investigations³. The content of individual elements varying within the chemical composition of the tested cast steel is shown in

Table I. The samples were investigated in the as-cast and heat treated condition. The annealing process was conducted at 900 °C for 300 hrs, then the samples were cooled down with furnace.

Table I
The content of Ti, Nb and Si [wt.%] in 0.3%C-18%Cr-30%Ni cast steel

Alloy no	Ti	Nb	Si
1	0.83	1.75	1.69
2	1.00	0.03	1.82
3	0.05	1.84	1.82
4	0.70	3.00	4.00
5	0.03	0.03	1.69
6	1.07	1.59	4.26
7	0.53	2.80	3.54
8	0.30	0.55	1.57
9	0.68	2.06	1.76

The phase constituents were investigated by X-ray diffraction method on cross-sections and isolates extracted from the as-cast and annealed alloys^{3,4}. The microstructure analysis was performed by optical and scanning microscopy.

Microhardness tests were carried out by the Vickers method, pressing statically the indenter under a load of 5G and at the 100 times magnification of a Buehler Micromet 2100 microhardness tester. The value of load was chosen basing on the results of the preliminary tests and studies. The measurements were taken on polished metallographic cross-sections of unetched specimens. One hundred random measurements were taken for each alloy tested.

The results of the measurements were processed with a Statistica software.

3. Results and discussion

The idea of applying microhardness measurements to describe the microstructure of austenitic cast steel is based on an assumption that different values of the hardness of individual phase constituents should give different modes on the histogram of microhardness distribution. One might also expect that changes in matrix due to the processes of precipitation, phase transformation and/or coagulation should leave their “fingerprints” on hardness distribution, too¹.

Before proper random microhardness measurements were taken, the preliminary tests had been done to estab-

lish the best choice of the indenter load values. To achieve this goal, 60 random measurements were taken on one of the examined cast steel specimens applying the loads of 50, 25, 10 and 5G. The results of the measurements in the form of respective histograms are shown in Fig. 1a and b.

The load of 50G gives a unimodal histogram of normal distribution. When the load is reduced, the run of the histogram changes. The distribution bar is reduced in height and enlarged in width. If the examined feature is microhardness of a single phase, a change of this type will suggest that the deviation of standard mean is increasing, and under such conditions reducing of load would practically make no sense.

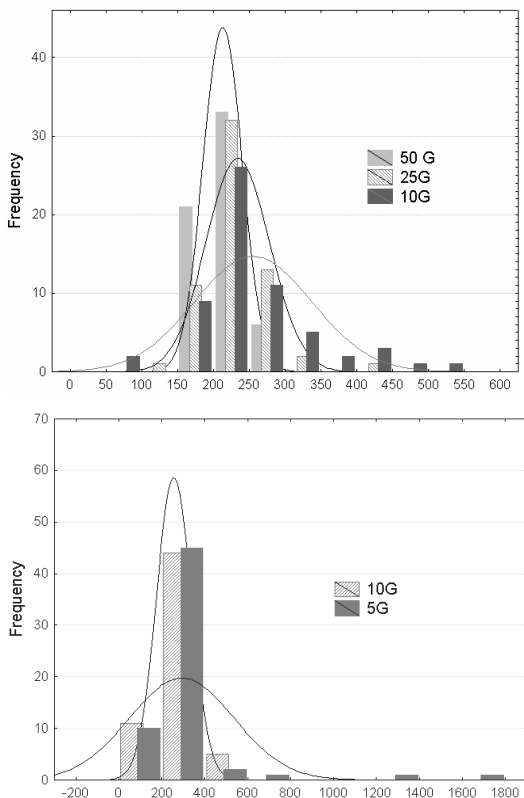


Fig. 1. Microhardness frequency distribution obtained for different load: a) 10, 25 and 50G, b) 5 and 10G

When the random measurements are taken on a multi-phase material, which the examined cast steel certainly is, an increase in the value of the examined feature proves that what is measured is the hardness of a single phase constituent. And this is precisely what the carried out tests aim to do. To obtain complex information on alloy microstructure, it is necessary to answer, first of all, the question whether it is possible to distinguish between the individual constituents of this microstructure. This is why reducing the load seems to be a proper course in measurements of this type, especially when the target is, for example, the estimation of volume fraction of the individual phase constituents. Smaller loads increase the prob-

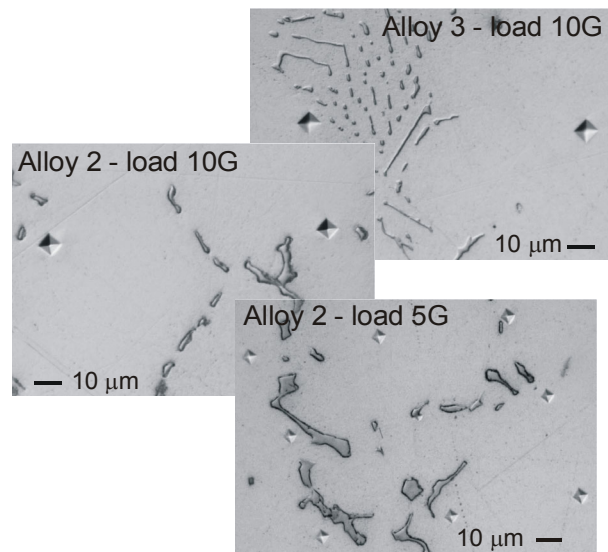


Fig. 2. Indentations made on the cross-section of alloys with Nb (alloy 3) and with Ti (alloy 2) under a load of 10 and 5G

ability of making indentations in the hard phase constituents, which have small size.

An example of indentations obtained on the cross-sections of alloys 2 and 3 under 10 and 5G load is shown in Fig. 2. As it has been assumed, the value of load should enable the indentation to be made in a selected monophase region only. For this purpose, the load higher than 5G seems to give too large indentations that extend through more than one phase, as can be observed, for example, in alloy 3, where the phase precipitates are very small, Fig. 2.

The measurements of microhardness were taken on all the examined alloys by making 100 random indentations under a load of 5G. The results of the measurements were processed to form binary histograms which compared changes in microhardness distribution obtained for each of the examined alloys before and after the process of annealing. Considering the type of changes, the alloys and the respective histograms of hardness distribution were divided into three groups:

- alloys in which no changes occurred (alloys 1 and 3),
- alloys which reduced the average matrix hardness (alloys 2, 5, 8 and 9), and
- alloys which increased the average matrix hardness and reported a quantitative increase in hardness HV on the right side of the histogram (alloys 4, 6 and 7).

The examples of histograms for each group are presented in Figs. 3–5. The range corresponding to the values below 100 HV was assigned to non-metallic inclusions or pores, often present in cast structure. The values above 500HV were assigned to other phase constituents⁵. The matrix is represented in the histograms by bars of the highest frequency of occurrence, and they create the prevailing mode of the histogram. Using mean hardness values in a given range and percent fraction of the measured hard-

ness values in this range, the mean hardness of the matrix and its changes ΔHV were calculated (Table II). Due to annealing, the mean matrix microhardness ΔHV either remains unchanged or changes in different modes, assuming positive or negative values.

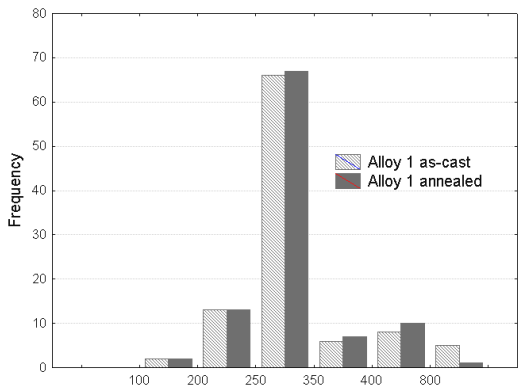


Fig. 3. Histogram of microhardness distribution in alloy no 1 in as-cast and annealing state

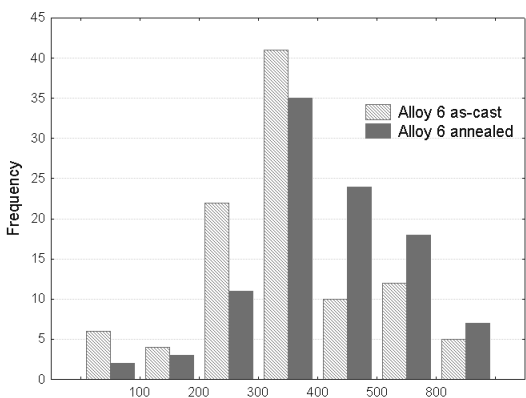


Fig. 4. Histogram of microhardness distribution in alloy no 6 in as-cast and annealing state

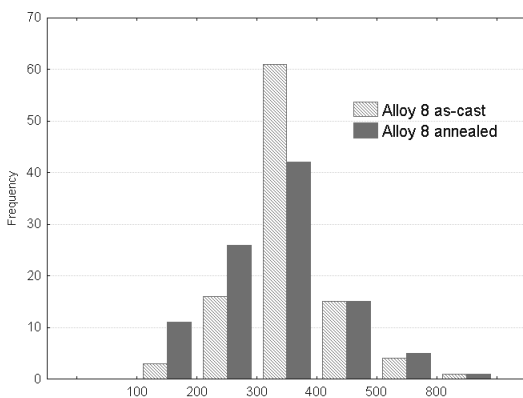


Fig. 5. Histogram of microhardness distribution in alloy no 8 in as-cast and annealing state

An increase of matrix hardness as well as a quantitative increase of the values corresponding to higher hardness levels (see Fig. 4) are related with the process of secondary precipitation and phase transformation occurring in the examined alloys³. This is the transformation of the simple MC type carbides (niobium and titanium carbides) into a high-silicon G phase, accompanied by a considerable increase in the volume of the precipitates, Fig. 6. The said transformation takes place within the temperature range of about 700–950 °C. Its intensity depends on the silicon content in alloy^{3,6} and on the content of Nb and Ti. Alloys with high content of these elements (alloys 4, 6 and 7) increase their hardness considerably. In alloys with the low content of Nb and Ti (alloys 2, 5 and 8) a drop of ΔHV has been reported to occur.

Table II
Microhardness of matrix, HV0.05

Alloy no	as-cast	annealed	ΔHV
1	294	295	1
2	277	247	-30
3	246	247	1
4	291	353	62
5	291	252	-39
6	310	331	21
7	260	318	58
8	343	315	-28
9	272	280	8

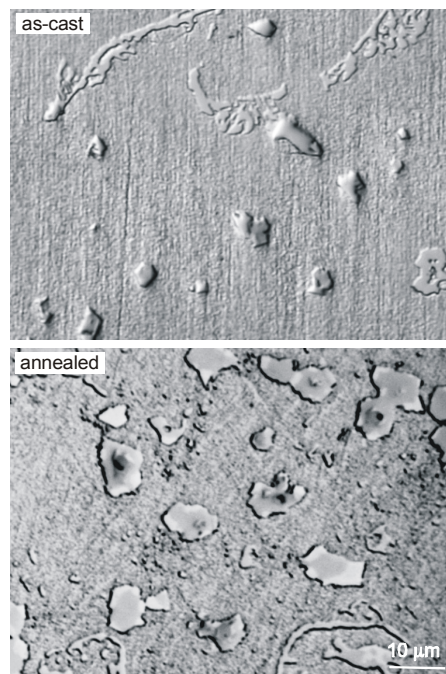


Fig. 6. Microstructure of alloy 6 in as-cast and annealed (900 °C, 300 hrs) condition

Changes in matrix microhardness (ΔHV) in function of the alloy chemistry were determined from a multi-dimensional regression analysis and described with equation (1), Fig. 7.

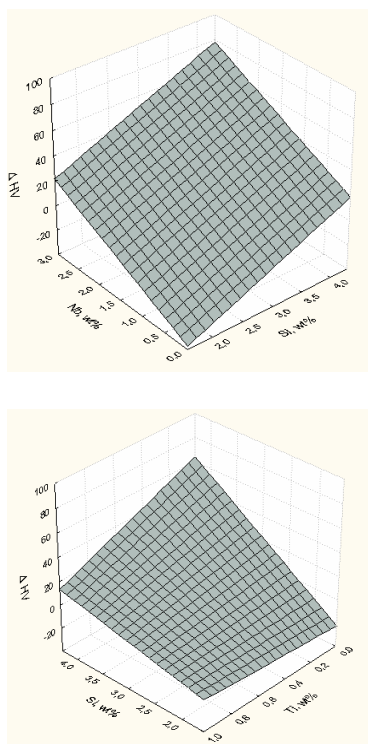


Fig. 7. Influence of Nb, Ti and Si on changes in the microhardness of matrix ΔHV due to annealing;

$$\Delta HV = -93.3 + 32 \cdot Si + 19.7 \cdot Nb + 45.4 \cdot Ti - 22.4 \cdot Si \cdot Ti; \quad (1),$$

$$R^2 = 0.9998, F = 2902$$

Very high correlation ($R^2 \sim 0.999$) was attained, which is indicative of underlying interrelationships between the chemistry, materials history and composition of non-homogeneous matrix.

In the group of the three examined elements, silicon is the one that has the greatest effect on changes in ΔHV , Eq. (1). High content of this element results in an increase of the matrix hardness, the greater, the more of niobium and the less of titanium are present in cast steel. Titanium confers to the examined cast steel the highest resistance to phase transformations. With maximum content of titanium, changes in matrix hardness due to the process of annealing are relatively small, Fig. 7.

4. Conclusions

The random measurements of microhardness under low loads enable complex evaluation of the microstructure

of a multi-phase material. Detailed analysis of microhardness distribution presented in the form of histograms enables, among others, the following:

- determination of mean matrix hardness,
- evaluation of the effect of alloy chemistry on changes in the matrix hardness due to annealing,
- tracing changes in microstructure caused by phase transformations and the secondary processes of precipitation through analysis of a quantitative increase in the value of HV.

A possibility also exists to use hardness distribution as a tool for quantitative evaluation of the phase constituents present in alloy microstructure. Increasing the sensitivity of measurements to improve the detectability of individual phases seems to be a key problem here. Because of the high hardness of phases present in the examined cast steel and their relatively small content, the applied method of microhardness measurements cannot allow further reduction of the load value and plotting a multimodal histogram in which the individual modes would describe single phase constituents. A solution might be here the random measurements using the method of nanoindentation.

REFERENCES

1. Christodoulou P., Garbiak M., Piekarski B.: *Mat. Sci. Eng.* 350, A457 (2007).
2. Xun Cai, Xiaoyu Yang, Pingnan Zhou: *J. Mat. Sci. Let.* 741, 16 (1997).
3. Garbiak M.: *PhD thesis*, Szczecin, 2006.
4. Chylińska R., Garbiak M., Piekarski B.: *Mat. Sci.* 348, 4 (2005).
5. Garbiak M., Chylińska R.: Microhardness of phase constituents present in creep-resistant cast steel. *Proc. LMV'2008, Herlany 3-5.11.2008*.
6. Ibañez R. A. P. et al: *Mat. Char.* 243, 30 (1993).

M. Garbiak (*West Pomeranian University of Technology*): **Applying Microhardness to Micro-Structure Analysis**

The random microhardness measurements of the creep resistant 0.3C-30Ni-18Cr cast steel with a varying content of Nb, Ti and Si were applied to characterize the changes in microstructure due to annealing at temperature 900 °C. The measurements were carried out using Vickers indenter and loading force of 5G. One hundred random measurements were taken from the metallographic cross sections for each alloy tested. The histogram analysis of changes in hardness distribution due to thermal processing of alloys was conducted with respect to the average hardness of matrix and phase precipitates. Multivariate linear regression analysis was implemented to determine quantitative relations between the changes in average microhardness of matrix and chemical composition of alloy.

A COMPARATIVE STUDY OF NANOINDENTATION MEASUREMENTS ON THIN COATINGS

**FRANTIŠEK LOFAJ^a, JIŘÍ NĚMEČEK^b,
and OLGA BLÁHOVÁ^c**

^a Institute of Materials Research of the Slovak Academy of Sciences, Watsonova 47, 040 01 Košice, Slovakia, ^b Czech Technical University in Prague, Thákurova 7, 166 29 Praha 6, Czech Republic, ^c University of West Bohemia, Univerzitní 8, 306 14, Plzeň, Czech Republic
flofaj@imr.saske.sk

Keywords: round robin test, nanoindentation, nanohardness, hard coatings

1. Introduction

Nanoindentation is a commonly used and accepted method for measuring local mechanical properties of the wide variety of materials ranging from biology to concretes and nanomaterials. Although nanoindentation was developed only two decades ago, it is already widely accepted experimental technique. The reason is that it provides unique information on hardness and elastic properties from very localized sites, which are unavailable by other mechanical methods. The method has been already standardized for both bulk metallic materials (ISO 14577 – Part 1 through Part 3 and ASTM E2546)^{1,2} as well as for metallic and non-metallic coatings (ISO 14577 – Part 4)³. However, the nanoindentation measurements and especially data interpretation are much more difficult in the case of very thin films on substrates with different hardness and elastic constants. Measurement on coatings requires the penetration depth is less than half of the coating thickness, no cracking can occur and the hardness of the coating is evaluated as a maximum or the plateau that appears in the hardness – penetration depth curve. Additional requirements include tip calibration, surface roughness $R_a < 5\% h_c$ (h_c is the penetration depth), and h_c must be smaller than 10–15 % of the film thickness to prevent substrate influence³. To satisfy this requirement, indentation load has to be reduced to μN or even nN range depending on the thickness and stiffness of the studied coatings. Partial unloadings during the loading in cyclic mode or in sinusoidal mode with much higher frequency provide very useful methods for the determination of full hardness – penetration depth curve and determination of the maximum or plateau indicating true hardness of the coating. Such techniques are available in most of the nanoindenter systems. However, the parameters of each nanoindentation system, e.g. frame stiffness, frequency range,

load accuracy, etc., are different, which affects the accuracy of the obtained data even if all testing parameters are identical. Additional effects that strongly influence the reliability of the obtained data involve the effects of the indentation size^{4,5}, surface roughness^{6,7} different tip geometry⁷, effects of grain size, residual stresses etc.⁸. An earlier international round-robin⁹, which was organized to evaluate the consistency of the data among different laboratories on the set of three different coatings indicated that the scatter within 7–14 % is achievable when the indenter area function is calibrated, thermal drift eliminated, the requirements on surface roughness fulfilled and full hardness-penetration depth curve is known. This work was done on model samples with very low roughness specially prepared for this purpose. The required parameters are often not available in the real samples because surface roughness $\leq 3\text{ nm}$ in the case of 500 nm films is difficult to achieve. Moreover, the accuracy and possibilities of nanoindenters continuously increase and new types are being introduced. Besides dedicated nanoindenters from the well established producers, nanoindentation heads are available for atomic force microscopes (AFM) and universal stands. Nanoindentation can also be performed by direct use of AFM tips. The comparison of the data obtained from such systems is not yet available. Therefore, the aim of the work is to investigate the consistency and reliability of nanoindentation data on a set of non-standard thin coatings obtained on different types of nanoindenters.

2. Experimental procedure

Three different types of coatings were deposited on the polished hardened steel substrates by PE-CVD method: WC-C, Cr-C and TiN coatings with Ti sublayers. The microstructure of the coatings was investigated by scanning electron microscopy in order to estimate their roughness and thickness. The thicknesses were in the range from 300 to 600 nm. Hardness range of these coatings was from several GPa up to 30 GPa. The set of three coatings on the substrates with the size of $20 \times 20 \times 3\text{ mm}^3$ were distributed to five participating laboratories, which included research and university institutions as well as company laboratories. The names of the participating laboratories are therefore intentionally denoted only as A, B, C, etc. The laboratories used different types of nanoindenters – three participants have dedicated nanoindenters and two laboratories used nanoindenter heads on the universal support and on the AFM base, respectively. Two basic modes were chosen for nanoindentation tests with the Berkovich indenter on the coatings: – single loading – unloading cycle with the loading up to 1.5 mN within 10 s, dwell time of 10 s and unloading in 10 s, and – sinusoidal/cyclic mode

with the maximum load of 10 mN reached within 20 s, dwell time of 10 s followed by unloading within 20 s. Because the testing conditions in the sinusoidal mode depend on the system possibilities, they were not identical in all laboratories. On the other hand, the tendency was to be close to the prescribed conditions. Two laboratories made over 180 indents for each coating, another 50 indents, then > 36 and the last laboratory made only one measurement. The last laboratory was therefore not included in the analysis. Three laboratories supplied complete sets of data and plots and two submitted only a table with final data. All the data was collected at one site for an independent evaluation.

3. Results and discussion

SEM observations of the coatings revealed that their thickness was ≥ 500 nm while their surface roughness varied: Cr-C coating was the smoothest, TiN film exhibited significant waviness with small amplitude. W-C coating was similar to Cr-C but its amplitude seemed to be bigger. It also contained local delamination “buckles”. All coatings contained agglomerates which are larger than the features on the remaining surface. However, the roughness was not measured prior to indentation.

The data provided by the participating laboratories included testing conditions, hardness and indentation modulus values with the corresponding standard deviations. They are summarized in Tab. I. The data was analysed using two different approaches: pure statistical which is based only on the measured values and more experimental approach, when the loading – unloading curves or hardness – penetration depth curves are taken into con-

sideration to determine of the value of the corresponding parameter.

Pure statistical approach indicates large scatter of the data and excessive differences among laboratories in some cases. Tab. II summarizes the scatter of the hardness and indentation modulus relative to the corresponding value reported by the laboratory. The scatter in single loading – unloading mode in W-C coating is always above 20 % in all laboratories, which is systematically larger than in the other coatings. Laboratory C even reported scatter > 150 % for hardness and around 80 % for indentation modulus. These values were considered problematic and they were not included in further analysis. Such a large scatter seems to originate from considerably larger set of indents made at this laboratory (around 200 indents) and consideration of all data without intentional selection rather than from the problems with the measurement. The smallest values of around 13 % are mostly obtained in Cr-C coating followed by TiN coating. The differences among the laboratories in these two coatings are relatively small. The scatter values obtained for indentation modulus are often slightly lower than in the case of hardness values: hardness scatter in single mode is in the range from 9 % to 66 % (153 % in lab. C) whereas that of indentation modulus is in the range 3.9 % to 49 % (79 %).

Scatter range is approximately the same or slightly more narrow in sinusoidal/cyclic mode. Hardness scatter is from 6 % to 35 % whereas indentation modulus from 5 % to 32 %. Obviously, elastic modulus exhibits slightly smaller scatter than hardness.

When single loading – unloading data from different laboratories are compared, the values from the laboratory A exhibit the lowest scatter and the highest scatter appears

Table I
Summary of the nanoindentation data from the participating laboratories

Sample	Lab.	Single (1.5 mode mN)		Sinus mode/ Cyclic (10 mN)	
		H _{IT} [GPa]	E _{IT} [GPa]	H _{IT} [GPa]	E _{IT} [GPa]
Cr-C	A	12.9 ± 1.7	179.8 ± 11.7	12.7 ± 2.2	184.4 ± 14.9
	B	19.0 ± 2.3	240.6 ± 21.3	12.9 ± 2.2	239.6 ± 48.0
	C	15.2 ± 6.9	221.8 ± 71.6	18.2 ± 3.5	257.9 ± 31.3
	D	11.7 ± 1.8	199.6 ± 15.0	–	–
	(0.5 mN)	10.7 ± 1.9	159.4 ± 14.3	–	–
W-C	A	14.2 ± 3.1	180.3 ± 23.0	13.2 ± 2.3	148.2 ± 22.6
	B	23.9 ± 6.6	388.8 ± 92.0	12.0 ± 5.0 at 80; 16.0 ± 4.0 at 30 nm	395.0 ± 156.0 at 80 nm 327.1 ± 69.1 at 30 nm
	C	3.9 ± 5.9	124.2 ± 98.6	–	–
	D	10.7 ± 2.9	245.5 ± 52.6	–	–
	E	3.1	18.7	–	–
TiN	A	5.2 ± 0.6	66.7 ± 2.6	5.1 ± 0.4	48.1 ± 15.2
	B	7.8 ± 1.0	164.7 ± 14.1	5.8 ± 2.0	181.0 ± 51.0
	C	5.6 ± 3.7	139.6 ± 68.6	7.8 ± 0.5*	175.2 ± 9.3
	D	5.7 ± 0.5	161.2 ± 9.6	–	–
	0.5 mN	6.1 ± 1.0	135.4 ± 12.2	–	–

Table II

The comparison of the relative scatter for the measurements of hardness and indentation modulus from each laboratory. The underlined values were not considered in further analysis

Lab./ sample	Single mode 1.5 mN $\pm H_{IT}$ [%]	mode $\pm E_{IT}$ [%]	Sinus/ Cyclic 10 mN $\pm H_{IT}$ [%]	mode $\pm E_{IT}$ [%]
A				
Cr-C	13.1	6.5	17.6	8.1
W-C	21.8	12.8	17.5	15.2
TiN	12.3	3.9	8.7	31.5
B				
Cr-C	12.1	8.8	16.8	20.0
W-C	27.5	23.7	24.8	21.1
TiN	12.9	8.6	34.5	28.9
C				
Cr-C	45.6	32.3	19.2	12.1
W-C	<u>(153.8)</u>	<u>(79.4)</u>	–	–
TiN	66.5	49.1	6.0	5.3
D				
Cr-C	15.4	3.0	–	–
W-C	27.1	21.4	–	–
TiN	8.8	5.95	–	–

in the data from laboratory C. In cyclic/sinusoidal mode, laboratory C reported the lowest scatter and laboratory B the largest. This may be due to larger number of indents in B and C compared to the number of indents in laboratory A and because laboratories B and C used maxima from depth penetration curves obtained in sinusoidal mode. Besides maximum scatter, the frequency of maximum and minimum values were considered to be negative and smallest scatter a positive in ranking the reliability of the data among the laboratories. Based on this approach, the data from laboratory A followed by laboratory D is the most consistent in single loading – unloading mode. Similar evaluation in cyclic/sinusoidal mode is more difficult, because this mode was not available in laboratory D and laboratory C provided data for only two coatings. Again, the data from laboratory A seems to be more consistent than that from laboratory B. When extrapolation to three measurements is used for the data from laboratory C, it is between the values obtained for A and B.

The drawback of such evaluation is that it does not consider experimental differences: only 36 indents were considered in A case and 150–200 indents were involved in B and C cases. The depth penetration curve from cyclic mode in A case often missed the maximum whereas it was usually pronounced in sinusoidal mode used in the laboratories B and C. According to the standard³, the maximum corresponds to the true value of the corresponding parameter, but the extreme values were considered as negative in ranking consistency of the data on statistical approach. The

necessity to involve experimental details in the evaluation of the consistency of the data is emphasized.

The review of 180 load – penetration depth curves in Cr-C sample in single loading-unloading mode showed the range of penetration depths from 80 nm to maximum of around 430 nm, but most of the curves were grouped below 80 nm. TiN coating, despite having slightly higher roughness exhibited very similar behavior. The situation was more complex in W-C coating. The range of the penetration depths was the same as in Cr-C, but the curves were distributed without preferential grouping. It results in extreme standard deviations in this coating (see Tab. I and Tab. II). The trends for each coating in cyclic mode were analogous.

Such behavior can be explained by the effects of surface roughness. It was estimated at one of the laboratories from surface profiles. The average amplitude of the surface profile in Cr-C sample was below 15 nm, but few occasional peaks with the amplitude up to 110 nm were present. In TiN, the amplitudes were usually from 20 to 70 nm but the number of large peaks in the excess of 200 nm was significant. Finally, the amplitudes in W-C coating were usually within the range of 150 nm with the peak values up to 500 nm.

Obviously, the conditions for surface roughness defined in ISO standard³ are not fulfilled. Penetration depths under load of 1.5 mN were usually < 100 nm and the maxima appeared in sinusoidal mode below the same depths. The condition of surface roughness $R_a < 5\%$ of penetration depth means that the amplitudes of surface profile have to be < 5 nm. This was not achieved even in the case of Cr-C coating. However, because the difference between the required and actual roughness was not excessive, only few indentation curves were strongly affected and most of the curves were within reasonably narrow band. The increase of surface roughness in TiN and W-C coatings led to deterioration of the conditions for the assumed geometry of the contact between the surface and indenter tip and to the increase of the scatter of measured parameters.

Despite the fact that the roughness of the studied coatings did not satisfy standard requirements, most of thin films on structural components would be in the same situation. Therefore, the ways to extract sufficiently reliable data from non-standard samples are essential for practical purposes. Careful selection of the main group of curves in single loading – unloading mode is the simplest but rather subjective approach suitable only for homogeneous materials. The location of indents only into flat and defect-free areas of the coating is another possibility. It can also be used in dual or multi-phase materials. Finally, sinusoidal mode and its detailed penetration depth dependencies offer much better resolution of „true“ values than cyclic mode where the maximum of the curve is often lost or as the single loading-unloading cycle when the resulting value depends strongly on the maximum load. The minimum depth to obtain reliable and physically meaningful data from sinusoidal mode on the coatings with the thickness of

500 nm is around 40 nm. It is more than < 20 nm found in the earlier mentioned round-robin⁹ achieved on coatings with considerably lower roughness.

4. Conclusions

The nanoindentation data from four (five) laboratories on three different coatings with non-standard roughness in single loading – unloading and cyclic/sinusoidal modes scatter from ~ 8 % to 30 %. Scatter up to 45 % or even > 100 % can be achieved depending on the extent of deviation of surface roughness from 5 % of penetration depth limit and the mode of loading (single loading – unloading, cyclic, sinusoidal). The lowest scatter was measured in Cr-C coatings with the roughness close to the limit and the highest scatter in W-C coating with excessive roughness. Surface roughness seemed to be the major factor determining scatter and reliability of nanoindentation hardness and modulus. The analysis of each indentation test is essential when sufficiently large statistical sets of indents are evaluated without their preliminary localization. The sinusoidal mode is preferred compared to the cyclic mode and single load-unload cycle in determination of true values on thin coatings. The depth limit for the determination of hardness and indentation modulus on the coatings with roughness above the limit of 5 % of h_c is around 40 nm.

The contribution of M. Ferdinandy with coating preparation and the work of H. Pfaff, M. Schaefer and S. Vinzelberg who carried out the measurements at their laboratories are acknowledged. This work was supported by the Slovak Research and Development Agency under the contract No. APVV 0034-07, by the VEGA No. 2/0088/08, MNT-ERA.NET HANCOG as well as within the frame of the project „Centre of Excellence of Advanced Materials with Nano- and Submicron- Structure“, which is supported by the Operational Program “Research and Development” financed through European Regional Development Fund.

REFERENCES

1. ISO 14577-1:2002 Metallic materials – Instrumented indentation test for hardness and material parameters – Part 1: Test method; ISO 14577-2:2002 Metallic materials – Instrumented indentation test for hardness and material parameters – Part 2: Verification and calibration of testing machines; ISO 14577-3:2002 Metallic materials – Instrumented indentation test for hardness and material parameters – Part 3: Calibration of reference blocks.
2. ASTM E2546 New Standard Practice for Instrumented Indentation Testing.
3. ISO 14577-4:2007 Metallic materials – Instrumented indentation test for hardness and material parameters – Part 4 Test method for metallic and non-metallic coatings.
4. Nix W. D.: *Mat. Sci. Eng. A* 234-6, 37 (1997).
5. Huang Y., Zhang F., Hwang K. C., Nix, W. D., Pharr G. M., Feng G.: *J. Mech. Phys. Solids* 54, 1668 (2006).
6. Jiang W.G., Su J. J., Feng X.-Q.: *Eng. Fracture Mech.* 75, 4965 (2008).
7. Bouzakis K. D., Michailidis N., Hadjiyiannis S., Skordaris G., Erkens G.: *Mat. Characterization* 49, 149 (2003)
8. Ling Z., Hou J. P.: *Compos. Sci. Technol.* 67, 3121 (2007).
9. Lee K. W., Chung Y. W., Chan C. Y., Bello I., Lee S. T., Karimi A., Patscheider, J., Delplancke-Ogletree M. P., Yang D., Boyce B., Buchheit T.: *Surf. Coat. Technol.* 168, 57 (2003).

F. Lofaj^a, J. Němeček^b, and O. Bláhová^c (^a*Institute of Materials Research of SAS, Košice, Slovakia*, ^b*Czech Technical University in Prague, Czech Republic*, ^c*University of West Bohemia, Plzeň, Czech Republic*):
A Comparative Study of Nanoindentation Measurements on Thin Coatings

The comparison of the nanoindentation data from four (five) laboratories on Cr-C, W-C and TiN coatings with non-standard roughness in single loading-unloading and cyclic/sinusoidal modes indicates the scatter from 8 to 30 % but the scatter > 100 % can be achieved when surface roughness significantly exceeds 5 % of penetration depth limit. Surface roughness is the major factor determining scatter and reliability of nanoindentation hardness and modulus. The scatter can be reduced by careful selection of meaningful indentation tests from sufficiently large statistical sets or location of indents in the areas with low surface roughness. The sinusoidal mode is preferred compared to the cyclic mode and single load-unload cycle. The depth limit for the determination of hardness and indentation modulus on the coatings with roughness above the limit of 5 % of h_c is around 40 nm.

DETERMINATION OF PARAMETERS OF VISCO-ELASTIC MATERIALS BY INSTRUMENTED INDENTATION. PART 3: RHEOLOGICAL MODEL AND OTHER CHARACTERISTICS

JAROSLAV MENČÍK*

University of Pardubice, Studentská 95, 532 10 Pardubice, Czech Republic
jaroslav.mencik@upce.cz

Keywords: mechanical properties, instrumented indentation, nanoindentation, viscoelasticity, viscous-elastic-plastic deformations

1. Introduction

This paper is a continuation of the article Determination of parameters of viscoelastic materials by instrumented indentation^{1,2}. These two papers have explained basic formulae for elastic-plastic materials and for viscoelastic-plastic materials, where the deformations depend not only on the load magnitude, but also on its duration. Also recommendations were given there for the preparation of indentation testing of viscoelastic materials and for the evaluation of results. Two kinds of tests were recommended: a long lasting test under constant load for obtaining the constants in the creep compliance function, and a quick load-unload test for obtaining the “fast” elastic modulus and hardness, useful also for the decomposition of the time-independent component of the creep function into reversible and irreversible part.

This last paper, based on the experience from actual tests, theoretical analysis and literature, brings first a more detailed discussion and instructions for indentation testing of viscoelastic-plastic materials and for the creation of suitable analytical models. The second part of the paper shows additional information obtainable from the nanoindentation data: time course of apparent hardness, components of indentation deformations, and relative proportions of the individual terms in the creep compliance function.

2. Preparation of tests

The tests should be arranged with respect to the character of the tested material and its potential use. The arrangement regards especially the indenter kind and duration of tests. The stresses under a pointed indenter are very high, able to cause not only reversible viscoelastic deforming, but also irreversible plastic and viscous flow. This viscous flow can sometimes last very long, longer than the time practicable with common nanoindentation devices. On the other hand, many viscoelastic or viscoelastic-plastic materials are used for long term loading, but under rather low stresses. For such cases it is necessary to know

the duration of reversible viscoelastic processes and whether the data from relatively short tests may also be used for long term loading. Reliable information of this kind can be obtained, for example, in tests with a spherical indenter, where the stresses are so low that no plastic deforming or irreversible viscous flow occurs. These tests can also reveal the yield strength or stress corresponding to the onset of permanent deformations.

3. Finding optimum rheological model

If a new material with viscoelastic-plastic properties is investigated, it is reasonable to fit the experimental $h(t)$ data by various creep compliance functions (S+KV, S+2KV, S+3KV, S+D+KV, S+D+2KV, ..., in which S stands for a spring, D for dashpot, K and V for Kelvin and Voigt units, respectively), and choose the model with the best fit (Fig. 1). The general form of the regression function for a pointed indenter is^{2,3}:

$$h^2(t) = PKJ'(t) = PK\{C_0 + c_v(t - t_R/2) + \sum C_j [1 - \rho_j \exp(-t/\tau_j)]\} \quad (1)$$

where h is the depth of penetration, t is time, t_R is the duration of load increase from 0 to the nominal value P , $K = \pi/(4 \tan \alpha)$ is a constant for the indenter with the tip semian angle α , $J'(t)$ is the creep compliance function (modified for the ramp loading), c_v is the reciprocal of viscosity η_v of the dashpot (D) arranged in series with other elements, C_0 is the compliance of the alone-standing spring (S) for time-independent deformations, the constants C_1, \dots are compliances of the Kelvin-Voigt bodies (K-V), τ_j are their retardation times, and ρ_j are correction factors for the load increase period ($j = 1, 2, \dots, n$). The number n of the Kelvin-Voigt bodies and the presence or absence of the viscosity term correspond to the used model. For practical procedure see Refs.^{2,3}. The optimum parameters in each model can be found by the least squares method; subroutines for finding a minimum of a nonlinear function with several variables are present in various softwares; an example is Solver in Excel.

For models with only a few constants ($n \leq 4$), Solver easily finds the “best” parameters (C_0, C_1, τ_1, \dots). In models with more than four constants, various „optimum“ values of parameters are sometimes found depending on their

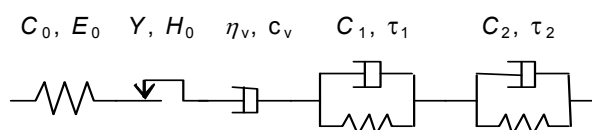


Fig. 1. Model of a viscoelastic-plastic body (S + D + 2KV)

starting values used in the search. The differences between the $J(t)$ curves for individual fits are often practically negligible. It is thus possible to choose fix retardation times τ_j , scaled in decades; for example $\tau_1 = 1$ s, $\tau_2 = 10$ s, $\tau_3 = 100$ s, etc. Solver then seeks only the constants C_0, C_1 , etc. In such cases, one should remember that C_1, C_2, \dots are no true physical constants, but rather parameters in the model, valid only for some range of loading time.

If several models give acceptable results, the particular model may be chosen with respect to its future use. Generally, the model need not be more complicated than necessary. For example, if a viscoelastic material will be used for applications with load lasting not longer than several seconds, the original universal complex model with several Kelvin-Voigt units and other terms, whose parameters were obtained in long-term tests, may be replaced by a simpler model with only three or four parameters, provided the quality of fit is sufficient for the expected interval of load duration.

When looking for a suitable model, one should keep in mind typical features of the response of a Kelvin-Voigt body (a spring in parallel with a dashpot in Fig. 1). Such body, whose response is described by expression $C_j[1 - \exp(-t/\tau_j)]$, is active within about two orders of time; roughly for $0.03 < t/\tau_j < 3.0$. For example, $1 - \exp(-0.03) \approx 0.03$; therefore, for $t/\tau_j < 0.03$, the body hardly started reacting, and until this time it behaves as if it were stiff. On the other hand, $1 - \exp(-3) \approx 0.95$, so that for $t/\tau_j > 3$ nearly the full deformation is reached, and the resultant response corresponds to the spring of compliance C_j alone.

If the viscoelastic-plastic material is assumed to be used for long-lasting loads, it is important to ascertain whether the indenter movement into the sample stops during the test (or exhibits the tendency to stop during a reasonable time), or not. The former case occurs, e.g., in tests with spherical indenters and low contact pressures, while the latter case is common in tests with pointed indenters, where the maximum contact stresses exceed the limit for enforced irreversible viscous flow.

If the indenter has stopped during the test, the number of K-V bodies should correspond to the number of time orders of this process. For example, if $t_{\text{stop}} = 1200$ s, four K-V bodies (with retardation times e.g. $\tau_1 = 1$ s, $\tau_2 = 10$ s, $\tau_3 = 100$ s and $\tau_4 = 1000$ s) are sufficient. In this case, the model may also be used for longer times.

If the indenter continues penetrating into the specimen at the end of test, the number of Kelvin-Voigt bodies should correspond to the duration of test, and the model may be used only for simulation of processes not significantly longer than this time. Extrapolation can be dangerous and large errors can appear; also the form of the creep compliance function $J(t)$ plays a role (Fig. 2). Thus, if there is no obvious tendency to indenter stopping, the test should last as long as possible, its duration (hours, days, weeks...) being limited by the time-stability of the indentation device.

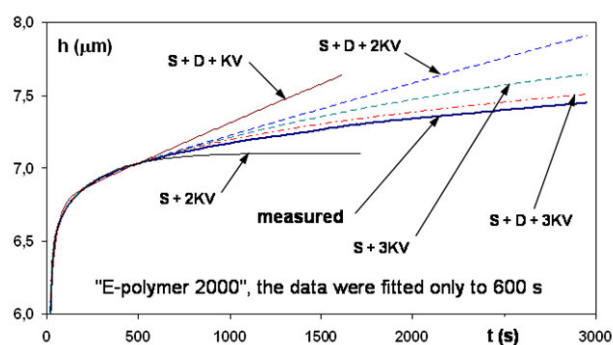


Fig. 2. Indenter penetration into a polymer: measured data and curves for various rheologic models

Also the load increase at the beginning of the test should be as fast as possible. The shortest retardation time, which can be revealed by the indentation test, τ_1 , will not be significantly shorter than the duration of load increase, t_R . Very short retardation times and processes with retardation times τ_j significantly shorter than t_R cannot be revealed, and their parameters are „hidden“ in the „instantaneous“ compliance constant C_0 . (For $t > 4\tau_1$, all K-V bodies behave practically as a spring alone, and their compliances add up to the „ideally instantaneous compliance $C_{0,\text{id}}$ “ and together make the „apparent instantaneous compliance C_0 “, obtained by fitting the $h(t)$ curve from the test under constant load. (Note that the rate of loading under harmonic loading by ultrasound frequency is higher than in common loading in nano-indentation tests, and also the values of elastic modulus, calculated from the velocity of sound propagation, are usually higher than those from indentation tests.)

4. Other characteristics from indentation into viscoelastic–plastic materials

Indentation tests can provide more information, for example the time course of apparent hardness. Useful also is the information about various components of the penetration depth, or about relative importance of individual deformation processes and their duration.

Apparent hardness $H(t)$

In nanoindentation tests, hardness is defined as the mean contact pressure under load, and characterises the resistance of material against penetration by another body. In viscoelastic materials, the mean contact pressure decreases with the time under (constant) load as

$$H(t) = P / A(t) \quad (2)$$

For a pointed indenter, $A(t) = kh_c^2(t)$. Cheng and Cheng⁴ have shown by finite-element modeling that the ratio of contact depth to the depth of penetration into viscoelastic materials is constant, independent on the rate or

duration of loading, $h_c/h = \text{const}$. According to Eq. (1), the squared depth of penetration is directly proportional to the creep compliance function, $h^2(t) \sim J(t)$. Therefore,

$$H(t) = \frac{P}{A(t)} = \frac{P}{k h^2(t)} \propto \frac{P}{J(t)} \quad (3)$$

so that $H(t)J(t) \sim P = \text{const}$. Thus, if the „instant“ hardness H_0 is known (from a quick load-unload test^{2, 3}), the apparent hardness $H(t)$, corresponding to the time t under load, can be calculated as

$$H(t) = H_0 \frac{J(0)}{J(t)} \quad (4)$$

where $J(0) = C_0$. Similar approach was used by Oyen⁵.

Components of indentation deformation

For design of parts loaded by a highly concentrated (pointed) load it is useful to know various components of the total deformation (permanent, time dependent, etc.). This knowledge also helps in formulating demands on the accuracy of indentation testing of a particular viscoelastic-plastic material. Best is the expression of individual quantities in relative form. Figure 3 shows the typical points on the displacement curve during a long-term load-unload test: h_1 is the depth at the end of quick loading, h_2 is the depth at the end of the dwell under load, h_3 is the depth at the end of quick unloading, and h_4 is the final (residual or permanent) depth, measured long time after unloading. These characteristic depths of penetration (corresponding to the times t_1, t_2, t_3, t_4) can be used in defining the following nondimensional quantities:

$h_1/h_2 =$
time-independent (“instantaneous”) component of the total deformation at time t_2 ,
 $(h_2 - h_1)/h_2 =$
time-dependent component of the total deformation at t_2 ,
 $(h_2 - h_4)/h_2 =$
total reversible component of the total deformation at t_2 ,
 $h_4/h_2 =$
total irreversible comp. of the total deformation at t_2 ,

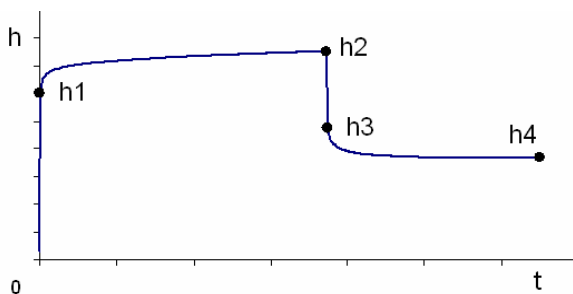


Fig. 3. Characteristic depths of penetration during indentation into a viscoelastic-plastic material

$(h_2 - h_3)/h_2 =$
time-independent reversible component of the total deformation at t_2 ,
 $(h_3 - h_4)/h_2 =$
time-dependent reversible deformation related to the total deformation at time t_2 ,
 $(h_2 - h_3)/h_1 =$
time-independent reversible component of the total time-independent deformation (at time t_1),
 $(h_3 - h_4)/(h_2 - h_1) =$
time-dependent reversible deformation related to the total time-dependent comp. of deformation at time t_2 ,
 $[(h_2 - h_1) - (h_3 - h_4)]/(h_2 - h_1) =$
time-dependent irreversible deformation related to the total time-component of deformation at time t_2 ,
 $[h_1 - (h_2 - h_3)]/h_1 =$
time-dependent irreversible deformation related to the total time-component of deformation at time t_2 .

Relative importance of individual deformation processes and their duration

The elements in a spring-and-dashpot model can correspond to various processes in the material, though these relations can be rather free. The individual constants C_0, C_1, C_2, \dots in the creep compliance function reflect the significance of processes of various duration (characterised by retardation times τ_1, τ_2, \dots), and can help in their identification. Nondimensional expressions $C_1/C_0, C_2/C_0, \dots$ or $C_0/C_\infty, C_1/C_\infty, C_2/C_\infty, \dots$ express the relative proportions of individual processes, and are more universal than the proportions of the components of the penetration. They can also be used to describe the spectrum of relaxation processes, common, e.g., in the characterisation of polymers exposed to periodic loading of variable frequency.

5. Conclusions

Viscoelastic-plastic response to load can be described by rheological (spring-and-dashpot) models and the corresponding creep compliance function $J(t)$. Standard creep compliance functions are very flexible. They can also be used in the commercial software for the finite element analysis. The parameters in the models can be determined from the time course of indenter penetration under constant load. For more complex models, they are no true physical constants, but parameters valid for some range of loading time. The test should last till the indenter stops penetrating, or as long as possible (with regards to the application). Extra-polation of $J(t)$ to very long times can sometimes cause significant errors.

It is impossible to distinguish directly the reversible and irreversible parts of the „instantaneous“ compliance C_0 . The corresponding quantities E_0 and H_0 are better obtained from separate tests with very fast loading and unloading.

Indentation tests can provide more information, for

example about the time course of apparent hardness $H(t)$, about the relative importance of various components of the depth of penetration, and about the relative importance of various deformation processes and their duration.

This work was supported by the Grant Agency of Czech Republic, project GAČR 103/08/1340.

REFERENCES

1. Menčík J.: Chem. Listy, in print (2010).
2. Menčík J.: Chem. Listy, in print (2010).
3. Menčík J., He L. H., Swain M. V.: J. Mechan. Behavior Biomed. Mater. 2, 318 (2009).
4. Cheng Y. T, Cheng Ch.-M.: J. Mater. Res. 20, 1046 (2005).
5. Oyen M. L.: Philosophical Magazine 86, 5625 (2006).

J. Menčík (University of Pardubice): Determination of Parameters of Viscoelastic Materials by Instrumented Indentation. Part 3: Rheological Model and Other Characteristics

The paper is a continuation of two previous articles^{1,2} on the characterisation of viscoelastic-plastic behaviour by nanoindentation. It explains the basic terms, shows characteristic features of the indentation response of these materials and brings instructions for their testing by depth-sensing indentation and for the creation of suitable analytical (spring-and-dashpot) models. Then it shows further information obtainable from the nanoindentation data: time course of apparent hardness, components of indentation deformations, and relative proportions of the individual terms in the creep compliance function.

ON THE EVALUATION OF ELASTIC PROPERTIES FROM NANOINDENTATION OF HETEROGENEOUS SYSTEMS

JIRÍ NĚMEČEK* and **JAROSLAV LUKÉŠ**

Czech Technical University in Prague, Thákurova 7,
166 29 Prague 6, Czech Republic
jiri.nemecek@fsv.cvut.cz

Keywords: nanoindentation, elastic properties, heterogeneity, deconvolution

1. Introduction

Nowadays, nanoindentation is a well established method used for obtaining quantitative data on elastic and inelastic material properties in small volumes, typically in submicron length scale. It is frequently used for extracting of intrinsic material properties of distinct phases that can be found in the microstructure of heterogeneous systems. Typical example of such system can be a composite material consisting of prevailing matrix phase and individual, layered or fiber inclusions. The microstructure of composites can be well defined if mixing proportions are known in advance and if the phases do not chemically react. However, this is not a case of many structural materials like metal alloys, cementitious materials and others. In the later case, the distinction of individual phases and their adjacent mechanical properties is not straightforward and some indirect (deconvolution) method for finding of individual component properties has to be involved^{1,2}.

The extraction of material properties from nanoindentation on a heterogeneous system often relies on the fact that the volume affected by an indenter is small enough not to mechanically interact with other phases. As a rule of a thumb, the indentation depth is usually chosen as 1/10 of the characteristic size of the measured inclusion or phase^{3,4}. Then, indentation focused on the inclusion or statistical grid indentation can be employed to receive intrinsic properties. However, these methodologies can provide the access to intrinsic phase properties only in case that the indentation response of one phase is not influenced by another. In the literature, the solution of a mutual influence in the matrix-inclusion system is rather rare. The situation of phases with different stiffness was studied for thin films placed on a substrate e.g. by Gao et al.⁵. It was shown by Gao that the substrate effects are negligible if the stiffness mismatch ratio is:

$$E_{\text{substrate}}/E_{\text{film}} \in [0.2; 5] \quad (1)$$

as long as the indentation depth is smaller than 10% of the film thickness.

The layered substrate-film system is not completely

equivalent to the disordered structural multiphase materials but it can be successfully used as the first estimate.

The FE solution of the hemispherical inclusion (with radius R) surrounded by the matrix with different elastic modulus was solved by Kabele et al.⁶ (Fig. 1). Elastic modulus was calculated from the unloading curve by the Oliver-Pharr⁷ method at different penetration depths and for different ratios of elastic moduli. Fig. 1 shows the dependence of the error in the resulting modulus on the penetration depth h for different ratios of matrix (E_1) and inclusion (E_0) elastic moduli. However, the presence of matrix with a different elastic modulus distorts the results. The error increases with increasing penetration depth and increasing difference between elastic moduli of matrix and inclusion.

For a typical ratio of $h/R=0.1$ the error in estimation of elastic modulus by Oliver-Pharr method can be in the range 13–25 % for the given stiffness mismatch ratio $(E_1-E_0)/E_0 \in [1;5]$ as shown in Fig. 1 for the case of soft inclusion laying in a hard matrix (i.e. positive values in Fig. 1). In case of hard inclusion embedded in a soft matrix (negative values in Fig. 1) the situation is even worse and the error can be doubled. Due to problems with numerical stability of the FE model only a few values are plotted in the negative range of Fig. 1 but the general trend of larger errors is indicated here.

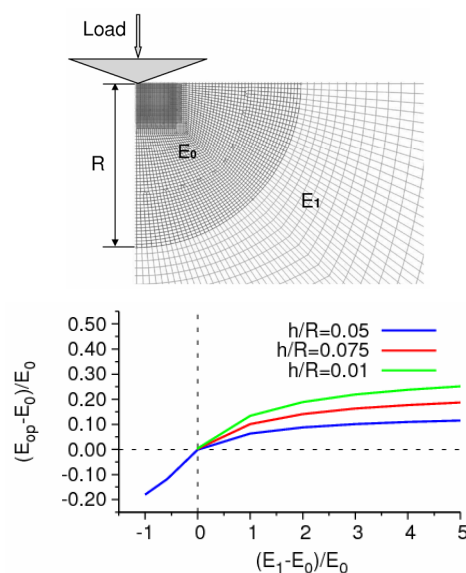


Fig. 1. Effect of hemispherical inclusion. Top: Axially symmetric FE model. Bottom: Normalized difference between the elastic modulus evaluated by Oliver-Pharr procedure (E_{op}) and the actual modulus of inclusion (E_0) for different normalized indentation depths (h/R) and different ratios between matrix and inclusion moduli $(E_1-E_0)/E_0$

2. Methods

In order to evaluate the mutual influence of phases in heterogeneous systems three types of samples (type A, B and C) based on soft epoxy, hard gypsum and the hardest zinc particles were prepared. The size of inclusions was chosen to be in micrometer range which is common in many composites. Separate samples of pure sample constituents were also prepared in order to assess their intrinsic material properties. Nanoindentation was employed in all micromechanical measurements. Samples A and B represent the case of stiff inclusions embedded in a soft matrix and samples C the case of soft inclusions lying in a hard matrix.

First, pure phases were indented and elastic properties in terms of reduced elastic moduli were evaluated⁷. Then, composite materials were indented by means of massive grid indentation in order to receive large statistical set of data from all phases. Large number (more than 300) of indents was performed on each sample and elastic properties were computed for individual imprints. The size of indents was chosen to be approximately less than 10 % of the characteristic inclusion size to minimize the effect of phase interactions. Individual results were analyzed again by standard method⁷. Subsequently, histograms of elastic properties of all phases were plotted and analyzed by means of statistical deconvolution^{1,2}.

If there were no interaction effects in composites the phase properties (found as peaks in histograms) should agree with intrinsic properties of the pure phases which was not the case as shown later in the paper.

3. Sample preparation

Samples of type A were made of gypsum matrix (dental gypsum powder Interdent® and water, 5:1 by weight, denoted as Gypsum1) mixed with hard zinc particles (see Fig. 2). These samples satisfy the condition given in Eq. (1). Samples of type B were prepared from soft epoxy matrix (Struers Epofix®) and zinc particles, exceeding the condition of Eq. (1). For type C, hard gypsum matrix was filled with soft Epofix particles obtained from grinding of the bulk Epofix material. Due to the addition of high surface particles into the composite the amount of water had to be increased for higher concentration (samples C2) to maintain workability (the water content was increased by 30 %, further denoted as Gypsum2). The average particle size of zinc was 3.4–3.9 μm (samples A and B) and similarly of Epofix inclusions (samples C).

Volume concentrations used for preparation of samples are summarized in Tab. I together with ratios of elastic moduli between the phases. Mechanical properties were measured by nanoindentation of separate phases and in a composite (see Tab. II). Trapezoidal loading diagram, consisting of 10 s of linear loading (0.1 mN s^{-1}), 10 s of holding at constant peak force 1mN and 10 s of unloading (0.1 mN s^{-1}), was prescribed for all indents. The corre-

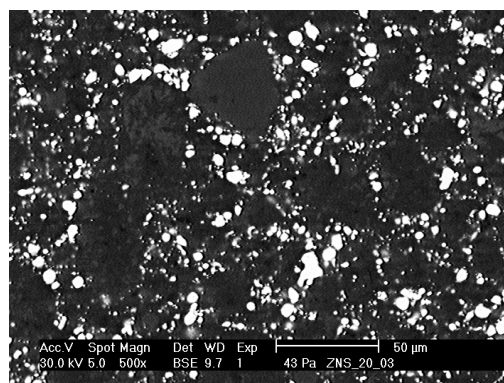


Fig. 2. ESEM image of Gypsum-Zinc sample A3 (Zn=11%)

sponding maximum penetration depths varied according to the indented phase from 80 to 450 nm with an average around 150 nm for samples A, 300 nm for samples B and 190 nm for samples C. The separation between individual indents was set 10 μm .

4. Results

Estimates of elastic properties and volume concentrations were obtained from statistical deconvolution in which two Gaussian distributions were optimally fitted into experimental histogram as illustrated in Fig. 4 for the sample A3. As expected, the estimates varied from that measured on pure phases depending on the stiffness mismatch ratio and phase volume concentrations in the matrix-inclusion system.

It can be seen in Fig. 3 that the major peak in the probability density function moves towards higher values as the concentration of zinc in the gypsum-zinc composite increases. For higher concentration (A3) a significant second peak appears in the histogram. It shows on the presence of the second phase (zinc) which could not be properly recognized for lower concentrations less than 11 % (A1 and A2). Similar situation can be found for Epofix-

Table I
Concentrations of sample components

Sample	Gypsum [vol. %]	Epofix [vol. %]	Zinc [vol. %]	$\frac{E_{r_matrix}}{E_{r_inclusion}}$
A1	96.4	–	3.6	0.41
A2	92.7	–	7.3	0.41
A3	89.0	–	11.0	0.41
B1	–	88.3	11.7	0.042
B2	–	67.9	32.1	0.042
B3	–	40.9	59.1	0.042
C1	98.3	1.7	–	9.67
C2	95.0	5.0	–	9.67

zinc system (Fig. 5). For concentrations higher than 11.7 % (B2 and B3), two peaks can be found with the mean shifting to higher values.

It has to be emphasized that neither the mean values of the peaks nor the volume concentrations do not strictly agree with those measured separately as shown in Tab. II. If the concentration of inclusions is small in the composite (case of A1, A2, B1 and C1) then the mean values evaluated by deconvolution are relatively close to the real ones for the matrix phase. Properties of inclusions are not determined well in any case of hard inclusions embedded in a soft matrix (A and B). On the other hand, if the concentration of inclusions increases the error caused by mutual phase influence is also increasing rapidly both for inclusions as well as for matrix properties.

If inclusions are soft compared to the matrix (samples C) then the deconvoluted properties are in better agreement with those measured separately for inclusions in terms of elastic moduli but the volume fractions are several times overestimated. Addition of Epofix inclusions to Gypsum2 matrix causes creating of the second peak in the histogram as shown in Fig. 6 mainly for C2 samples. Errors in the assessment of elastic properties and volume concentrations, computed as

$$\text{error} = \frac{(E_r^C - E_r^S)}{E_r^S}$$

are shown in Tabs. III and IV for all matrices and inclusions, respectively.

Table II
Elastic (reduced) moduli (GPa) of sample components and their volume fractions

	Component	Measured separately	Measured in composite	
		E_r^S [GPa]	E_r^C [GPa]	[vol. %]
A1	Gypsum1	42.83±10.49	44.76±6.82	94.4
A1	Zinc	105	70.41±10.9	5.6
A2	Gypsum1	42.83±10.49	45.43±6.60	84.9
A2	Zinc	105	66.36±8.18	15.1
A3	Gypsum1	42.83±10.49	50.06±8.69	76.1
A3	Zinc	105	73.28±6.09	23.9
B1	Epofix	4.43±0.45	5.35±0.87	94.1
B1	Zinc	105	14.95±7.85	5.9
B2	Epofix	4.43±0.45	4.99±0.86	71.7
B2	Zinc	105	12.97±7.55	28.3
B3	Epofix	4.43±0.45	7.36±1.99	69.5
B3	Zinc	105	23.97±11.0	30.5
C1	Gypsum1	42.83±10.49	41.09±14.25	93.9
C1	Epofix	4.43±0.45	10.40±2.56	6.1
C2	Gypsum2	42.23±14.98	29.77±16.89	73.9
C2	Epofix	4.43±0.45	4.95±1.14	26.1

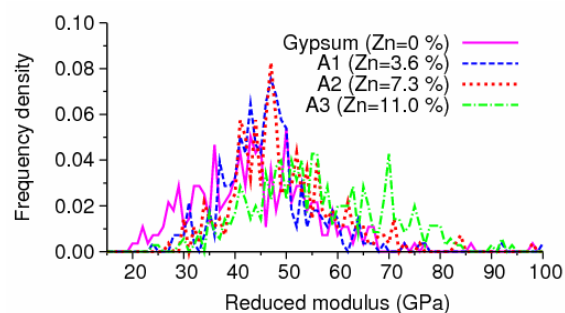


Fig. 3. Experimental probability density functions of gypsum-zinc system (samples A)

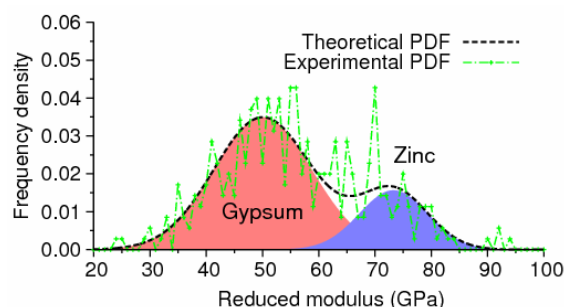


Fig. 4. Deconvolution of experimental probability density function of gypsum-zinc system (sample A3) in two phases

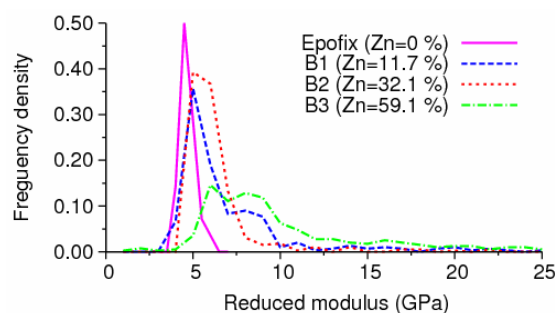


Fig. 5. Experimental probability density functions of Epofix-zinc system (samples B)

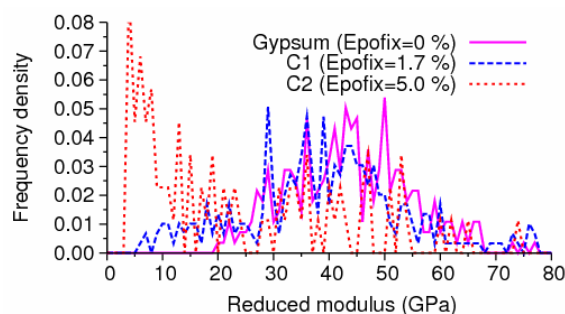


Fig. 6. Experimental probability density functions of gypsum-Epofix system (samples C)

5. Conclusions

By a series of nanoindentation tests on different types of heterogeneous matrix-inclusion systems it was found that the mutual influence of differently stiff phases prevents direct utilization of standard evaluation of elastic properties combined with the statistical deconvolution method in many cases. Although indent's dimension did not exceed 10% of the inclusion size their true intrinsic properties could be evaluated only if the inclusion was softer than the matrix (samples C2). Error in the estimation of elastic modulus was 11.7 % (Tab. III) in this case which agrees well with numerical results (13 %, Fig. 1) for the given stiffness mismatch ratio.

Matrix properties could be estimated well if inclusions were hard or soft and their concentration was low, up to 30 % (samples A1, A2, B1, B2 and C1). Otherwise in-

clusions can influence the estimated matrix stiffness especially in case of soft matrix filled with high concentration of hard particles (samples B3, error = 66.1 %, Tab. III).

Volume concentrations were not estimated well in almost all studied cases, especially in case of inclusions where it can reach hundreds of percent.

The presented study points out a very important effect of mutual influence of matrix and inclusion systems that can be considered as model systems of many natural composites including metal alloys, cementitious composites, inclusion reinforced composites, etc. If a heterogeneous system contains large differences in stiffness between the phases or the concentration of one phase is high compared to others than the error in stiffness or concentration estimates can reach more than 100 %. Thus, the situation is more dramatic compared to layered systems (e.g. thin films on a substrate)

Table III

Errors in estimation of elastic moduli and volume concentrations for matrices

Sample	Matrix	Error in E_r ^a [%]	Error in volume concentration [%]
A1	Gypsum1	4.5	-2.1
A2	Gypsum1	6.1	-8.4
A3	Gypsum1	16.9	-14.5
B1	Epofix	20.8	6.6
B2	Epofix	12.6	5.6
B3	Epofix	66.1	69.9
C1	Gypsum1	-4.1	-4.5
C2	Gypsum2	-29.5	-22.2

^a+...overestimation, -...underestimation

Table IV

Errors in estimation of elastic moduli and volume concentrations for inclusions

Sample	Inclusion	Error in E_r ^a [%]	Error in volume concentration [%]
A1	Zinc	-32.9	55.6
A2	Zinc	-36.8	106.8
A3	Zinc	-30.2	117.3
B1	Zinc	-85.8	-49.6
B2	Zinc	-87.6	-11.8
B3	Zinc	-77.2	-48.4
C1	Epofix	134.8	258.8
C2	Epofix	11.7	422.0

^a+...overestimation, -...underestimation

Supports of the Czech Science Foundation (GAČR 103/09/1748) and Academy of Sciences (IAA200710801) are gratefully acknowledged. P. Kabele and D. Davydov (CTU Prague) are acknowledged for their help with FE computations.

REFERENCES

- Constantinides G., Chandran K. R., Ulm F.-J., Vliet K. V.: *J. Mater. Sci. Eng. A* 430 (2006).
- Němeček J., Forstová K., Němečková J.: *Proc. of the 12th International Conference on Civil, Structural and Environmental Engineering Computing, Civil-Comp Press, 2009.*
- Buckle H.: American Society for Metals, (J. W. Westbrook, H. Conrad, ed.) 1973.
- Durst K. et al.: *J. Mater. Res.* 19 (1) (2004).
- Gao H., Chiu C., Lee J.: *Int. J. Solids and Structures* 29 (20) (1992).
- Kabele P., Davydov D., Jůn P., Němeček J., Jirásek M.: *Proceedings of Concreep 2008.*
- Oliver W., Pharr G.: *J. Mat. Res.* 7 (1992).

J. Němeček and J. Lukeš (*Czech Technical University in Prague, Faculty of Civil Engineering*): **On the Evaluation of Elastic Properties from nanoindentation of Heterogeneous Systems**

The paper describes errors that can be encountered in the estimation of elastic properties and volume concentrations by nanoindentation of a heterogeneous composite system using standard methodology (Oliver-Pharr method and statistical deconvolution). Several examples of matrix-inclusion systems (hard or soft matrices) showed on the importance of the knowledge of inclusion size, concentration and stiffness mismatch ratio of the phases. Standard procedures and estimates based on statistical grid indentation can lead to more than 100% errors for high concentrations or high stiffness ratios as documented on several examples of artificial composites.

MICROINDENTATION STUDY OF ELECTRON BEAM IRRADIATED POLYAMIDE SAMPLES

GALINA ZAMFIROVA*^a,
V. GAYDAROV^a,
T. ZAHARESCU^b, and **L. G. A. SILVA**^c

^aTransport University "T. Kableskov", 158, Geo Milev Str., 1576-Sofia, Bulgaria, ^bInstitute for Electrical Engineering, (INCDIE ICPE CA), 313 Splaiul Unirii, P. O. Box 149, Bucharest 030138, Romania, ^cInstituto de Pesquisas Energéticas e Nucleares (IPEN / CNEN - SP) Av. Professor Lineu Prestes 224205508-000 São Paulo, SP, Brazil.
 gzamfirova@mail.bg

Keywords: polyamide, Vickers microhardness, total microhardness, irradiation annealing.

1. Introduction

It has been established that when polymers are irradiated with elementary particles (electrons, neutrons, gamma rays, protons, alpha particles, X-rays or other particles, or their combinations) they inject energy into the material. E-beam radiation is a form of ionizing energy which is characterized generally by its low penetration and high dosage rates¹. The energy from the electrons absorbed could provoke some molecular or supermolecular changes and as a consequence leads to the structural modification of the irradiated materials. Moreover, the dosage of the radiation and not the dose rate is important in producing the desired improvement.

In polymers such as polyamide, the irradiation produces competing reactions, scission or cleavage and cross linking depending predominately on the dosage of irradiation, but also on the temperature, environment and on other conditions^{2,3}.

The cleavage reaction, which predominates at low irradiation doses, results in the breakdown of the long polymer chains into shorter ones. The cross-linking reaction, which predominates at high irradiation doses, results in the association of the polymer molecules into a network structure. At intermediate doses there is a mixture of the two reactions. Cleavage normally results in a decrease of tensile strength and modulus of elasticity, whereas cross-linking increases both the tensile strength and the modulus of elasticity. If the dosage is excessive, complete cross-linkage may take place but the samples become brittle. It is desirable the dosage to be such as to enhance the cross-linking without producing brittleness. According to the US

Patent 4,015,133 the irradiation dosage should be between $10^4 - 10^{10}$ rads⁴.

The study reports on polyamide 6 samples irradiated by an electron beam and the changes in their microhardness parameters provoked by irradiation. The aim is to establish the optimal irradiation dosage regarding the mechanical properties of the material. The supposed structural changes during the radiation are described by the results from the microindentation studies.

2. Experimental

Material

Polyamide 6 (PA 6) samples were supplied by Radici Plastics Ltd. The injection equipment was Battenfeld TM 1000. The thickness of the samples is 2 mm, which guarantees no influence of the subtract hardness. The density is $1.12 - 1.15 \text{ g cm}^{-3}$ and melting point is $215 - 220 \text{ }^\circ\text{C}$.

The preexposure doses were 100, 200, 400 and 600 kGy at a dose rate of 22.4 kGy s^{-1} .

Methods

Vickers microhardness device (mhp -160 at microscope UN-2) was used. The indenter was a regular square diamond pyramid, with top angle 136° . The measurements were provided at room temperature. Loads between 1.25÷160 g were used.

The microhardness methods used and characteristics measured were the following:

Mayer's lines are a logarithmic dependence between applied load P and dimension of indentation diagonals d . This dependence comes from Mayer's power law:

$$P = ad^n \quad (1)$$

Respectively in a logarithmic form;

$$\lg P = \lg a + n \lg d$$

where a and n are physical parameters. Constant a depends on the strength properties and constant n depends on the plastic features of the investigated material. The slope of these lines n is sensitive to non-uniformity of the structure in the depth of the sample. When $n < 2$ or $n > 2$ it means that microhardness decreases or increases, respectively, in the depth of the sample. If $n = 2$ Vickers microhardness is approximately constant along the depth.

Vickers microhardness MHV is a physical value characterizing the local resistance against plastic deformation during penetration. It is connected with the irreversible component of the deformation and is calculated according to the equation:

$$MHV = KP/d^2 \quad (2)$$

where d is the projected diagonal length of the imprint after releasing the indenter and K is a constant, depending on the geometry of the pyramid.

Total microhardness MHT^5 , which is connected with the total deformation, includes elastic, plastic and viscoelastic components. It is given by a similar equation:

$$MHT = KP/D^2 \quad (3)$$

where D is the projected diagonal length of the indentation in the loaded state. Thus defined this value can be considered as a measure for the total penetration resistance of the material.

Microhardness profiles are dependences of the microhardness as a function of the depth of indentation, h , respectively, of the applied load, P .

$$MHV=f(h); MHT=f(h); MHV=f(P); MHT=f(P) \quad (4)$$

It should be noted that if in the depth h MHV , respectively MHT , are determined, this value does not correspond to the real microhardness exactly in this depth. This value includes microhardness properties of all the layers situated between the surface and this depth.

3. Results and discussion

Mayer's lines

Fig. 1 shows the Mayer's lines and n – calculated from their slope parameter. For all samples n value is larger than 2, which shows the general tendency for hardness increasing in the direction perpendicular to the surface. This type of hardness nonuniformity is characteristic for semicrystalline polymers because the crystals in the surface layers are not well formed compared with the inner layers as a result of faster cooling during sample preparation. Steric reasons also contribute to this tendency. All irradiated samples have parameter n smaller than that of the initial material, which means the irradiation promotes diminishing of this undesirable tendency.

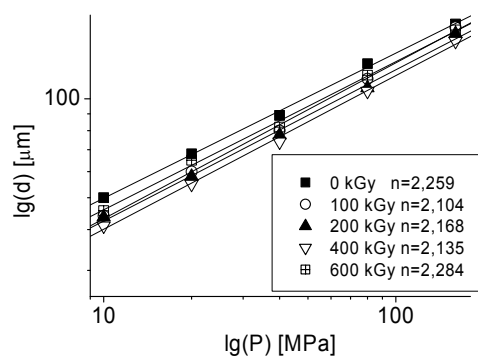


Fig. 1. Mayer's lines

Microhardness profiles

Vickers microhardness profiles for all samples are revealed in Fig. 2. These dependencies specify how MHV values change in the direction perpendicular to the surface. As seen the above mentioned hardness increasing in the depth as a tendency is related predominantly to the surface layer (till $h \approx 80 \mu\text{m}$ and $P \approx 40 \text{g}$), then MHV values remain almost constant. For the nonirradiated sample MHV increases continuously in the whole investigated range of applied loads. Consequently the irradiation favours the structural equalization in the inner layers, but not that in the surface layers.

The straight lines in Fig. 2b connect the MHV values for all samples measured at one and under the same load. Only the data for the sample irradiated with dose 600 kGy do not lie on the linear dependences. That means some drastic changes in the material structure take place in the interval 400–600 kGy.

It is interesting that these lines are almost parallel, except the line at 10 g, revealing that the MHV change with the indentation depth remains the same and does not depend on the applied load.

$$\text{If } P = \text{const} \rightarrow \Delta MHV / \Delta h \approx \text{const}. \quad (5)$$

Fig. 3 presents the MHT profiles of the initial PA sample and the irradiated samples plotted versus applied

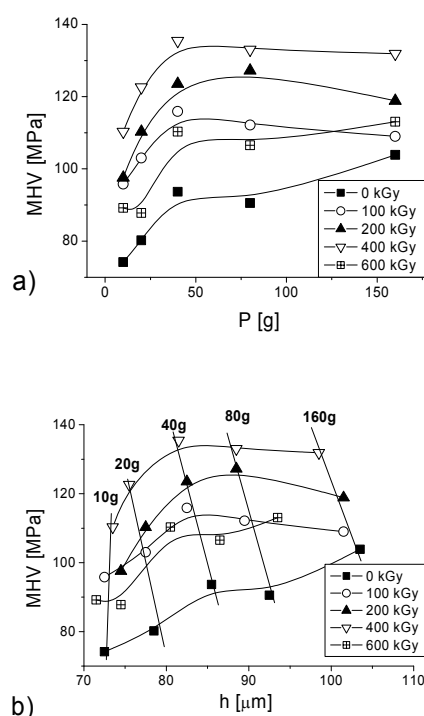


Fig. 2. MHV profiles for initial sample and for samples irradiated with different dose plotted vs. applied load (a) and vs. indentation depth (b)

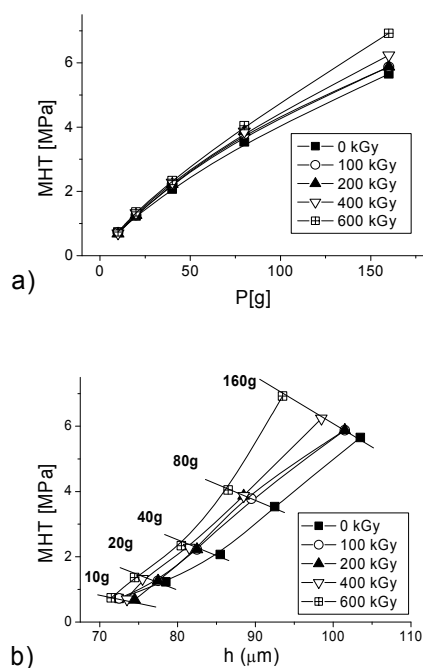


Fig. 3. MHT profiles for initial sample (□) and for samples irradiated with different doses plotted vs. applied load (a) and vs. indentation depth (b)

load P (Fig. 3a) and versus indentation depth h (Fig. 3b). The trend of these curves could be interpreted as follows: Although the total microhardness is a local characteristic, it forms its values not only from the material layers which the indenter penetrates but also from a larger material zone under the indenter, where the material is deformed not only plastically but elastically as well. That is why at bigger applied loads, deeper penetration, respectively, usually the total resistance against penetration increases similar to the resistance increase in the compressed spring – the bigger applied load, the stronger resistance.

The deviation from ideal straight line is due to the presence of the plastic deformation component, but the slope of these dependencies, if approximate to a straight line, could be a rough measure for the elastic properties of the samples. In this case the increasing of the irradiation dose improves the elastic properties.

Influence of the irradiation dose

Comparing Fig. 4a and Fig. 4b, presenting the influence of irradiation dose on Vickers microhardness and total microhardness respectively, it is evident that absorbed energy causes a different effect on these mechanical characteristics. The fast electrons provoke increasing of MHV till about 400 kGy and then a decreasing, while MHT is almost not sensitive to irradiation dose.

Knowing that Vickers microhardness characterizes

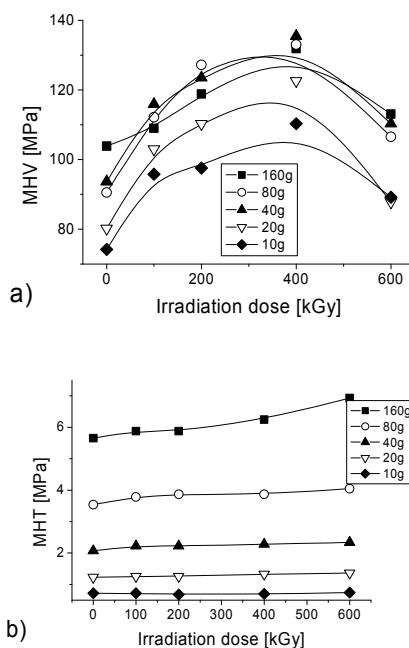


Fig. 4. Vickers microhardness (a) and Total microhardness (b) vs. irradiation dose

plastic resistance against local deformation, for crystal polymers consisting of crystal and amorphous phases, this value could be considered as a constitutive from the inherent contribution of each of the both phases. It is the so called additive law:

$$MHV = f \cdot MHV_c + (1-f) \cdot MHV_a \quad (6)$$

where f is the degree of crystallinity and MHV_c and MHV_a are the inherent Vickers microhardness of the crystal and amorphous areas. But as usual $MHV_a \ll MHV_c$ and practically could be ignored.

$$MHV = f \cdot MHV_c \quad (7)$$

So, Vickers microhardness as a measure of plastic resistance against penetration depends predominantly on quantity and quality of the crystals. In this case irradiation influences mainly the crystal phase, respectively, the plastic properties of the material and almost does not influence the elastic ones. As Vickers microhardness is in a power ratio to modulus of elasticity, E ($MHV = aE^b$, a and b are material constants) MHV increase roughly signifies a modulus increase also.

As mentioned in the introduction many authors prove that at small doses the scission processes prevail and crosslinking dominates at higher doses. It has been established for PE, and probably it is true for polyamides also, that Vickers microhardness is sensitive to molecular weight only for relatively short macromolecules ($M_n < 10^5$). For larger molecules this parameter does not influence

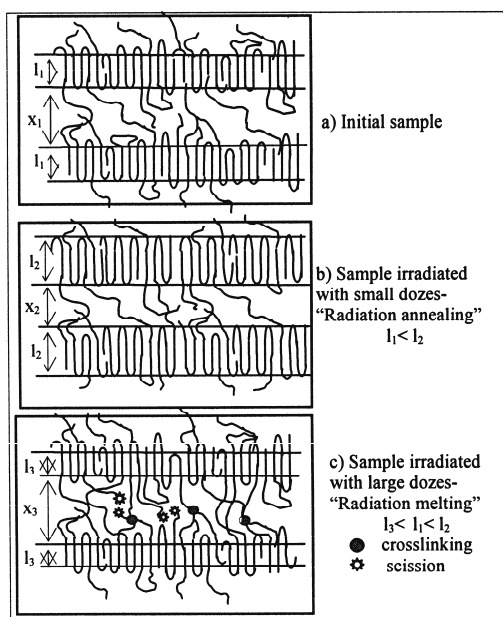


Fig. 5. Scheme of supermolecular structure of the initial sample (a) and the supposed structural changes during irradiation annealing (b) and radiation melting (c); l – lamella thickness, x – interlamella distance

MHV values. Crosslinking on principle takes place in the amorphous zones increasing resistance against elastic deformation, but in our case of microindentation measurement this effect is not remarkable. So, all chemical changes provoked by irradiation do not have direct influence on the micromechanical properties, but changes in the supermolecular structure, especially in the crystal phase, cause the changes in the micromechanical behavior.

We suppose that the small quantity of the irradiation contributes to so called "irradiation annealing"⁶. It consists in decreasing the lamella defects and interlamella stresses. Also a little enlarging of the lamella thickness and improving the lamella surface take place on account of the molecule ends or molecule loops.

When irradiation doses are high the structural changes are related to the so called "radiation melting"⁶. It consists in pushing some defects or mayhems in the crystal lamella to its surface. Most probably it is due to the transport of energy by excitons along the macromolecules and in this way the lamella surface becomes more defective, hence lamella thickness decreases a little. Destructions and crosslinkings occur simultaneously predominately in disordered zones. Fig. 5 shows the scheme of the supposed structural changes.

4. Conclusions

Irradiation of polyamide 6 with an electron beam influences the mechanical properties in the following way:

- Till about 400 kGy resistance against local plastic deformation increases, the module of elasticity increases, respectively. This is due to changes in the crystal phase known as a "radiation annealing". At higher doses Vickers microhardness and modul of elasticity decrease because of so called "radiation melting".
- Total microhardness does not change during the irradiation.
- Microhardness profiles demonstrate nonuniformity in sample structure. Surface layers are softer than the inner ones. Irradiation prevents the undesirable tendencies and leads to structural equalization in the inner layers, but not of the surface ones.

The study was supported by the NSF – Bulgaria, (D002-138/2008-2011).

REFERENCES

1. Timus D. M., Cincu C., Bradley D.A., Craciun G.: Appl. Radiat. Isot. 53, 937 (2000).
2. Zaharescu T., Silva L. G. A., Jipa S., Kappel W.: Radiat. Phys. Chem., Article in Press.
3. Ferro W. P., Silva L. G. A.: Radiat. Phys. Chem. 71, 269 (2004).
4. Ferrari H.: Method of producing string of polyamide and stringed rackets and stringed musical, US Patent 4,015,133, 29 Mar., 1977.
5. Zamfirova G., Dimitrova A.: Polym. Test. 19, 533 (2000).
6. Nedkov E., Tsvetkova S.: Radiat. Phys. Chem. 43, 397 (1994).

G. Zamfirova^a, V. Gaydarov^a, T. Zaharescu^b, and L. G. A. Silva^c (^aTransport University "T. Kableshkov", Sofia, Bulgaria, ^bInstitute for Electrical Engineering, Bucharest, Romania, ^cInstituto de Pesquisas Energéticas e Nucleares São Paulo, SP. Brazil.): **Microindentation Study of Electron Beam Irradiated Polyamide Samples**

The study reports on PA samples irradiated by an electron beam and the changes in their microhardness parameters provoked by irradiation. It has been established that total microhardness is not sensitive to irradiation dose, while Vickers microhardness passes through a maximum for samples irradiated with dose of 400 kGy. That means that irradiation affects predominantly the crystal phase. The crystal structure passes through the so called "irradiation annealing", followed by "irradiation melting".

DETERMINATION OF PLASTIC ZONE BY UCI TECHNIQUE ON THIN STEEL SHEETS

LUBOMÍR AMBRIŠKO*^a, LADISLAV PEŠEK^a, and STANISLAVA HLEBOVÁ^b

^a Department of Material Science, Faculty of Metallurgy, Technical University of Košice, Park Komenského 11, 043 85 Košice, Slovakia, ^b Faculty of Mechanical Engineering, Technical University of Liberec, Studentská 2, 461 17 Liberec 1, Czech Republic
lubomir.ambrisko@tuke.sk

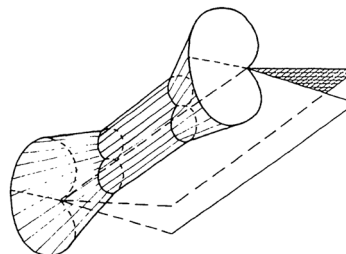


Fig. 1. Three-dimensional plastic zone²

Keywords: plastic zone, UCI, videoextensometry, thin sheet

1. Introduction

The size of the plastic zone at the tip of a crack is a very important factor in the fracture behavior of metallic materials. Depending on the size of the plastic zone, brittle, quasi-brittle and ductile materials are differentiated. In the fracture of non-brittle materials nearly all the energy consumed is made up of the energy dissipated in the plastic zone, and only a small fraction of it is spent in breaking bonds. Dimensional specifications for fracture toughness test specimens are based on the dimensions of the plastic zone. Therefore, studies of the crack tip plastic zone appear to be of fundamental importance in describing the process of failure from a macroscopic standpoint and in constituting the criteria of fracture¹.

The plastic zone size depends strongly on whether plane strain or plane stress conditions exist. In cracked bodies, plane stress conditions exist in thin sections. In thick sections, plane stress ($\sigma_z = 0$) conditions exist on the surface and plane strain ($\epsilon_z = 0$) conditions exist in the interior. The 3-dimensional plastic zone in a thick section cracked body is schematically shown in Fig. 1. The state of stress (plane stress vs. plane strain) also depends on the extent of yielding. Large plastic zones cause unconstrained or free yielding. For example, if plastic zone is equal to the plate thickness, unconstrained yielding in the thickness direction will take place, causing plane stress conditions to develop.

The sizes and shapes of the plastic zones calculated for plane strain ($\epsilon_z = 0$) and plane stress ($\sigma_z = 0$) conditions are shown in Fig. 2. The plane strain plastic zone size is three times smaller than the plane stress plastic zone².

The strip yield model, also known as the Dugdale-Barenblatt model, assumes a long slender plastic zone in a nonhardening material under plane stress conditions. Thus, by necessity it is only valid for thin sheets². The original analyses were performed for cracks in infinite

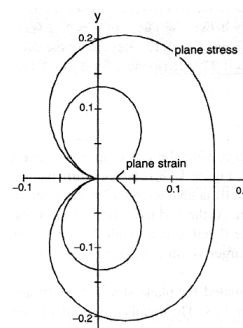


Fig. 2. Plots of the plastic zones associated with plane stress and plane strain³

sheets subjected to uniform stress. Therefore, the assumption of a slender plastic zone is reasonable. The radius of the plastic zone, r_p , is given by^{2,4}:

$$\frac{r_p}{a} = \frac{1}{\cos\left(\frac{\pi\sigma}{2R_c}\right)} - 1$$

where σ – applied stress, R_c – yield strength, a – crack length.

If $\sigma/R_c \ll 1$, r_p may be approximated by:

$$\frac{r_p}{a} = \frac{1}{2} \left(\frac{\pi\sigma}{2R_c} \right)^2$$

An increase in the notch radius would result in an increase in the size of the plastic zone and less constriction along the crack axis and vice versa.

However, small changes in the notch radius do not have a large effect on the plastic zone. The effects of the notch radius on plastic zone are also smaller at higher applied stresses.

For small loads, an increase in tip radius results in an increase in the plastic zone size and vice versa. The influence of the notch radius on the plastic zone size becomes insignificant at high applied stresses¹.

The plastic zone size and shape can be predicted by measuring hardness along and across the unbroken ligament⁵.

2. Material and methods

The materials used in this study are two grades of deep drawing thin steel sheets: XSG and HR 45, Fig. 3. XSG is deep drawing interstitial free steel with ferrite microstructure. HR 45 is microalloyed steel with ferrite-pearlite microstructure. Samples from laser welded tailored blanks (producer: Arcelor) were used for the experiments. Thickness t and mechanical properties of the steels used are in Tab. I.

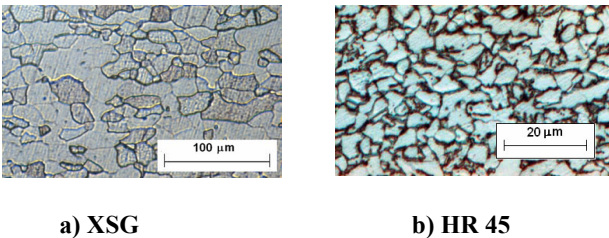


Fig. 3. Microstructure of the steels used

Table I
Mechanical properties of the steels used

Grade	t [mm]	R_c [MPa]	R_m [MPa]	A [%]
XSG	1.95	182	299	45.2
HR 45	1.80	382	493	24.7

The plastic zones were generated by stable crack growth. Stable crack growth was monitored with videoextensometry techniques on the CT (Compact Tension, Fig. 4) specimens with a notch (tip radius 0.4 mm) and with an electrospark produced notch (tip radius 0.1 mm) respectively.

Specimens were loaded by eccentric tension, whereby the deformation in the area around the notch was recorded by a non – contact displacement measurement – a videoextensometry technique.

Videoextensometry is an experimental technique for strain component measurement on the surface of specimens. The technique enables to record the displacements of contrast dots. The specimen is illuminated by diffuse light and its surface is recorded with a camera. Contrast

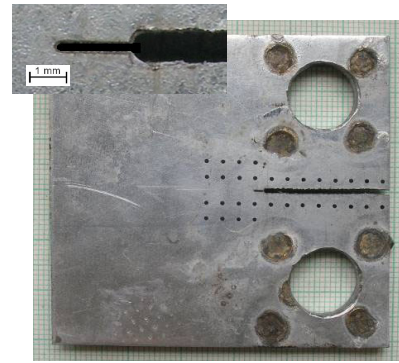


Fig. 4. CT specimen with contrast dots in the recorded area around an electrospark produced notch

dots were applied properly in the recorded area. Opening of the notch was determined by continual recording of coordinates of the centre of gravity of dots by appropriate software.

The plastic zone-size and -shape is also determined by measuring hardness along and across the unbroken ligament. The procedure consists in simple hardness indentation measurement ahead or around the crack tip and in determining the boundary of the plastic zone from the sudden variation in hardness. The hardness is measured using a low load hardness tester MICRODUR (Fig. 5) by Ultrasonic Contact Impedance (UCI) method⁶.

UCI is an experimental method for indirect measurement of hardness. A Vickers diamond is attached to one end of a magnetostrictive metal rod. The diamond tipped rod is excited to its natural frequency by a piezoelectric converter. The resonant frequency of the rod changes as the free end of the rod is brought into contact with the surface of a tested specimen. The change in the frequency is proportional to the surface area of the indentation. This relation depends also on elastic properties, given by elastic modulus, of the "indenter – specimen" system.

UCI hardness test is easy and simply to use. A disadvantage of this method is that the tested object should be

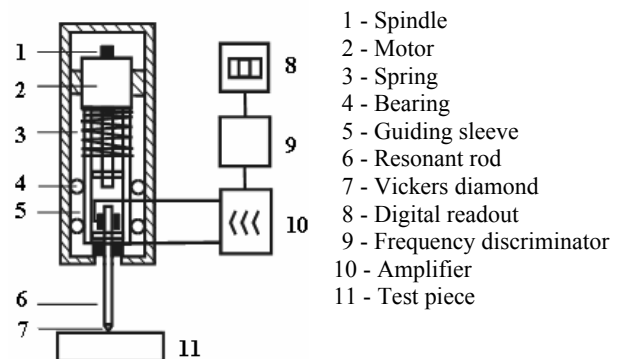


Fig. 5. Basic diagram of MICRODUR

heavy. The weight of the measured object should be at least 200 g (ref.⁷). This is the reason why thin sheets specimens were fixed on another bulk piece of steel. Two adhesive materials were tested and the more appropriate one was used in all experiments.

3. Results

Experiments were performed using two automotive zinc coated steel grades. The zinc coating affected the global hardness (HV 1) of the substrate – coating system, Fig. 6. The influence of the zinc coating is greater by HR 45, because this material is harder than XSG and the depth of indent is smaller.

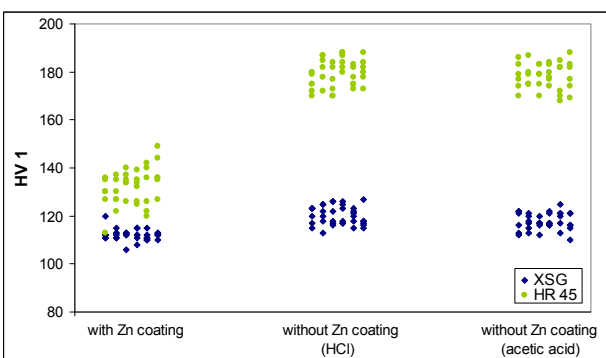


Fig. 6. The influence of the zinc coating on hardness

The zinc coating was removed using two different media. The hardness of steels without zinc coating does not vary with statistical significance in dependence on the removal medium used, Fig. 6.

Indentations on sheet surface without zinc coating were realized with different spacing between the indents' centers (0.2; 0.3; 0.5 and 0.7 mm). These distances are sufficient for individual indentations not to be affected by each other (Fig. 7). The distance between centres of in-

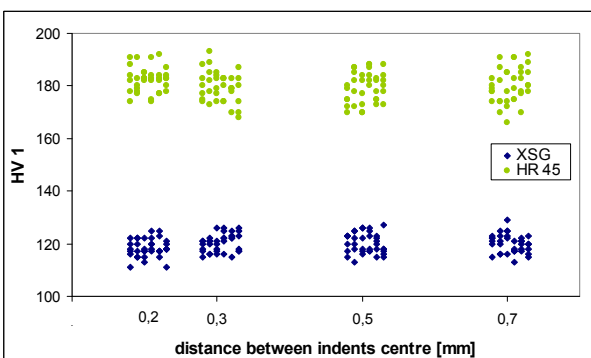


Fig. 7. The relation between hardness and distance between centres of indents

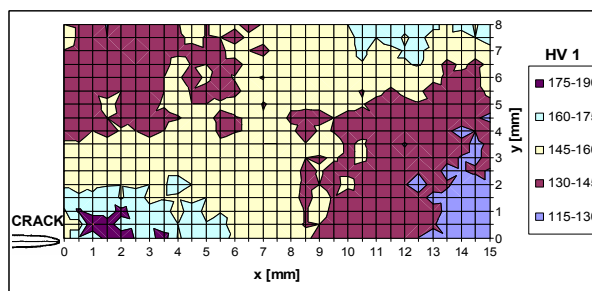


Fig. 8. The plastic zone of XSG at the crack tip

dentations in the measurement of the plastic zones was 0.5 mm. The plastic zones generated by stable crack growth on the CT specimens with notch are shown in Fig. 8, 9. The plastic zone of XSG is larger. The hardness of materials before deformation reaches the low limit of the range. This range shows the border of the plastic zone.

The size of the plastic zone on the CT specimens with an electrospark produced notch was measured in the x-axis direction at different distances from the crack tip. Electrospark notch have smaller size of the plastic zone in the x-axis direction in comparison with specimens with notch, Fig. 10.

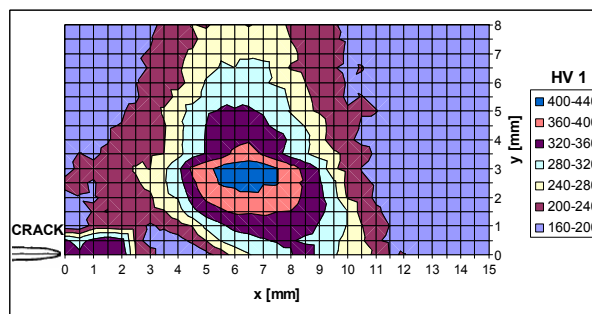


Fig. 9. The plastic zone of HR 45 at the crack tip

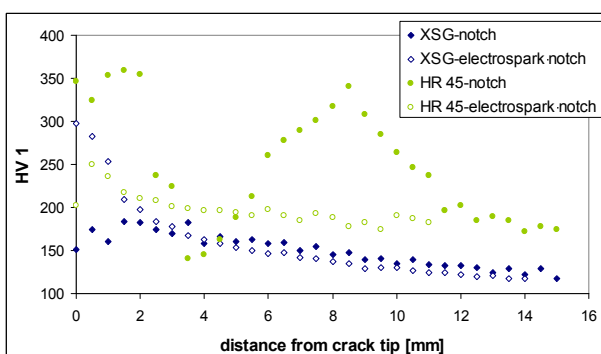


Fig. 10. The relation between hardness and distance from the crack tip

In another work (ref.⁷), power relations between the hardness HV 1 and longitudinal deformation in uniaxial tension for investigated steels were found:

$$HV = 111.69 + 20.52 \cdot \varepsilon^{0.198} \quad \text{for XSG}$$

$$HV = 164.88 + 4.11 \cdot \varepsilon^{0.739} \quad \text{for HR 45}$$

Using these relations deformation was determined from hardness values, Fig. 11. These values are too high and do not math with real values. Using the videoextensometry, deformation in the y-axis at the crack tip was determined at the base length of 4 mm – XSG: 38.3 % and HR 45: 22.4 %. The stress-state in the plastic zone differs from that in uniaxial tension, therefore the relation⁷ is not suitable to predict deformation in the plastic zone.

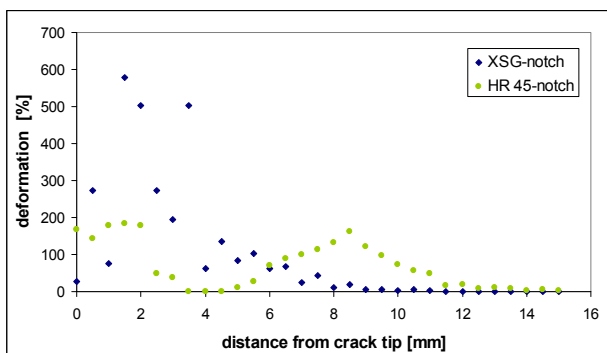


Fig. 11. The relation between deformation calculated according⁷ and distance from the crack tip

4. Conclusions

Automotive steels are usually coated with zinc coatings. The zinc coating affects the global hardness of the substrate – coating system.

The plastic zone of XSG (IF steel) measured on the CT specimen with a notch is larger than the plastic zone in HR 45 (ferrite-pearlite) steel.

The CT specimen with electrospark notch has smaller plastic zone in x-axis direction in comparison with specimens with notch.

Using the power relations between the hardness HV 1 and longitudinal deformation in tension it is not possible to predict deformation for another stress states.

This work was performed within the framework of projects APVV - 032 - 07 and VEGA No. 1/4149/07.

REFERENCES

1. Zhang J.-P., Venugopalan D.: Eng. Fracture Mechanics 26, 913 (1987).
2. Saxena A.: *Nonlinear Fracture Mechanics for Engineers*, 472 p. CRC Press, 1998.
3. Hosford W. F.: *Mechanical Behavior of Materials*, 425 p. Cambridge University Press, New York 2005.
4. Trebuňa F., Buršák M.: *Medzné stavy*, 348 p. Lomy, Košice 2002.
5. Kulkarni D. M., Prakash R., Talan P., Kumar A. N.: Sadhana – Academy Proceedings in Engineering Sciences Vol. 29, Part 4, August 2004, p. 365–380.
6. Rudnayová E., Hvizdoš P., Arató P., Pešek L.: Key Engineering Materials, Vols. 175–176, 2000, p. 335–340.
7. Zubko P., Ambriško E., Pešek L.: In: *YUCOMAT 2009: Herceg Novi, Montenegro, 31.8. – 4.9.2009. Belgrade: Serbian Academy of Science & Arts, 2009. In print.*

E. Ambriško^a, L. Pešek^a, and S. Hlebová^b
^{(^a Technical University of Košice, Faculty of Metallurgy, Department of Material Science, ^b Faculty of Mechanical Engineering, Technical University of Liberec, Czech Republic): **Determination of Plastic Zone by UCI Technique on Thin Steel Sheets**}

The main goal of this paper is the determination of the size and shape of the plastic zone in thin steel sheets. The aim of experiments was to analyze the influence of the material and type of the initial crack on the dimensions of the plastic zone.

The plastic zone size and shape is also predicted by measuring hardness (HV 1) along and across the unbroken ligament. The hardness is measured by using UCI (Ultrasonic Contact Impedance) technique. The hardness values varied in dependence on the material and the initial crack. In this paper, the CT (Compact Tension) specimens of two steel grades with a notch and with an electrospark produced notch were used. Specimens were loaded by eccentric tension, whereby the deformation in the area around the notch was recorded by non-contact displacement measurement – a videoextensometry technique.

INFLUENCE OF PRE-OXIDATION ON LOCAL MECHANICAL PROPERTIES OF Zr1Nb ALLOY

OLGA BLÁHOVÁ*

New Technology Research Centre, University of West Bohemia, Univerzitní 8, 306 14 Plzeň, Czech Republic
blahova@ntc.zcu.cz

Key words: Zr alloys, LOCA, Nanoindentation

1. Introduction

Zirconium alloys are used in nuclear power generation primarily due to their low thermal neutron absorption cross section, good mechanical properties and corrosion resistance. They are used, for instance, for production of cladding tubes. Zirconium ($T_i = 1.860$ °C) is an allotropic metal with a low-temperature form α (hcp) stable up to about 860 °C and a high-temperature form β (bcc).

Zirconium shows a high affinity for hydrogen, oxygen and nitrogen, forming stable hydrides, oxides, nitrides and interstitial solid solutions.

Other alloying elements are added to Zr for the purpose of improvement of mechanical and corrosion-related properties: Sn, Nb, Al, Cu, V, Mo... High corrosion resistance in alloys containing Nb (0.1 to 2 wt.%) can be achieved by preparing a microstructure with finely distributed β -Nb precipitates on the α -phase grain boundaries and within the matrix.

During the operation of the VVER pressurised-water reactor, the outer wall of the tube is in contact with the cooling water at the temperature of 320 °C and the pressure of 16 MPa, which results in Zr oxidation and release of hydrogen, part of which is absorbed by the alloy. The forming oxide creates a water-metal barrier inhibiting the corrosion.

A loss of coolant accident (LOCA) may occur in water-cooled reactors, which involves a failure of the main piping and a leak of the coolant. The loss of moderator then occurs within less than 10 seconds and the fission stops. The temperature of the fuel cladding rises to about 1000 °C. A reaction between the steam and the cladding tube occurs, resulting in high-temperature (HTO). After certain delay, emergency systems flood the reactor with water and the fuel cladding tubes will be cooled down rapidly¹.

UJP Praha a.s. carries out simulations of this type of accident under laboratory conditions². During heating, a portion of oxygen forms oxides, while the other portion dissolves in the metal.

The amount of oxygen dissolved in the metal increases with temperature and an oxygen concentration gradient forms. At higher temperatures, the α -phase trans-

forms to the β -phase, where β might contain certain maximum proportion of dissolved oxygen. Even at high temperatures, oxygen causes the transformation of the β -phase back to the hcp-phase termed α -Zr(O) which remains stable during cooling. On cooling, the remaining β -phase undergoes a transformation to the α -phase (usually called prior β ^{1,2}).

Microstructure of the material upon high-temperature oxidation and cooling consists of the ZrO₂ oxide layer, oxygen-stabilized α -Zr(O)-phase and the α -phase (prior β). The α -Zr(O) layer is very brittle, and thus it is the α -phase which provides the residual ductility and toughness of material³.

2. Experimental

The evaluated Zr-alloy contains: 1.0–1.1 wt.% Nb, 840 ppm O, 100 ppm C, 20 ppm N and 3 ppm H. Tubes with the length of 30 mm, an outer diameter of 9 mm and a wall thickness of 0.6 mm were used as experimental samples. Specimens were subjected to high-temperature oxidation in steam (exposure temperatures: 1100 °C, 1110 °C, 1150 °C and 1200 °C, exposure time: 0 to 30 min) and quenched in a mixture of water and ice. Before this treatment, some specimens had been pre-oxidized at lower temperatures to simulate the state of material after certain period of service, see Tab. I.

Upon high-temperature oxidation and quenching, the tubes were sectioned with a diamond-disc cutter at UJP to annular rings with the height of 3 mm and then embedded in resin and polished for metallographic observation. The specimen preparation and evaluation are described in the report². Specimens were examined by an X-Ray diffractometer and a scanning electron microscope with EDAX⁴.

Nanoindentation measuring was carried out using Nano Indenter XP and a Berkovich indenter. With this equipment, it is possible to conduct an instrumented indentation test recording the load-indentation depth curve ($F-h$) during loading and unloading phases and thus determine the indentation hardness, elastic modulus and other characteristics. The indentation hardness is defined by the standard⁵:

$$H_{IT} = \frac{F_{\max}}{A_p}$$

where F_{\max} is the maximum loading force and A_p is the projected indentation contact area.

The indentation modulus of elasticity is defined by⁵:

$$E_{IT} = \frac{1 - (v_s)^2}{\frac{1}{E_r} - \frac{1 - (v_i)^2}{E_i}}$$

Table I
Experimental samples and measured mean values

Sample: temperature [°C] / thickness of pre-oxide [μm] / time [min]	H_{IT} [GPa]	E_{IT} [GPa]
1100 / 0 / 3	3.76 ± 0.28	108.9 ± 2.9
1100 / 0 / 6	3.98 ± 0.28	113.8 ± 5.1
1100 / 0 / 9	4.11 ± 0.24	112.4 ± 3.9
1100 / 0 / 15	3.82 ± 0.21	108.7 ± 3.3
1100 / 0 / 30	4.34 ± 0.26	109.4 ± 3.2
1100 / 2 / 3	3.50 ± 0.51	110.6 ± 4.0
1100 / 2 / 6	3.96 ± 0.25	111.1 ± 4.3
1100 / 2 / 9	3.86 ± 0.22	111.9 ± 4.3
1100 / 2 / 15	4.23 ± 0.29	113.4 ± 3.6
1150 / 0 / 0	3.14 ± 0.27	111.3 ± 3.8
1150 / 0 / 3	3.98 ± 0.22	113.0 ± 3.7
1150 / 0 / 9	4.62 ± 0.24	118.8 ± 4.2
1150 / 0 / 30	4.83 ± 0.33	112.9 ± 5.1
1150 / 10 / 0	3.28 ± 0.26	110.9 ± 3.7
1150 / 10 / 3	3.90 ± 0.25	109.5 ± 3.8
1150 / 10 / 6	4.30 ± 0.24	112.7 ± 3.8
1150 / 10 / 9	4.27 ± 0.26	115.1 ± 4.3
1150 / 10 / 15	4.01 ± 0.32	109.5 ± 4.2
1150 / 10 / 30	4.50 ± 0.37	112.1 ± 7.3
1200 / 0 / 3	4.67 ± 0.20	116.1 ± 3.0
1200 / 0 / 6	4.61 ± 0.38	106.9 ± 1.9
1200 / 0 / 9	5.44 ± 0.33	116.4 ± 3.6
1200 / 0 / 15	4.98 ± 0.29	106.9 ± 3.0
1200 / 2 / 3	4.27 ± 0.26	114.5 ± 2.4
1200 / 2 / 6	4.28 ± 0.17	110.6 ± 3.4
1200 / 2 / 9	4.36 ± 0.97	115.9 ± 3.6

where the indices i and s are related to properties of the indenter or the sample material (modulus of elasticity, Poisson ratio) and E_r is reduced modulus of elasticity:

$$E_r = \frac{S \cdot \sqrt{\pi}}{2 \cdot \beta \sqrt{A_p}(h_c)}$$

where S is the contact stiffness (the initial slope of the unloading curve), β is a correction constant for the indenter shape (for Berkovich indenter: $\beta \approx 1.034$), A_p is the projected contact area and h_c is the contact depth:

$$h_c = h - \varepsilon \frac{P_{\max}}{S}$$

where ε is constant dependent on the indenter geometry⁶.

Indentations were made under the load of 8 mN in three or four parallel rows starting at the oxide-metal inter-

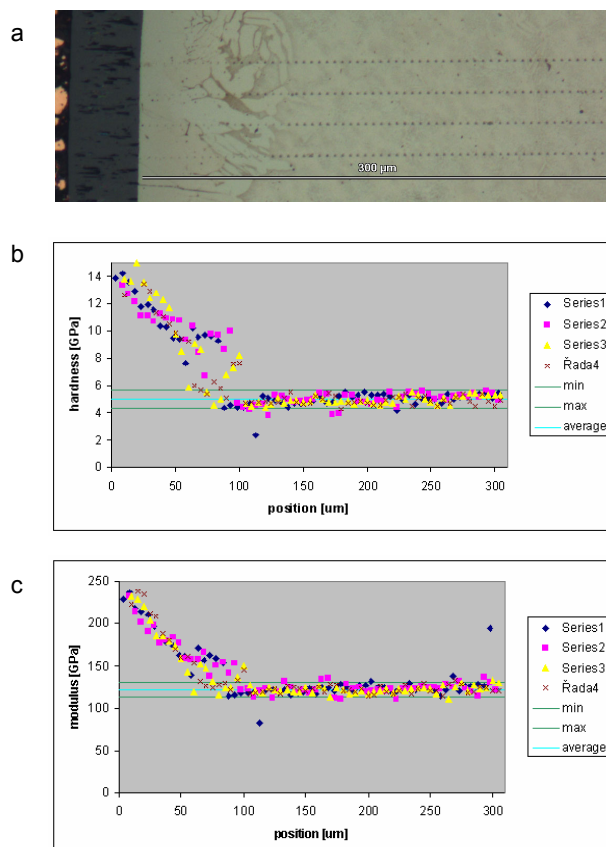


Fig. 1. a) Micrograph of sample with exposition temperature 1150 °C and time 6 min, b) measured value of indentation hardness, c) measured value of indentation modulus of elasticity

face with a pitch of 5 μm. Indentations were documented with a light microscope (Fig. 1a).

The min–max intervals were recorded (Fig. 1b,c), with the assumption that they correspond with the α phase properties, then mean values were calculated.

Calculated values of indentation hardness and modulus of elasticity of the α (prior β) phase are shown in Tab. I and Fig. 2 and 3.

The indentation hardness generally increases with the temperature of exposure. It depends on higher oxygen content⁴.

The indentation modulus of elasticity is nearly constant: 112.2 GPa ± 3.0 GPa (standard deviation is approximately 3 % of the mean value).

The ratio of measured values of indentation modulus of elasticity E_{IT} and indentation hardness H_{IT} is shown in Fig. 4. This ratio mostly decreases with the exposure temperature.

Pre-oxidized samples have slightly lower hardness and a slightly higher ratio of indentation modulus of elasticity and indentation hardness. Apparently, the oxide created during pre-oxidation with the thickness 2 or

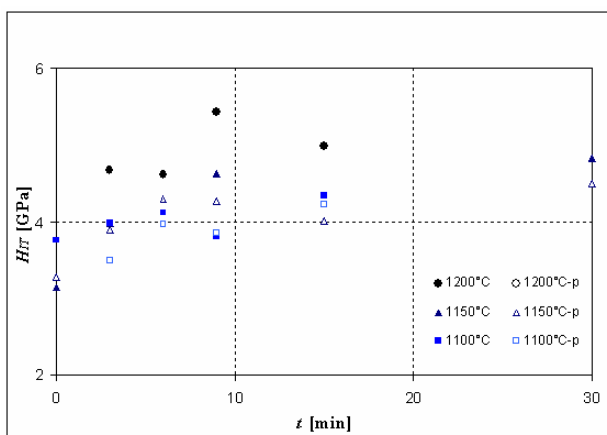


Fig. 2. Indentation hardness of samples with different exposure temperature vs. exposure time (-p indicates pre-oxidized samples)

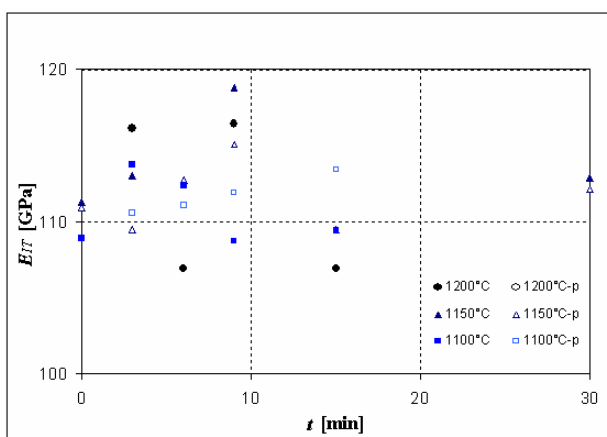


Fig. 3. Indentation modulus of elasticity of samples with different exposure temperature vs. exposure time (-p indicates pre-oxidized samples)

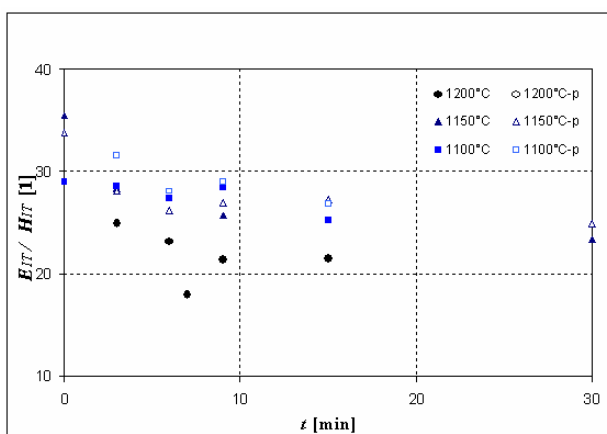


Fig. 4. Ratio of measured values of indentation modulus of elasticity E_{IT} and indentation hardness H_{IT} vs. exposure time (-p indicates pre-oxidized samples)

10 μm slows down the degradation of mechanical properties of Zr alloys during high temperature oxidation with subsequent severe cooling.

Samples were measured at UJP Praha by the pressure testing method at 135 $^{\circ}\text{C}$ and their ductility was determined². Samples are considered brittle when their hardness is more than 4.3 GPa (see Fig. 5).

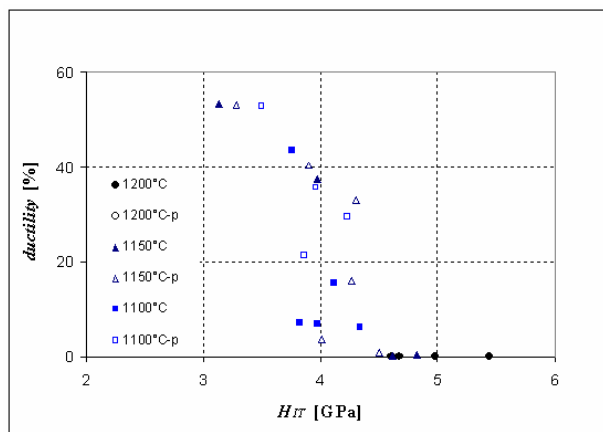


Fig. 5. The ductility vs. indentation hardness of samples with different exposure temperature (-p indicates pre-oxidized samples)

3. Conclusion

This paper deals with evaluation of local mechanical properties of a new Zr1Nb alloy using the nanoindentation method.

Specimens were subjected to high-temperature oxidation in steam and quenched in a mixture of water and ice. Before this treatment, some specimens had been pre-oxidized at lower temperatures to simulate the state of material after certain period of service.

The indentation hardness of the α (prior β) phase was determined and it was found out that the indentation hardness increases with the temperature of exposure. On the contrary, the indentation modulus of elasticity is nearly constant so that the ratio indentation hardness and indentation modulus decreases with the temperature of exposure.

The pre-oxidized samples have slightly lower hardness and slightly higher ratio of indentation modulus of elasticity to indentation hardness. Therefore, the pre-oxide slows down the degradation of mechanical properties of Zr alloys during high temperature oxidation with subsequent severe cooling.

The indentation hardness correlates with ductility measured by the pressure testing method.

This work was supported by project the MPO ČR no. 2A - 1TP1/03.

REFERENCES

1. Cox B.: J. Nuclear Mater. 336, 331 (2005).
2. Vrtílková V. et al.: *Výzkumná zpráva 1164* (Research report). Praha: UJP Praha a. s. 2005.
3. Chung H. M.: Nuclear Eng. Technol. 37, 327 (2005).
4. Bláhová O., Medlín R., Říha J.: *Conference proceeding Metal 2009, Ostrava*. p. 359. Tanger, 2009.
5. ISO14577-1:2002, *Metallic materials - Instrumented indentation test for hardness and materials parameters – Part 1: Test method*.
6. Oliver W. C., Pharr G. M.: J. Mater. Res. 7, 1546 (1992).

O. Bláhová (*New Technology Research Centre, West Bohemia University, Plzeň*): **Investigation of Local Mechanical Properties of Zirconium Alloys Using Nanoindentation**

The paper deals with evaluation of a zirconium alloy developed for production of cladding tubes for nuclear reactor fuel rods. The specimens were subjected to high-temperature oxidation (at various exposure times and temperatures) and subsequently cooled. The process was a simulation of the loss of coolant accident (LOCA). Before this treatment, some specimens had been pre-oxidized at lower temperatures to simulate the state of material after certain period of service. The microstructure was documented by means of light microscope. Local mechanical properties (indentation hardness and modulus of elasticity) were tested by means of nanoindentation.

POTENTIAL UTILISATION FOR NANOTESTERS

**PETR BOHAC^{*a}, RADIM CTVRTLÍK^b,
and MARTIN STRANYANEK^a**

^a Institute of Physics, AS CR, v.v.i, Na Slovance 2, Prague 8, Czech Republic, ^b Joint Laboratory of Optics, Palacky University and Institute of Physics AS CR, 17. listopadu 50, Olomouc, Czech Republic
bohac@fzu.cz

Keywords: local mechanical properties, utilization of nanotester, DSI, XRD, nanocompression

1. Introduction

Hardness is defined as resistance of material to plastic deformation, usually by indentation. Two approaches to phenomenon named hardness have been developed for its application and explanation during last about one hundred years. Since beginning of the 20th century Brinell approached the problem as an engineer interested in comparing the properties of various materials, especially different batches of steel. The main role was adjudged to plastic deformation of materials caused by a hard asperity indented into a softer metal. The Brinell hardness test uses a desk top machine to press a 10 mm diameter, hardened steel ball into the surface of the test specimen. The machine applies a load of 5 kN for soft metals such as copper, brass and thin stock. A 15 kN load is used for aluminum castings, and a 30 kN load is used for materials such as iron and steel. The load is usually applied for 10 to 15 seconds. After the impression is made, a measurement of the diameter of the resulting round impression is taken. It is measured to plus or minus 0.05 mm using a low-magnification portable microscope. The hardness is calculated by dividing the load by the area of the curved surface of the indentation.

The Rockwell hardness tester measures resistance to penetration like the Brinell test, but in the Rockwell case, the depth of the impression is measured rather than the diametric area. With the Rockwell tester, the hardness is indicated directly on the scale attached to the machine. This dial like scale is really a depth gauge, graduated in special units. The Rockwell hardness test is the most used and versatile of the hardness tests.

The Vickers testing method is similar to the Brinell test, but the Vickers machine uses a penetrator that is square in shape, but tipped on one corner so it has the appearance of a playing card "diamond". The Vickers indenter is a 136 degrees square-based diamond cone (or pyramid), the diamond material of the indenter has an advantage over other indenters because it does not deform

over time and use. The impression left by the Vickers indenter is a dark square on a light background. The Vickers impression is more easily "read" for area size than the circular impression of the Brinell method. Like the Brinell test, the Vickers number is determined by dividing the load by the surface area of the indentation ($H = P/A$). The load varies from 1 to 120 kN.

Berkovich triangular pyramid-shaped diamond with a nominal angle 65.3° between the face and the vertical axis was developed as a sharper tip which manufacturing can comply with the ideal shape. These engineering approaches have been based on study of residual impression. The different scales of hardness were then established on the size of the impression.

The other approach was based on physical reasoning of measurements using theory of contact of different bodies, theory of plasticity or elastoplastic contacts. It enables to clarify the physical nature of behavior of different materials by indentation. The basic works on this idea were published by Archard, Bowden, Tabor, Sneddon and Loubet.

Both these approaches augmented by technical progress achieved a milestone consisting in a depth / displacement sensing indentation (DSI) technique. A typical test involves moving the indenter to the surface of the material and measuring the forces and displacements associated with the indentation process by continual recording of indentation depth vs. loading of the tip. It enables to derive many mechanical properties such as hardness, elastic modulus, strain energy (elastic, plastic, total), etc. from measured curves. In recent years, the study of mechanical properties of materials on the nanoscale has received much attention, as these properties can be size-dependent. These studies have been motivated partly by the development of nanocomposites and the application of very thin films for miniaturization of engineering and electronic components, and partly by newly available methods of probing mechanical properties in small volumes. The nanoindenter is maturing as an important tool for probing the local mechanical properties of materials.

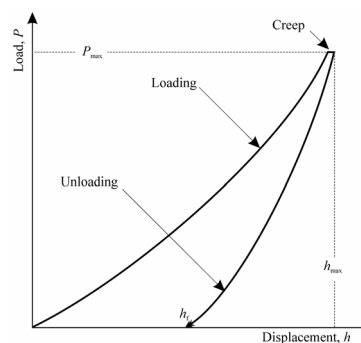


Fig. 1. The typical DSI curve

$$S = \frac{dP}{dh} = \frac{2}{\sqrt{\pi}} E_{\text{eff}} \sqrt{A} \quad (1)$$

While originally derived for stiffness from theory of elastic contact for a conical indenter, it was established later that Eq. (1) holds equally well for spherical and cylindrical indenters and it may be applied to other geometries as well^{1–3}. Here, A is the projected area of the elastic contact; E_{eff} is the effective elastic modulus

$$\frac{1}{E_{\text{eff}}} = \frac{1-\nu^2}{E} + \frac{1-\nu_i^2}{E_i} \quad (2)$$

ν is Poisson's ratio, and i is label of indenter ($\nu_i = 0.07$, $E_i = 1141$ GPa for diamond). By measuring the initial unloading stiffness and assuming that the contact area is equal to the optically measured area of the hardness impression, the modulus can thus be derived from Eqs. (1) and (2). Stiffness $S = dP/dh$ is derived from the upper portion of the unloading data of DSI curve (Fig. 1).

The hardness is then calculated from its common definition:

$$H = \frac{P_{\text{max}}}{A} \quad (3)$$

where P_{max} is the peak indentation load and A is the projected area of the hardness impression. There are two approaches to calculation of H (programmed in software of different equipments). Doerner and Nix⁴ suggested that the unloading stiffness can be computed from a linear fit of the upper one-third of the unloading curve. Point of intersection with axis of displacements they labeled as plastic depth h_{plast} . With knowledge of the indenter geometry, the plastic depth can then be used to obtain the projected area in contact with the indenter. If the final depth rather than the plastic depth is used, a significant overestimate of the hardness will result due to the significant decrease in depth during elastic recovery. If the Vicker's pyramid is used, the projected area is $24.5 (h_{\text{plast}})^2$. Hardness is accordingly marked as H_{plast} and calculated from P_{max} . Oliver and Pharr⁵ published more precise and sophisticated method of analyse of unloading part of DSI curves. They reveal that unloading curves can be accurately described by the power law relation

$$P = \alpha(h - h_f)^m \quad (4)$$

where $(h - h_f)$ is elastic displacement (elastic recovery is taken into account), and α , m are material constants. It is assumed that projected contact area at peak load is a function of the contact depth h_c , $A = F(h_c)$. The functional form of F must be established experimentally prior to analysis – by calibration, e.g. The function is proposed in polynomial form with 9 terms which approach non-ideal shape of indenter.

Resolutions of such nano-equipments are in level of

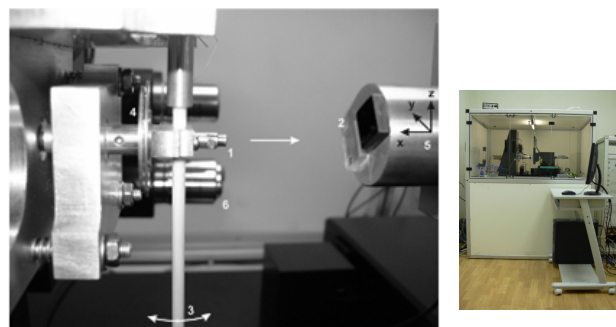


Fig. 2. General view and measuring node of NT600: 1 – indenter, 2 – samples, 3 – pendulum, 4 – capacitor plates, 5 – sample holder (x-y-z directions of moving), 6 – microscope

tithes of nm for displacements and in μN for loadings. Common loadings are in range of tens or hundreds mN and velocities in nm s^{-1} .

Measurements of hardness on bulk materials (steels) are correlated with stress investigation by X-ray diffraction (XRD), nanoindentations of plasma spray coatings and thin carbon based sputtered films. Thereinafter are briefly mentioned possibilities of utilization of nanotest devices.

2. Experimental device

Nanotester NanoTest™ NT600 (Micro Materials, Ltd.) was applied for all below mentioned experiments, Fig. 2. Details and accessories are described elsewhere⁶.

3. Utilisation

The nanotester NanoTest™ NT600 is fated to nanoindentations first of all. The set of analyzed samples was prepared from five *Fe alloys*^{7,8}: carbon ferrite steel ČSN 12 050 (A), Mn-Cr steel 14 220 (B), Cr-Mo corrosion-resistant steel 17 135 (C), low-alloyed tool steel 19 313 (D), and Mo-W-Co rapid steel 19 852 (E). XRD stress analysis was performed on a Siemens goniometer with $\text{CrK}\alpha$ radiation. Macroscopic and microscopic lattice strains were evaluated from the $\alpha\text{-Fe}$ {211} diffraction line detected for nine tilt angles ψ ($\sin^2\psi = 0, 0.1, 0.2, \dots, 0.8$). The X-ray elastic constants $\frac{1}{2}s_2 = 5.76 \cdot 10^{-6} \text{ MPa}^{-1}$, $-s_1 = 1.25 \cdot 10^{-6} \text{ MPa}^{-1}$ were used in stress calculations. Fig. 3 shows a strong correlation between surface microscopic stresses and hardness.

*Investigation on metallographic polished cross section of plasma sprayed conventional titania (TiO_2) coating*⁹ revealed bimodal distribution of hardness – see histogram, Fig. 4. One maximum is at 11.9 GPa and the second one at 7.6 GPa. Plasma sprayed TiO_2 coating using conventional powder exhibits microhardness of about 8.5 GPa. The bimodal character is attributed to the presence of two different phases in the deposit.

Nanoindentations on DLC thin films (few μm) depos-

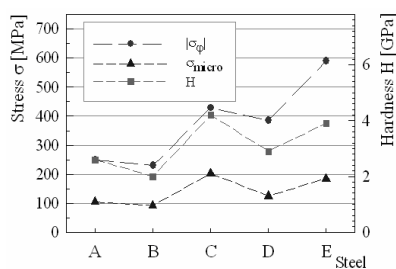


Fig. 3. Surface compressive macroscopic stresses $|\sigma_\phi|$, microscopic stresses σ_{micro} (XRD) and the hardness H (DSI) for 5 batches of steel

ited by magnetron sputtering on steel substrates. All the films are amorphous.

Structure of films with presence of hydrogen tends to polymer behaviour (very low hardness, strong influence of substrate on elastic modulus), Fig. 5. While elastic modulus for all presented films shows significant differences from substrate one and tends to some value of inter-layer, the hardness tends to the substrate one.

Indentations of microscopic subjects such as crystals of zeolites

The local mechanical properties of columnar silicalite-1 crystals of a roof-prism shape with dimensions in μm of approx. $220 \times 40 \times 40$ were investigated in state as-synthesized as well as calcined ones (i.e., crystals free of organic template), Fig. 6. Calcination was performed by heating (550°C) these crystals in a dry-air stream for 24 hours. In fact, these crystals are porous twins with zig-zag channels having their pore mouth openings on all four lateral faces¹⁰.

Hardness of as-synthesized crystals, calcined crystals and fused silica bulk was compared. All silicalite-1 crystal twins have roughly the same elastic modulus (i.e., about 38 GPa), which is greater than one half of value for fused silica (71.6 GPa). Calcined crystals appear to be about twice harder (4.0 GPa) than as-synthesized ones (2.4 GPa) but they are about twice softer than fused silica (8.6 GPa)¹¹.

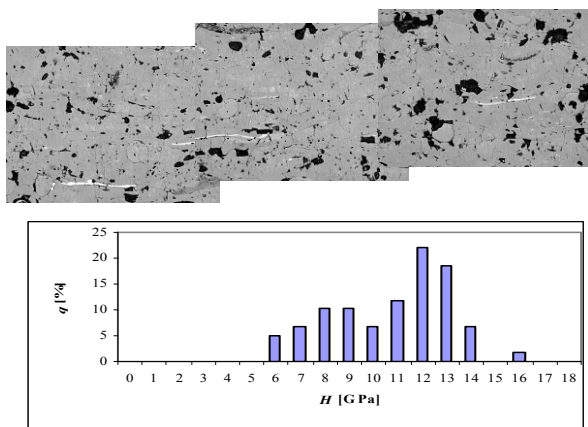


Fig. 4. Histogram of hardness from 100 indents scattering a cross-section of TiO_2 coating

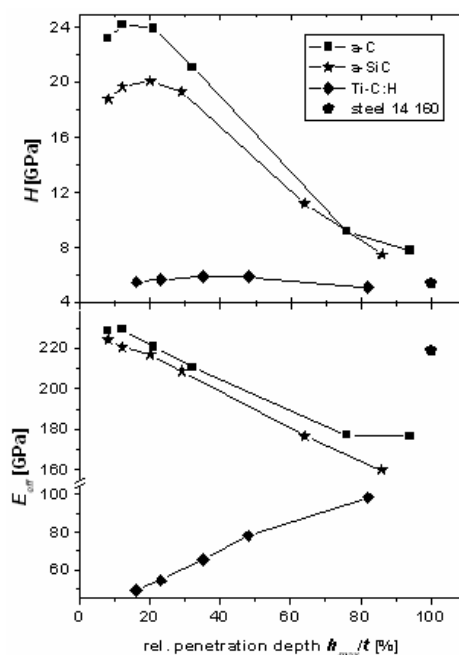


Fig. 5. Depth profiles of hardness and elastic modulus in DLC films sputtered on the manganese-chromium steel CSN 14 160

Nanocompression/nanoindentation experiments were performed on samples consisting of a sandwich composed of a Si substrate, an intermediate W-based film, and the investigated Al–Cu film. For nanocompression experiments were from these samples prepared cylindrical pillar with a diameter of $1.3 \mu\text{m}$ (height/diameter ratio of the pillar equal to 1.6) and to remove the Al and W films around the pillar by focused ion beam (FIB) milling, Fig. 7. The diameter of the removed zone was chosen to be $25 \mu\text{m}$, to ensure that the operating punch will not touch

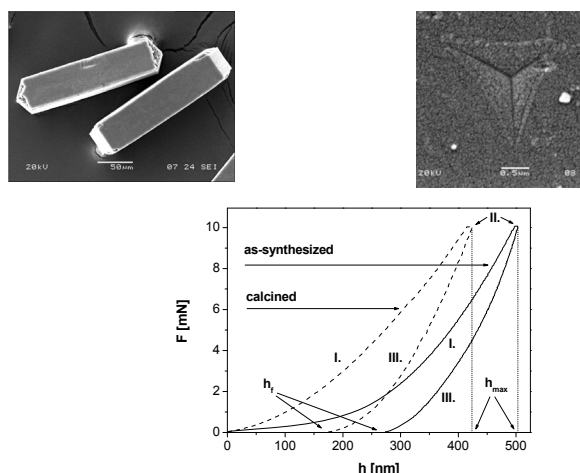


Fig. 6. SEM image of silicalite-1 crystals (400x), residual impression into crystal, and the typical DSI curves for as-synthesized and calcined crystals

any other object except the pillar. The conical diamond punch was used for all compression experiments. Its flat contact face had an irregular, approximately circular section of diameter of about 10 μm . The relatively large diameter of the flat punch face compared to pillar diameter ensured that despite a slight aiming misalignment, the selected pillars were always uniformly uniaxially deformed. It was also checked that the upper face of deformed pillars remained flat after the compression suggesting that it was completely covered with the flat tip. The nanocompression test was complemented with standard Berkovich tip nanindentation, which enables one to measure independently elastic properties and to correct the nanocompression stress–strain curve from parasitic elastic strains. Such a procedure thus provides a useful tool for the mechanical testing of thin films in condition of homogeneous stress state with improved precision of the stress–strain data¹².

4. Conclusions

Since beginning of the 20th century when Brinell first impressed his ball into the surface of the test specimen to differ various materials, especially different batches of steel, and theorists began investigate fields of strains and stresses under contact of two bodies, the technical progress enables to converge both these approaches. Sophisticated devices are able to determine not only hardness but due to analyses of DSI curve also elastic modulus and other mechanical properties in very small volumes.

There are briefly presented applications of the nanotester to indentations of bulk materials as well as thin films in this contribution. Investigation of local mechanical properties on specimens of microscopic sizes is referred as well. The nanotester with flat punch was used also for nanocompressions of micropillars prepared from

thin film. All mentioned items represent stable/quasi stable measurements and were performed and published by authors. Moreover, various accessories for dynamic testing can extend spectrum of applications (adhesion, scratch and tribology tests, impact test, etc.).

Nanotesters are able to verify validation of laws of continuum mechanics for small volumes of materials as well.

Financial support from the Academy of Sciences of the Czech Republic: project KAN301370701, grant No. KJB201240701, and from Grant Agency of the Czech Republic project No. 106/07/0805 is acknowledged.

REFERENCES

1. Bulychev S. I., Alekhin V. P., Shorshorov M. Kh., Ternovskii A. P., Shnyrev G. D.: *Zavod. Lab.* 41, 1137 (1975).
2. Pharr G. M., Oliver W. C., Brotzen F. R.: *J. Mater. Res.* 7, 613 (1992).
3. King R. B.: *Int. J. Solids Structures* 3, 1657 (1987).
4. Doerner M. F., Nix W. D.: *J. Mater. Res.* 1, 601 (1986).
5. Oliver W. C., Pharr G. M.: *J. Mater. Res.* 7, 1564 (1992).
6. Čtvrtlík R., Stranyánek M., Boháč P., Jastrabík L.: *Mater. Struct.* 13, 90 (2006).
7. Ganev N., Čerňanský M., Boháč P., Drahokoupil J., Čtvrtlík R., Stranyánek M.: *Proc. 22nd Danubia – Adria Sympos. Exp. Meth. In Solid Mech., Parma, Italy, Sept. 28 – Oct. 1, 2005*, 38.
8. Drahokoupil J., Ganev N., Čerňanský M., Boháč P., Čtvrtlík R., Stranyánek M.: *Z. Kristallogr. Suppl.* 27, 89 (2008).
9. Ctibor P., Bohac P., Stranyanek M., Ctvrtlik R.: *J. Eur. Ceram. Soc.* 26, 3509 (2006).
10. Caro J., Noack M., Richter-Mendau J., Marlow F., Petesohn D., Griepentrog M., Kornatowski J.: *J. Phys. Chem.* 97, 13685 (1993).
11. Brabec L., Boháč P., Stranyánek M., Čtvrtlík R., Kočířík M.: *Micropor. Mesopor. Mat.* 94, 226 (2006).
12. Kruml T., Stranyanek M., Ctvrtlik R., Bohac P., Vysytavel T., Panek P.: *J. Mater. Res.* 24, 1353 (2009).

P. Bohac^a, R. Ctvrtlik^b, and M. Stranyanek^a
^a*Institute of Physics, AS CR, v.v.i, Prague, Czech Republic,* ^b*Joint Laboratory of Optics, Palacky University and Institute of Physics AS CR, Olomouc, Czech Republic):*
Potential Utilisation for Nanotesters

There are briefly presented applications of the nanotester to indentations of bulk materials as well as thin films in this contribution. Investigation of local mechanical properties on specimens of microscopic sizes is referred as well. The nanotester with flat punch was used also for nanocompressions of micropillars prepared from thin film. All mentioned items represent stable/quasi stable measurements and were performed and published by authors.

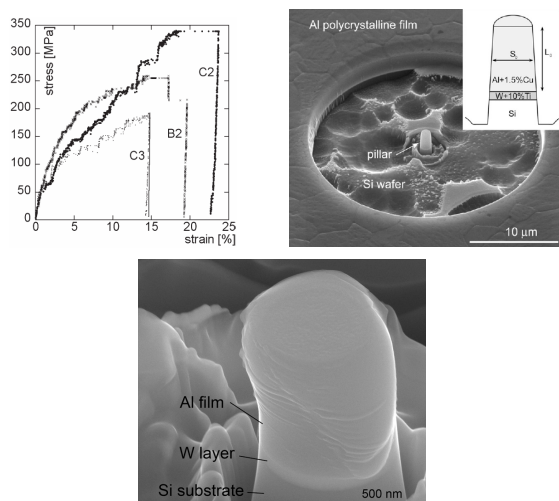


Fig. 7. SEM pictures of pillar C2 before (right) and after (below) nano-compression and stress – strain curves for different pillars

USE OF GENETIC ALGORITHM FOR IDENTIFICATION OF NONLINEAR CONSTITUTIVE MATERIAL MODELS

JAN BRUMEK*, **BOHUMÍR STRNADEL**,
and **IVO DLOUHÝ**

VŠB – TU Ostrava, 17. listopadu 15, Ostrava
jan.brumek@vsb.cz

Keywords: Instrumented indentation test, material model, genetic algorithm

1. Introduction

Instrumented indentation is experimental method, which enables estimation of the values of mechanical properties from the record of dependence of indenter penetration depth on applied force. This method is especially suitable for construction materials, such as steel, if small dimensions of the specimen do not allow the use of conventional mechanical testing methods.

The instrumented indentation test used in this case is based on the well known Brinell's hardness test. Equipment of testing machines with a system for accurate recording of force and indenter penetration depth has enabled the development of methods for estimation of mechanical properties¹, such as elastic modulus, yield stress and strain hardening exponent. The Automated Ball Indentation Test² (ABI) is among the most widely used evaluation instruments. Due to repetitive indentation of spherical indenter into one spot, estimation of real stress and deformation can be realized. Typical process of an indentation test with the use of spherical indenter (Fig. 1) consists of loading part and unloading part.

Elastic modulus (3) is determined from the unloading phase of indentation test (Fig. 2). The value of elastic modulus is directly proportional to unloading curve slope.

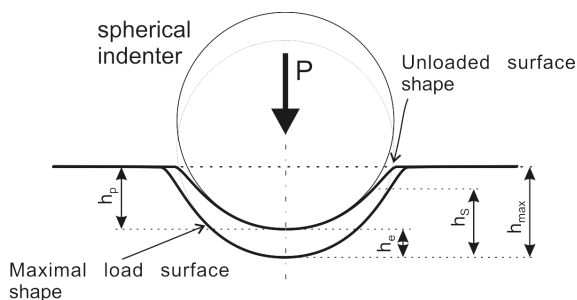


Fig. 1. Indent imprint – cross section

$$H = \frac{P_{\max}}{A} \quad (1)$$

$$E_r = \frac{\sqrt{\pi}}{2\sqrt{A}} \frac{dP}{dh} \quad (2)$$

$$\frac{1}{E_r} = \frac{1 - \nu_m^2}{E_m} + \frac{1 - \nu_i^2}{E_i} \quad (3)$$

P_{\max} is the maximal loading force, E_m and E_i are the elastic moduli of the tested material and indenter tip, and E_r is reduced indentation modulus.

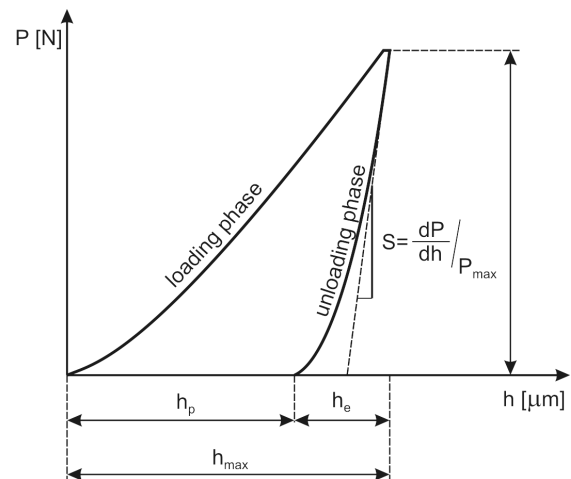


Fig. 2. Force - displacement indentation curve

Development of numerical modelling methods enables their use for the estimation of parameters in material models. The material properties estimation is based on searching for the minimum of function, which expresses the difference between a measured and a calculated process of indentation test. Non-linear material model in the finite element method is used for the analysis of a contact problem.

2. Finite element model description

For target function evaluation it is necessary to determine the indentation dependence by means of a numerical model. The indentation test is solved as a quasi-static axisymmetric problem with a non-linear material model. Finite element model assumes that a rigid spherical indenter is loaded with a normal force P and penetrates into the surface of an axisymmetric homogenous specimen occu-

pying the domain $\Omega \{0, 2\pi\}$ (Fig. 3). Uniaxial quasi-static indentation process is simulated by monotonically increasing the value ($h > 0$) of the penetration depth.

Another condition is that this process runs without any additional moments and friction. As this is a symmetric problem, a consequential axisymmetric contact problem is modelled for penetration depth $h = \{0; h_{\max}\}$. The indentation is modelled by the following contact problem finding the displacement field $u(x,y) = (u1(x,y), u2(x,y))$ in the solution of the unilateral problem:

$$\begin{cases} -\frac{\delta}{\delta x}(x\sigma_{11}(u)) - \frac{\delta}{\delta y}(x\sigma_{12}(u)) + \sigma_{33}(u) = 0, \\ -\frac{\delta}{\delta x}(x\sigma_{12}(u)) - \frac{\delta}{\delta y}(x\sigma_{22}(u)) = 0, \quad (x,y) \in \Omega \subset R^2; \end{cases} \quad (4)$$

The contact condition is:

$$\begin{cases} u_2(x,y) \leq -h + \varphi(x), \sigma_{22}(u) \leq 0, \\ [u_2(x,y) + h - \varphi(x)]\sigma_{22}(u) = 0, \\ \sigma_{12}(u) = 0, (x,y) \in \Gamma_0; \end{cases} \quad (5)$$

and boundary condition are defined:

$$\sigma_{11}(u) = 0, \sigma_{12}(u) = 0, (x,y) \in \Gamma_\sigma \quad (6)$$

$$u_1(0,y) = 0, \sigma_{12}(u) = 0, (x,y) \in \Gamma_1 \quad (7)$$

$$\sigma_{12}(u) = 0, u_2(x,0) = 0, (x,y) \in \Gamma_u \quad (8)$$

Where

$$\Omega = \{(x,y) \in R^2 : 0 < x < l_x, 0 < y < l_y\}, \quad l_x, l_y > 0$$

$$\Gamma_\sigma = \{(l_x, y) : 0 < y < l_y\} \quad \Gamma_0 = \{(x, l_y) : 0 \leq x \leq l_x\}$$

$$\Gamma_1 = \{(0, y) : 0 < y < l_y\} \quad \Gamma_u = \{(x, 0) : 0 \leq x \leq l_x\}$$

and $\varphi(x) = \sqrt{R^2 - x^2}$ is a function of the curve of the spherical indenter with the radius R .

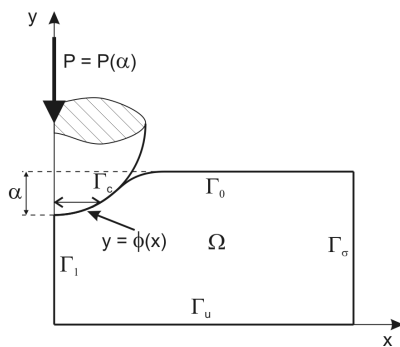


Fig. 3. Geometry of the indentation problem

Non-linear constitutive model (Fig. 4) used in analysis is:

$$\sigma = \sigma_y + C_1 \varepsilon_{pl} + \gamma(1 - e^{-C_2 \varepsilon_{pl}}) \quad (9)$$

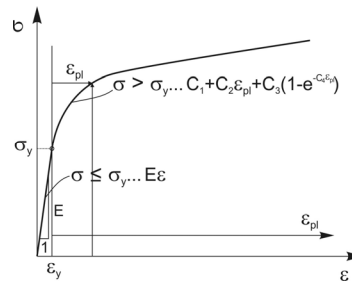


Fig. 4. Constitutive model for material non-linearity

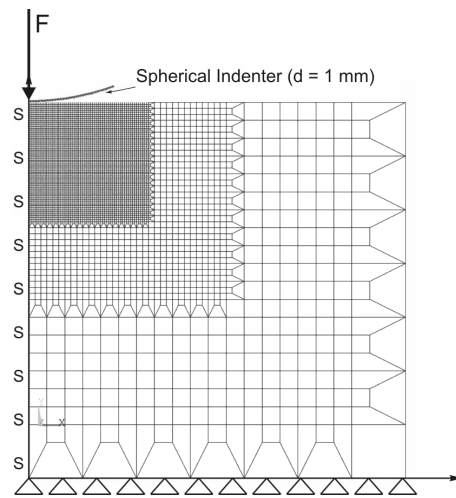


Fig. 5. Finite element mesh

3. Optimization algorithm

An optimization method using a genetic algorithm is utilized for the location of the target function minimum. Target function is composed of the measured indentation curve and indentation dependence calculated with a finite element model. The form of the target function proposed for this model:

$$F(X_1, X_j, \dots, X_m) = \int_{i=1}^n \sqrt{(Y_i - Y_i^*)^2} \quad (10)$$

The genetic algorithms start with randomly chosen parent chromosomes from the search space to create a population. They work with chromosome genotype. The population “evolves” towards the better chromosomes by applying genetic operators modelling the genetic processes occurring in the natural selection, recombination and mutation. The selection compares the chromosomes in the population aiming to choose these, which will take part in

the reproduction process. The selection occurs with a given probability on the basis of fitness functions. The fitness function plays a role of the environment to distinguish between good and bad solutions. The recombination is carried out after selection process is finished. It combines, with predefined probability, the features of two selected parent chromosomes forming similar children. After recombination offspring undergoes mutation. Generally, the mutation refers to the creation of a new chromosome from one and only one individual with predefined probability. After three operators are carried, the offspring is inserted into the population, replacing the parent chromosomes from which they were derived, producing a new generation. This cycle is performed until the optimization criterion is met (Fig. 6).

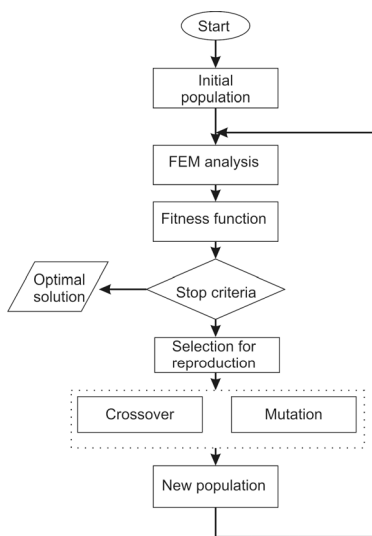


Fig. 6. Flow diagram of genetic algorithm

4. Experiment

For verification of the proposed method a set of steels was selected, on which experimental measurements were realized. The materials are listed in Table I. The experiment was processed with constant speed of loading. Samples surfaces were polished before the experiment until a mirror gloss was achieved.

Table I
Specimens' microstructure characterization

Mark	Micro-structure
R7T	Ferrite + pearlite
34CrMo	Bainite
CrMoV	Bainite
11375	Ferrite + pearlite

5. Discussion and results

Material model parameters for steel samples are estimated on the basis of the proposed method and experimental test. The results of the analysis are summarized in Table II. Values of yield stress and ultimate tensile stress from uniaxial tensile test are given in the right part of the table.

Table II

Mark	σ_y	C_1	γ	C_2	Re
R7T	532	345	419	27,8	552
34CrMo	1032	116	134	16,2	1053
CrMoV	682	151	203	33,2	708
11375	232	453	202	26,2	252

The final processes of a single materials indentation curve are depicted and compared with loading parts processes calculated with numerical model (Fig. 7).

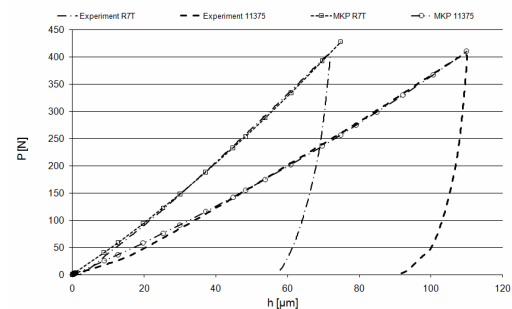


Fig. 7. Indentation curves comparison (R7T and 11375 samples)

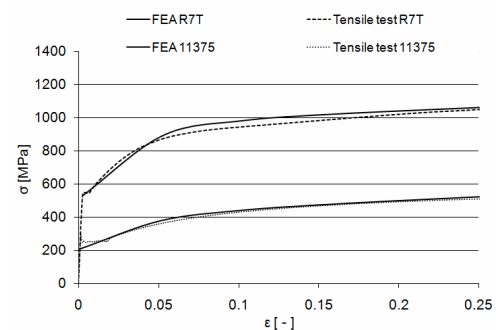


Fig. 8. Comparison of the material model and tensile test curve (R7T and 11375 samples, plotted in true stress-strain values)

6. Conclusion

The proposed method for the estimation of mechanical properties by instrumented indentation was verified on a set of construction materials. Optimization algorithm for searching of minimum of target function through evolution techniques was proposed. This system accomplished a reduction of the number of iteration steps in the process of searching for optimal solution. The results reached with the proposed method were compared to a true stress and true strain curve process from uniaxial tensile test. Results of predicted properties are in good correspondence.

The work was supported by Ministry of Industry and Trade of Czech Republic no. 2A-TP1/023.

REFERENCES

1. Oliver W. C., Pharr G. M.: *J. Mater. Res.* 7, 1564 (1992).
2. Taljat B., Zacharia T.: *Int. J. Solids Structures* 35, 4411 (1998).
3. Haggag F. M., Nanstad R. K., Braski D. N., in: *Innovative Approaches to Irradiation Damage and Fracture Analysis* (Mariott D. L., Mager T. R., Bamford W. H., ed.), vol. 170, pp. 101–107. ASME PVP, 1989.

J. Brumek, B. Strnadel, and I. Dlouhý (*VŠB – TU Ostrava*): Use of Genetic Algorithm for Identification of Nonlinear Constitutive Material

Indentation technique was focused on the prediction of the strain hardening behaviour of carbide steels. An improved technique to determine the plastic properties of material from the load-displacement curve from a ball indentation test was proposed. The time needed for finding an optimal solution for a non-linear constitutive model depends on a number of design variables. Common methods like gradient methods or linear programming can fail due the fact that they drop to the local minimum. The advantage of a genetic algorithm is that it does not require the knowledge of target function. Proposed method was applied to the data from the instrumented indentation technique. The results were found to be in good agreement with the data from conventional standard tests, and in less time.

APPLICATION OF THE SURFACE ROUGHNESS SPECTRUM ANALYSIS AT DIAGNOSING FUNCTIONAL PERFORMANCE OF ARMAMENT COMPONENTS

RENATA DVOŘÁKOVÁ*, EMIL SVOBODA, and KAREL MAŇAS

*Department of Mechanical Engineering, University of Defence Brno, Kounicova 65, 66210 Brno
renata.dvorakova@unob.cz*

Keywords: properties, surface, surface texture, roughness, power spectral density, frequency spectrum

1. Introduction

The performance of surface layers in various components can be strongly influenced by the character of load in operation. Another important factor, which should be investigated, is the micro-topology of contacting surfaces. Standard characteristics: Ra, Rq, Rt, Rsk, Rku, or RΔq, Rsm are largely applied to measure and quantify the surface texture. But these classic parameters are rather limited and inadequate to decide proper methods of machining, assessing functional properties of the surface or characteristics of the machine tool.

Integral methods based on the statistic, correlation and frequency analyses are not used in the meantime. Advantage of the statistic characteristics is in describing profiles or areas of the surface by minimum number of parameters, incorporating not only the peak to valley heights, but also the frequency and profiles in the surface.

The article describes the application of an integral method in the surface assessment to examine changes in a specimen surface at a fatigue test, using the acquired data to predict functional performance of components, namely the functional performance of the barrel bore top end.

The article's aim is to evaluate the relation between the surface quality and its functional performance by unconventional and non-standard characteristics.

2. The Surface Texture Characteristics

Prospective of the surface texture integral characteristics appear: autocorrelation function and power spectral density, and the related frequency spectrum of the profile. They may become powerful diagnostic tools capable of revealing e.g. slight changes in the surface texture produced by the cutting tool, undetectable by the classic parameters, or changes in the surface texture functional performance, seeming to be small by the classic parameters.

Autocorrelation function (ACF) can evaluate periodicity or randomness in surface profile features. The autocorrelation function can be used to evaluate surface condition, e.g. the zero points or disintegration of autocorrelation function, to calculate the index of plasticity at analysing rate and/or character of deformations in the surface projections. The autocorrelation can distinguish randomness from periodicity within a signal, i.e. to differentiate random and periodic processes. Besides, it enables to reveal a periodicity component in a mix with random components.

Power spectral density (PSD) function allows analysing surface profile density components by the individual frequencies. The function records the maximum value of the basic component profile; but there are other harmonic components, expressed as multiples of primary density. It describes variations in the inspected surface, both in terms of frequency (peak to valley spacing) or spectral density wavelengths, and their amplitude (magnitude). Higher spectrum density and volume involve higher number of harmonics and their magnitude. To analyse the surface spectral density, use may be made e.g. of the wavelength corresponding to the most recurring frequency (100% value).

The function can be applied in practice, e.g. at textured surface analysis, namely when a tiny change in size is found out in the classic roughness parameters (Ra, Rz etc.), but resulting in roughness change (often even markedly) of the analysed surface both in the frequency (variations in the surface texture spacing) or in the wavelength variations and their amplitudes.

In the graphics, the vertical axis shows the power spectral density in μm^2 , i.e. the amplitude area A^2 . The vertical axis shows the wavelengths λ [μm] ($\lambda = 1/f$). There are dominant wavelengths seen in the graphics. Their amplitude equals the square root of the corresponding value on the vertical axis.

Frequency spectrum of the profile (FS) implies frequencies of the range given by their wavelengths to ease their identification. The height of the spectrum line indicates the power (force) of a period in the profile. Spectral analysis allows to set-up the periodicity and orientation of a phenomenon that exists along with the roughness, namely by means of a frequency picked from the spectrum. If the profile involves a periodic phenomenon, then the frequency spectrum line (or a series of lines) will step high.

In the graphics, the wave number of spectral lines is plotted on the horizontal axis. The first spectral line corresponds to the profile length L ; the second spectral line corresponds to $L/2$, third to $L/3$ etc. Thus e.g. the spectral line of λ (12) = $4/12 = 0.333$ [mm] for the profile of the length of 4 mm (see Table I on the left, 4th row) corresponds to 12, the spectral line of the wave-

length λ (12) = $4/12 = 0.333$ [mm]. The spectral lines in the left part of the spectrum correspond to long wavelengths (i.e. to low frequency); the spectral lines in the spectrum right part correspond to short wavelengths (i.e. to high frequencies).

The graphic's vertical axis presents amplitudes of the relevant wavelengths, i.e. the signal power or intensity of the relevant frequency. The wave number with dominant magnitude (amplitude) is highlighted.

3. Fatigue of Materials

Fatigue of materials is a serious problem – affecting 90% of engineering components and structures. It develops in components under cyclic load, to crack at stresses much lower than their material strength and yield point proved in their static test.

Hence, a fatigue crack is the most frequent cause of component failures, initiating new surfaces. It develops from cyclic loads, totally restructuring the dislocation field, redistributing dislocations in the loaded material, splitting up the almost defect-free metallic matrix, with multivariate internal interface lines, into the so-called mosaic blocks. The dislocations are mostly concentrated into certain zones (e.g. interface lines of the mosaic blocks), whereas the greater part of matrix volume has few dislocations. This irregularity increases with the number of fatigue cycles, causing dislocations to amass increasingly on mosaic block interfaces, whereat the micro cracks grow. In other words, the fatigue localizes the deformation, making its distribution irregular. This is the reason why the cyclic loaded components can bear much lower load (amplitude) than is their static strength.

Repeated changes in the fatigue load cause the irregularities to intensify the dislocation distribution and more intensive interactions among them. Gradually, they develop into a "wall" that becomes impenetrable for the dislocations in motion. Such "walls" then segment the crystal into blocks, with only few dislocations to remain. Although they are movable, their movement is limited by the boundaries of the mosaic block. The dislocation density then intensifies along those boundaries.

Outwardly, these material structure changes will grow exactly in the surface texture changes in form of surface roughness or waviness.

4. Application of the Surface Texture Integral Characteristics

Two unconventional characteristics were applied to assess the surface texture changes of the specimens, namely the power spectral density (PSD) and the frequency spectrum (FS), added up for illustration with amplitude distribution (density) and material ratio curve. These tests were carried out at pure bending of flat speci-

mens. The experiments proved that significant changes occurred in the surface texture during the tests. These changes were gauged by the contact confocal gauge Taly-surf CLI 1000 to check roughness, assessed by the above described characteristics, and compared against the standard parameters.

Table I shows specimen surface roughness profiles before and after the fatigue test with the usually applied Ra parameter (mean arithmetic deviation of the assessed profile within the basic interval). The growth of Ra value by 1.85 is evident. Also evident after the test are extreme valleys and peaks that cause huge growth of roughness Rt profile height. The second row in Table I showed the amplitude density curves (grey histogram), and material ratio curves of the profile. Well visible here are the changes in the amplitude on the surface texture before and after the test, in the direction of amplitude spectrum distribution width narrowing against a major rise of the amplitude.

The third row in Table I showed the comparison of the power spectrum densities. Apparent are here the changes in the surface texture before and after the test. They are actually changes both in the relief division, but mainly in the area size under the PSD curve. The major differences are at wavelengths $\lambda = 0.8$ – 1.4 mm, when the PSD value increases approx 10 times. The fourth row in the Table is an additional assessment, presenting the profile of frequency spectra. There are visible changes in the single wave numbers, whereat a transformation occurs from the wave numbers 4–15 with the dominant wave number 12 (on the profile before fatigue test) into two dominant wave numbers (4 and 5), with the doubled amplitude.

The fatigue test results were used to assess functional performance changes of the rifled bore surface texture. The rifled surface texture was assessed in the course of the barrel performance, always after 1,000 gunshots. The initial value represented the rifled surface texture of a new barrel. The surface roughness profile of the new barrel rifles was uniform, while after 5 thousand gunshots it has shown removal of the unevenness peaks as a result of wear, with major valleys (of stratified nature). Also the division of amplitudes and material ratio corresponded to this state. The firing barrel standard parameter Ra average growth was 15%.

Different results were attained in the assessment by PSD (and FS) parameter. Figs. 1 and 2 show that significant changes occurred in the surface texture during the barrel performance. Fig. 1 shows comparison of the power spectral density for the new barrel (hatched area) and for the fired barrel (white area). This, so far not normalized parameter, shows a major increase of values in the area of the wavelengths $\lambda = 0.286$ – 0.105 mm, namely more than 3.5 times. There can be detected three dominant wavelength areas, namely for $\lambda \approx 0.2$ mm, $\lambda \approx 0.5$ mm, $\lambda \approx 0.8$ mm. These three dominant wavelength areas increased their power spectra by 1.5 up to 3.6 times, not so evident with the other wavelengths (see Table II).

Table I
Review of Surface Roughness Characteristics for the Fatigue Test

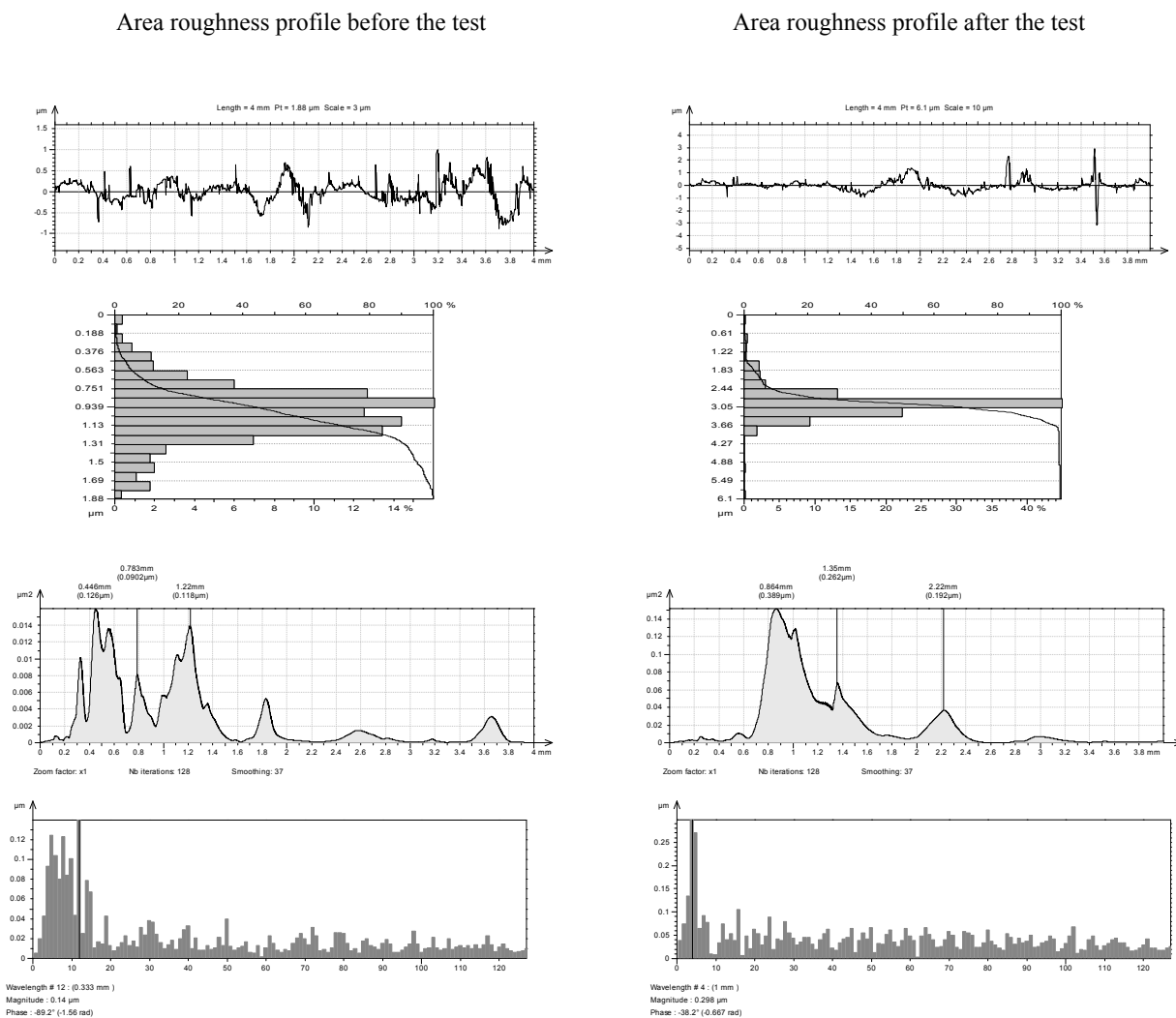


Table II
Review of the dominant wavelengths for a new barrel and a firing barrel

New barrel			Barrel after 5 000 shots		
λ [mm]	A [μm]	PSD [μm^2]	λ [mm]	A [μm]	PSD [μm^2]
0.111	0.030	0.012	0.111	0.299	0.017
0.222	0.050	0.015	0.222	0.210	0.055
0.800	0.180	0.035	0.800	0.230	0.045

Fig. 2 shows the frequency spectra for both barrels – black colour means wave numbers with their relevant amplitudes for the new barrel, while grey colour is for the firing barrel. Also here are evident changes with ampli-

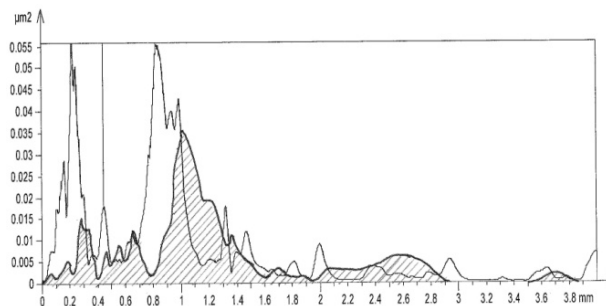


Fig. 1. Comparing a new barrel PSD (hatched area) with a barrel after 5,000 gun shots (white area)

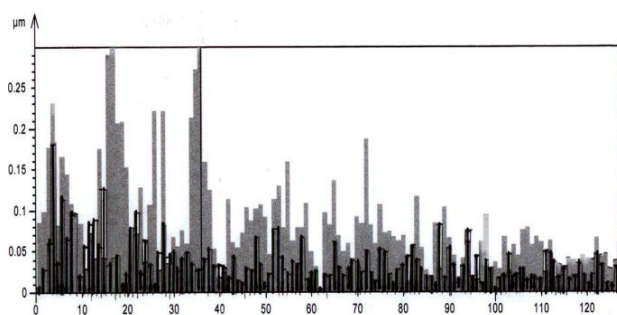


Fig. 2. Comparing a new barrel FS (black curves of wave number) with a barrel after 5,000 gunshots (grey curves)

tudes of single wave numbers. The largest amplitude increments are at the wave numbers (14 – 38), what corresponds to values $\lambda = 0.286\text{--}0.105$ mm given in Fig. 2 graphic chart. Another area with huge amplitude changes is for the wave numbers (2–6), what corresponds to values $\lambda = 2.00\text{--}0.667$ mm in Fig. 2 graphic chart. The amplitude value increments matching single wave numbers are even (10 up to 20) multiples.

Table II shows a review of dominant wavelength parameters for a new and a fired barrel. There are three dominant wavelengths chosen for both barrels described above, namely $\lambda = 0.111$ mm (wave number 36), $\lambda = 0.222$ mm (wave number 18), and $\lambda = 0.800$ mm (wave number 4). Data shown in the next column are amplitudes for these wavelengths readout from Fig. 2; the PSD value is readout from Fig. 1.

5. Conclusions

Advantage of the unconventional parameters is that they describe a profile or area primarily by frequency and shape parameters of the surface. These parameters can detect even small variations in the surface texture due to cutting tool, machine, or material, which are undetectable by the classic parameters.

This method is able to identify also changes in the surface texture performance, becoming evident in slight changes of the classic parameters, proved both in the measurement on the barrels mentioned herein, and in the measurement of surface roughness at the fatigue tests, i.e. with roughness altered to higher wavelengths (waviness).

Application of the unconventional parameters used in the assessment of the functional performance tends towards the processing of textured surfaces, i.e. the surfaces

based on their own physical substance, and with features corresponding to the required functional performance (a "tailor-made" surface). Exactly these textured surfaces are normally characterized by the wavelength of profile roughness, statistic and spectral characteristics.

This contribution was sponsored by the research intent MO0FVT0000404 "Research and Development of Modern Materials and Technologies for the Military Equipment Applications" and the grant GA CZR 106/08/1243 "Research of the Plasma Nitriding of Internal Cavities".

REFERENCES

1. Whitehouse D. J.: *Handbook of Surface Metrology*, pp. 44 – 101, and 251–264. Institute of Physics Publishing Bristol and Philadelphia 1994.
2. Whitehouse D. J.: *Surfaces and their Measurement*, Kogan Page Science, 2004.
3. Novák Z.: *Prostorové hodnocení textury povrchu (Spatial Assessment of the Surface Texture)*. Studie. Brno 2006.
4. ČSN EN ISO 4288 *Geometrical Product Specifications (GPS) – Surface Texture: Profile Method – Rules and Procedures for the Assessment of Surface Texture*. ČSNI 1999.
5. Fiala J., Kraus I.: *Povrchy a rozhraní (Surface and Interface)*, pp. 108–152. ČVUT, Praha 2009.

R. Dvořáková, E. Svoboda, and K. Mañas
(University of Defence Brno): **Application of the Surface Roughness Spectrum Analysis at Diagnosing Functional Performance of Armament Components**

The article describes the application of an integral method in the surface assessment to examine changes in a specimen surface at a fatigue test, using the acquired data to predict functional performance of components, namely the functional performance of the barrel bore top end. The article's aim is to evaluate the relation between the surface quality and its functional performance by unconventional and non-standard characteristics. Application of the unconventional parameters used in the assessment of the functional performance tends towards the processing of textured surfaces, i.e. the surfaces based on their own physical substance, and with features corresponding to the required functional performance. Exactly these textured surfaces are normally characterized by the wavelength of profile roughness, statistic and spectral characteristics.

EFFECT OF TIME ON NANOINDENTATION ELASTIC MODULUS OF THREE DIFFERENT DENTAL RESTORATIVE COMPOSITES

**RENATA EICHLEROVÁ^{a*}, JAROSLAV
LUKEŠ^a, SVATAVA KONVIČKOVÁ^a,
and PAVEL BRADNA^b**

^aLaboratory of Biomechanics, Department of Mechanics, Biomechanics and Mechatronics, Faculty of Mechanical Engineering, Czech Technical University in Prague, Technická 4, 166 07 Prague 6, Czech Republic; ^bInstitute of Dental Research, 1st Faculty of Medicine, Charles University, General Faculty Hospital in Prague, Karlovo náměstí 32, 121 11 Prague 2, Czech Republic
eichlerova.renata@seznam.cz

Keywords: nanoindentation, restorative composites, elastic modulus, time dependency

1. Introduction

Filling composite materials are widely used in dentistry in the last 15 years for their aesthetic aspects, good biocompatibility and no toxicity. The reasons against use of amalgam alloys were aesthetic aspects, toxicity and environmental pollution by mercury waste. Lifetime of composite filling is satisfactory but there is still a need for improvement. Fractures of filling, secondary caries or loss of filling sometimes occur. Due to mechanisms such as occlusal loading and shrinkage of composites could create stresses in filling and adhesive layer and these stresses cause failures of the tooth-restoration interface and undermine marginal integrity¹. The value of stress can be influenced by cavity shape and use of suitable materials. The problem could be solved through the minimizing of interfacial stress by optimizing the cavity shape using modern shape optimizing techniques. For stress analysis and design of cavity shape a finite element program are used². Value of elastic modulus of resin-composite in performed analyses is considered to be constant in time. The intent of this study was to determine elastic modulus of different filling materials for the use in such analysis and to observe changes of mechanical properties in different time after polymerization. Due to better knowledge of material properties more accurate results of analyses could be reached.

2. Materials and Methods

Nanoindentation modulus of three different materials was tested in this study. First chosen material FiltekTM Silorane (3M ESPE, Dental Products, St. Paul, U.S.A.) is

a visible-light activated, low-shrink restorative composite for posterior restorations. The main advantage of this composite is excellent marginal integrity and reduced risk of secondary caries due to lowest polymerization shrinkage (<1%). This low shrinkage significantly reduce polymerization stress thereby decrease the risk of enamel fractures and postoperative sensitivity. FiltekTM Silorane has excellent compressive strength for stress-bearing restorations and high flexural strength protecting the tooth from fractures. Second chosen material FiltekTM Supreme XT (3M ESPE, Dental Products, St. Paul, U.S.A.) is a visible-light activated, universal restorative composite designed for use in anterior and posterior restorations. This material is based on 3M ESPE's nanotechnology, which combines excellent strength with low abrasion and polymerization shrinkage (<2,5%). FiltekTM Supreme XT contains bis-GMA, UDMA, TEGDMA, and bis-EMA resins. All shades except for the translucent shades are radiopaque. The fillers for the radiopaque shades are a combination of zirconia/silica and silica filler with an average primary particle size of 5-20 nm. Third chosen material Charisma (Heraeus Kulzer GmbH, Hanau, Germany) is microglass universal hybrid composite for posterior restorations. Charisma is based on bis-GMA matrix. The content of filler is 64% (by volume) and is combination of barium aluminium fluoride glass (0,02–2 microns) and highly dispersive siliciumdioxide (0,02–0,07 microns). Charisma is light curing and radio-opaque composite with high strength and wear resistance provide long-lasting restorations. These materials represent different types of filling restorative composites used in dentistry nowadays.

Three disc specimens (4 mm in diameter and 2 mm in height) of each material were prepared in Teflon mould. Moulded material was covered from both sides by transparent plastic film and was pressed between two glass slides. Polymerization of material was activated by using of light curing unit (Translux Power BlueTM, Heraeus Kulzer GmbH, Germany) for time period according to instructions for use. Each specimen was irradiated only from one side and this side was tested. After polymerization the specimen was finished mechanically in grinding machine with abrasive papers with subsequently decreasing abrasiveness up to 4000-grit and then was polished. Thus prepared specimen was stick on magnetic metal thin plate in order to prevent movement of specimen during indentation.

The nanoindentation testing was performed using a Hysitron's TriboLab® (Hysitron, Inc., Minneapolis, USA) at the CTU in Prague. System possess the option of *in-situ* SPM imaging, extended force transducer SN5-484-01, active vibration isolation and piezo automation with precision of the indent placement less then 0,1 µm. A Berkovich tip was a nanoindenter used for material

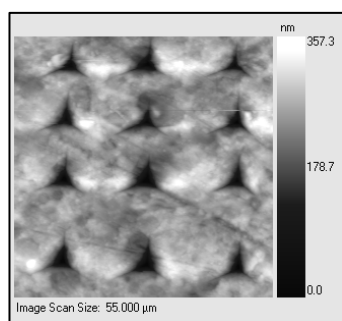


Fig. 1. Detail of indentation area

properties testing. A shape of the tip is a three sided pyramid with a total included angle of 142,3 degrees and a half angle of 65,35 degrees. The Berkovich tip has the same projected area to depth ratio as a Vickers indenter, but it is easier to grind this tip to a sharp point and so is more readily employed for nanoindentation type tests³. Load function of the load control testing cycle consisted of three segments: loading, holding at the peak of load and fully unloading. Each part of trapezoidal function lasted 10 seconds and maximum applied load was 15 mN. Twelve indentations were placed in matrix 3×4 about separation of 15×20 μm in order to avoid the mutual influence, as in Fig. 1. These indentations on randomly selected areas were performed on each specimen in every time of measurement.

The model chosen to interpret the indentation data were that of Oliver and Pharr³. Indentation elastic modulus E_r has the following relationship (I) with the elastic modulus of the material, namely:

$$\frac{1}{E_r} = \frac{(1-\nu^2)}{E} + \frac{(1-\nu_{tip}^2)}{E_{tip}} \quad (I)$$

where E and ν are elastic modulus and Poisson's ratio of the sample, E_{tip} and ν_{tip} are elastic modulus and Poisson's ratio of the indenter, respectively^{4,5}. Mentioned above elastic modulus and Poisson's ratio of the indenter and indentation modulus must be known in order to determine the elastic modulus of the material. The elastic properties of the diamond Berkovich indenter are already known as: $E_{tip} = 1141$ GPa and $\nu_{tip} = 0,07$ (ref.⁶). Poisson's ratio $\nu = 0,3$ for resin-composites is used⁴. The indentation modulus is one of many material properties that can be gained from the load-displacement graph of the nanoindentation test (Fig. 2).

In order to observe effect of time on indentation modulus, different time intervals between nanoindentations of specimens were determined as follows: 1 hour, 1 day, 1 week and 1 month after specimen manufacturing. Specimens were stored in dark and dry place at room temperature all the time.

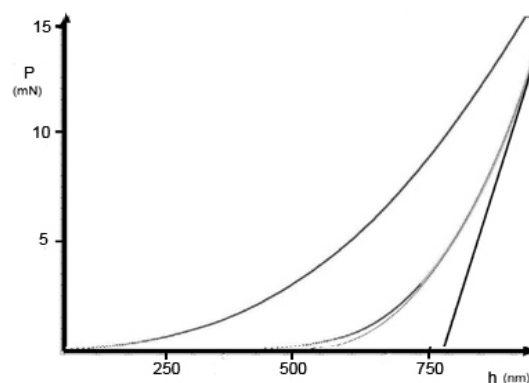


Fig. 2. Typical load-displacement graph of the nanoindentation where the loading, holding and unloading segments are evident

3. Results

The mean elastic moduli of all three tested materials are presented in Tab. I. The data were analyzed by analysis of variance and T-test. Statistically significant differences among the time groups at $P < 0,05$ revealed. Each tested material presented significant increase of elastic modulus between the first and the third time interval. For FiltekTM Supreme XT and FiltekTM Silorane, significant decrease of elastic modulus was observed between the third and the fourth time interval which was not the case of the Charisma.

Table I

Mean elastic moduli and variation coefficients of the resin-composite tested in different times after manufacturing of specimens

Time interval	Mean elastic modulus E [GPa] (variation coefficient [%])		
	Filtek TM Supreme XT	Filtek TM Silorane	Charisma
1 hour	13,1 (6,1)	11,9 (1,6)	5,8 (3,4)
1 day	14,2 (0,8)	12,4 (10,2)	6,4 (4,4)
1 week	17,6 (4,5)	14,2 (6,4)	7,8 (3,8)
1 month	12,5 (2,4)	10,8 (15,7)	8,0 (6,2)

4. Discussion

Poisson's ratio of 0,3 was assumed for all materials. If the Poisson's ratio of the material was different the calculated elastic modulus would decrease quadratically with increasing Poisson's ratio⁴. No significant differences between the three specimens made of the same material and measured at the same time was found. Each tested material showed significant increase in modulus after 1 week

(standard deviation in parenthesis): Filtek™ Silorane (11,9 (0,2) – 14,2 (0,9)), Filtek™ Supreme XT (13,1 (0,8) – 17,6 (0,8)), Charisma (5,8 (0,2) – 7,8 (0,3)). Decrease of modulus occurred for both 3M ESPE materials after 1 month: Filtek™ Silorane (10,8 (1,7)), Filtek™ Supreme XT (12,5 (0,3)). Modulus of Charisma remained almost unchanged with small increase: Charisma (8,0 (0,5)). The highest modulus had Filtek™ Supreme and Charisma had lower modulus than Filtek™ Silorane. In parallel with this research, elastic moduli were examined also by the three-point bending test. The elastic moduli were lower in comparison with nanoindentation testing. Time set for the three-point bending test prescribed in ISO 4049:2000 is 24 hours after the specimen manufacturing. The results obtained by nanoindentation testing showed that the elastic modulus of resin-composites take different values in time and this effect could not be examined by three-point bending test. No standards for dental resin-composites nanoindentation testing are available at the moment.

5. Conclusions

Nanoindentation is an effective method for elastic modulus evaluation. Due to non-destructive character of this method in terms of possibility to measure one specimen in different areas more than once we can determine the effect of time on mechanical properties, namely on elastic modulus. The sample surface preparation is very important for obtaining correct results because the use of nanoindentation technique requires a very smooth and flat sample surface. Results from nanoindentation revealed that the time has a considerable effect on the development of elastic moduli of the tested samples. These changes can be explained by the setting reaction of polymer matrix and filling particles after polymerization. We conclude that elastic modulus of tested materials vary in time.

The research was supported by the Ministry of Education project: Transdisciplinary research in Biomedical Engineering II, No. MSM 6840770012 and Research Plan MSM 6840770003.

REFERENCES

1. Hickie R.: *Eur. Ceram. Soc.* 2008, 7278.
2. Shi L., Fok A. S. L., Qualtrough A.: *Dental Material*, 24, 1444 (2008).
3. Fischer-Cripps A. C.: *Nanoindentation*, Mechanical Engineering Series, 223 Spring Street, NY, 10013, USA: Springer Science+Business Media, LLC, 2nd ed., 2004.
4. Masouras K., Akhtar R., Watts D. C., Silikas N.: *J. Mater. Sci.: Mater. Med.* 19, 3561 (2008).
5. He H. L., Swain M. V.: *J. Dentistry* 35, 431 (2007).
6. Ziopus P., Rogers K. D.: *J. Bionic Engineer.* 3, 019 (2006).

R. Eichlerová^a, J. Lukeš^a, S. Konvičková^a, and P. Bradna^b (^a *Department of Mechanics, Biomechanics and Mechatronics, Faculty of Mechanical Engineering, Czech Technical University in Prague;* ^b *Institute of Dental Research, 1st Faculty of Medicine, Charles University, General Faculty Hospital in Prague*): **Effect of Time on Nanoindentation Elastic Modulus of Three Different Dental Restorative Composites**

The intention of this study was to determine elastic modulus of different resin-composite filling materials for the use in FEM analyses and to observe changes of mechanical properties in different time after polymerization. Nanoindentation was chosen as suitable non-destructive method for elastic modulus determinations. Each tested material presented changes in modulus in dependence on time after specimens moulding. We conclude that elastic modulus of tested materials vary in time. These changes can be explained by the setting reaction of polymer matrix and filling particles after polymerization.

DETERMINING THE TRUE STRESS-STRAIN RELATIONSHIP BY DEPTH SENSING INDENTATION ON TWO STRUCTURAL MATERIALS

PETRA GAVENDOVÁ^a, PAVOL ZUBKO^b, LADISLAV PEŠEK*^b, and OLGA BLÁHOVÁ^c

^aInstitute of Materials Research, Slovak Academy of Sciences, 043 53 Košice, Slovakia, ^bDepartment of Materials Science, Technical University of Košice, Faculty of Metallurgy, 042 00 Košice, Slovakia, ^cNew Technologies-Research Centre, University of West Bohemia, Univerzitní 8, 306 14 Plzeň, Czech Republic
petgav@post.sk

Keywords: Depth Sensing Indentation, spherical indentation, stress-strain curve

1. Introduction

The increasing need for evaluation of the mechanical properties of small volumes of materials caused rapid development in depth sensing indentation technique (DSI) over the last decade. Loading force, F , and indentation depth, h , are continuously recorded during the loading and unloading cycle. In DSI, the test result is an indentation curve¹. However, sharp indenter does not enable one to measure various deformation states, a spherical indenter has been used more often for this purpose. A sphere has the advantage that the effective strain changes as a function of indentation depth. Thus, wide range of indentation strains can be obtained with the increasing force at the same spot without changing the indenter². Therefore, the stress – strain, $\sigma - \epsilon$, curve can be determined by spherical indentation. The mean contact pressure differs in different stages of the ball indentation³. For the initial elastic regime, the mean contact pressure (p_m) increases linearly with the square root of the indentation load. When p_m reaches the elastic limit, the plastic zone will develop beneath the indenter as shown in Fig. 1. In the elastic-plastic regime, the mean contact pressure increases gradually. After the plastic zone expands to the surface of the specimen, the mean contact pressure increases slightly⁴.

The true stress and true strain values determined from uniaxial tensile test data can be compared with both indentation stress – strain data according to the following equations⁵:

$$\sigma_{\text{indentation}} \approx p_m / \psi \approx \sigma_{\text{uniaxial tension}} \quad (1)$$

$$\epsilon_{\text{indentation}} \approx 0,2a / R \approx \epsilon_{\text{uniaxial tension}} \quad (2)$$

where p_m is the mean contact pressure, R is the indenter radius, a is the contact radius and ψ is the constrain factor. In the elastic regime, the value of ψ increases linearly up

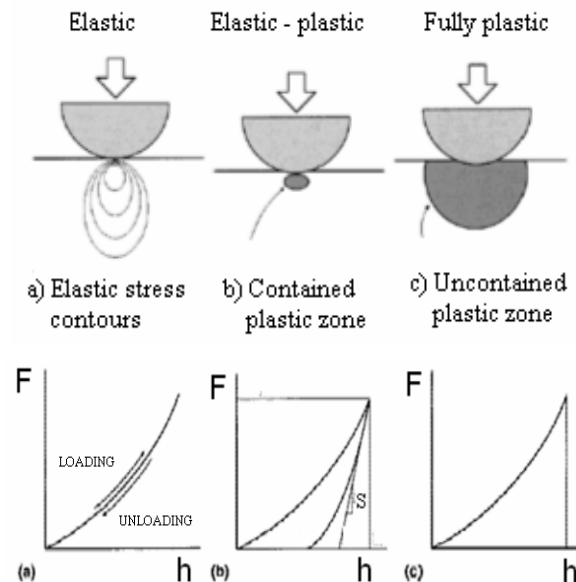


Fig. 1. Schematic representation of plastic zone expansion during ball indentation⁴

to about 1.1. It increases gradually through the elastic-plastic regime, and is almost constant in the fully plastic regime⁴.

This paper deals with the determination of true stress – true strain curve on two materials, aluminium AA6063 and steel St 52, and with the comparison of the results from indentation with those of uniaxial tensile test.

2. Materials and experimental methods

The indentation experiments were performed using a NanoIndenter XP with the CSM (Continuous Stiffness Measurement) technique⁶. The spherical indenter tip of 600 μm diameter were made of ruby. For each sample, 10 measurements were performed and the average value was calculated. The uniaxial tensile test was performed using FP 100/1 tensile testing machine. The result of the tensile test is a force – extension, $F - \Delta L$ diagram, from which engineering stress, R , and strain, ϵ , were obtained using the following formulas:

$$R = \frac{F}{S_0} \quad (3)$$

$$\epsilon = \frac{\Delta L}{L_0} \quad (4)$$

where F is the loading force, S_0 is a specimen cross-section area, ΔL is the elongation, $L = L_0 + \Delta L$.

The true stress, σ , and true strain, Φ , values were calculated according to equations:

$$\sigma = R(1 + \varepsilon) \quad (5)$$

$$\Phi = \ln(1 + \varepsilon) \quad (6)$$

3. Results and Discussion

3.1. Indentation tests

Typical indentation curves from single loading-unloading tests for both materials studied are illustrated in Fig. 2. These tests provide only one value of hardness and indentation modulus from each measurement.

However, when using the CSM method, the dependencies of hardness, H , and indentation modulus, E' , on the indentation depth, h , can be obtained (Fig. 3 and Fig. 4, respectively). As it can be seen, E' and H measured by

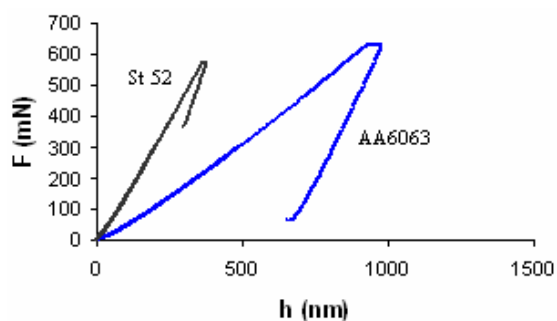


Fig. 2. Indentation curves for AA6063 and St 52

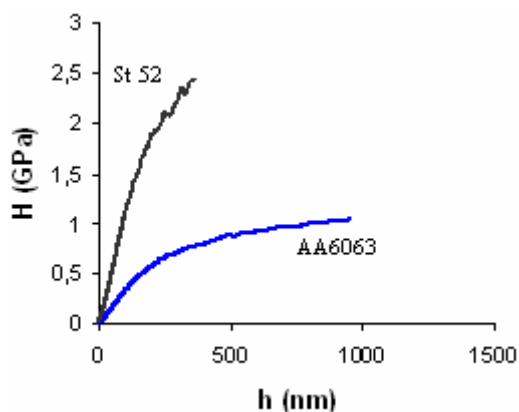


Fig. 3. Dependence of hardness, H , on the indentation depth, h , for AA6063 and St 52

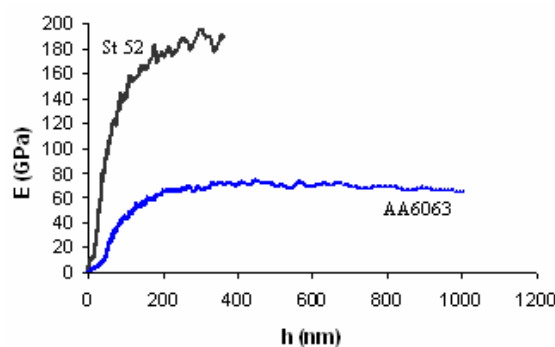


Fig. 4. Dependence of indentation modulus E' on the indentation depth for AA6063 and St 52

CSM method rise from zero until saturation values. They correspond to typical values for both, aluminium⁷ and steel⁸.

It is also known that the values of indentation modulus E' are influenced by the effects of pile-up or sinking-in² of the material around the indentation. The agreement between the measured and literature data indicate that these effects are not important in our case and confirm the correctness and reliability of current DSI measurements. On the other side, the first contact of the indenter with the specimen surface is usually biased by significant measurement errors due to undefined indenter shape, surface roughness and shape function. Hence, the beginning of the curves (up to approximately 50 nm depth) is considered to be non-relevant.

The stress-strain curves, σ – ε , (Fig. 5 and Fig. 6) were calculated using the Eq. (1) and Eq. (2) for both materials. The corresponding curves are plotted in Fig. 5 and Fig. 6. No clearly defined yield strength points are visible on the curves. Note that only the parts of the curves extending slightly about the yield strength limits known for these materials from the literature are drawn because of significant plasticity of both materials.

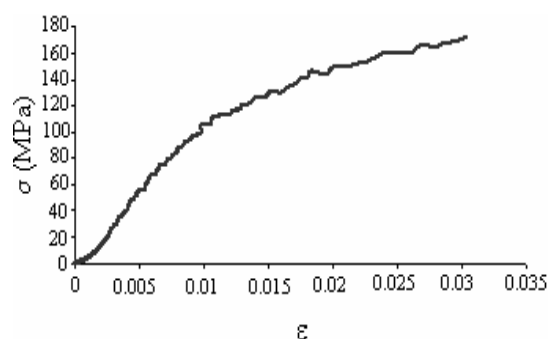
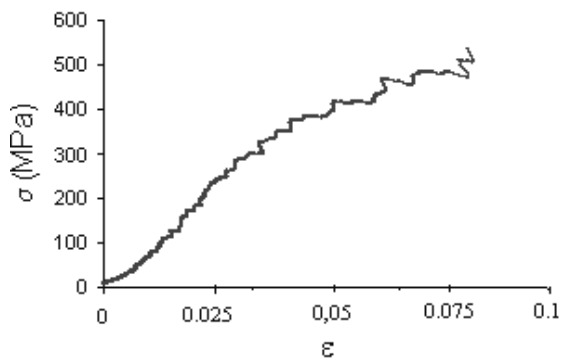
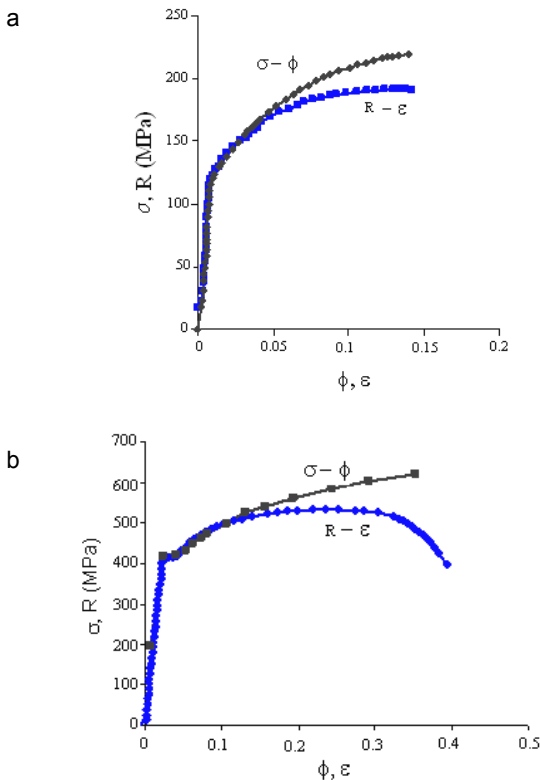


Fig. 5. Stress σ – strain ε curve for aluminium AA6063

Fig. 6. Stress σ – strain ε curve for steel St 52

3.2. Uniaxial tensile tests

Fig. 7 a–b show the true and engineering stress – strain curves for both investigated materials obtained in uniaxial tensile tests. Yield strength is clearly defined in both cases and the differences between true and engineering strains appear only at strain values exceeding 5 % strains.

Fig. 7. The engineering stress R – strain ε and true stress σ – true strain Φ curves for; a) AA6063 b) St 52

3.3. Comparison of the results

The comparison of stress – strain curves obtained from uniaxial tensile testing and indentation testing for both materials is illustrated in Fig. 8 and Fig. 9, respectively. In the case aluminium, both curves are in good agreement in the elastic regime (Fig. 8). Curves differ in the elastic-plastic regime above the yield strength defined by tensile test. As discussed earlier, pile-up effects may cause deviations in contact area estimation. Subsequently, large differences may appear in contact stress determination and stress evaluation. The pile-up effect around the indent was not taken into account in our case, therefore, the deviations between both curves can be attributed to this effect.

The lack of pronounced yield strength limit on DSI curves in aluminium forced us to use $R_{p0.2}$ as a criterion. The corresponding data are summarized in Table I.

In case of St 52, the curves differ already in the elastic regime. It is known that this type of steel exhibits Luders deformation at the yield point which leads to strong

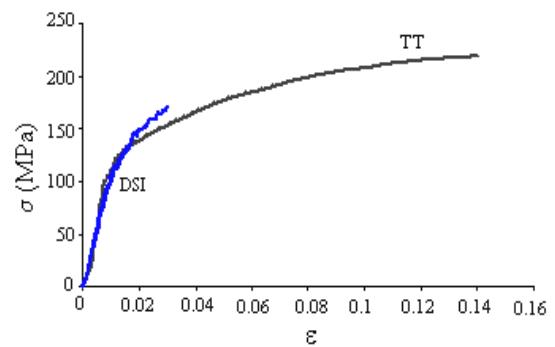
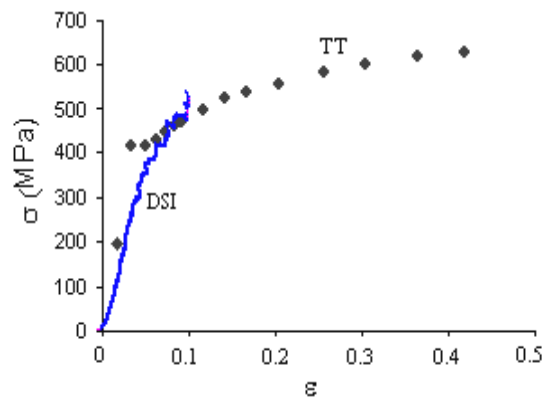
Fig. 8. True stress σ – ε true strain curves for AA6063; a) uniaxial tensile test (TT), b) indentation test (DSI)Fig. 9. True stress σ – ε true strain curves for St 52; a) uniaxial tensile test (TT), b) indentation test (DSI)

Table I
Values of yield strength

	AA6063 ($R_{p0.2}$) [MPa]	St 52 (R_e^* , $R_{p0.2}$) [MPa]
Uniaxial tensile test	100	410*
DSI	110	450

pile-up. Quantifying of the pile-up effect is difficult and its absence in the evaluation of the stress – strain curve seems to result in the observed differences. However, despite the differences already in the elastic regime, the yield strength values obtained from DSI based on $R_{p0.2}$ approach and from the tensile tests differ within 10 %.

4. Conclusions

The comparison of uniaxial tensile tests and DSI with spherical indenter using CSM method on aluminium AA6063 and steel St 52 revealed acceptable agreement between the stress – strain curves obtained from both techniques. The yield strength can be estimated from the stress – strain curve calculated from DSI/CSM technique using $R_{p0.2}$ approach. The obtained values exceed by 10% the values obtained from tensile tests. The deviations were attributed the unaccounted pile-up effects.

The values of indentation modulus measured by DSI are in good agreement with the real values of the Young's modulus of both materials.

DSI technique with spherical indenter is a promising method to determine stress – strain curves of bulk materials in case of lack of experimental material for tensile testing.

This work was supported by the Scientific Grant Agency of Slovak republic under the following grant projects: Slovak-Czech bilateral co-operation SK-CZ-0108-07, VEGA project No. 1/0846/09 and VEGA project No. 2/0138/10.

REFERENCES

1. Fischer-Cripps A. C.: *Nanoindentation*. Springer, New York 2002.
2. ISO 14577: 2001, *Metallic materials-Instrumented indentation test for hardness and materials parameters*, Part 1: test method, International organization for Standardization, 2001.
3. Tabor D.: *The Hardness of Metals*. Clarendon Press, Oxford 1951.
4. Choi Y., Kwon D.: *Derivation of tensile flow properties of thin films using nanoindentation technique*, pp. 525–531. Elsevier, Current Applied Physics 2, 2002.
5. Herbert E. G., et al.: *On the measurement of stress-strain curves by spherical indentation*. In: Mat. Res. Soc. Symp. Proc., Vol. 649, MRS, 2001.
6. *Nanoindenter XP Manual*, MTS Innovation Center, 2004.
7. Aalco: Aluminium alloys [online] 1. May 2000 [Quoted on 23.March 2009]. Available at <http://www.azom.com>.
8. *Product catalogue*, Výskumný a skúšobný ústav, VSŽ ocel' 95/96.
9. Zubko P.: *PhD. Thesis*. Technical University, Košice 2007.

P. Gavendová^a, P. Zubko^b, L. Pešek^{*b}, and O. Bláhová^c (^a *Institute of Materials Research, Slovak Academy of Sciences, Košice, Slovakia* ^b *Department of Materials Science, Technical University of Košice, Faculty of Metallurgy, Košice, Slovakia* ^c *New Technologies-Research Centre, University of West Bohemia, Plzeň, Czech Republic*): **Determining the True Stress-Strain Relationship by Depth Sensing Indentation on Two Construction Materials**

The aim of this paper is the determination of the true stress – true strain, $\sigma - \epsilon$, curves by depth sensing indentation (DSI) on both aluminium (AA6063) and steel (St 52) using a spherical indentation. Hardness, H , indentation modulus, E' , and a part of the indentation stress – strain, $\sigma - \epsilon$, curve were determined using a spherical indenter with 600 μm diameter using a NanoIndenter XP with CSM technique. Yield strength was defined as $R_{p0.2}$ for DSI. Uniaxial tensile test were performed for comparison of both techniques. The stress – strain curves obtained on basis of DSI technique agree within 10% accuracy with the values obtained from tensile tests. The deviations were attributed the unaccounted pile-up effects.

LOCAL ASPECTS OF SHEAR-MODE CRACK PROPAGATION IN AUSTENITIC STEEL

LIBOR HOLÁŇ, JAROSLAV POKLUDA,
and KAREL SLÁMEČKA*

Brno University of Technology, Faculty of Mechanical Engineering, Technická 2, 616 69 Brno, Czech Republic
slamecka@fme.vutbr.cz

Keywords: shear cracks, local roughness, crack growth rate, growth micromechanisms, austenitic steel

1. Introduction

While the principal micromechanisms of fatigue crack growth under modes I and II are well known, there is a lack of any plausible interpretation in case of a pure mode III crack propagation¹. Most of experiments allowing mode II and mode III crack propagation were performed in a pure torsion or asymmetrical 4-point bending (e.g. in ref.^{2–8}). Except for the paper by Nayeb-Hashemi et al.⁴, however, no detailed examinations of the micromechanism of shear mode crack growth were reported in these studies. Therefore, the investigation of shear crack growth mechanisms constitutes a rather big challenge.

A careful fractographical observation of mode II and III growth under pure shear remote loading in the region of very low cycle fatigue were performed by Pokluda et al.⁹. These investigations indicated that the microscopic mode of the pure remote mode II crack extension was rather a mixed I+II mechanism. Similarly, the mode II and the combined mode I+II were dominating microscopical fracture micromechanisms also during the remote mode III loading. The crack growth rate in mode II was found to be about five times higher than that in mode III (ref.⁹).

This paper presents a study on the near-threshold crack propagation under shear modes II and III. In this case, the local (microstructural) effects on the crack growth are dominant since the size of the cyclic plastic zone at the crack tip becomes less than that of a characteristic microstructural distance^{10,11}. The crack flanks are, therefore, microscopically tortuous and related friction forces extremely rise and diminish the shear-mode crack driving force. As a consequence, the crack tip might tend to incline to a mode I loading by creating local mode I branches. Such cracks can no longer be considered to grow under a shear mode loading and measured “shear-mode” fatigue characteristics become irrelevant. In order to identify such processes, a local three-dimensional analysis of the fracture surface topology in a microscopic region close to the precrack tip had to be performed by means of the SEM stereo-photogrammetry.

2. Experimental arrangements and methods

Two original testing setups (cells) have been designed and utilized in order to assure both pure remote shear modes II and III crack propagation in a single cylindrical specimen. The loading scheme of the first cell is depicted in Fig. 1. The cracks at the “top” and “bottom” sites of the specimen grew under a pure mode II loading while those at the “front” and “back” sites propagated under a pure mode III loading (the mixed mode II+III in all other crack front points). A circumferential V-notch with a precrack was introduced by a blade mechanism. Finally the specimens were compressed by 20 kN to sharpen the precrack. Five specimens made of the austenitic steel X5NiCrTi26-15 with the outer diameter of 8 mm and the inner diameter of 4 mm were tested by using the shear stress loading range of 180 MPa and the cyclic ratio $R = 0.1$.

The second special cell for loading specimens was manufactured to enable higher loadings (see Fig. 2). Five specimens with the outer diameter of 25 mm and the inner diameter of 12 mm were tested by using the $\Delta\tau_n$ -values of 160 MPa (2 specimens), 200 MPa (2 specimens) and 220 MPa (1 specimen) and the cyclic ratio $R = 0.1$. After the shear mode tests, all specimens were fractured by the cyclic tensile loading.

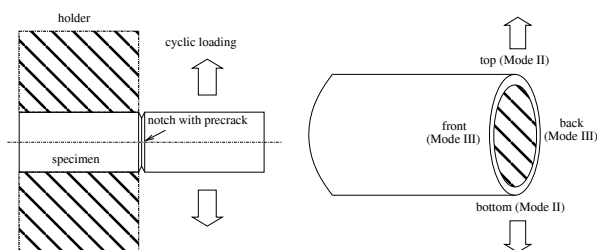


Fig. 1. The loading scheme for small specimens and, the loading modes operating at different specimen sites

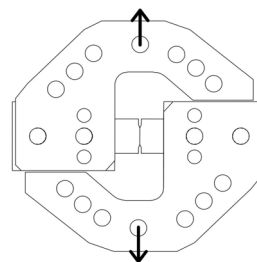


Fig. 2. The scheme of the loading cell. The loading direction is indicated

In order to determine the mode II and mode III stress intensity factors at the crack tip, a numerical analysis was performed by means of the ANSYS code¹².

The spatial crack tortuosity in a close vicinity of the precrack was determined by means of the stereo-photogrammetry in the scanning electron microscope (SEM). The stereo-photogrammetry is a method that makes use of the stereoscopic principles in order to obtain topographical data of fracture surface under investigation. Inputs of the method are two images of the analyzed region taken from different positions of view (so-called stereopairs, stereopair) and some additional parameters that characterize a projection used during their acquisition. Usually, SEM equipped with the eucentric holder is employed and the stereopair is obtained by tilting the specimen in the microscope chamber by an angle that depends on a local roughness of the surface. The stereopair is processed via a matching algorithm in order to find corresponding points on both images (homologue points) and the relative z -coordinates of homologue points are calculated. The 3D model of depicted surface area usually consists of 10–20 thousand non-equidistant points and so called Delaunay triangulation must be performed¹³.

3. Theoretical and experimental results

In order to determine the mode II and mode III stress intensity factors at the crack tip, a numerical analysis was performed by means of the ANSYS code¹². Although the loaded specimen was modelled as a rotationally symmetric, a full linear-elastic 3D solution had to be used owing to a different symmetry of the loading. Very precise values of the stress intensity factors K_I , K_{II} and K_{III} could be calculated in this way. The ratio of maximal values in pure shear modes II and III was found to be $K_{III\max}/K_{II\max} = 1.37$ and the values of $K_{I\max}$ were found to be negligible (in two orders lower). The results of this theoretical analysis were used to determine stress intensity factors for all experimental specimens investigated in this study.

Typical two-dimensional fracture morphology of pure mode II and III shear cracks is shown in Fig. 3. In this figure, the regions corresponding to a precrack, shear mode propagation and final fracture are highlighted as white boundaries. Since the length of the shear mode cracks was an order lower than that of the pre-crack, a nearly constant crack growth rate during the shear propagation could be assumed. Therefore, the crack-growth-rate was calculated simply by dividing the total length of shear cracks by corresponding numbers of cycles. The near-threshold crack growth curves for both the mode II and the mode III propagation in the austenitic steel are plotted in Fig. 4. The related regression curves follow the Klesnil-Lukas relationship $da/dN = A(\Delta K^n - \Delta K_{th}^n)$ (ref.¹⁴). The fatigue thresholds $\Delta K_{IIth} = 3.5 \text{ MPa m}^{1/2}$ and $\Delta K_{IIIth} = 4.7 \text{ MPa m}^{1/2}$ are different ($A_{II} = 1.13 \cdot 10^{13}$, $A_{III} = 2.72 \cdot 10^{13}$ – calculated from inputs in MPa, m units). On the

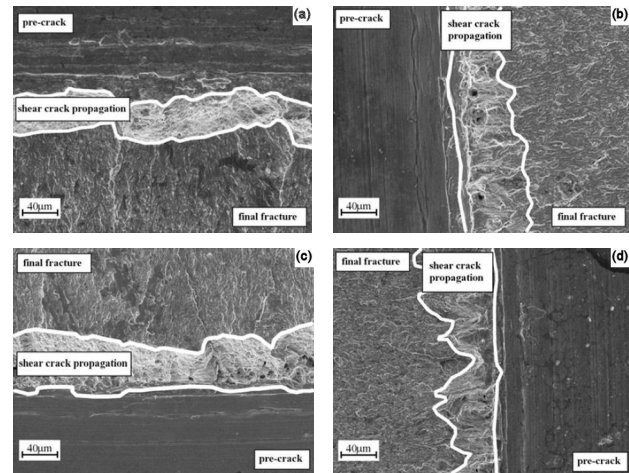


Fig. 3. **Typical fracture surfaces:** (a) top (mode II), (b) front (mode III), (c) bottom (mode II), (d) back (mode III)

other hand, the exponents are similar ($n_{II} = 5.6$, $n_{III} = 5.1$). One can also clearly see that, for the same value of the applied ΔK range, the crack growth rates for the mode II loading are about 6 times higher than those for the mode III loading. This is in agreement with results achieved in the low-cycle fatigue region⁹ and confirms the diversity of the mechanisms of mode II and mode III crack propagation in metals¹.

Typical fracture morphology and local topology profiles related to both mode II and III cracks near the pre-crack tip are shown in Fig. 5. This figure shows a big topological difference between mode II and III cracks. Indeed, practically all the mode II shear crack fronts were globally inclined from the shear plane in the direction perpendicular on the crack front. This means that the mode II cracks immediately started to propagate under a local mode I in order to avoid the retarding friction stress. Averaged de-

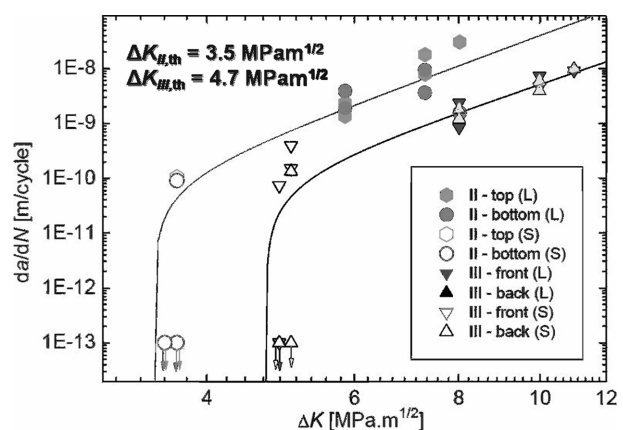


Fig. 4. **The crack-growth rate curves for mode II and III in the near-threshold region;** (S) – small specimens, (L) – large specimens

flection angles in the direction perpendicular to the crack front were found to be of $54^\circ \pm 16^\circ$. The roughness of inclined branches was very low and the associated crack path was microscopically smooth. This means that the roughness-induced crack closure was negligible and the cracks could propagate under a rather high effective crack driving force in the local mode I. On the other hand, the roughness of fracture surfaces of mode III cracks was extremely high and the related morphology typically consisted of factory-roof patterns. The deflection angles of factory roof micro-walls were in the range of $48^\circ \pm 9^\circ$. Because the mode III shear displacements were oriented perpendicularly to these asperities, their strong interlocking (clinching) took place during the cyclic loading. The theory of interaction of factory-roof asperities¹⁵ shows that the roughness-induced closure produced in such a way diminishes the crack driving force to a very low level particularly in the near threshold region. This is the main reason why the crack growth rate under the remote mode III was found to be much lower than that under the mode II in spite of the fact that both kinds of cracks propagated locally along the mode I branches.

It should be emphasized that no local measurements of 3D micromorphology were performed before the publication of the paper¹. Thus, a majority of previously published values of the shear-mode crack growth thresholds (e.g. in ref.⁷) are, most probably, irrelevant since they correspond to mode I branches. In order to achieve real shear-mode propagation at least at its initiation stages, the pre-crack tip must be made as sharp as possible which enables to constrain the crack tip plastic zone to a narrow strip within the shear plane. Moreover, the roughness of pre-crack flanks near the crack tip must be substantially diminished in order to avoid a parasitic mode I loading induced by a bending contact of asperities localized near the crack tip. Such precracks were produced in the Erich-Schmid Institute of Materials Science in Leoben, Austria, by

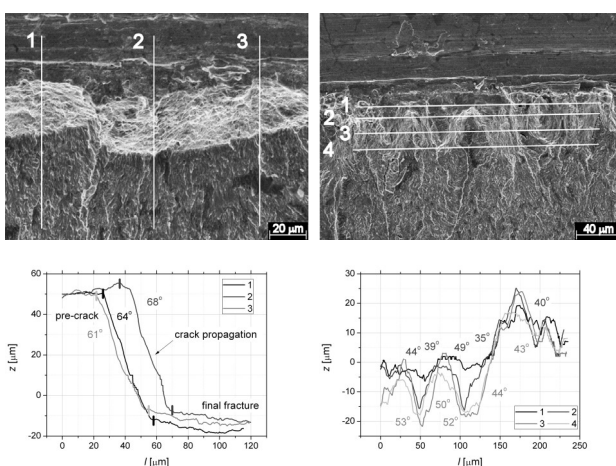


Fig. 5. SEM images and related height profiles for mode II (left) and mode III (right) crack propagations

Table I
Roughness analysis

	R_q [μm]	R_L [-]	R_V [-]
Original precrack	2.15 ± 1.15	1.27 ± 0.65	0.57 ± 0.70
New precracks	0.87 ± 0.47	1.08 ± 0.03	0.32 ± 0.08

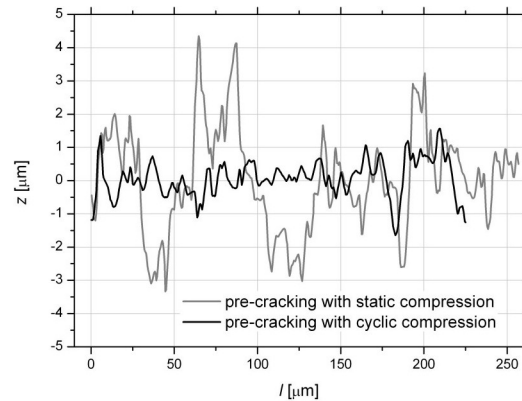


Fig. 6. Height profiles of the surface roughness near the crack front for the original precracks (static compression) and the new ones (cyclic compression)

means of a generation of a short fatigue precrack under compressive cyclic loading. In order to compare the local roughness of original and new precracks, the stereogrammetrical roughness analysis was performed on both types of precracks. The investigated parameters were the root mean square roughness (standard deviation of height coordinates), R_q , the linear roughness, R_L , defined as the ratio of the true profile length L and its projected length L' , and the vertical roughness R_V , calculated as $R_V = h/L'$, where h is the sum of height differences between adjacent profile points.

A comparison of local roughness in the z -direction (heights) and the roughness parameters for both types of precracks is shown in Fig. 6 and Tab. I, respectively. The profiles after cyclic compression become substantially smoothed, as can be seen from Fig. 6. All of the investigated roughness parameters for the new precracks are also significantly lower than those for the original ones. By means of such precracks, indeed, sufficiently extended shear-mode crack propagation has been already achieved. The assessment of the related experiments is currently in progress.

4. Conclusion

A prototype experiments on the near-threshold crack growth enabled a simultaneous remote mode II and mode III fatigue crack growth in specimens made of the austenitic steel. The stereo-photogrammetrical analysis of

the microroughness near the precrack tip revealed that, in both remote mode II and III cases, the cracks propagated under the local opening mode I. The main results of the study can be summarized in the following points:

- (i) The near-threshold crack growth rate under the remote mode II was much higher than that under the remote mode III. The threshold value ΔK_{IIth} was found to be of $3.5 \text{ MPa m}^{1/2}$, whereas $\Delta K_{IIIth} \approx 4.7 \text{ MPa m}^{1/2}$ was determined.
- (ii) All cracks propagated under the local mode I loading by forming either deflection of the whole crack front (mode II) or the factory roof patterns (mode III). Therefore, the measured crack-growth data can not be considered to be shear-mode material characteristics.
- (iii) The difference in the crack growth rate under modes II and III can be explained by a significant difference in the related micromechanisms. While the fracture topology of mode II cracks is smooth, that of the mode III cracks is rough which causes an interlocking of crack-flank asperities localized near the crack front. This significantly reduces the effective crack driving force for the mode III loading.

In general, the results of the local approach to shear-mode crack growth have shown that a majority of previously published values of mode II and III thresholds are irrelevant since they, most probably, correspond to mode I branches.

This research was supported by the Ministry of Education, Youth and Sports of the Czech Republic in the frame of projects MSM 0021630518 and project NPVII-2E08017. Authors greatly appreciate the help of Prof. Reinhard Pippan and Anton Hohenwarter from the Erich-Schmid Institute of Materials Science, Austrian Academy of Sciences, who significantly contributed to the development of experimental device as well as to the assessment of fractographic data.

REFERENCES

1. Pokluda J., Pippan R.: *Fat. Fract. Engng. Mater. Structures* 28, 179 (2005).
2. Ritchie R. O., McClintock F. A., Nayeb-Hashemi H., Rittler M. A.: *Metall. Trans. A13*, 101 (1982).
3. Tschegg E. K.: *Mater. Sci. Eng. A54*, 127 (1982).
4. Nayeb-Hashemi H., McClintock F. A., Ritchie R. O.: *Int. J. Fracture* 23, 163 (1983).
5. Hellier A. K., Corderoy D. L. H., McGirr M. B.: *Int. J. Fatigue* 9, 95 (1987).
6. Hellier A. K., McGirr M. B., Cordero D. J. H., Kutajczyk L. A.: *Int. J. Fracture* 42, R19 (1990).
7. Pook L. P.: *Crack Paths*. Wit Press, London 2002.
8. Murakami Y.: *Metal fatigue: Effects of small defects and nonmetallic inclusions*. Elsevier, Amsterdam 2002.
9. Pokluda J., Trattnig G., Martinschitz C., Pippan R.: *Int. J. Fatigue* 30, 1498 (2008).
10. Pokluda J., Pippan R.: *Mater. Sci. Eng. A462*, 355 (2007).
11. Pokluda J., Kondo Y., Slámečka K., Šandera P., Horníková J.: *Key Eng. Mater.* 385-387, 49 (2008).
12. Horníková J., Šandera P., Pokluda J.: *Key Eng. Mater.* 417-418, 321 (2010).
13. Slámečka K., Pokluda J., Ponížil P., Major Š., Šandera P.: *Eng. Fract. Mechanics* 75, 760 (2008).
14. Klesnil M., Lukas P.: *Fatigue of Metallic Materials*. Elsevier, Oxford 1980.
15. Vaziri A., Nayeb-Hashemi H.: *Eng. Fract. Mechanics* 72, 617 (2005).

L. Holáň, J. Pokluda, and K. Slámečka (*Brno University of Technology, Faculty of Mechanical Engineering*): **Local Aspects of Shear-Mode Crack Propagation in Austenitic Steel**

Two prototype experiments allowing a simultaneous mode II and mode III fatigue crack propagation in a single specimen are described and discussed. The cylindrical specimens made of austenitic steel with circumferential V-notch were prepared. In order to indicate differences between the mechanisms of mode II and mode III crack growth, several roughness parameters were determined by a stereo-photogrammetrical analysis within a microscopic region on the fracture surface close to the artificial precrack. The analysis revealed that both macroscopically shear-mode cracks propagated locally under the opening mode I loading. Unlike in the mode II case, moreover, an intensive interlocking of large asperities took place during the mode III crack growth. Therefore, the mode III crack-growth threshold (crack-growth-rate) was found to be higher (lower) than the mode II one. The results also revealed that, in order to achieve a local shear-mode growth, new experiments using specimens with sharper and microscopically smoother precracks must be arranged.

EVALUATION OF MECHANICAL PROPERTIES OF HVOF SPRAYED COATINGS BY THE CSM INDENTATION METHOD

ŠÁRKA HOUDKOVÁ^{a*}, OLGA
BLÁHOVÁ^b, and FRANTIŠEK
ZAHÁLKA^a

^a ŠKODA VÝZKUM, s.r.o., Tylova 57, 316 00 Plzeň, Czech Republic, ^b University of West Bohemia, Univerzitní 22, 300 00 Plzeň, Czech Republic
sarka.houdkova@skodavyzkum.cz

Keywords: Thermal spraying, HVOF, WC-Co, Cr₃C₂-NiCr, coating, mechanical properties, nanoindentation

1. Introduction

Tribological properties of surfaces of parts, namely their wear resistance and friction properties, are in many cases the determining factors for their proper function. In order to improve the surface properties, it is possible to create hard, wear resistant coatings by thermal spray technologies. With these versatile coatings, the lifetime, reliability and safety of parts can be improved. In the case of evaluation of thermally sprayed coatings, it is necessary to take into consideration their unique lamellar microstructure. Together with materials characteristics, such as hardness, Young's modulus of elasticity or fracture toughness, the coatings' porosity, cohesive strength, the content of oxides and other microstructure defects also play their role^{1,2}.

In the wide range of available thermally sprayed coatings, the high velocity oxy fuel HVOF hardmetal coatings show, thanks to their specific properties, the best results in application on surfaces demanding high resistance to abrasive and erosive wear, as well as corrosion resistance. The HVOF spraying technology is generally considered as the best spraying process for deposition of hardmetal coatings. Due to the high velocities of particles, the coatings are well bonded to the substrate and have high cohesion strength and low porosity. Moreover, the peening effect of molten droplets enables to produce coatings with low tensile stress and even with compressive stress³.

While the mechanisms of formation of such coatings have been rather well investigated, detailed information on mechanical properties still remains difficult to obtain because of the heterogeneity of the coatings. Macro-scale methods such as four point bending or microhardness at relatively high loads do not capture the effect of strongly heterogeneous structure composed from hard particles and a soft binding matrix. The indentation methods, particularly the instrumented indentation, allow to determine

properties such as hardness, viscoelastic properties and elastic modulus in very small material volumes and have a potential to determine not only intrinsic material characteristic in the range of one splat, but also the properties of a single hard particle and binder material. The knowledge of basic mechanical properties, hardness and Young's modulus of each structure component, as well as their *E/H* ratio, which characterize the elastic-plastic behavior of measured materials, is important not only for wear resistance prediction, but also necessary for determination of other mechanical characteristics, such as indentation fracture toughness. This information can be crucial for estimation of wear behavior of hardmetals, particularly under abrasive conditions, where sharp edged abrasive media attack the coating surface in a manner very similar to indentation.

While for other materials, e.g. bulk materials, thin coatings, etc. the indentation methods are commonly used, in the area of thermally sprayed coatings it has not been widespread so far. Up to now, the mechanical properties of hardmetal coatings have been evaluated mostly in terms of the composite scale range. Traditionally, the indentation tests are used for determination of surface hardness of thermally sprayed coatings (HR15N) and their microhardness (HV 0.3 or HV 0.1) measured on the coating cross-section. The instrumented indentation was used several times for evaluation of structure component properties⁴ and for evaluation of properties in the range of one splat^{5–11}. Only in a few works, the method of continuous stiffness measurement (CSM) was used to characterize the hardness and Young's modulus across a wide range of microstructure scale^{5,11,12}.

In present work, the WC-17%Co, Cr₃C₂-25%NiCr and (Ti,Mo)(C,N)-18.5%Ni18.5%Co coatings were measured by Nanoindenter XP MTS with a CSM module. The results show that with sufficient number of measurements there is a possibility to distinguish between the indents made into the hard particles and indents made into the binder material. The shape of CSM hardness and Young's modulus dependence curves on the load used (or on indentation depth) enables to follow the transition from the area of properties of a single structure component to properties of the composite material and to determine the properties of both.

2. Experimental

The coatings examined in this study were sprayed onto flat grit blasted surfaces of samples using the Praxair JP 5000 HVOF spraying system in ŠKODA VÝZKUM s.r.o. All coatings were created using previously optimized parameter sets which could be found elsewhere¹³. The

coating materials are commercially available as FST K-674.23 (WC-17%Co) and Tafa 1375 VM (Cr_3C_2 -25%NiCr). The $(\text{Ti},\text{Mo})(\text{C},\text{N})$ -37%NiCo powder with core-rim structured hard phases was an experimental powder, first tested by Berger¹⁴. Thickness of coatings varies from 300 to 500 μm . The hardmetal coatings microstructures contain hard particles embedded in tough matrix. The size range of hard phases differs for each coating. The size of WC carbides varies between 1–5 μm and the size of Cr_3C_2 carbides between 5–10 μm . In the case of carbides and nitrides in the $(\text{Ti},\text{Mo})(\text{C},\text{N})$ -NiCo coatings, the size is rather difficult to estimate due to special core-rim structure of hard phases, but it could be evaluated as smaller than 3 μm . Moreover, the hard phases do not have exact boundaries: their composition changes from the rim to the centre¹⁷. The microstructure characterization of measured coatings could be found elsewhere^{15,17}.

The indentation measurement was realized in the New Technologies Research Centre of the University of West Bohemia in Plzeň using the MTS NanoIndenter XP with a CSM module (Continuous Stiffness Mode). CSM testing is based on oscillating load with an amplitude several orders of magnitude smaller than the nominal load. This oscillating load is superposed onto the primary nominal load. Indentation is performed automatically and the position for indentation is chosen with high precision, with the possibility to program a set of experiments. The output of experiments is generally the indentation curve (displacement into surface as a function of the load on the sample). The CSM module allows to continuously measuring hardness and indentation modulus as a function of indenter depth penetrating into the tested material.

For each coating, more than 50 measurements were done on the coatings polished cross-sections, embedded in resin. Nanoindentation measurements were performed with the Vickers indenter. The indentation procedure consists of a loading period with the maximum load 10 N, followed by dwell time (30 s) and unloading.

Additionally, single measurements were performed using 10 N, 5 N, 2 N, 1 N, 200 mN, 100 mN, 20 mN and 2 mN loads to evaluate the size of indent with respect to the coating's microstructure. The Oliver-Pharr¹⁶ method was used to calculate the values of instrumented hardness (H) and Young's elastic modulus (E).

3. Results and Discussion

For each coating, the dependence of H and E on displacement into surface was evaluated. In Fig. 1 and 2 there are the dependencies for Cr_2C_3 -NiCr coating. The H and E values of single measurements, corresponding to a defined load, are also illustrated in the graphs.

Sufficient number of CSM measurements enables to get enough information to identify measurements corresponding to the hard phases, matrix or mixture of both. The analysis of the CSM dependencies indicates that for

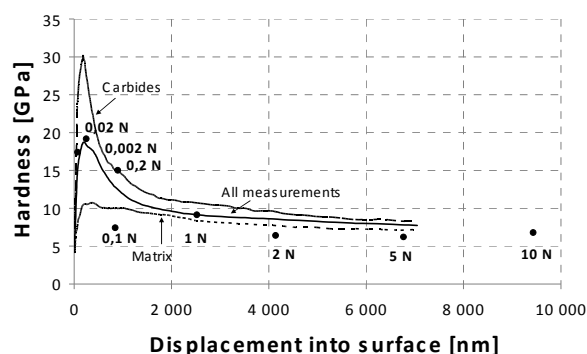


Fig. 1. Hardness vs Displacement into surface dependence for Cr_2C_3 -NiCr coating

the Cr_3C_2 -NiCr coating, the maximum of H and E modulus could be measured in the depth of 0.15 μm . Beyond the 0.15 μm depth, the hardness and elastic modulus values of single phase (matrix or hard phase) are influenced by their surrounding.

The second transition depth, that indicates the onset of influence of other microstructure features, such as pores, boundaries of splats, oxides and others, can be – in the case of the Cr_3C_2 -NiCr coating – identified at the 2 μm depth of indentation. Beyond the 2 μm depth of indentation, the coating properties are measured. Further increasing of indentation depth (load) leads to a slight continuous decrease of H and E values.

To confirm the transition depth, measurements at defined loads were made and the sizes of the indents were analyzed using SEM. The indents and corresponding load-displacement curves for individual indentations made at 10 N, 1 N, 200 mN and 100 mN loads can be seen in Figs. 3–6. For lower loads, the indents were too small to be recognized in the SEM.

The comparison of indents with the microstructural phases in Figs. 3–6 shows, that while the 10, 5, and 1 N indents cover several splats (the thickness of the spread

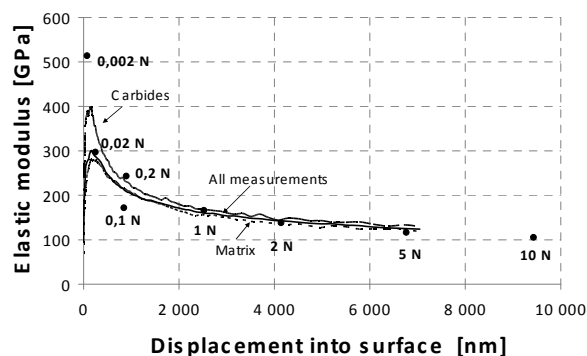
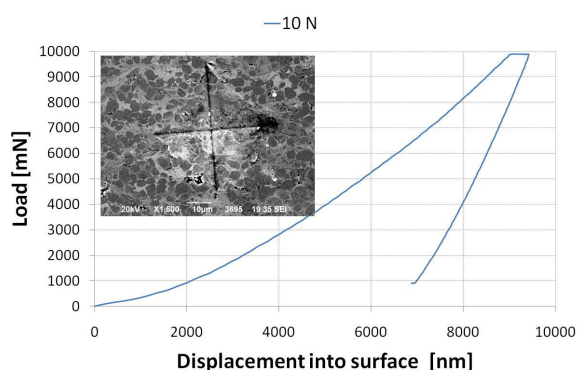
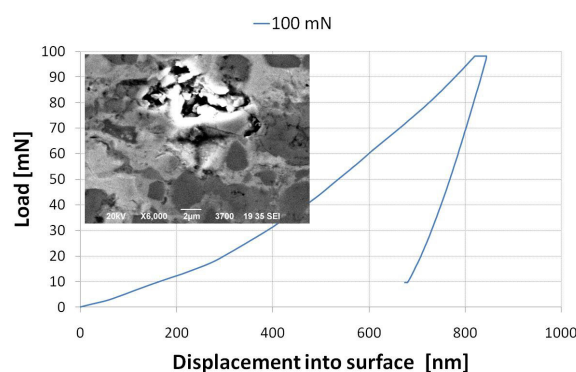
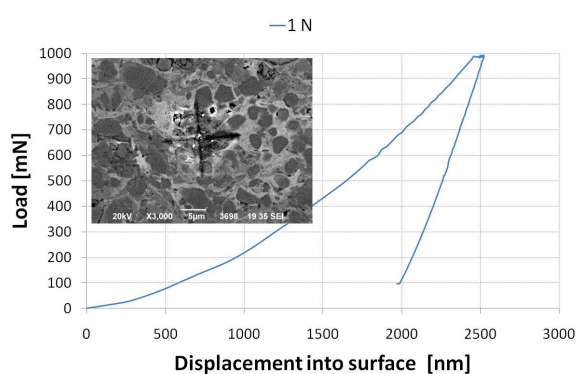
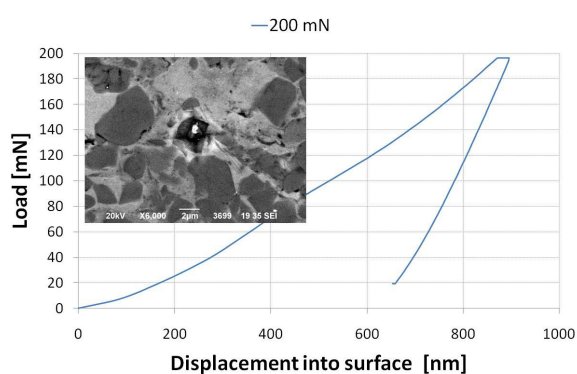


Fig. 2. Elastic Modulus vs Displacement into surface dependence for Cr_2C_3 -NiCr coating

Fig. 3. Indentation using 10 N load in the Cr_2C_3 -NiCr coatingFig. 6. Indentation using 100 mN load in the Cr_2C_3 -NiCr coatingFig. 4. Indentation using 1 N load in the Cr_2C_3 -NiCr coatingFig. 5. Indentation using 200 mN load in the Cr_2C_3 -NiCr coating

splat on the cross-section is around 1–2 μm), the load in range of 100–500 mN produces indents that cover several grains of hard phases and also the matrix between them.

The indents made at load lower than 100 mN were too small to be found, but it could be supposed that they

were located in one grain of hard phase or in the matrix. Observations from SEM micrographs of indents are in a good correlation with the conclusion made from CSM curves analyses.

The same analyses were made on two other coatings materials with similar conclusions. For the WC-15% Co coating, the maximum values of H and E were recorded at 0.17 μm and 0.28 μm resp. The transition between the composite microstructure's and the coating's properties can be determined at around 1.5 μm . In the $(\text{Ti}_x\text{Mo})(\text{C}_y\text{N})$ -39%NiCo coating, the maximum values of H and E were recorded at 0.23 μm and 0.18 μm resp. The transition between the composite microstructure's and the coating's properties can be determined also at about 1.5 μm .

The measured H and E values for all coatings are summarized in the Tab. I.

The measured data are in agreement with those referred in the literature^{18,19}. For sintered materials, the E of Cr_3C_2 -25% NiCr is about 320 GPa (ref.¹⁸), for WC-15%Co 560 GPa (ref.¹⁸). It is stated^{20,21}, that the elastic modulus of thermally sprayed coatings reaches 20–30 % of E in sintered materials in dependence on the amount of pores, microcracks and splat boundaries. The microstructure of HVOF sprayed coatings includes a very low amount of inhomogeneities such as pores or microcracks, so the ratio

Table I
 H and E values of coatings [GPa]

	Hard phase		Coating ^a	
	H	E	H	E
Cr_3C_2 -NiCr	30±1.0	398±14	8.0±0.8	143±15
WC-Co	28±1.5	526±50	15±1.2	260±27
$(\text{Ti}_x\text{Mo})(\text{C}_y\text{N})$ -NiCo	20±3.0	354±56	9.5±0.6	183±14

^a The H and E values in the coatings were calculated as an average from all measurements in the range of displacement into surface of 2000 nm – final depth

of the E values in sintered and HVOF sprayed material is lower.

The referred values of hard phases are also comparable with the measured values. W. Lengauer¹⁹ presents $E = 380$ GPa and $H = 27$ GPa for Cr_3C_2 , $E = 707$ GPa and $H = 23$ GPa for WC and $E = 450$ GPa and $H = 28$ GPa for TiC.

Even if there is some discrepancy (especially in case of WC), the degree of agreement is sufficient with respect to different measuring techniques used and possible influence of the matrix.

4. Conclusions

The instrumented nanoindentation was found to be a useful technique to measure the elasto-plastic behavior of thermally sprayed hardmetals. The measured H and E values, thanks to high number of measurements, could be considered representative of the complicated microstructure of thermally sprayed hardmetal coatings and can be further used in evaluation of more complex properties, such as wear resistance or indentation fracture toughness.

The differences in measured values in different load ranges, expressed by the depth of indentation, show the necessity of careful choice of a measurement method for purposes such as prediction of the coating's wear resistance. The load range of indentation should always be selected with respect to the mechanism and load range of the studied wear process.

The paper was prepared thanks to the financial support from the project No: MSM 4771868401 and MSM 4977751303.

REFERENCES

- Erickson L. C., Hawthorne H. M., Troczynski T.: *Wear* 250, 569 (2001).
- Holmberg K., Matthews A.: *Coatings Tribology*, Elsevier, Amsterdam, 1998.
- Stern K. H.: *Metallurgical and Ceramic Protective Coatings*, p. 28–283. Chapman&Hall, 1996.
- Gee M. G., Roebuck B., Andren H.-O., Lindahl P.: *Mat. Sci. Eng., A* 209, 128 (1996).
- Guilemany J. M., Torrell M., Dosta S., Miguel J. R.: *Proc. of Int. Thermal Spray Conference and Exhibition ITSC 2008, Maastricht, The Netherlands, June 2–4, 2008*, p. 305–308.
- Ma X. Q., Gandy D. W., Frederick G. J.: *Proc. of Int. Thermal Spray Conference and Exhibition ITSC 2008, Maastricht, The Netherlands, June 2–4, 2008*, p. 403–409.
- Stravato A., Mochalin V., Picardi S. C., Knight R.: *Proc. of Int. Thermal Spray Conference and Exhibition ITSC 2008, Maastricht, The Netherlands, June 2–4, 2008*, p. 637–641.
- Hall A., Yang P., Brewer L., Buchheit T., Roemer T., Hall A., Brewer L., Boyce B., Roemer T.: *Proc. of Int. Thermal Spray Conference and Exhibition ITSC 2008, Maastricht, The Netherlands, June 2–4, 2008*, p. 616–620.
- Bolelli G., Cannillo V., Lusvardi L., Rauch J., Killinger A., Gadow R.: *Proc. of Int. Thermal Spray Conference and Exhibition ITSC 2008, Maastricht, The Netherlands, June 2–4, 2008*, p. 657–662.
- Abdel-Samad A., Lugscheider E., Bobzin K., Maes M.: *Proc. of Int. Thermal Spray Conference and Exhibition ITSC 2004, Osaka, Japan, May 10–12, 2004*.
- Santana Y. Y., La Barbera-Sosa J. G., Caro J., Puchi-Carbera E. S., Staia M. H.: *Surf. Eng.* 24, 374 (2008).
- Barbera-Sosa J. G., Santana Y. Y., Staia M. H., Chicot D., Lasage J., Caro J., Mesmacque G., Puchi-Cabrera E. S.: *Surf. Coat. Technol.* 202, 4552 (2008).
- Houdková Š., Zahálka F., Kašparová M.: *Proc. of Int. Thermal Spray Conference and Exhibition ITSC 2008, Maastricht, The Netherlands, June 2–4, 2008*, p. 1497.
- Berger L.-M., Nebelung M., Vuoristo P., Mäntylä T.: *Beschichtungspulver und Verfahren zu seiner Herstellung*, DE 196 40 788 (filing date: 02. 10. 1996), WO 98/14630, US 6.162.276, EP 0948659, CA 2.267.960, BR PI 9711858-3, NO 321957.
- Berger L.-M.: *Int. Cong. On Adv. Mater., Proc. and Apl.*, October 2001, München, CD ISBN 3-88355-302-6, p. 10.
- Oliver W. C., Pharr G. M.: *J. Mater. Res.* 7, 1564 (1992).
- Berger L.-M., Thiele S., Vuoristo P., Mäntylä T.: *Proc. of Int. Thermal Spray Conference ITSC 2002, Essen, Germany, March 4–6, 2002*, p. 727–723.
- Hussainova I., Kubarsepp J., Pirso J.: *Wear* 250, 818 (2001).
- Lengauer W.: *Transition Metal Carbides, Nitrides and Caronitrides, Handbook of Ceramic Hard Materials*, p. 202. Wiley-VCH, Weinheim 2000.
- McPherson R.: *Surf. Coat. Technol* 98/40, 173 (1989).
- McPherson R.: *Thin Solid Film* 112, 89 (1984).

Š. Houdková^a, F. Zahálka^a, and O. Bláhová^b
^aŠKODA VÝZKUM s.r.o., Plzeň, Czech Republic, ^bNTC ZČU, Plzeň, Czech Republic): **Evaluation of Mechanical Properties of HVOF Sprayed Coatings by the Indentation CSM method**

In the present study, the H and E values of three types of Cr_3C_2 -25%NiCr, WC-17%Co and (Ti,Mo)(C,N)-39% NiCo HVOF coatings were evaluated by CSM method. It was shown that the measurement technique used is a viable method for evaluation of the coating's properties despite of the complicated microstructure. With a sufficient number of measurements the measured values can be considered reliable. The scale dependence of H and E values on the depth of indentation with respect to the coatings' microstructure was shown.

MECHANICAL PROPERTIES OF DUPLEX SYSTEM: ZrN COATING ON PLASMA NITRIDED STAINLESS STEEL

ZDENĚK JOSKA, MIROSLAV
POSPÍCHAL*, TEREZA MRÁZKOVÁ,
and JIŘÍ SUKÁČ

*Department of Mechanical Engineering, University of
Defence in Brno, Kounicova 65, 612 00 Brno, Czech Re-
public
Miroslav.Pospichal@unob.cz*

Keywords: Universal hardness, Zwick ZHU 2.5, Duplex system, Mechanical properties

1. Introduction

The steel X12CrNi 18 8 (1.4300) is widely used in food-processing industry and in medicine for surgical instruments due to its excellent corrosion resistance. However, it also has low hardness and poor wear performance, which offers impose strong limitations in many cases.

A combination of plasma nitriding and PVD coating with ZrN as a surface treatment has been shown to improve hardness and wear resistance of the material.

Plasma nitriding is known as a very versatile surface treatment process. When applied to austenitic stainless steels (e.g. X12CrNi 18 8)^{1,2}, it produces a modified layer with a high nitrogen concentration, known as supersaturated or expanded austenite, which has a high hardness and good corrosion resistance.

Thin hard coatings were developed and extensively utilised to protect different substrates against wear and corrosion in extreme conditions. Refractory metal coatings such as ZrN, TiN and DLC show a very high hardness and can be deposited by plasma assisted PVD. ZrN coating is one of the most widely used materials due to its excellent mechanical and tribological properties, added to its chemical stability and its very high corrosion resistance in strong acids.

Due to very low thickness of this type of coatings, the applied load is mainly supported by the substrate. If the material has not sufficient strength, as is usually the case with austenitic stainless steels, plastic deformation leading to a premature coating failure occurs. To overcome this limitation, thermochemical treatment prior to the hard-coating deposition were undertaken. This duplex surface treatment led to significant improvements in surface and sub-surface properties, which were unobtainable through any other techniques^{3,1}.

The aim of the present investigation was to study local mechanical properties of X12CrNi 18 8 stainless

steel treated with duplex surface treatment consisting of a plasma nitriding process and a subsequent ZrN PVD coating. Systematic instrumental hardness tests of treated samples were performed under different normal loads in the range of 2 N – 1000 N. Optical and electron microscopy were applied to investigate the tested samples.

2. Experimental Material and Surface Treatment

Samples of X12CrNi 18 8 stainless steel in an untreated state were sized 50 × 30 mm and had the thickness of 2 mm. The substrate had a microhardness of about 170 HV. Before the ion nitriding process, the specimens were wet ground using silicon carbide paper from 120 down to 500 grit.

Plasma nitriding was carried out in PN 60/60 equipment according to the following parameters: temperature 550 °C, time 8 h, flow of H₂ 8 l min⁻¹, flow of N₂ 32 l min⁻¹, flow of CH₄ 1.5 l h⁻¹. Pre-nitrided samples were afterwards coated with ZrN by PVD using arc industrial equipment, HTC 625 Multilab ABSTM, in order to obtain the desired duplex surface treatment. The conditions of coating deposition were: temperature of 450 °C, pressure of Ar₂+N₂ 0.5 Pa, voltage –70 V.

3. Experimental Methods

Chemical composition of the substrate material was measured by GDOES/Bulk method. The nominal compositions can be found in Table I. Glow Discharge Optical Spectroscopy (GDOES) measurement was performed in a LECO SA-2000 atomic emission spectroscopy analyzer, with an argon Glow Discharge Plasma excitation source.

Scanning electron microscope (SEM) Vega TS 5135 with the microanalyzer Noran Six/300, was used for the EDXS analysis of Fe and Zr.

Confocal laser microscope LEXT OLS 3000 allows for observation of surfaces and obtaining both 2D and 3D images. It also enhances the quality of acquired images and enables to measure lengths, shapes and surface roughness. It allows for 3D observation as well as high precision

Table I
Chemical composition of X12CrNi 18 8 stainless steel

Element	C	Mn	Cr	Ni	Si	P	S
%wt	0.045	21.78	18.6	8.6	0.45	0.027	0.002

3D measurement in real time. Thanks to its outstanding resolution of $0.12\ \mu\text{m}$ and a magnification range from $120\times$ to $14\,400\times$, the confocal microscope LEXT can operate within the limits of common optical microscopes and scanning electron microscopes.

Instrumental hardness measurements were made on a Zwick Universal testing machine with a hardness measurement head (Zwick Z 2.5, Zwick GmbH & Co., Ulm, Germany). The initial head speed for approaching the specimen was $300\ \text{mm}\ \text{min}^{-1}$. After the head touched the specimen, the approach speed of the diamond indenter until initial contact with the specimen was $50\ \text{mm}\ \text{min}^{-1}$. Indentations were made on the surface of the specimen. The tests were carried out from 2 N up to 1000 N indenter load. The working test force has been maintained for 3 s.

The Martens (universal) hardness was calculated automatically by the software (TestXpert®, Zwick GmbH & Co, Ulm, Germany) and was expressed as volume hardness. Martens hardness was measured on the surface upon duplex surface treatment and plasma nitriding. Vickers indenter was used for the indentation test. The following equations can be used in calculating Martens hardness HM and the elastic part of indentation work η_{IT} values of the test samples^{4,5}.

$$HM = F_2 / (f_{IT} \cdot h_2^2)$$

$$\eta_{IT} = W(\text{elast}) / W(\text{total}) \cdot 100\%$$

where HM is Martens hardness in $\text{N}\ \text{mm}^{-2}$, F_2 is force at the point of load application after the dwell time in N, f_{IT} is a coefficient of the indenter (26.43 for Vickers), h_2 is indentation depth at the maximum force in mm, $W(\text{elast})$ is elastic part of indentation work in Nmm, $W(\text{total})$ is total indentation work in Nmm. Indents were documented by light and electron microscopes.

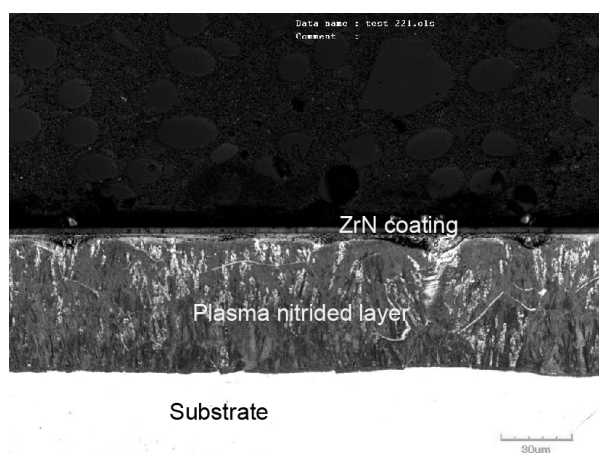


Fig. 1. Morphology of the cross-sectional of the duplex coating - substrate system upon etching (NITAL), confocal micrograph

4. Experimental Results

Fig. 1 shows an micrograph of a cross-section of the surface of an X12CrNi 18 8 sample treated by a combination of plasma nitriding and PVD coating. Nitrogen that diffused into the material during the plasma nitriding process formed a continuous nitrided layer with the thickness of $57\ \mu\text{m}$. The ZrN coating subsequently deposited by PVD was approximately $2.5\ \mu\text{m}$ thick.

Fig. 2 shows quantitative elemental analysis of an indent. The elemental analysis was made for elements Fe and Zr. Iron is shown in the area where the coating became delaminated and Zr is uniformly distributed across the rest of the area. No other elements were observed.

Fig. 3 presents the typical force – displacement curves for these materials. It is not surprising that the plasma nitrided sample shows higher indentation depth, particularly in the area of lower load. Indentation depth for the force of 1000 N is similar for both plasma nitrided and duplex treated samples. The indents were documented by confocal microscope. Figs. 4, 5 show the development of average values of universal hardness HM and the elastic part of indentation work to load for the duplex treatment sample and plasma nitrided sample.

The obtained values of universal hardness HM and elastic part of indentation work η_{IT} for the duplex treated sample are higher than for the plasma nitrided sample at force up to 200 N. Beyond this force, the values for both samples become equal.

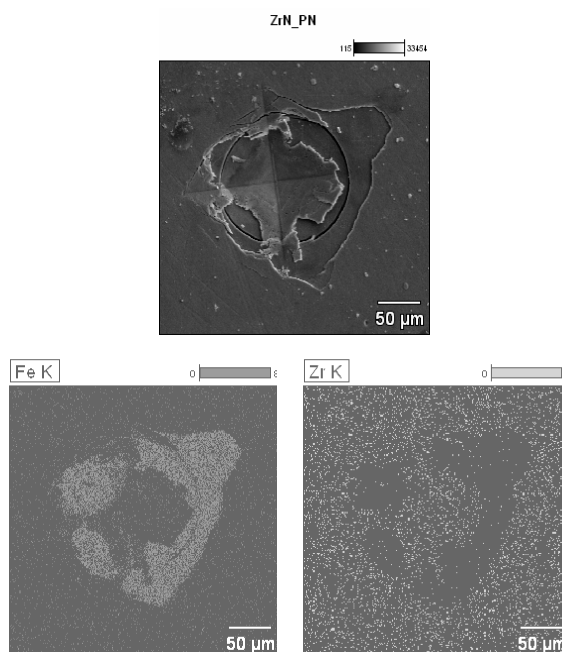


Fig. 2. Micrograph (SEM) of Vickers indent (load 30 N) in duplex treated sample and elemental distribution maps of Fe and Zr (EDXS)

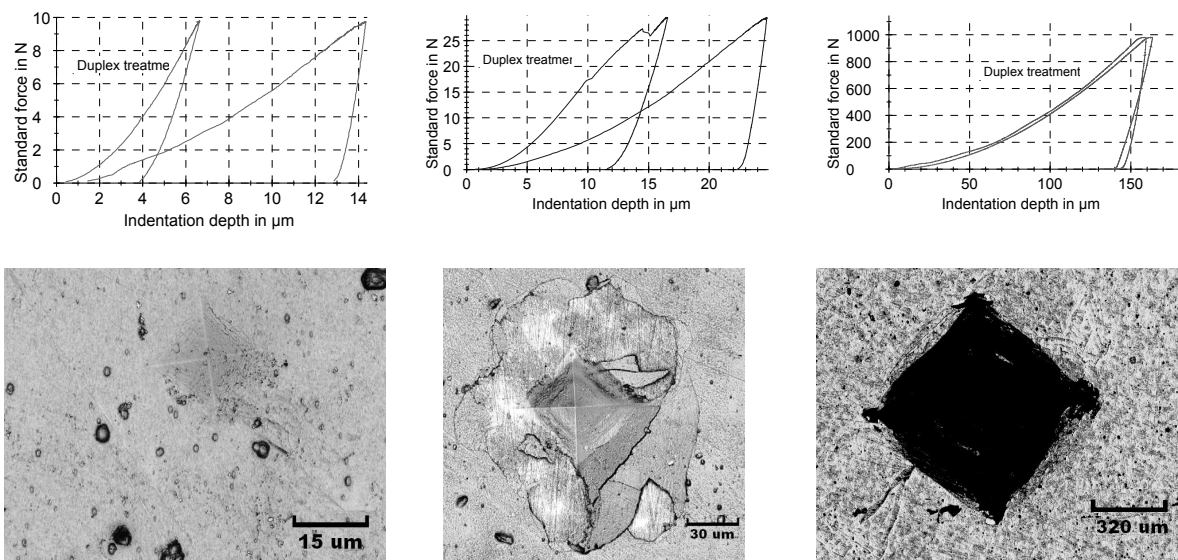


Fig. 3. The indentation curves of both plasma nitrided and duplex treated samples and micrograph of Vickers indents in duplex treated sample for loads 10 N, 30 N and 1000 N (light microscopy)

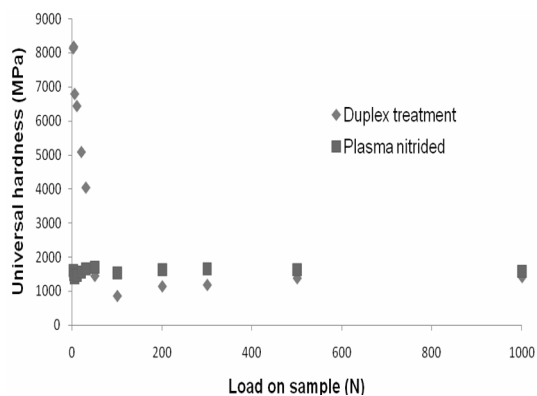


Fig. 4. Universal hardness – force graph for the plasma nitrided and duplex treated surface

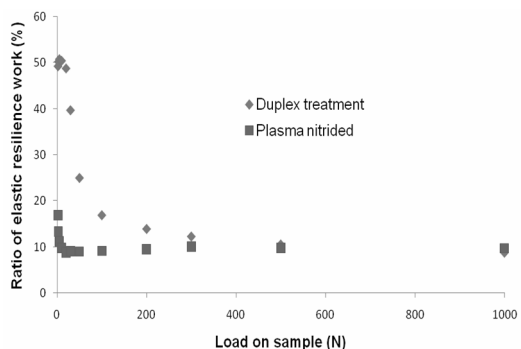


Fig. 5. Elastic part of indentation work (ratio of elastic resilience) – force graph for plasma nitrided and duplex treated surface

The highest value of universal hardness is more than 8000 MPa and the elastic part of indentation work is around 50 %. The highest influence of ZrN coating on the duplex treatment surface can be observed up to 50 N.

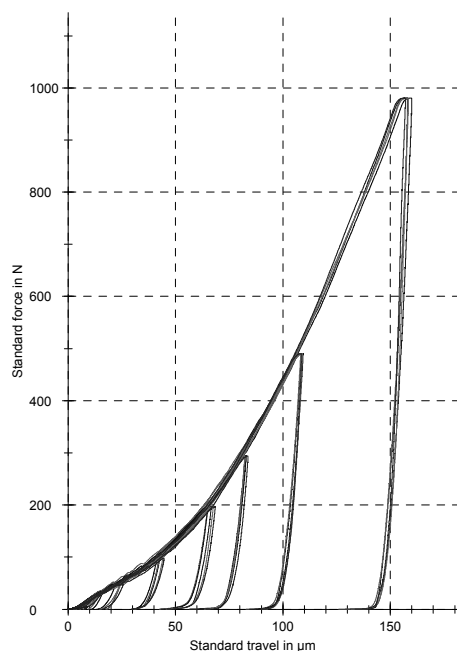


Fig. 6. Indentation curves. Results for four separate indentations on the duplex treated specimen are represented by four curves

Above 100 N, the value of universal hardness becomes lower than the universal hardness of plasma nitrided surface. It is caused by delamination of the coating. The elastic part of indentation work is the highest – around 50 % – for the force up to the value of 30 N where the ZrN coating is not disrupted after cracking (as shown in Fig. 3), the value of elastic work continuously decreased and around 200 N became equal as in the plasma nitrided sample.

Indentation curves in duplex treated sample, which were achieved, are shown in Fig. 6. The deepest indent is 160 μm deep. Steps were observed on loading part of indentation curves between 50 N and 100 N. Delamination of coating is the possible reason for it. These results confirmed that the measurement of duplex system as a single unit is achieved using Zwick ZHU 2.5.

The work was supported by a research project of the Ministry of Defence of the Czech Republic, project No. MOOFVT 0000404 and Czech Science Foundation, Grant number: 106/08/1243. The company HVM Plasma Brno is acknowledged for deposition ZrN coating.

REFERENCES

1. Joska Z., *Diploma thesis*, University of Defence, Brno, 2006.
2. Joska Z., Mrázková T.: *Plazmová nitridace oceli X12CrNi 18 8*, chapter 24, p. 169–173, *Proceeding of IDET 2009, Brno, University of Defence*.
3. Kadlec J., Hruby V., Novak M.: *Vacuum 41*, 2226 (1990).
4. ČSN EN ISO 14577-1 *Kovové materiály – Instrumentovaná vnikací zkouška stanovení tvrdosti a materiálových parametrů – Část 1: Zkušební metoda*. (Metallic materials – Instrumented indentation test for hardness and materials parameters – Part 1: Test method).
5. Musil J., Kunc F., Zeman H., Poláková H.: *Surf. Coat. Technol. 154*, 304 (2002).

Z. Joska, M. Pospíchal, T. Mrázková, and J. Sukáč (*University of Defence Brno, Czech Republic*):
Mechanical Properties of Duplex System ZrN Coating on Plasma Nitrided Stainless Steel

Austenitic stainless steels are widely used in industrial applications with a combination of plasma nitriding and PVD coating. The surface treatment has been used to improve material properties without affecting the corrosion performance. In the present work, duplex treatment was investigated. The duplex treatment consists of plasma nitriding and subsequent ZrN coating processes applied on X12CrNi 18 8 steel. This is a study of mechanical properties of a duplex system using indentation methods. The measurement was carried out using the universal hardness tester Zwick ZHU 2.5. Universal hardness, the elastic part of indentation work and adhesive and cohesive behavior of the coating were measured. The results were compared with results of measuring in confocal and electron microscopes.

ADHESIVE-COHESIVE STRENGTH OF Cr_3C_2 -NiCr HVOF SPRAYED COATINGS

MICHAELA KAŠPAROVÁ*, ŠÁRKA HOUDKOVÁ, and FRANTIŠEK ZAHÁLKA

ŠKODA VÝZKUM Ltd., Tylova 1/57, 316 00 Plzeň, Czech Republic
michaela.kasparova@skodavyzkum.cz

Keywords: Cr_3C_2 -NiCr, adhesive strength, cohesive strength, HVOF, IFT

1. Introduction

Thermally sprayed coatings are one of the possibilities how to protect the surface of the machine parts. They belong to the successful protection, which is commonly used against undesirable influences of the environment, such as different types of wear (abrasion, erosion, adhesion, cavitation,...), oxidation, high temperatures, etc. In industrial applications there are used several technologies for the preparation of thermally sprayed coatings: HVOF/HVAF, arc, flame, plasma and other unique technologies. Each of these technologies is distinguished by typical properties of final coatings. Coatings properties significantly differ with the used technology. It means e.g. different microstructure (oxide content, phase formation, cohesion between individual splats, cracks, porosity), surface hardness, microhardness, surface roughness, wear resistance, coating bond strength, etc. The investigation of the coating behaviour on the “coating-substrate” boundary and the cohesive strength between individual structure particles surely belongs to the evaluation of the coatings mechanical properties. Coatings are bonded with the base material (substrate) mainly by mechanical interlocking. Further the van der Waals forces (molecular interaction) and diffusion of elemental species across splat boundaries participate. Other important factors which influence the coating strength are the melting and localized alloying of the contact surfaces between particles and between the substrate and adjoining particles. All these factors influence the adhesive-cohesive strength of the coatings very much. The coating adhesive-cohesive behaviour depends on two spray parameters above all: the flame temperature and particles kinetic energy.

The ideal particles distribution is mainly influenced by the substrate roughness¹. Wang et al.² stated that the adhesive strength of the HVOF sprayed coatings (WC-Co and NiCrBSi specifically) deposited on the substrate with the roughness lower than $R_a = 1.7$ is identical with the adhesive strength of the coatings deposited on the un-

roughened, polished substrate. Further the authors found that if the substrate roughness is higher than $R_a = 5.7$ the coating adhesive strength is manifold higher. Day et al.³, Paredes et al.⁴ and Staina et al.⁵ achieved identical results. Required surface roughness is attained by substrate grit blasting process if the grit blasted medium is of a sufficient surface hardness and if the right impact velocity acts simultaneously. Staina⁵ stated additional associated influences to surface blasting, which influence the adhesive-cohesive strength of the coatings, such as the particles size of the grit blasting medium, the grit blasting pressure, the grit blasting time, the distance of the grit blasting and the grit blasting angle. However, the dependencies and conclusions between all mentioned grit blasting factors are very inconsistent with respect to other studies^{5–9}. The temperature also closely relates with the surface roughness, because the preheating temperature has significant influence on the degree of the surface roughness¹⁰. This temperature ensures the adhesive and cohesive bond strength of the coating in the wide range of the substrate surface roughness. It means that without using the preheating process the substrate is necessary to be more roughened for ensuring high coating adhesion and cohesion^{4,10,11}. Other factor that influences the coating bond strength is the thickness. With the coating thickness increasing the coating adhesive and cohesive strengths decrease. However this relation is not linear, but the decrease of the coating adhesive and cohesive strength appears after exceeding the certain thickness limit. Godoy et al.¹² stated the critical coating thickness that is approximately around $450 \mu\text{m}$. After exceeding this thickness the adhesive strength decreases very intensively. The authors clarify this statement by the residual stresses. The residual stresses change in the coating and in the coating-substrate boundary as the coating thickness increases or decreases. In the HVOF coatings mostly occurs the compressive stress, which decreases with the increasing coating thickness. This negative effect can be suppressed by the coating post-heat treatment, which helps to minimize the tensile stresses. Decreasing of the residual stresses in the coatings significantly contributes to the improvement of the adhesive and cohesive strength in the coating and in the coating-substrate boundary¹².

It is obvious that the coating adhesive and cohesive strength is influenced by many factors and therefore it is necessary to optimize and ensure the adequate coating bond strength together with achieving the high coating quality. The adhesive-cohesive strength is usually evaluated using the so-called adhesive test or using the coating bond strength test. The indentation, shear and tensile test rank among the most advanced methods¹³. The tensile test procedures are described in the EN 582 (ref.¹⁴) and the ASTM C633 (ref.¹⁵) Standards. The problematics of the adhesive-cohesive behaviour of the coatings is still inten-

sively investigated in many research works. The main aim of this work was to evaluate the adhesive-cohesive strength of the HVOF thermally sprayed $\text{Cr}_3\text{C}_2\text{-NiCr}$ coatings using the tensile test in accordance with the both mentioned Standards. The coatings were sprayed using different spray parameters. Specifically the spray angle (90° , 75° , 60° , 45° , 30°) was changed and the coatings mechanical properties were studied. For ensuring the optimal coating properties the stream of spray particles should impact the target surface as close to normal (90°) as possible. Spraying under the normal angle should be used only as a last possibility, bearing in mind that some coating property deviation from the optimum can be expected^{16,17}.

Besides the adhesive-cohesive behaviour the indentation fracture toughness (IFT) was also investigated. The IFT measurements give detailed information about the cracks initiation and propagation, and thus it helps to investigate the bonding strength between individual structure particles (splats) and in the coating-substrate boundary. The indentation fracture toughness of the thermal sprayed coatings strongly differs from the IFT of bulk materials of the same composition due to their unique microstructure. The coatings lamellar structure causes the anisotropy of the coating resistance against the cracks propagation. The IFT value of thermally sprayed coatings depends mostly on the coatings porosity, the presence of oxides and the shape, size and distribution of the structure particles¹⁸. For the IFT evaluation of the thermal spray coatings the Vickers indenter is generally used.

The results of this work contribute to the understanding of the adhesive-cohesive strength of thermally sprayed cermets coatings, which are based on the principle “hard carbide particles embedded in the ductile metal matrix”, along with the support of the IFT measurements.

2. Experiment

2.1. Samples preparation

The commercially available (15–45 μm) $\text{Cr}_3\text{C}_2\text{-NiCr}$ powder (75 wt. % CrC, 25 wt. % Co) was coated on low-carbon steel substrates by the JP-5000 HP/HVOF equipment. The substrates were cleaned by grit-blasting with (0,8–1 mm) brown corundum. The TTN 24 Sand Blaster was used, the blasting distance was 12 cm and the blasted pressure was 6 atm. The substrate roughness was $R_a = 9 \mu\text{m}$. The coatings were prepared by the optimized spray parameters, only the spray angle was changed (90° , 75° , 60° , 45° and 30°). The final coatings thickness was approximately 300 μm for all sprayed samples. After spraying, the samples were cut for the metallographic preparation in two directions, in the cross section and in the longitudinal section. Two sections were necessary due to using different spray angles, which cause different particles distribution on the substrate and the anisotropy in the coatings microstructure.

2.2. Experimental measurements

The adhesive-cohesive strength of coatings was measured in accordance with EN 582 and ASTM C633. The scheme of the test is shown in Fig. 1a. The tested sample ($\varnothing 25 \text{ mm} \times 7.5 \text{ mm}$) covered with coating on one facing surface was bonded with the bolstering element and with the load element using the suitable glue (HTK Ultra Bond 100) and loaded with the contact pressure of 70 N cm^{-2} . The constant contact pressure was ensured using two screws in the special tool, see Fig. 1b. The glued-joint was hardened at temperature 190°C for 35 min. Then the samples were subjected to the tensile strength test and the breaking force was recorded.

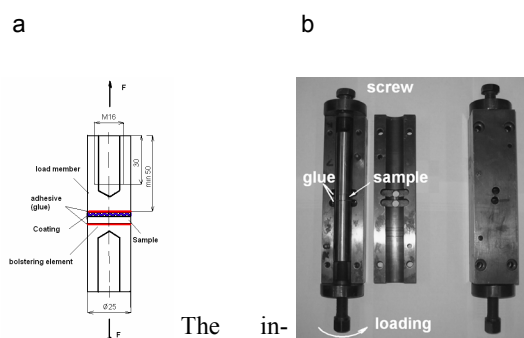


Fig. 1. Determination of coatings tensile adhesive-cohesive strength, a) schematic draft of the test, b) the special tool for ensuring of axially joining of the sample

Indentation fracture toughness was determined using the “Revetest” Scratch Tester in the Academy of Sciences in Plzeň Czech Republic. 10 indentations were prepared by the Vickers diamonds indenter in the cross sections. The load was selected so as cracks, which start from the corners of the indents, to be possible to obtain, Fig. 2. The $\text{Cr}_3\text{C}_2\text{-NiCr}$ cermet is very hard and rigid and due to these properties it was necessary to use high load of 200 N for cracks initialization. The cracks length was measured and the IFT values were calculated using the one select model (LEM):

$$\text{LEM theory: } K_{\text{IC}} = 0,0134(L/c^{3/2})(E/H)^{1/2} \quad (\text{ref.}^{19})$$

Where $a = 1/2$ of the length of the indent's diagonal [m], $c =$ the length of the crack + a [m], $E/H =$ constant [–], $K_{\text{IC}} =$ fracture toughness [$\text{MPa m}^{1/2}$].

Besides the IFT testing also the measurements of the acoustic emission (AE) were performed for recording the first signal of the cracks initiation. The IFT was measured

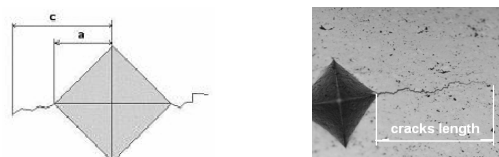


Fig. 2. IFT evaluation of the $\text{Cr}_3\text{C}_2\text{-NiCr}$ coating

on the cross sections and longitudinal sections of the samples. The standard method for the metallography preparation of hardmetals described in²⁰ was used for preparing the sections.

3. Results and discussion

The results of the tensile test, of the IFT and AE measurements are recorded in Tab. I. and in Tab. II. These results are graphically represented in the diagram in Fig. 3. From the curves in the Fig. 3 it is evident that the bond strength of the coating strongly corresponds with the IFT values measured in both coatings sections. The trend of the curves is nearly identical. The highest bond strength and IFT were found for the coatings sprayed under the angle 75° and 45° and the lower bond strength for the other coatings. The results of the AE also correspond with these results very strongly, see Fig. 4. The maximal force (Fc), where the crack started to grow, conforms to IFT results, mainly during the measurements on the coatings longitudinal section. In the cross section the results differ for the coating sprayed under the angle of 30°. However, in this case only the adhesive failure and no cohesive failure between the structure particles was observed after the tensile test. This corresponds with the good cohesion between the individual “splats” but with the worst adhesion in the coating-substrate boundary as the results of the tensile test show.

From the visual observation of the coatings' damaged surfaces after the tensile test the adhesive-cohesive failure

Table I
Results of IFT measurements and of the tensile test

Angle of spraying	Bond strength [MPa]		LEM [$\text{MPa m}^{1/2}$]			
	St. dev.		IFT-longitudinal section	St. dev.	IFT - cross section	St. dev.
90°	55.68	2.59	0.78	0.11	0.78	0.11
75°	77.33	3.72	1.26	0.35	0.98	0.26
60°	57.65	2.52	0.68	0.11	0.70	0.12
45°	66.82	3.63	1.24	0.33	0.80	0.30
30°	50.73	2.25	0.62	0.05	0.80	0.17

Table II
Results of AE measurements

Angle of spraying	Fc [N]			
	Longitudinal section	St. dev.	Cross section	St. dev.
90°	72	10	72	10
75°	96	2	78	16
60°	69	9	58	10
45°	82	6	68	13
30°	71	4	83	6

was found except for the coating sprayed under the angle 30°. As it was already mentioned, only the adhesive failure in the coatings-substrate boundary was visible. In all other coatings (90°, 75°, 65°, 45°) the fractures caused by the cohesive failure between individual structure particles were observed. The fracture appearance was similar for all coatings. The SEM micrographs of the fractures are recorded in Figs. 5 and 6. In Fig. 5a the fracture of the coating represents the coatings with a lower adhesive-cohesive strength and a lower IFT (90°) is depicted. This figure shows the adhesive-cohesive behaviour of the coating, where the uncovered substrate and the fracture across the coating are evident. In Fig. 5b the plastic deformation of the binder phase as the main failure mechanism is visible. The same failure mechanism was found also for the coating representing the coatings with a higher adhesive-cohesive strength and IFT (45°), see Fig. 6.

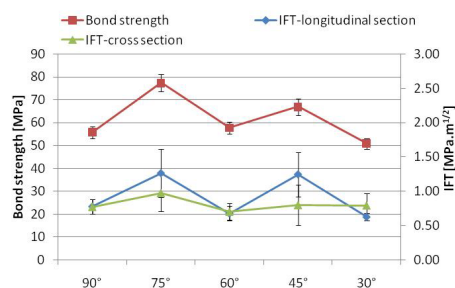


Fig. 3. The dependence of the IFT values and adhesive-cohesive strength of the coating on the deposition angle

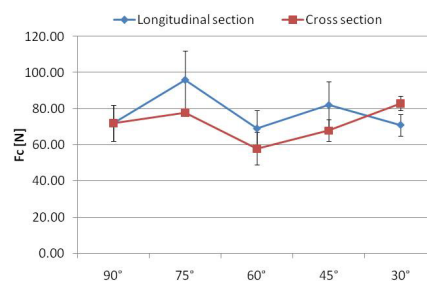


Fig. 4. The force (Fc) of the first signal of the AE in dependence on the spray angle

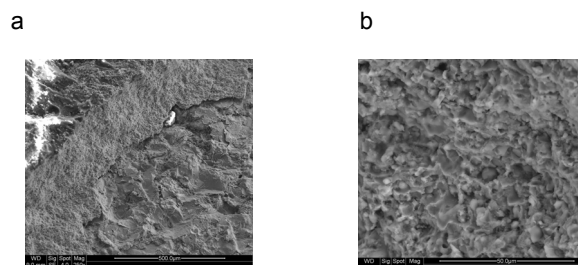


Fig. 5. The fracture in the coatings sprayed under the angle 90°, a) surface-coating boundary, coatings (adhesive-cohesive) behaviour; b) plastic deformation of the NiCr binder phase

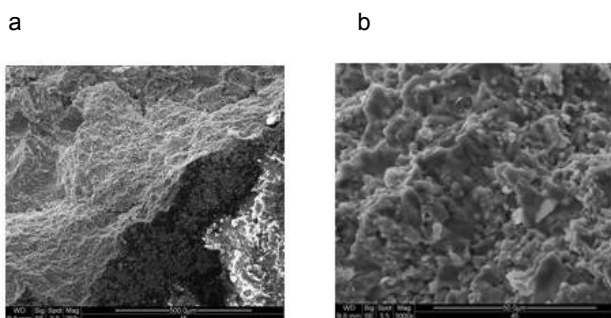


Figure 6. The fracture in the coatings sprayed under the angle 45°, a) surface-coating boundary, coatings (adhesive-cohesive) behaviour; b) plastic deformation of the NiCr binder phase

4. Conclusion

In this work the adhesive-cohesive strength and indentation fracture toughness of the HVOF thermally sprayed Cr_3C_2 -NiCr cermet, which was sprayed under five different deposition angles, were investigated. The adhesive-cohesive strength was measured using the tensile test for the coatings' bond strength evaluation and the IFT was investigated using the impression of the Vickers indenter by the action of the specific load. The highest bond strength and highest IFT was found for the coatings sprayed under the angles 75° and 45°. It is very surprising because it is generally known that spraying under the normal angle (90°) ensures the optimal coating properties and the deflection from this spray direction causes certain deterioration of the coating properties. Our results relatively contradict this statement. The properties of the coatings sprayed under the angle are very specific, especially the local mechanical properties such as IFT and cohesive strength between the individual particles (splats). The bond strength is highly affected by the melting degree of the sprayed particles, by the kinetic energy and most of all by the impact direction of the melted particles. As the results of this work feature, the IFT measurements are a good possibility for the investigation of the cracks initialization and their propagation. The results confirmed that the IFT measurement is a suitable alternative for the coatings' cohesive or adhesive strength measurement in addition to the classical tensile test of the bond strength. Along with the IFT measurements the results of the acoustic emission were found advantageous for recording the maximal force signal when the cracks start to grow.

This work was supported by the project of the Ministry of Education, Youth and Sports, No. VZ/MSM 4771868401.

REFERENCES

1. Fukunuma H., Ohno N.: *Proceedings of ITSC 2003*. Orlando (Florida, USA), 2003, 1361.
2. Wang Z. Z., Li C. J., Ohmori A.: *Thin Solid Films* 458, 141 (2005).
3. Day J., Huang X., Richards N. L.: *J. Therm. Spray Technol.* 14, 471 (2005).
4. Peredes R. S. C., Amico S. C., d'Oliveira A. S. C. M.: *J. Surf. Coat. Technol.* 200, 3049 (2006).
5. Staia M. H., Ramos E., Carrasquero A., Roman A., Lesage J., Chicot D., Mesmacque, G.: *Thin Solid Films* 377, 657 (2000).
6. Harris A. F., Beevers A.: *Int. J. Adhes.* 19, 445 (1999).
7. Amada S., Hirose T.: *Surf. Coat. Technol.* 102, 132 (1998).
8. Mellali M., Grimaud A., Leger A. C., Fauchais P., Lu J.: *J. Therm. Spray Technol.* 6, 217 (1997).
9. Amada S., Satoh A.: *J. Adhes. Sci. Technol.* 14, 27 (2000).
10. Watanabe M., Kuroda S., Yokoyama K., Inoue T., Gotoh Y.: *J. Surf. Coat. Technol.* 202, 1746 (2008).
11. Bahbou F., Nelén P.: *Proceedings of ITSC 2005*. Basel (Switzerland), 2005, 1027.
12. Godoy C., Souza E. A., Lima M. M., Batista J. C. A.: *Thin Solid Films* 420–421, 438 (2002).
13. Berndt C. C., Lin C. K.: *J. Adhes. Sci. Technol.* 7, 1235 (1993).
14. ČSN EN 582, *Žárové stříkání–stanovení přilnavosti v tahu*. Czech Institut of Standards, 1995.
15. ASTM C633-01, *Standard Method of Test for Adhesion or Cohesive Strength of Thermal Spray Coatings*. American Society for Testing and Materials, Philadelphia (Pennsylvania, USA), 2001.
16. Kašparová M., Zahálka F., Houdková Š.: Vliv úhlu nástřiku na vlastnosti HVOF stříkaného Cr_3C_2 -NiCr povlaku, Int. doc. No. VYZ0999/07, 2007.
17. Kašparová M., Enžl R., Zahálka F.: Vliv úhlu nástřiku na vlastnosti HVOF stříkaného WC-Co povlaku, Int. doc. No. VYZ0833/05, 2005.
18. Houdková Š., Bláhová O., Svitáková E.: *Proceedings of the conference LMV06*, 2006, 70.
19. Lawn B. R., Evans A. G., Marshall D. B.: *J. Am. Ceram. Soc.* 63, 574 (1980).
20. Bjerregaard L., Geels K., Ottesen B., Ruckert M.: *Metallog Guide, Struers A/S*, 1996, 35.

M. Kašparová, Š. Houdková, and F. Zahálka,
(ŠKODA VÝZKUM Ltd., Tylova 1/57, 316 00 Plzeň, Czech Republic)

In the presented study the adhesive-cohesive strength of thermally sprayed coatings was investigated. The bond strength, IFT and AE measurements were performed and their relationship was taken into account. The results showed that the IFT measurement is an advantageous way for the coatings cohesive or adhesive strength determination however deeper verification is needed.

THE MECHANICAL PROPERTIES CHANGES OF OFHC COPPER AFTER ECAP PROCESSING

**RÓBERT KOČIŠKO^a, PAVOL ZUBKO^b,
JURAJ ĎURIŠIN^c, MÁRIA MOLNÁRO-
VÁ^{c*}, ANDREA KOVÁČOVÁ^a, MICHAL
KVAČKAJ^a, and JÚLIUS BACSÓ^a**

^a Department of Metals forming, Faculty of Metallurgy,
Technical University of Košice, 042 00, Košice, Slovakia,

^b Department of Material science, Faculty of Metallurgy,
Technical University of Košice, 042 00, Košice, Slovakia,

^c Institute of materials research, Slovak Academy of Sci-
ences, 043 53, Košice, Slovakia
mmolnarova@imr.saske.sk

Keywords: OFHC, ECAP, substructure, TEM

1. Introduction

Ultra fine grained (UFG) materials are well-known due to their improved mechanical properties^{1,2}. For preparation of metallic materials with UFG to nanocrystal (NC) structure several methods that utilize structure formation through severe plastic deformation (SPD) have been suggested. The most utilised method for UFG structure preparation by SPD in laboratory conditions is Equal Channel Angular Pressing (ECAP)³. Principle of ECAP process is based on extruding the workpiece through angular die that includes two together crossed channels having the same cross-section. Angle between vertical and horizontal channel Φ is in range of 60°–135° (ref.⁴, Fig. 1), which is chosen in dependence on plastic properties of processed material. ECAP process is based on repeated plastic deformation of processed workpiece. During every pass through ECAP die the same intensity of plastic deformation is cumulated into samples. Every ECAP pass makes increase of total intensity of plastic deformation in elaborated workpiece possible. Maximum number of ECAP passes is dependent on demand on final properties, or on plasticity fatigue of investigated material. The limit of plasticity of metals in ECAP process can be demonstrated in three ways:

1. *High strengthening of extruded material*, that can cause stop of the ECAP process influenced by destruction of equipment working parts, or low used load. This condition can possibly happen if material is extruded at wrong temperature (Ti, Mg and others), at hardened state (hardened alloys Al, Cu) and all.

2. *When plastic deformation reaches the limit value* and subsequent destruction of extruded samples occurs. This state is characteristic for powder materials extrusion

(without ECAP back pressure), or if material is extruded at wrong temperature (Ti, Mg and others.)

3. *High degree of plastic deformation – pre-deformation*, when degradation of mechanical and physical properties of extruded material occurs. This state occurs when H-P relationship is already invalid, eventually if deformation induced recrystallization of extruded material occurs.

Topic of the article is evaluation of mechanical properties and microstructure of OFHC (Oxygen Free High Conductivity) copper during ECAP processing.

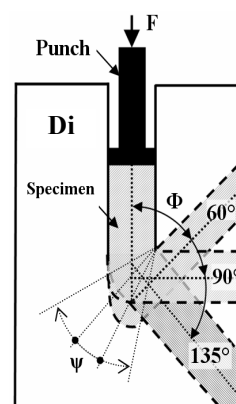


Fig. 1. The scheme of ECAP matrix

2. Experiment

High-purity copper (99.99 % in mass) was used in this study. This copper was supplied in state after zonal refining. Initial microstructure was with average grain size of $d_g \approx 8 \mu\text{m}$. Experimental samples were in rod shape with diameter $\phi = 10 \text{ mm}$ and length $l = 80 \text{ mm}$. Microstructure of Cu samples was formed by ECAP extrusion at room temperature. The ECAP die has two channels with circular cross-section, that are crossed together in angle $\Phi = 90^\circ$. Samples were rotated around their axis at 180° between each pass, it is way C. Extrusion rate was 1 mm s^{-1} . Total number of ECAP passes was 16. Mechanical properties were observed after each even-numbered ECAP pass. Static tensile test was made on small samples according to Fig. 2. Vickers microhardness HV 0,01 was measured on polished surface of samples cross-section at load 10 gf. Nanoindentation measurement on polished surface in CSM regime was made into indentation depth of $2 \mu\text{m}$ by Berkovich indenter. Substructure was observed on thin foils by transmission electron microscopy (TEM), that were prepared from samples in longitudinal direction. They were further thinned with a twin-jet electro-chemical

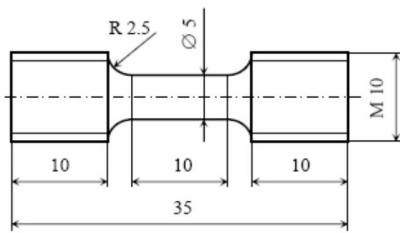


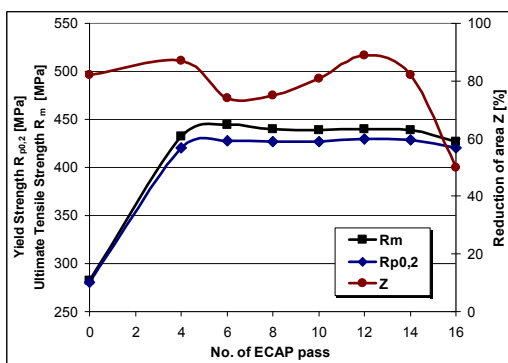
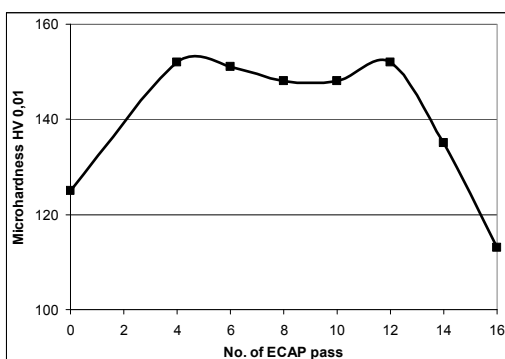
Fig. 2. The shape and dimensions of tension test specimen

polisher Struers TenuPol-5 using a solution of 33 % HNO_3 + 67 % CH_3OH by temperature -30°C and electric voltage 20 V.

3. Results and discussion

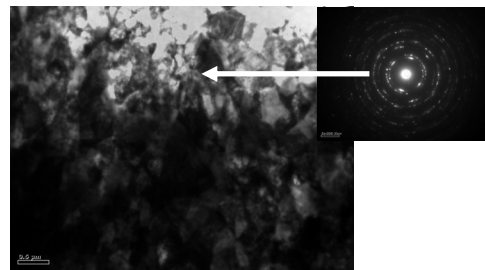
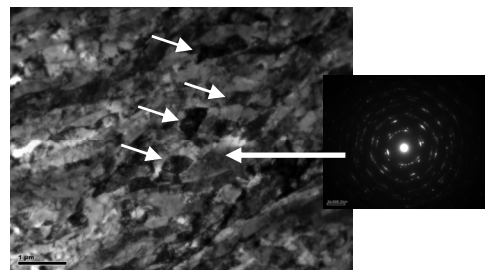
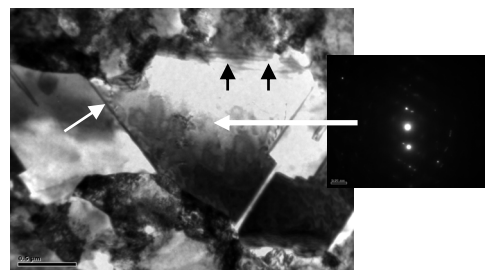
Influence of SPD on mechanical properties and microstructure development of OFHC copper

Change of mechanical properties during 16 ECAP passes is displayed in Fig. 3 and Fig. 4.

Fig. 3. Change of mechanical properties during 16th ECAP passesFig. 4. Change of microhardness of Cu during 16th ECAP passes

On this diagrams we can see that highest increase of $R_{p0.2}$ and R_m is up to the 4th pass. Steady state is observed between the 6th and 12th pass. After the 12th pass these properties decrease. Reduction of area Z as an effective index of plastic properties records the first decrease after the 4th pass and second expressive decrease after the 12th pass. Microhardness has a similar character as Z , where after the 12th pass accordingly we can see expressive decrease.

TEM analysis has been performed after 12, 14 and 16 ECAP passes. Development of substructure is displayed in Fig. 5–7. Substructure after the 12th ECAP pass consists of subgrains with medium value $d_{sg} = 190$ nm, that are greatly misoriented as it can be seen on diffraction pattern. Medium subgrain size after the 14th pass descend to $d_{sg} = 160$ nm (Fig. 6). In deformed UFG Cu substructure an anomaly has been observed after the 14th pass in form of recrystallized subgrains in size $d_{sg} = 500$ nm. Recrystallization of the UFG materials becomes evident also by

Fig. 5. TEM microstructure of OFHC Cu after the 12th ECAP passFig. 6. TEM microstructure of OFHC Cu after the 14th ECAP passFig. 7. TEM microstructure of OFHC Cu the after 16th ECAP pass

decrease of the microhardness and reduction of area as could be seen after the 14th ECAP pass. From numerical simulations⁴ of ECAP process, we can conclude that cumulated effective deformation in samples after the 1st pass is $\varphi_{ef} \approx 1.1$, whereby effective deformation after the 14th pass is reaching the value $\varphi_{ef} = 15.4$. Attaining the value $\varphi_{ef} = 15.4$ recrystallized grains were observed in deformed microstructure.

In Fig. 7 is displayed the substructure after the 16th pass, where recrystallized grains with size up to 1 μm were observed. White arrays indicate recrystallized grains that are generally characterised by twins. Copper is metal characterized by low stacking fault energy, therefore the recovery of deformation structure should occur by dynamic recrystallization mechanism (DRX). Dynamic recrystallization usually develops on grain boundaries and is usually called deformation induced boundary motion (strain induced boundary migration – SIBM)⁵. Actual research in dynamic recrystallization nucleation emphasizes the role of twins and also deformation induced lattice rotation within high angle grain boundaries^{6,7}. Based on experiment results and literature analysis we suppose, that after achieving some degree of deformation by ECAP process at OFHC copper local dynamic recrystallization, or let us say meta-dynamic recrystallization influenced by plastic deformation occurs.

Influence of SPD on local mechanical properties of OFHC Cu (H_{IT} , E_{IT})

On observed samples the indentation hardness H_{IT} and Young's modulus E_{IT} were measured after 0, 10 and 16 ECAP passes, Fig. 8. Indentation hardness H_{IT} after the 10th ECAP pass increases from initial 1.42 GPa up to 1.79 GPa. Measured data hit good correlation with measured data of HV 0,01, in agreement with relation $HV\ 0,01 = 92.5 \cdot H_{IT}$ (ref.⁸). Between the 10th and 16th ECAP pass no expressive change in H_{IT} was observed, whereby in 16th ECAP pass expressive decrease of HV 0,01 was recorded. This disagreement of results is probably caused by the fact that during nanoindentation (unidentified) local recrystallization UFG substructure was missed.

In Fig. 9 is displayed change of E_{IT} by nanoindentation for samples after 0, 10 and 16 ECAP passes. In de-

pendence on chemical purity of Cu is Young's modulus in interval $E = 110\text{--}128$ GPa (ref.⁹). On Cu sample without deformation was measured $E_{IT} = 126$ GPa. This value is from the interval from literature⁹. In metals and alloys the Young's modulus depends on chemical composition, temperature and texture crystallographic orientations. Young's modulus is changing¹⁰ with plastic deformation during cold forming, or with heat treatment.

Benito et al.¹⁰ reported that cold plastic deformation reduces the Young's modulus. These changes are well-known for iron, carbon steels and other metals and alloys. Morestin et al.¹¹ reported that E for steels decreases up to 20 % of its initial value just after a 3–5 % plastic strain applied by a tensile test machine. Ledbetter et al.¹² found that Young's modulus in polycrystalline aggregates of copper diminishes with cold working and then recovers with additional working. These authors suggested that the E parameter decreases due to the increase of the non-pinned dislocations.

In the process of strengthening by SPD was in the 10th and 16th ECAP pass observed an increase of Young's modulus of about $\Delta E_{IT} \approx 15$ GPa toward initial state. This result of Young's modulus was verified by static tensile test. On Cu sample without deformation was measured $E = 124.8$ GPa. This measurement confirmed correctness of nanoindentation measurement of Young's modulus in the state without plastic deformation. On sample after the 10th ECAP pass was measured $E = 110.6$ GPa. Fig. 10 shows that Young's modulus decrease with the plastic deformation ($\varphi_{ef} \approx 11$) of about $\Delta E = 14.2$ GPa, representing ≈ 11 % drop.

Young's modulus depends on type of inter-atomic bonding and lattice parameter a . We supposed, that increase of Young's modulus measured by nanoindentation is caused by change of lattice parameter a . Lattice parameter a measured by RTG analyses was after the 10th and 16th ECAP pass in interval $< 0.3611; 0.36145 >$ nm, whereby lattice parameter Cu without SPD was $a = 0.3615$ nm. From these results follows that no volumes change of lattice parameter a occurred due to SPD.

Important influence on Young's modulus has also substructure crystallographic orientation. The microstructure after ECAP process is characterized by different crystallographic orientation in longitudinal and cross direction

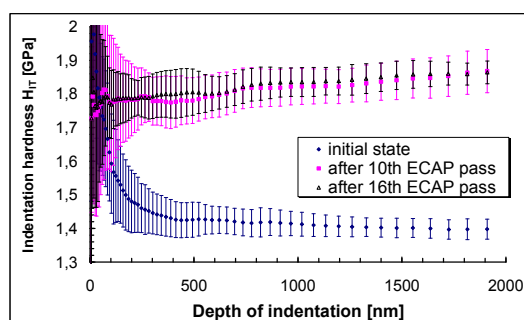


Fig. 8. Change of indentation hardness H_{IT} after ECAP

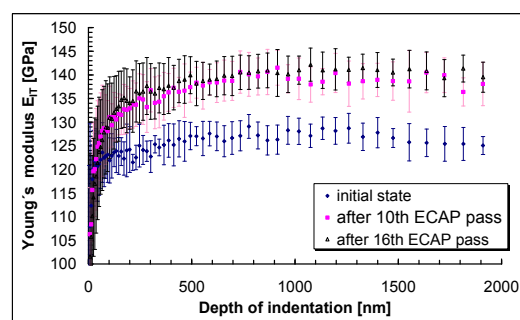


Fig. 9. Change of Young's modulus E_{IT} after ECAP

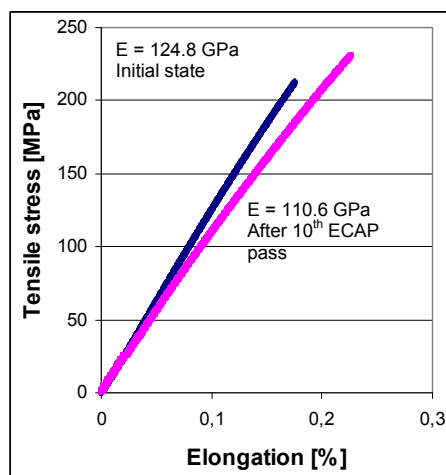


Fig. 10. Measurement of E by static tensile test

of samples¹³. Difference between E and E_{IT} after SPD can be attributed to the change of substructure crystallographic orientation because E of static tensile test was measured in longitudinal direction of samples, whereby nanoindentation measurement of E_{IT} was made in cross-section of samples. This supposition has not been verified in this article.

4. Conclusions

The article was focused on the impact of SPD on mechanical properties and microstructure of OFHC copper. Based on analyzing the experimental results, we can formulate the following conclusions:

1. Substructure of high purity copper is strongly formed in each ECAP pass. The most significant changes occur up to the 4th ECAP pass where mechanical properties are significantly increasing.
2. In deformed UFG copper substructure after the 14th ECAP pass anomaly in form of recrystallised subgrains with mean size $d_{sg} \approx 500$ nm was observed. We assume that after reaching the level of deformation ($\varphi_{ef} = 14.4$) using the ECAP process in OFHC copper, local dynamic recrystallisation and/or meta-dynamic recrystallisation due to plastic deformation occurs.
3. Maximum values of mechanical properties of OFHC copper, at these conditions of ECAP process can be reached after the 12th pass. If the number of passes is greater than 12, the degradation of UFG microstructure influenced by the dynamic recrystallisation or meta-dynamic recrystallisation occurs.
4. After the 10th ECAP pass indentation hardness H_{IT} increased from the original value 1.42 up to 1.79 GPa.
5. By static tensile test has been demonstrated that Young's modulus decreases with plastic deformation during ECAP ($\varphi_{ef} \approx 11$) by $\Delta E = 14.2$ GPa, which represents $\approx 11\%$ decrease.

The authors acknowledge the support given by the APVV – 20 – 027205, VEGA No.2/7195/27.

REFERENCES

1. Bidulská J., Kvačkaj T., Bidulský R., Actis Grande M.: High Temp. Mater. Process. 27, 203 (2008).
2. Bidulská J., Kvačkaj T., Bidulský R., Actis Grande M.: Kovove Mater. 46, 339 (2008).
3. Kvačkaj T., Bidulská J., Fujda M., Kočiško R., Pokorný I., Milkovič O.: Mater. Sci. Forum, 633–634, 273 (2010).
4. Kočiško R., Zemko M., Kuskulič T., Kvačkaj T., Kováčová A.; In: Metallography 2007, 13th International Symposium on Metallography, 2.–4.may, 2007, Stará Lesná, Slovakia, p. 397 – 404.
5. McDonald D.T., Humphreys F.J., Bate P.S., Brough I.: Mater. Sci. Forum 558–559, 449 (2007).
6. Miura H., Sakai T., Magawa R., Gottstein G.: Scripta Mater. 51, 671 (2004).
7. Wusatowska-Sarnek M., Miura H., Sakai T.: Mat. Sci. and Eng. A 323, 177 (2002).
8. Fischer-Cripps A.C.: Nanoindentation, 2004 Springer-Verlag New York.
9. <http://en.wikipedia.org/wiki/Copper>; This page was last modified on 3 March 2009, at 09:06.
10. Benito J.A., Manero J.M., Jorba J. and Roca A.: Met. and Mat. Trans. A Vol. 36A (2005), p.3317.
11. Morestin F., Boivin M.: Nuclear Eng. and Design Vol. 162 (1996), p. 107.
12. Ledbetter H.M., Kim S.A.: Mater. Sci. Eng. A Vol. 101 (1988) p.87.
13. Khorashadizadeh A., Winning M., Raabe D.: Materials Science Forum Vols. 584–586 (2008) p. 434–439.

R. Kočiško^a, P. Zubko^b, J. Ďurišin^c, M. Molnárová^c, A. Kováčová^a, M. Kvačkaj^a, and J. Bacsó^a (^a Department of Metals forming, Faculty of Metallurgy, Technical University of Košice, Slovakia, ^b Department of Material science, Faculty of Metallurgy, Technical University of Košice, Slovakia, ^c Institute of materials research, Slovak academy of sciences, Košice, Slovakia): **The Mechanical Properties Changes of OFHC Copper After ECAP Processing**

This paper deals with changes of mechanical properties and microstructure of OFHC (Oxygen-Free High thermal Conductivity) copper after ECAP (Equal Channel Angular Pressing). Mechanical properties were measured after each even numbered pass. Local mechanical properties were measured by nanoindentation method, hardness H_{IT} and Young's modulus E_{IT} . Microstructure was investigated in longitudinal section of the samples by TEM (Transmission Electron Microscopy). Substructure after the 14th pass was created by subgrains with average diameter of $d_{sg} \approx 160$ nm. An anomaly was observed in form of recrystallized subgrains sized $d_{sg} \approx 500$ nm in deformed UFG copper substructure.

IMPACT TEST OF SURFACE

**ANTONÍN KRÍŽ^{a*}, PETR BENEŠ^b,
and JIRÍ ŠIMEČEK^b**

^a *Research Centre of Rail Vehicles*, ^b *Department of Material Science and Technology, Faculty of Mechanical Engineering, University of West Bohemia, Plzeň, Czech Republic*
kriz@kmm.zcu.cz

Keywords: Impact tester, Rail Vehicle Wheel Materials

1. Introduction

In numerous industrial applications, machine parts are subjected to high contact load. Mechanical interaction of two surfaces results in such conditions, which may lead to their degradation. Such damage is usually the limiting factor of their service life. This is why methods for elimination or at least controlling such degradation are sought¹.

One of available techniques for investigation of contact degradation is impact testing. With an impact tester it is possible to determine the response of materials to dynamic impact contact wear. The resistance to impact contact load can be examined not only in bulk materials but also in surface-treated materials. Another type of test, which can be run on the impact tester, is investigation of contact impact fatigue. Contact impact fatigue is an important material parameter, as it controls the initiation of fatigue cracks throughout the volume of the piece, which eventually results in the machine part failure^{2,3}.

2. Impact Tester Designs

The impact force is not exerted through the free fall of the indenter but by magnetic force generated by an electromagnetic coil. The arm in this type of impact tester is actuated by a coil, which exerts the required force. The indenter is mounted on the arm. The holder with the indenter is returned to their initial position by a spring force. The test piece is mounted on a rotating and extending stage. Owing to the guiding mechanism of the stage, it is possible to arrange the impact sites in a straight line, which is beneficial for some types of measurements. In order to apply the load at other angles, the stage can be modified by adding a positioning device. This type of impact tester will be extended in near future with additional measuring equipment (for accelerometric and acoustic emission measurements). These modifications will significantly expand its application potential.

Dynamic contact wear does not rank among the basic wear modes. It is a combination of mechanisms involving adhesive, abrasive, fatigue and vibration wear. With impact test it is possible to determine the contact fatigue strength of selected materials. Testing based on scratch-test techniques (progressive penetration of a stylus into surface under increasing load) or tribological procedures might be inadequate for simulation of conditions, where the surface of material is subjected to both fatigue load and erosive wear. The impact test is a more accurate simulation of a real-world situation affecting the service-life of material (e.g. “pulsating” contact between the cutting tool and work piece due to vibrations).

3. The Use of Impact Testing for Rail Vehicle Wheel Materials

One of important areas of application of impact test is measurement of impact fatigue life of rail vehicle wheels. In this case, the instrument was used for bulk material. The advantage of investigation of impact fatigue life of rail vehicle wheel materials with the impact tester lies in the fact that the simulation of the wheel load is very similar to the real-world application conditions. The impact load acts on the wheel surface when it rolls across railway turnouts, joints or expansion gaps. In all these cases, the wheel surface is subjected to dynamic impacts. This might induce a particular type of response of material and cause damage, such as formation of cracks, defects, etc. Since presence of cracks in a rail vehicle wheel is undesirable, formation and propagation of cracks due to impact fatigue load requires great attention.

Cracks may form due to various factors and in different ways. Each of crack formation modes is specific to the given material and, particularly, to its internal structure. It cannot be thought of as applicable to other types of materials. This indicates the importance of investigation of mechanisms, which take place in the material as a result of contact fatigue loads. Dynamic loading of wheels in operation can be most accurately simulated with an impact tester, which outperforms any other laboratory testing methods in this respect.

The microstructure of the material in question consisted of ferrite and pearlite and some areas of Widmannstätten-type microstructure. The presence of the Widmannstätten microstructure might have an adverse effect on mechanical properties of steel and might lead to premature crack formation. Impact testing provided no evidence of the Widmannstätten microstructure being the initiation site for cracks. The indenter was a 6 mm diameter tungsten carbide ball. Thanks to its hardness, this material shows excellent resistance to dynamic contact load, which makes

it an ideal candidate for impact testing. In order to clarify the damage mechanism and to capture the progressive wear of the specimen surface and the formation of impact sites, various numbers of impacts were used for the test: 500; 1000; 2500; 5000; 10 000 and 100 000. The rail vehicle wheels were tested with the indenter impact energy of $E = 0.078$ J.

After as few as 500 impacts, numerous defects were observed in the fringe area of the impact site. In some locations, these defects coalesced, which gave rise to continuous bands of cavities. The concentration of the bulk of defects in the fringe area of the impact site is related to the distribution of the tensile stress, which reach their peak in this location. As a result, cracks and defects form in this area and may coalesce. On the contrary, the prevailing type of stress in the impact site centre is the compressive stress. Even the initial surface showed numerous defects. It is therefore likely that the resulting defects did not form during the impact but, instead, were present on the specimen surface and grew or coalesced due to impact-induced surface and subsurface stresses. Microscopic observation of the centre of the 500-impact impact site did not reveal any defects. However, they might have been closed by the forging action of the indenter.

After 1000 impacts, the fringe area of the impact site showed a network of fine cracks. Propagation of cracks into other areas than the impact site was not detected. Those fringe areas, where no cracks were found, showed defects, same as the specimen upon 500 impacts.

With the growing number of impacts, the number of defects in the fringe areas of the impact site was decreasing. By contrast, the number of defects in the centre of the impact site was increasing.

Upon 100 000 impacts, it was found that the source of hairline cracks are the defects in the fringe areas of the impact site (Fig. 2). This finding suggests that the material responds to high-cycle impact fatigue load by forming microscopic cracks. One can assume that upon increasing the number of impacts, these hairline cracks would propagate further and serious damage of the material would occur. It is impossible to verify this hypothesis using the existing low-frequency impact tester, as the high-cycle

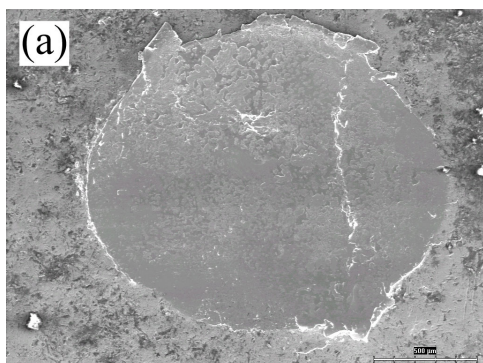


Fig. 1. Impact site upon 100 000 impacts

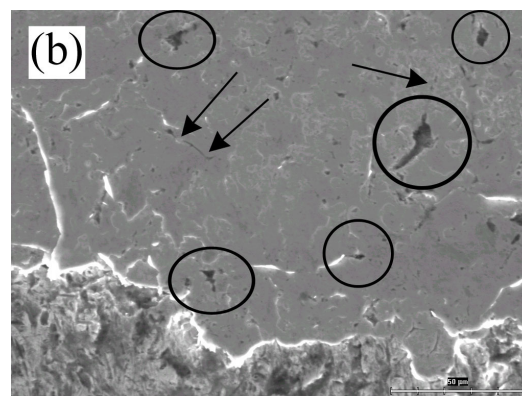


Fig. 2. Detailed view of the impact site (Fig. 1) fringe area; clusters of defects (marked with a circle), hairline cracks (marked with an arrow)

testing (above 100 000 impacts) would be very time-consuming.

The crack, which had been revealed during machining of the specimen (Fig. 3a,b), propagated rapidly in the course of the 100 000-impact loading cycle. The crack was outside the impact site. Since the crack propagated from the area of specimen, which was under the clamping flange that held the specimen in the testing instrument, it can be assumed that the crack propagation was due to the propagation of the impact load throughout the whole volume of material. The shock waves emanate from the impact site and reach all parts of the material. The shock wave energy reduces the critical stress for the crack growth. As a result, the crack easily enters the sound material outside the impact site. Moreover, fastening the specimen with a flange introduces further stresses in the material. Those become another factor promoting the propagation of existing cracks outside the impact site. More cracks were found in the neighbourhood of the crack in question (Fig. 3b). It was not established whether these cracks were formed as a results of the impact loading.

It is evident that propagation of cracks existing in the material can be induced by impact energy introduced by a blow of the indenter on the specimen surface and reaching the crack tip.

4. Development of Impact Tester and the Testing Procedure

Defects produced by contact loading are often so minute that they cannot be observed without light or scanning electron microscopes. Therefore, investigation methods must be very accurate in order to capture initiated changes even at time of testing. For this reason, acoustic emission signal is recorded over the course of the impact test and provides an indication of significant crack propagation. Another useful feature of the instrument is a strain

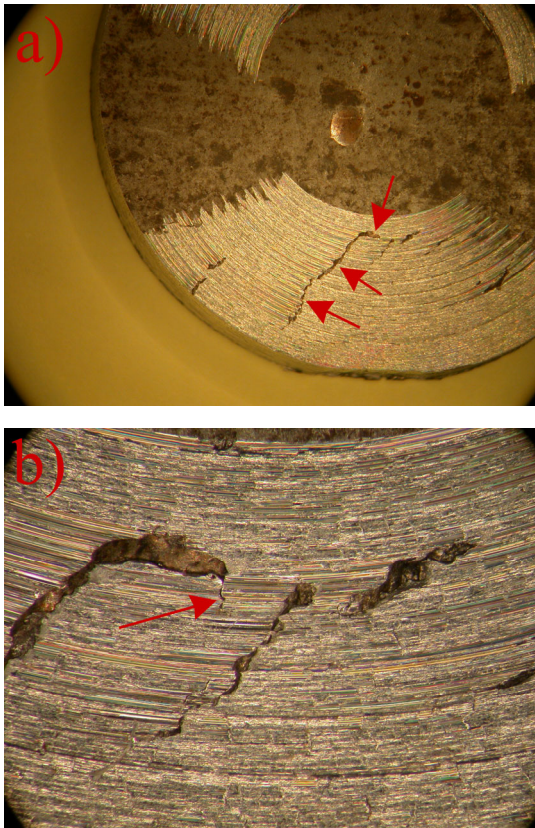


Fig. 3. (a) A crack outside the impact site - the crack was growing during the impact test, (b) detail of the crack end, where further propagation in the form of a hairline crack is visible

gauge. It measures the individual impact force for the purpose of verification of the equipment settings and also reveals the signs of hardening and softening processes. With such data it is possible to identify the key moment of the contact loading process. The hardening process, i.e. formation of dislocation pile-ups in slip systems, leads to propagation of cracks during the period of further loading. Combining the outputs of both instruments can reveal the degradation processes – which play a crucial role in contact loading – at an early stage.

Fig. 4 shows further planned design modifications. Fixtures for multi-axis loading and bending on a mandrel are being manufactured. With this design modification, more faithful simulation of complex loading conditions will be available. These design modifications are particularly important in testing of bulk materials where the initial crack is often closing due to a compressive load. Where the part operates under tensile load, rapid degradation takes place. This often occurs in practice but it could not have been simulated on the basis of tests under simple loading conditions performed thus far.

Further design modifications also stem from practical requirements. Testing of railway wheels and materials for

rails requires the presence of a liquid, which significantly alters the stress effects. A special chamber will be designed to provide required temperatures and environments and to allow exploration of effects of climatic and thermal conditions on properties of materials and on development of degradation processes.

These new design solutions will entail fine-tuning of current testing methods. Current testing conditions typically include low loading forces and a high number of cycles. With these settings, individual changes taking place in the material can be detected accurately. Images of the impact crater were captured with a light microscope, scanning electron microscope and a laser scanning confocal microscope. Their evaluation focused not only on formed local defects (their size is often on the order of micrometers) but also on the magnitude of plastic deformation. New methods are being developed, which rely on measurement of residual stresses in the impact crater area and its surroundings. The measurement must be performed immediately upon the exposure, which is why a simple

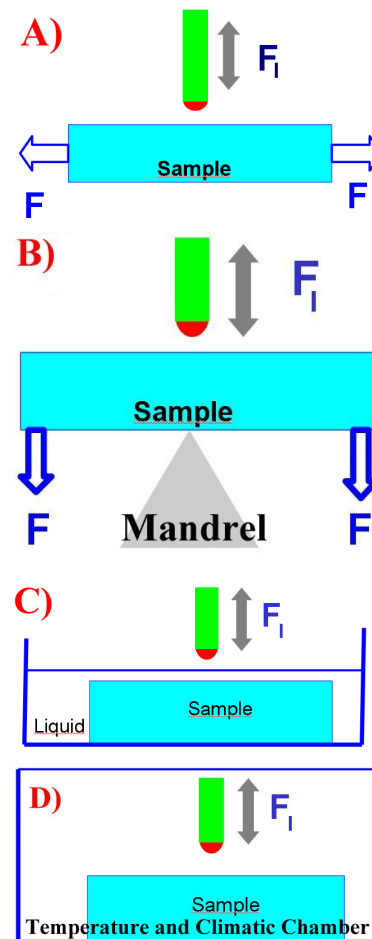


Fig. 4. Contact load testing alternatives, A) multi-axis loading, B) opening a crack, C) loading with the presence of liquid, D) testing under special climatic conditions

Barkhausen noise method will be used. Alternative methods include the measurement of remanent magnetism and residual stress by means of the MMM method (Magnetic Memory of Metals). Measurement of properties and identification of processes taking place during contact loading requires a greater number of tests under a single load and a variable number of cycles. The most common procedure consists in specifying limit conditions for measuring and then performing the measurement. The limits are the number of cycles upon which changes in material begin to take place and the number of cycles leading to such catastrophic destruction that it does not yield any information. There are a number of available testing procedures. Their selection must be based on the service load of the material and on required results.

5. Conclusion

The impact tester represents one of the newest and most promising methods for investigation of behaviour of materials subjected to impact contact load. Dynamic loads in the impact tester are concentrated in a small volume of material. This enables examination of behaviour of not only bulk materials but also that of surface films and coatings. The instrument can be expanded with additional measuring equipment, depending on its design. Unique descriptions of behaviour of materials can be obtained using this measuring equipment. No other measuring methods in materials engineering can provide such data. Damping characteristics of materials can be measured using accelerometric measurements. With acoustic emission-based methods, the formation and propagation of impact-induced cracks can be measured based on the amount and frequency of introduced strain energy. The high-frequency impact tester (50 Hz and higher) provides data for plotting Woehler curves. Therefore, the residual life of a part can be assessed using a small sample taken from the part. Another advantage of the high-frequency impact tester is its process of operation, which is closer to the real-world processes involving high frequency impact. A typical example is a cutting process, in which the cutting edge of a tool impacts the work piece surface repeatedly within a short time interval.

The previous chapters contained descriptions of some basic options for testing materials using impact testers and results and conclusions to be derived from the measurements.

REFERENCES

1. Matthews A., Bantle R.: *Thin Solid Films*, Elsevier, 2004.
2. Bouzakis K.-D., Asimakopoulos A., Michailidis N., Kompogiannis S., Maliaris G., Giannopoulos G., Pavlidou E., Erkens G.: *Thin Solid Films* 469–470, 254 (2004).
3. Kříž A., Beneš P.: *Acta Mechanica Slovaca, EQUILIBRIA*, s. 174–180, 2008.

This paper was prepared with the funding of the MŠMF 1M0519 project Research Centre of Rail Vehicles and the internal institutional grant.

A. Kříž^a, P. Beneš^b, and J. Šimeček^b (^a*Department of Material Science and Technology, University of West Bohemia, Faculty of Mechanical Engineering, Czech Republic,* ^b*Research Centre of Rail Vehicles*): **Impact Test of Surface**

This paper deals with selected applications of testing of materials using an impact tester. An impact tester is a piece of testing equipment for investigation of response of materials to repeated impact loads. The principle of the test consists in repeated impacts of a testing body onto the surface of specimen with a specific force. Impact testing is most widely used for testing fatigue properties of those components, which are subjected to repeated impacts and concurrent strong impact shocks. These include machining tools, railway wheels, piston rings and others.

The paper presents results of experiments obtained with an impact tester of authors' own design. It also introduces envisaged development planned for near future: both in terms of design and methodology.

DYNAMIC NANOINDENTATION OF BOVINE INTERVERTEBRAL END PLATE

JAROSLAV LUKEŠ*, JOSEF ŠEPITKA,
and JIRÍ NĚMEČEK

Czech Technical University in Prague, Faculty of Civil Engineering, Thákurova 7, 16629 Prague 6, Czech Republic
jaroslav.lukes@fs.cvut.cz

Keywords: nanoindentation, DMA, viscoelasticity, end plate, intervertebral disc

1. Introduction

According to recent studies the nanoindentation appears to be a very effective tool to analyze mechanical properties of biomaterials especially in case of hardly accessible soft tissue. Machining of biological material to standardly shaped samples for tensile testing is quite difficult. This paper presents a study of viscoelastic properties of bovine intervertebral disc's end plate (EP) by nanoscale quasistatic and dynamic mechanical analysis (nanoDMA).

Cartilaginous end plate is a part of intervertebral disc that creates the transition zone between hard vertebral body and soft anulus fibrosus (AF). The process of calcification within AF lamellae and EP (Fig. 1) is crucial for mechanical behavior of intervertebral disc. It is observed as the clinical syndrome in childhood and elderly population¹. Sometimes the etiology is unclear. The previous trauma, surgical intervention or overloading are suggested. Calcification of end plate has critical influence on salute flow to avascular anulus fibrosus end nucleus pulposus and initiates the IVD degeneration². Nanoindentation is an experimental method, which can tell us more about tissue mechanics of end plate³.

2. Methods

2.1. Sample preparation

Sagittally halved bovine spine was obtained from the butchery. The lumbar spine motion segments were immediately dissected and five millimeter thick plates of vertebral body, end plate and anulus fibrosus were cut and polished under running water condition. Samples were placed into the physiological solution right after. The plate of the sample was glued to the bottom of the Petri dish and surrounded by physiological solution again. The surface was water free and ready to be indented.

2.2. Testing conditions

Quasistatic and nanoDMA load controlled experiments were performed on Hysitron TriboLab[®] system with the Berkovich diamond tip at the temperature 22.3 °C. Quasistatic loading consisted of three segments 1×50×10 seconds with maximum force $P_{\max} = 800 \mu\text{N}$ that corresponded to the contact indentation depths $h_c = 497.66 \pm 74.09 \text{ nm}$. The time of loading segment $\tau_L = 1 \text{ s}$ and default sampling frequency 0.017 s provided enough datapoints for the loading curve evaluation. Moreover, it simulated the Heaviside step load function needed for measuring of the pure creep material response. Holding time $\tau_H = 50 \text{ s}$ corresponded to our previous experience for maximum dwell period of creep data acquisition which is not influenced by the thermal drift error⁴. Unloading segment $\tau_U = 10 \text{ s}$ was set according to the condition of "fast unloading" described in Vandamme & Ulm⁵.

The same static load was applied to the tip during nanoDMA experiments. Harmonic loading with dynamic load amplitude 20 μN was prescribed for the harmonic frequency range 5–300 Hz. Stiffness K_i and damping C_i of the sensor was measured by running a frequency sweep in the air, which is controlled by the software of the Hysitron's system. The procedure was adopted from Asif et. al.⁶ as well as the analysis of dynamic data.

3. Theory

3.1. NanoDMA

Dynamic driving force $P_0 \sin(\omega t)$ with amplitude P_0 and frequency $f = \omega/2\pi$ is superimposed on quasistatic loading P_{\max} and stands for particular term in an equation of motion of the indenter relative to the indenter head:

$$P_0 \sin(\omega t) = m\ddot{x} + C\dot{x} + Kx \quad (1)$$

The solution to the above equation, where compliance $C = C_i + C_s$ and stiffness $K = K_i + K_s$ of the system on Fig. 2 are defined respectively, is a steady-state displacement oscillation at the same frequency as the harmonic loading

$$x = X_0 \sin(\omega t - \varphi) \quad (2)$$

where X_0 is the amplitude of the displacement oscillation and Φ is the phase shift of the displacement with respect to the driving force. Both terms in Eq. (2) are recorded by the nanoindentation system.

The standard analytical solution for the model on Fig. 2, that assumes that the machine frame stiffness K_m is infinite, follows.

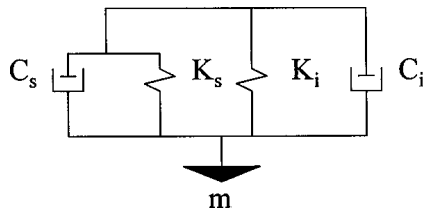


Fig. 2. Dynamic model of indenter system in contact with the specimen, where m is the indenter mass, C_i is the damping coefficient of the air gap in the capacitive displacement sensor, C_s is the damping coefficient of the specimen, K_s is the contact stiffness, and K_i is the spring constant of the leaf springs that hold the indenter shaft. Adopted from Asif et al. ⁶

The amplitude of the displacement signal is

$$X_0 = \frac{P_0}{\sqrt{(K_s + K_i - m\omega^2)^2 + [(C_i + C_s)\omega]^2}} \quad (3)$$

and the phase shift between force and displacement is

$$\varphi = \tan^{-1} \frac{(C_i + C_s)\omega}{K_s + K_i - m\omega^2} \quad (4)$$

where m is the indenter mass, ω is the frequency in rad/s, C_i is the damping coefficient of the air gap in the capacitive displacement sensor, C_s is the damping coefficient of the specimen, K_i is the spring constant of the leaf springs that hold the indenter shaft and K_s is the contact stiffness⁶.

These calculated values for stiffness and damping of the sample are then used to determine the viscoelastic properties of reduced storage modulus (E_r'), loss modulus (E_r'') and $\tan \delta = E_r''/E_r'$ as

$$E_r' = \frac{K_s \sqrt{\pi}}{2\sqrt{A_c}} \quad (5)$$

$$E_r'' = \frac{\omega C_s \sqrt{\pi}}{2\sqrt{A_c}} \quad (6)$$

and

$$\tan \delta = \frac{C_s \omega}{K_s} \quad (7)$$

where A_c is the contact area based on tip area function related to the contact depth at quasistatic loading⁷. The storage and loss modulus of the sample E_s' and E_s'' , re-

spectively, are related to the reduced storage and loss moduli by

$$\frac{1}{E_r'} = \frac{(1-\nu_i^2)}{E_i} + \frac{(1-\nu_s^2)}{E_s'} \quad (8)$$

$$\frac{1}{E_r''} = \frac{(1-\nu_i^2)}{E_i} + \frac{(1-\nu_s^2)}{E_s''} \quad (9)$$

where subscripts i and s refer to the indenter and sample materials, respectively, and ν is the Poisson's ratio⁸.

The storage modulus and the loss modulus are related to the complex modulus $E_s^* = E_s' + iE_s''$ and indicate the ability of the sample to store and return energy (recoverable deformation; E_s') and dissipate energy (E_s''). The ratio of the loss modulus to the storage modulus (i.e., $\tan \delta$) reflects the viscoelastic behavior of the material. It is a material parameter independent of the tip-sample contact area.

3.2. Linear Viscoelastic Analysis

In this study, we employed Vandamme and Ulm's isotropic linear viscoelastic model for the nanoindentation creep data analysis³⁻⁵ that adopts two assumptions: (i) material is linearly viscoelastic and (ii) viscous deformation (creep) is associated only with deviatoric deformations. Viscoelastic parameters can be obtained directly from the history of indenter displacement measured during the dwell period at which the load is kept constant. The model utilizes the functional formulation:

$$\varepsilon(t) = \int_0^t C(t-\tau) : \frac{d}{dt} \sigma(\tau) d\tau \quad (10)$$

where t is time; ε is deviatoric strain tensor; σ is deviatoric stress tensor and $C(t)$ is fourth order tensor of creep functions of the material. The deviatoric compliance function of the 1-D linear viscoelastic Kelvin-Voigt-Maxwell model can be derived in the form:

$$C^d = \frac{1}{G_0} + \frac{1}{G_V} \left(1 - e^{-\frac{-G_V t}{\eta_V}} \right) + \frac{1}{\eta_M} \quad (11)$$

in which G_0 is the shear modulus, η_M stands for viscosity in Maxwell series unit and G_V , η_V are shear modulus and viscosity in the parallel Voigt unit, respectively. The volumetric behavior was considered as purely elastic. Elastic modulus E_0 and associated shear modulus $G_0 = E_0/2(1-\nu_0)$ were estimated by the software implemented standard Oliver and Pharr method⁷. Poisson's ratio ν_0 was supposed to be time independent for the given material. By the analogy with classical functional formulation of linear viscoe-

Table I
Material parameters from three fits of indentation creep data

Indent No.	E_r [GPa]	E_0 [GPa]	G_0 [GPa]	η_v [GPa.s]	η_M [GPa.s]	G_v [GPa]
1	3.580279	3.223733	1.221111	137.2005	0.2373	0.544
2	3.871679	3.487004	1.320835	151.0563	0.2296	0.5991
3	4.890535	4.408564	1.669911	194.5456	0.6515	1.1106
Avg.	4.114164	3.706434	1.403952	160.934133	0.3728	0.751233
St. dev.	± 0.688	± 0.622	± 0.236	± 29.922	± 0.241	± 0.312

lasticity (Eq. (10)) Vandamme and Ulm identify the fundamental step load solution $Y(t)$ as the indentation creep function⁵:

$$y(t) = \frac{1}{P_{\max}} \int_0^t Y(t-\tau) \frac{d}{dt} P(\tau) d\tau \quad (12)$$

Once $Y(t)$ is known, the dimensionless indentation response $y(t)$ can be determined for any monotonically increasing load history it means loading $y_L(t)$ and holding $y_H(t)$ segment of indentation curve. Fitting the creep nanoindentation data by Vandamme and Ulm solution $y_H(t)$ the viscoelastic parameters are determined as

$$h(t) = \sqrt{\frac{\pi P_{\max} y(t)}{2 M_0 4 \tan \theta}} \quad (13)$$

where M_0 is the instantaneous indentation modulus and θ is the half-apex angle of conical indenter. In case of the Berkovich tip the angle $\theta=70.32^\circ$ (ref.⁵).

4. Results

Shear modulus G_0 is the first input parameter of Vandamme and Ulm's⁵ five parameters viscoelastic model (including Poisson's ratio). The fit of nanoindentation creep data (Fig. 3) derives the next three viscoelastic material constants η_M , η_v , G_v (Tab. I). Storage and loss moduli are the characteristics that describe the viscoelastic properties of EP as well. Storage moduli indicate the dependence on frequency as was reported for polymers⁸ and articular cartilage⁹, respectively. The values have the increasing trend with the increasing frequency. On the other hand the loss modulus shows almost no dependence on frequency (Fig. 4). The values of storage moduli at low frequencies correspond to elastic reduced moduli from quasistatic indentation $E_r = 4.11 \pm 0.69$ GPa quite well.

5. Discussion and conclusions

The nanoDMA testing was found to be straightforward method for the identification of viscoelastic parameters of hardly accessible intervertebral cartilaginous end plate. Nanoindentation technique allows biological samples to be surrounded by a physiological solution which prevents a long term degradation of the sample by drying. The experimental set up is very simple in the contrary to standard tensile or compression testing.

Fulcher et al.⁹ reported the characteristic limit frequency which was exhibited as a plateau of E' values at the range to 92 Hz. Such behavior is characteristic for polymer materials where so called glass transition occurs. In case of the cartilage, the plateau could be associated with development of microcracks in the tissue as proposed by Fulcher. However, we did not observe any plateau in storage moduli values over the full range of frequencies 5–300 Hz (Fig. 4). Actually according to this study, the end plate tissue is able to store more energy with higher load rate without the occurrence of inner failures. Further structural studies of EP must be employed in explanation of this end plate behavior.

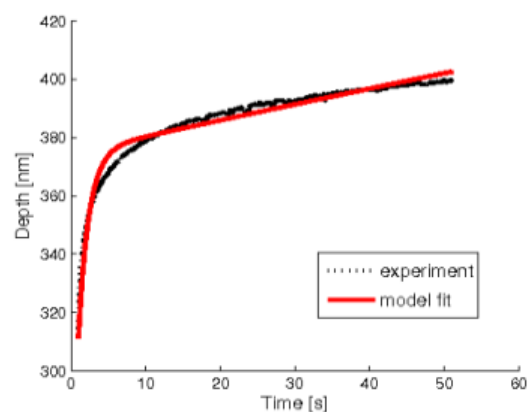


Fig. 3. Nanoindentation creep data fit

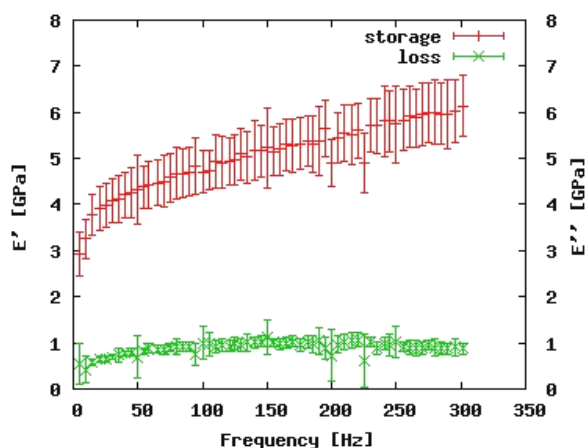


Fig. 4. Storage and loss moduli from nanoDMA

Increasing frequency is connected with the rising load rate. E' clearly showed this dependence which is another proof of a viscoelastic manner of the material.

The Maxwell-Kelvin-Voight model's viscoelastic parameters complement the information about the material of the end plate. The material behavior during the dwell period clearly confirmed the viscoelastic behavior of the EP as well. Especially, the viscosity of the Maxwell unit was quite significant.

Generally, the material properties of biological tissues change from region to region. This is due to the microstructural heterogeneities and varying architecture. Mapping of mechanical properties at different region was left as a future task. This study shows novel approach and potential utilization of nanoindentation technique for biomechanics and tissue mechanics, respectively.

Supports of the Ministry of Industry and Trade of Czech Republic MPO CZ, FT-TA3/131 and Ministry of Education of the Czech Republic MSM 6840770003 are gratefully acknowledged.

REFERENCES

1. Chanchairujira, K., Chung, C. B., Kim, J. Y., Papanikolaou, O., Lee, M. H., Clopton, P., Resnick, D.: *Radiology* 230, 499 (2004).
2. Peng, B., Hou, S., Shi, Q., Jia, L.: *Chinese Medical J.* 114, 308 (2001).
3. Lukes, J., Mares, T., Nemecek, J., Otahal, S.: *IFMBE Proceedings* 23, 1792 (2009).
4. Lukes J., Nemecek J., Minster J.: *25th Danubia-Adria Symposium on Experimental Methods in Solid Mechanics*, 161–162 (2008).
5. Vandamme M., Ulm F.-J.: *Int. J. Solids Structures* 43, 3142 (2006).
6. Asif S. A. S., Wahl K. J., Colton R. J.: *Rev. Sci. Instrum.* 70, 2408 (1999).
7. Oliver W. C., Pharr G. M.: *J. Mater. Res.* 7, 1564 (1992).
8. Chakravartula A., Komvopoulos K.: *Appl. Phys. Lett.* 88, 131901 (2006)
9. Fulcher G. R., Hukins D. W. L., Shepherd D. E. T.: *BMC Musculoskeletal Disorders* 10, 61 (2009).

J. Lukeš^a, J. Šepitka^a, and J. Němeček^b (^a*Czech Technical University in Prague, Faculty of Mechanical Engineering*, ^b*Czech Technical University in Prague, Faculty of Civil Engineering*): **Dynamic Nanoindentation of Bovine Intervertebral End Plate**

According to recent studies nanoindentation appears to be a very efficient tool to analyze mechanical properties of biomaterials especially in case of hardly accessible soft tissue. This paper presents a study of viscoelastic properties of bovine intervertebral disc's end plate (EP) by nano-scale quasistatic and dynamic mechanical analysis (nanoDMA). The sample was kept in physiological conditions although the surface was water free. The effect of frequency on storage modulus E' , loss modulus E'' and a comparison with simple linear viscoelastic solution fitted from the dwell period in quasistatic loading have been shown and discussed in this paper in some details.

CHANGES OF MICROMECHANICAL PROPERTIES OF ULTRA HIGH MOLECULAR WEIGHT POLYETHYLENE AFTER ELECTRON BEAM IRRADIATION AND UNIAXIAL COMPRESSION

JOANNA MASZYBROCKA*, **JERZY CYBO**, and **ADRIAN BARYLSKI**

*University of Silesia, Faculty of Computer Science and Materials Science, Sniezna 2, 41-200 Sosnowiec, Poland
joanna.maszybrocka@us.edu.pl*

Keywords: ultra-high-molecular-weight polyethylene, uniaxial compression, electron beam irradiation, micromechanical properties.

1. Introduction

For over 40 years, UHMWPE (Ultra High Molecular Weight Polyethylene) has been a material widely applied in the production of bearing elements of endoprostheses used in total alloplasty of joints. In spite of the numerous undeniable advantages of this material, there are certain factors which reduce the possibility of long-lasting presence of an implant in the human organism. High susceptibility of polyethylene to plastic deformation and abrasive wear is considered one of the most serious problems^{1,2}. A key element in selecting and forecasting operational durability of a material and its upper layer is the ability to identify its micromechanical properties. Consideration of the relationship between the properties obtained as a result of modifications and their changes induced by operational factors cannot be neglected, either. These results from the fact that the main effect of the tribological process is undoubtedly associated with local changes of the micromechanical properties, which occur on the friction surface and in the subsurface layer (to 20 μm).

The research conducted by the authors has shown that the friction surface exhibits numerous traces of permanent deformation in the form of crosswise projections, located along the irregularities consistent with the friction direction²⁻⁴. The size and distance between the projections testify to susceptibility of the polymer to plastic flow (Fig. 1). A simultaneous reorientation of lamellae on the friction surface and in the upper layer is a consequence of permanent deformation induced by friction²⁻⁴.

Among the contemporary methods of mechanical testing, those performed using the microindentation method play an increasingly important role. Availability of methods of continuous and precise recording of the depth of penetration of an indenter of a known geometry as a function of prescribed load and time enables determining not only hardness and the elastic modulus, but also a number of elastic and plastic properties, thereby ensuring

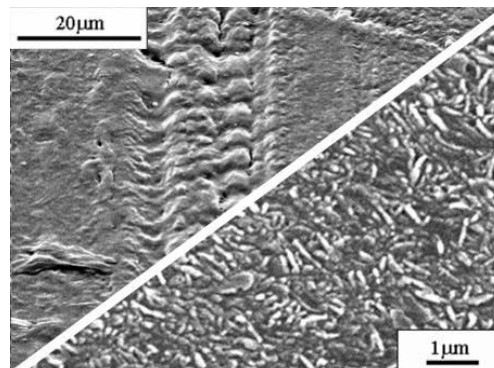


Fig. 1. Plastic deformation of the friction surface of polymer and lamellae orientation in the friction zone

a comprehensive characterisation of micromechanical properties of the material.

This paper aims to evaluate the effectiveness of radiation modification of polyethylene intended for endoprosthesis elements in reducing the consequences of plastic deformation in microregions of the upper layer. The results obtained are an important link in the discussion focused on the description of the phenomena (on different scales) and processes which provide a theoretical basis for effective shaping of polyethylene intended for frictional interaction in the polymer – metal system. The discussion also includes an analysis of the nature and scale of consequences of the tribological process.

2. Research Material

The object of the research consisted of the currently produced ultra high molecular weight polyethylene for medical applications, GUR 1050 (Poly Hi Solidur Deutschland GmbH). Irradiation of the material with an electron-beam (of 10 MeV) and with doses of different values (0 kGy, 2 \times 26 kGy, 4 \times 26 kGy) enabled obtaining variants with a variable degree of cross-linking. The specimens were loaded (compressed) uniaxially, so as to obtain diverse effective plastic deformation (e_f) in the polymer material. Total deformation of $Z_c = 0-80\%$ was applied and various levels of effective plastic deformation were obtained: $e_f = 0-0.7$ (ref.⁵). The value of effective plastic deformation was calculated as:

$$e_f = \ln \frac{h_0}{h_k} \quad (1)$$

where: h_0 – initial height of the specimen, h_k – height of the specimen after work hardening (5 days after test).

3. Research Methodology

The degree of crystallinity of the polymer variants investigated was determined via differential scanning calorimetry (DSC), using a thermoanalyser of TA Instruments, type DSC 2010. The melting point was determined on a thermogram for the maximum of an endothermic peak of melting. The degree of crystallinity was calculated from the formula:

$$C_{\text{DSC}} = \frac{\Delta H_f}{\Delta H_c} \cdot 100\% \quad (2)$$

where ΔH_f – the heat of phase transition (i.e. melting) of the investigated polymer specimen, determined from a DSC thermogram [J g^{-1}]; ΔH_c – the heat of phase transition of completely crystalline polyethylene (empirically determined value amounting to 290 J g^{-1}).

Measurements of micromechanical properties were performed using Micron-Gamma equipment. A Berkovich indenter with a pyramid angle of 65° was used under the load of 1 N, at a speed of load escalation and unloading rate of 1 N min^{-1} , and load time of the specimen under maximum pressure: 15 s.

The hardness was determined as a ratio of the maximum load imposed on the indenter and the projection contact area, A_p , the latter being a function of the indenter shape at the contact depth, h_c :

$$H = \frac{P_{\text{max}}}{A_p} \quad (3)$$

where P_{max} – maximum load imposed on the indenter, A_p – projection contact area.

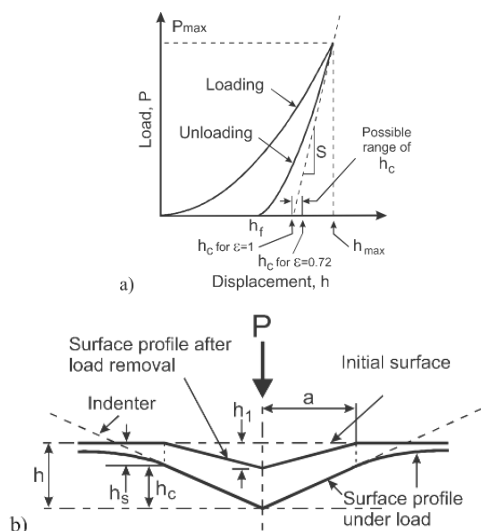


Fig. 2. a) Loading-unloading curve as a function of displacement, b) material deformation during hardness examination

According to the Olivier-Pharr method⁶, the elastic modulus was determined while taking into account the slope of tangent to the initial part of the unloading curve (Fig. 2). The unloading curve is described with an exponential function in the following form:

$$P = \alpha(h - h_f)^m \quad (4)$$

where α – a constant including the elastic modulus and Poisson's ratio of materials of the specimen and the indenter, h_f – the depth of indentation after unloading, m – an exponent depending on the indenter geometry.

By differentiating the equation (4) with respect to the penetration depth h and calculating the value for $h = h_{\text{max}}$, the slope of the initial portion of the unloading curve (S) was determined:

$$S = \left(\frac{dP}{dh} \right)_{h=h_{\text{max}}} \quad (5)$$

$$S = \alpha m (h_{\text{max}} - h_f)^{m-1} \quad (6)$$

On this basis, the contact depth, h_c , was determined:

$$h_c = h - \varepsilon \frac{P_{\text{max}}}{S} \quad (7)$$

where ε – constant dependent on the indenter geometry.

The formulas quoted above allowed determining a reduced elastic modulus of, E_r , from the dependence:

$$E_r = \frac{\sqrt{\pi} \cdot S}{2 \cdot \beta \cdot \sqrt{A_p}(h_c)} \quad (8)$$

where S – contact stiffness, A_p – contact area, with taking account of permanent deformation, β – correction constant for the indenter tip shape (for Berkovich indenter, $\beta \approx 1,034$).

The reduced modulus, E_r , is used to account for the fact that elastic displacements occur in both the indenter and the sample. The elastic modulus of the test material, E , is calculated from E_r , using:

$$\frac{1}{E_r} = \frac{1 - \nu^2}{E} + \frac{1 - \nu_i^2}{E_i} \quad (9)$$

where E , ν – elastic modulus and Poisson's ratio for the investigated material, E_i , ν_i – elastic modulus and Poisson's ratio for the material of the indenter (for diamond $E = 1141 \text{ GPa}$, $\nu = 0.07$).

The loading-unloading curve was the source of information on the trend of material deformation during the test (Fig. 3 a–c) and enabled determining the following

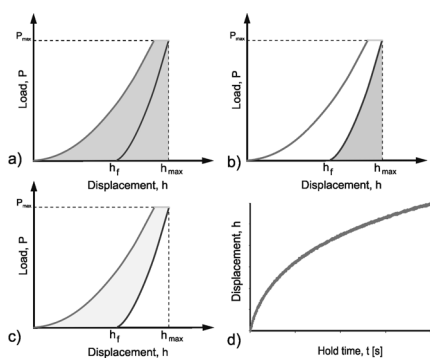


Fig. 3. Analysis of the loading-unloading curve: a) The total work of indentation, b) elastic work of deformation, c) plastic work of deformation, d) creep during the indentation test

parameters: W_{tot} – the total work of indentation (the entire area under the recorded loading curve), W_{sp} – elastic work of deformation (the area under the unloading curve), W_{pl} – plastic work of deformation (the area between the loading and unloading curves).

During the indentation test, UHMWPE specimens were exposed to the maximum load at $t = 15$ s, and, at the same time, an evaluation of susceptibility of the individual material variants to flow, Δh , was made (Fig. 3d).

4. Results and Discussion

The changes in the structure and properties of polyethylene induced by radiation modification have a significant impact on the behaviour of the material un-

der load during service.

When analysing the specimens that were not subjected to radiation modification (input polymer BZ), it has been found that compressive stresses and the resultant UHMWPE work hardening induced a reduction of hardness, H , and elastic modulus, E , proportional to plastic deformation, e_f (Fig. 4e–f). An increasing degree of work hardening also results in higher susceptibility of the material to creep, as well as to plastic, W_{pl} , and elastic deformation, W_{sp} (Fig. 4a–d). The electron beam irradiation results in increased hardness and elastic modulus of the polyethylene variants tested (Fig. 4e–f), which depends on the dose applied ($2 \times$, $4 \times$). Moreover, susceptibility to creep becomes reduced as well, which is manifested through decreased increment of the depth of penetration under load, Δh (Fig. 4d). An increased irradiation dose provokes a decreased value of the work of indentation, W_{tot} , and its components, W_{sp} and W_{pl} , (Fig. 4a–c) and an increase of the energy necessary to create a permanent indentation of unit volume, thereby indicating reduced susceptibility of the polymer to deformation during exposure to service load.

In view of the fact that examinations of the polymer morphology are pending, the attempt to explain the observed trends in changes of the micromechanical properties was based on an analysis of the degree of crystallinity (Fig. 5). A convergence was found between the changes of the degree of crystallinity and the trend of changes of the micromechanical properties (H , E).

Irradiation of the material with an electron beam results in an increased degree of crystallinity, which depends on the dose applied. In both, the initial material and the electron-irradiated material, the degree of crystallinity decreases as the plastic deformation grows, which means

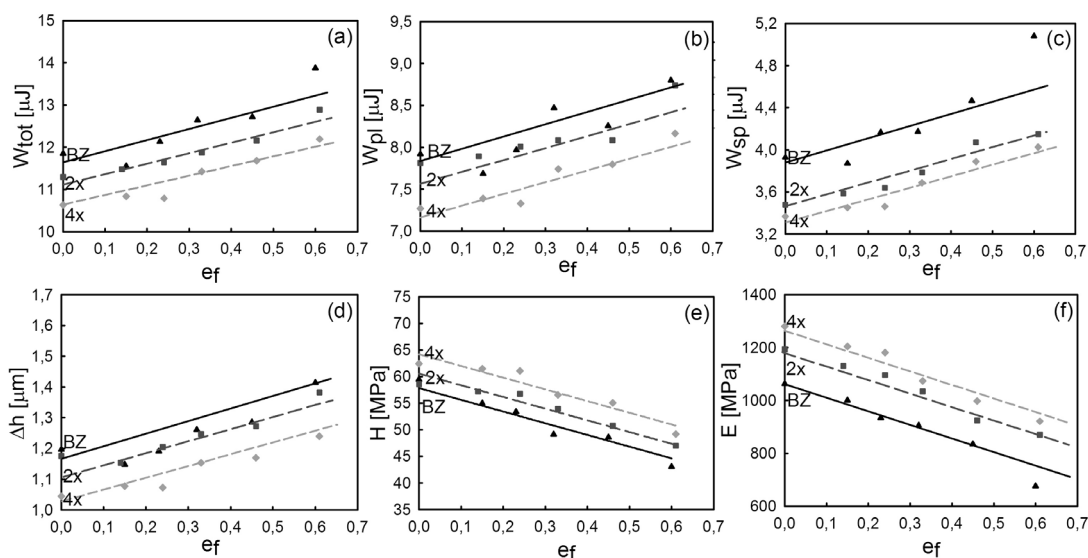


Fig. 4. Micromechanical characteristics of the samples GUR 1050

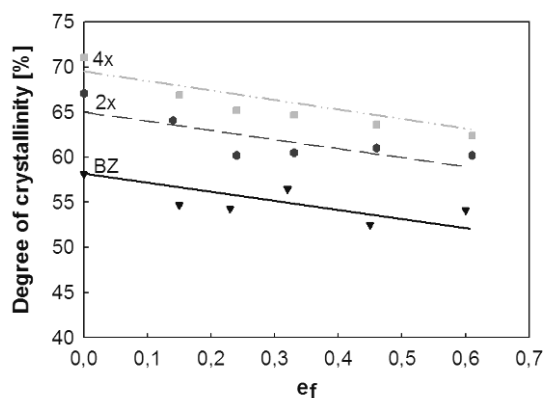


Fig. 5. A change of the degree of crystallinity of the specimens

that modification through radiation does not prevent the particular variants from a decrease in the degree of crystallinity in the whole range of deformation.

5. Conclusions

It is shown in the paper that an evaluation of micro-mechanical properties by means of microindentation is a significant link in the evaluation of the effectiveness of factors shaping the structure and properties of polyethylene, including, in particular, microregions in the upper layer, and of the influence of operational factors on their change. It is extremely important for reasons regarding the application of this polymer. An insignificant change of its local micromechanical properties may result in increased wear and occurrence of undesirable wear products (such as submicron particles) which, in consequence, lead to osteolysis⁷. The method applied responds very sensitively to both the irradiation conditions (total radiation dose) and the deformation degree of the specimen. It has been shown that cross-linking of polyethylene as a result of electron irradiation of the input polymer GUR 1050 ensures: a reduction of creep, decreased susceptibility to absorbing the deformation work, enhanced resistance to permanent deforma-

tion and increased hardness and elastic modulus in the whole range of work-hardening. The determined local micromechanical characterization of polyethylene will, in the subsequent research phase, be supplemented with morphological and macro tests carried out on tribological testers.

REFERENCES

1. Kurtz S., in book: *The UHMWPE Handbook: Ultra-High Molecular Weight Polyethylene in Total Joint Replacement*. Elsevier Academic Press, San Diego 2004.
2. Maszybrocka J., in PhD thesis: *Micromechanical properties and effects of operation in friction couple of polyethylene formed by means of initial deformation and irradiation with electrons.*, University of Silesia, Katowice 2005.
3. Maszybrocka J., Cybo J., Frąckowiak J.: *Mater. Sci. Forum* 513, 75 (2006).
4. Maszybrocka J., Cybo J., Cwajna J.: *Mater. Characterization* 60, 1139 (2009).
5. Barylski A., Cybo J., Maszybrocka J.: *Czasopismo Techniczne* 3, n3 (2009).
6. Oliver W. C., Pharr G. M.: *J. Mater. Res.* 7, 1546 (1992)
7. Zhu Y. H., Chiu K. Y., Tang W. M.: *J. Orthopaedic Surgery* 9, 91 (2001).

J. Maszybrocka, J. Cybo, and A. Barylski
(University of Silesia, Faculty of Computer Science and Materials Science, Poland): **Changes of Micromechanical Properties of Ultra High Molecular Weight Polyethylene after Electron Beam Irradiation and Uniaxial Compression**

The microindentation method was applied in the study to determine a complex micromechanical characterization of microregions of the UHMWPE polymer applied for endoprosthesis cups. It has been shown that the methodology applied responds very sensitively to both the irradiation conditions (total radiation dose) and the deformation degree of the specimen, constituting thereby a significant link in the evaluation of the effectiveness of factors shaping the structure and properties of polyethylene and, in particular of microregions of the upper layer.

EVALUATION OF AU THIN FILM ON POLYETHYLENE AND GLASS

**ROSTISLAV MEDLÍN^{a*}, OLGA
BLÁHOVÁ^a, and VÁCLAV ŠVORČÍK^b**

^aNew Technologies – Research Centre, University of West Bohemia, Univerzitní 8, 306 14 Plzeň, Czech Republic,

^bDepartment of Solid State Engineering, Institute of Chemical Technology, 166 28 Prague, Czech Republic
medlin@ntc.zcu.cz

Keywords: polyethylene, glass, plasma treatment, Au sputtering, mechanical properties, surface morphology

1. Introduction

Metal-polymer composites are suitable for many applications, especially in microelectronics¹. Mutual interaction between metal and polymers is generally very weak but it can be increased if the polymer surface is modified before metal deposition. Several techniques of modification (physical, chemical or their combination) have been suggested for enhancing the metal adhesion^{2,3}.

Gold nanoparticles, due to their unique electrical, optical and photophysical properties, are expected to provide a variety of potential applications for electronics^{4–7}. Well known properties such as stability, non-reactivity and bioinertness of gold are used with advantage in medical diagnostics⁸, Raman spectroscopy⁹, biological imaging¹⁰ and biosensors¹¹. Gold nanoparticles are promising structures for biomedical applications, structures combining gold nanoparticles with polymers^{12–14}.

Since gold is the most inert metal, the adhesion between gold particles and polymers is expected to be very poor. However, gold can easily react with thiol (–SH) groups, which can be fixed on the polymer surface modified in a proper manner. The polymer surface can efficiently be modified by irradiation with plasma, ultraviolet light from an excimer lamp or by ion irradiation^{15–18}.

Polyethylene (PE) and glass were treated in Ar plasma discharge and then grafted from methanol solution of 1,2-ethanedithiol to enhance the adhesion of gold nanoparticles or sputtered gold layers. The modified PE samples were either immersed into freshly prepared colloid solution of Au nanoparticles or covered with 50 nm thin sputtered gold nanolayer.

In this work, the surface of the substrate was modified by plasma discharge and subsequently grafted with 1,2-ethanedithiol to introduce thiol (–SH) groups. Short dithiol is expected to be fixed via one of –SH groups to radicals created by the preceding plasma treatment. Next, the free –

SH groups are allowed to interact either with gold nanoparticles or with gold atoms from the sputtered Au nanolayer.

The main goal of this study is to examine the effect of the plasma treatment and dithiol grafting on the binding of gold nano-particles and on the adhesion of sputtered gold layer on the substrate.

The surface morphology was studied by AFM. The nanoindentation equipment was used to determine micro-hardness and elasticity modulus and to perform nano-scratch tests. SEM was used for documentation of scratches.

2. Experimental Materials

The gold layers were sputtered on 2 × 2 cm microscopic glass (1 mm thick). Surface roughness of glass of $R_a = 0.34$ nm was measured in an area of 1.5 mm². The sputtering was accomplished with Balzers SCD 050 device from a gold target (99.99% purity, supplied by Goodfellow Ltd.). Oriented, high-density polyethylene (PE, $\rho = 0.952$ g cm⁻³) in the form of 40 μ m thin foils (supplied by Granitol Ltd., Czech Republic) was used in the next experiments. The samples were modified in diode plasma discharge with Balzers SCD 050 device for the time of 240 s. DC Ar plasma was obtained under the following conditions: Ar gas purity of 99.997 %, discharge power of 8.6 W.

Four glass samples were modified by plasma for 100 and 400 s, respectively. Two plasma-modified samples were then grafted for 12 h from methanol solution of 1,2-ethanedithiol. In the next experiment both pristine, plasma modified and dithiol grafted glass samples were coated with 50 nm thin sputtered Au layer (see Fig. 1). The sputtering was performed with the same Balzers SCD 050 device.

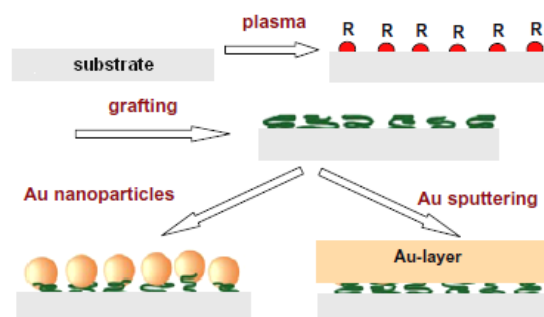


Fig. 1. Scheme of polymer modification with plasma discharge (R-radical), grafting by dithiol and by either coating with Au nanoparticles or by sputtering of Au nanolayer¹⁹

3. Experimental Techniques

The thickness of the metal layer for chosen sputtering times was examined using atomic force microscopy (AFM). The AFM images were taken under ambient conditions on a Digital Instruments CP II device. A large area scanner was used, allowing an area up to $100 \mu\text{m}^2$ to be imaged (see Fig. 2).

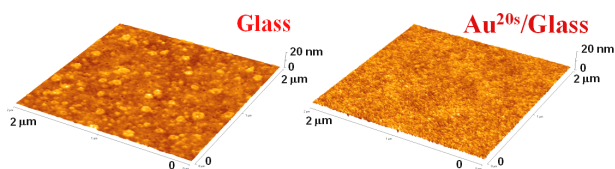


Fig. 2. AFM image of the glass (Glass) and glass 20 s sputtered with Au ($\text{Au}^{20\text{s}}/\text{Glass}$)

Nanoindentation and nanoscratches were carried out by Nano Indenter XP with CSM module (Fig. 3). This additional device allows recording of the contact stiffness during the whole process of indentation. The principle of this measurement is oscillation along the primary load direction with the frequency from 0.05 to 200 Hz and amplitude from 60 to 300 mN. The instrument analyses the dynamic response of the tested material and according to the response, the device can estimate material parameters like hardness and modulus of elasticity.

The contact depth h_c was determined as follows:

$$h_c = h - \varepsilon \frac{P_{\max}}{S} \quad (1)$$

where h is the total indenter displacement corresponding to the load P_{\max} , ε is a correction factor for the non-circular shapes of the indenter (for Berkovich indenter $\varepsilon = 0.75$), and S is the contact stiffness. The reduced elastic modulus E_r was determined from the dependence:

$$E_r = \frac{\sqrt{\pi} \cdot S}{2 \cdot \beta \cdot \sqrt{A_p(h_c)}} \quad (2)$$

where S is contact stiffness, A_p is contact area, taking account of permanent deformation, β is correction constant for the indenter shape (for Berkovich indenter $\beta \approx 1.034$). The reduced modulus E_r is used to account for the fact that elastic displacements occur in both the indenter and the sample. The elastic modulus of the test material E is calculated from E_r using:

$$\frac{1}{E_r} = \frac{1 - \nu^2}{E} + \frac{1 - \nu_i^2}{E_i} \quad (3)$$

where E , ν is elastic modulus and Poisson's ratio for the investigated material, E_i , ν_i is elastic modulus and Pois-

son's ratio for the material of the indenter (for diamond $E = 1141 \text{ GPa}$, $\nu = 0.07$).

The hardness was determined as a ratio of the maximum load P_{\max} imposed on the indenter and the projection contact area A_p with a function of the indenter shape at the contact depth (h_c):

$$H = \frac{P_{\max}}{A_p(h_c)} \quad (4)$$



Fig. 3. Nanoindenter XP and SEM Quanta 200

4. Results and discussion

Figs. 4 and 5 show the measured curves representing the dependency of indentation hardness and modulus of elasticity on the indentation depth. For grafted polymer (modified in plasma 100 and 400 s – ST1 and ST4), it is apparent that both hardness and modulus of elasticity have slightly increased. Changes in SP1 and SP4 (glass treated 100 and 400 s) were negligible when compared with the S specimen (pristine glass with Au layer).

Created scratches were documented using SEM Quanta 200. In the process of creation of this scratch the tip was gradually loaded from 0 to 20 mN. Fig. 6 shows tracks of the indenter in the 50 nm thick Au film deposited on pristine PE (A – PE/Au), plasma treated PE (B – PE/plasma/Au) and plasma treated and dithiol grafted PE (C – PE/plasma/SH/Au). Measurement showed that grafting of the plasma activated PE surface with dithiol significantly increases the adhesion of sputtered Au nanolayer on modified polymer (see¹⁹).

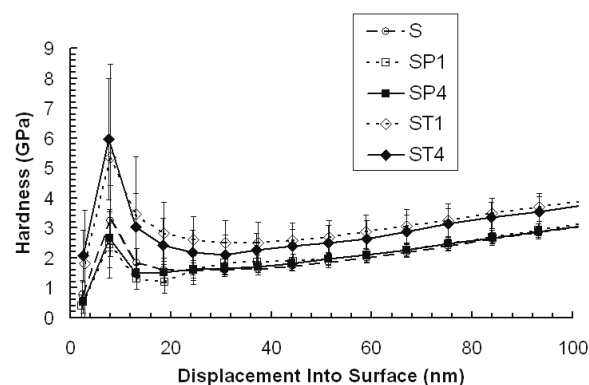


Fig. 4. Dependence of indentation hardness on the indentation depth

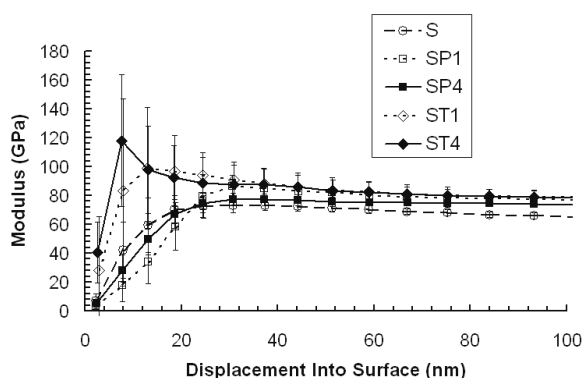


Fig. 5. Dependence of indentation modulus hardness on the indentation depth

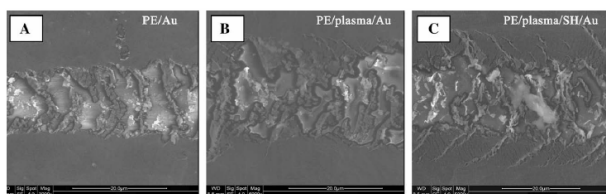


Fig. 6. SEM images of the scratch path on the Au layer on (A) pristine PE, (B) plasma treated PE and (C) plasma treated and dithiol grafted PE¹⁹

The scratches were measured for evaluation in the place where the indenter reached the substrate.

Fig. 7 shows scratches in ST1 and ST4 specimens. Fig. 8 shows the initial part of scratch of the Au film. Initial sections of scratches have been documented in order to determine the critical load: photographs were used for measurement of the distance, at which the indenter penetrated the film and reached the substrate (see Fig. 9).

All scratches have been documented by means of SEM and the locations where substrate was revealed have been identified. Known loading rate and travel speed of the specimen were used to determine the critical load L_c , needed for the indenter to penetrate the film and reach the substrate.

The values of the critical load L_c for penetration of the Au layer and reaching substrate are in Table I.

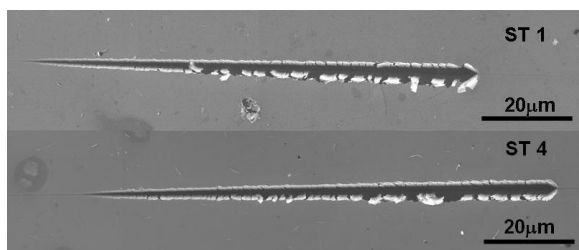


Fig. 7. SEM image of the scratch – composed of multiple snapshots

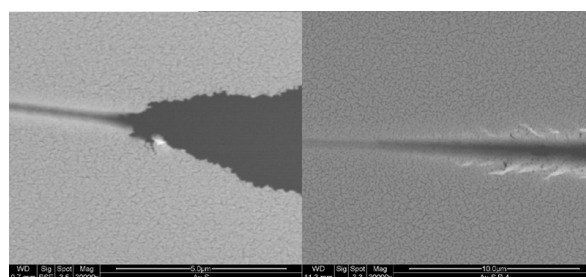


Fig. 8. SEM image of the initial part of scratch path on glass (S-left) and plasma treated glass (SP4-right)

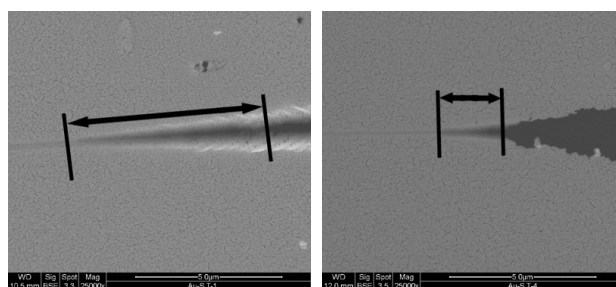


Fig. 9. Measure of critical loads from SEM images on ST1 (left) and ST4 (right)

Table I
Critical load for measured samples

Sample	S	ST1	ST4	SP1	SP4
L_c [mN]	0.11	0.68	0.44	0.12	0.44

5. Conclusions

Specimens with the Au film on glass were tested by nanoindentation, which yielded the values of indentation hardness and indentation modulus of elasticity. In addition, a nanoscratch test has been carried out.

Results show that the critical loads for Au layers were very small, but depended on substrate preparation. For glass modified only 100 s (ST1), L_c is higher than for glass treated 400 s (ST4 and SP4).

Furthermore, it was found that the sole plasma treatment does not affect local mechanical properties, in contrast to specimens, which underwent the grafting process and exhibited a slight increase in hardness and modulus of elasticity. Nanoscratch measurement showed that the grafting of plasma activated glass surface with dithiol increases significantly the adhesion of sputtered Au nanolayer to glass.

The work has been supported by the GACR under projects 106/09/0125 and 108/10/1106.

REFERENCES

1. Li Z., Friedrich A., Taubert A.: *J. Mater. Chem.* 18, 1008 (2008).
2. Švorčík V., Kotál V., Slepíčka P., Bláhová O., Šutta P.: *Polym. Eng. Sci.* 46, 1326 (2006).
3. Kotál V., Švorčík V., Slepíčka P., Bláhová O., Šutta P., Hnatowicz V.: *Plasma Proc. Polym.* 4, 69 (2007).
4. Haruta M.: *Gold Bull* 37, 27 (2004).
5. Tahara M., Cuong N. K., Nakashima Y.: *Surf. Coat. Tech.* 174, 826 (2003).
6. Daniel M. C., Astruc D.: *Chem. Rev.* 104, 293 (2004).
7. Goia D. V.: *J. Mater. Chem.* 14, 451 (2004).
8. Cheng M. M. C., Cuda G., Bunimovich Y. L., Heath J. R., Mirkin C. A., Nijdam A. J., Terracciano R., Thundat T., Ferrari M.: *Curr. Opin. Chem. Biol.* 10, 11 (2006).
9. Hering K., Cialla D., Ackermann K., Dorfer T., Moller R., Mattheis R., Fritzsche W., Rosch P., Popp J.: *Anal. Bioanal. Chem.* 390, 113 (2008).
10. Hainfeld J. F., Slatkin D. N., Smilowitz H. M.: *Phys. Med. Biol.* 49, 309 (2004).
11. Sinha A. K., Seelan S., Tsubota S., Haruta M.: *Top. Catal.* 29, 95 (2004).
12. Taubert A., Wiesner U. M., Muellen K.: *J. Mater. Chem.* 13, 1090 (2003).
13. Tseng R. J., Huang J. X., Ouyang J.: *Nano Lett.* 5, 1077 (2005).
14. Ishida T., Kuroda K., Minagawa W., Haruta M.: *J. Colloid Interf. Sci.* 323, 105 (2008).
15. Bačáková L., Walachová K., Švorčík V., Hnatowicz V.: *J. Biomat. Sci. Polym.* 12, 817 (2001).
16. Heitz J., Švorčík V., Bačáková L., Ročková K., Ratajová E., Gumpenberger T., Bauerle D., Dvořánková B., Kahr H., Graz I., Romanin C.: *J. Biomed. Mater. Res.* 67A, 130 (2003).
17. Slepíčka P., Kolská Z., Náhlík J., Hnatowicz V., Švorčík V.: *Surf. Interf. Anal.* 41, 741 (2009).
18. Siegel J., Slepíčka P., Heitz J., Kolská Z., Sajdl P., Švorčík V.: *Appl. Surf. Sci.* 256, 2205 (2010).
19. Švorčík V., Chaloupka A., Záruba K., Král V., Bláhová O., Macková A., Hnatowicz V.: *Nucl. Instr. Meth. B* 267, 248 (2009).

R. Medlín^a, O. Bláhová^a, V. Švorčík^b (^a*New Technologies – Research Centre, University of West Bohemia, Plzeň*, ^b*Department of Solid State Engineering, Institute of Chemical Technology, 166 28 Prague, Czech Republic*):
Evaluation of Au Thin Film on Polyethylene and Glass

Polyethylene and glass were treated in Ar plasma discharge and then grafted from methanol solution of 1,2-ethanedithiol to enhance the adhesion of gold nanoparticles or sputtered gold layers. Properties of the plasma modified, dithiol grafted and gold coated glass were studied using nanoindentation and SEM. Nanoindentation was used to determine microhardness and elasticity modulus and to perform scratch tests. Nanoscratch measurement showed that the grafting of plasma activated glass surface with dithiol increases significantly the adhesion of sputtered Au nanolayer to glass.

THE HARDNESS ANALYSIS OF THE IF STEEL SHEET AFTER A PLASTIC DEFORMATION

MÁRIA MIHALIKOVÁ*, **LUBOMÍR AMBRIŠKO**, and **LADISLAV PEŠEK**

*Department of Materials Science, Faculty of Metallurgy, Technical University of Košice, Letná 9, 042 00 Košice, Slovak Republic
maria.mihalikova@tuke.sk*

Keywords: plastic deformation, automotive steel sheet, hardness

1. Introduction

Automotive steels can be classified in several different ways. One is by a metallurgical designation. Common designations include low-strength steels (interstitial-free and mild steels); conventional HSS (carbon-manganese, bake hardenable, high-strength interstitial-free, high-strength, low-alloy steels); and the newer types of AHSS (dual phase, transformation-induced plasticity, complex phase, and martensitic steels). Additional higher strength steels for the automotive market include ferritic-bainitic, twinning-induced plasticity, nano, hot-formed, and post-forming heat-treated steels^{1,2}. Another classification method important to part designers is strength of the steel. One such system defines High-Strength Steels (HSS) with yield point R_y from 210 to 550 MPa and tensile strength R_m in the range 270–700 MPa, while Ultra-High-Strength Steels (UHSS) steels have yield strength higher than 550 MPa and tensile strength higher than 700 MPa. These arbitrary ranges suggest discontinuous changes, when moving from one category to another. The steel characteristics drafted as was mentioned enable, that the automobile designer can realize their imaginings to reduce of a construct weight and to increase crew safety personnel on a craft accident^{1–3}.

Behavior of IF steel has been observed in this contribution. Steels were loaded by static tension by the loading rate 1.3 mm min^{-1} . Videotensometry method has been used for scanning of the distribution of deformation just before fracture. Several experimental techniques exist for non contact deformation measuring.

Experimental equipment consists of CCD (Charge Coupled Device) camera and computer, which serves for the process of the camera signal by corresponding software. Suitable contrast marks (dots) are dashed on the scanned surface of the specimen and after the specimen is illuminated during the measurement by diffuse light in such manner to obtain the best contrast between the specimen surface and dashed dots. PC program records co-

ordinates of the gravity centre of individual dots during test and also enables to save a picture sequences synchronously^{4,5}.

2. Experimental material and methods

Specimens from IF (interstitial free) cold rolled steel sheets with thickness of 1.8 mm were used for tensile tests. Mechanical properties are specified in Tab. I and chemical compositions in Tab. II. Specimens were taken transversal to the rolling direction.

Microstructure of steels (Fig. 1) was observed by light microscope OLYMPUS.

Table I
Mechanical properties

Steel	Mechanical properties		
	$R_{p0.2}$ [MPa]	R_m [MPa]	A_5 [%]
IF	185	300	45

Table II
Chemical compositions

Steel	C	S	Mn	Al	Nb	V	Ti
IF	0.001	0.010	0.082	0.055	0.001	0.002	0.040

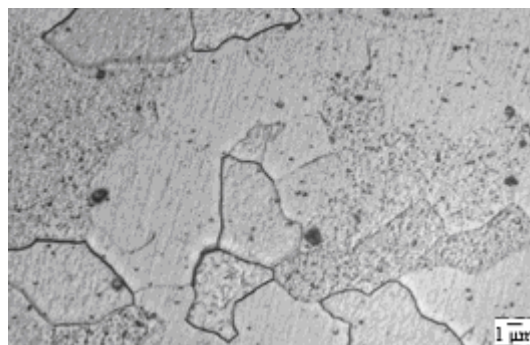


Fig. 1. Microstructure of the IF steel

Due to absence of interstices the IF steels have low yield point and high ductility. These steels are immune towards ageing process and they are suitable for large shapes complicated car body pressworks. IF steel is used mainly for extremely deep drawing. High plasticity is available by reducing of carbon contents less than

$C < 0.005\%$ and by micro-alloyed process with Ti, Nb, or combination Ti + Nb, which completely bind interstices elements C, N on a stable precipitates (Fig. 1).

Tensile test was performed on a plane specimens. The width of specimen was reduced from both sides approx. 1 mm in the centre on a length of 20 mm. The reduction caused that fracture will occur just in this area. Record of the test was made by CCD camera with a resolution of 640×480 pixels. A scanning area of specimen was covered with a grid of 9×22 dots with 1.0 mm step. Surface of specimen was scanned during whole tensile test by CCD camera and longitudinal deformations ε_y (parallel with the direction of loading) and transverse deformations ε_x (perpendicular to the loading direction) were evaluated after the test^{6–8}.

The localization of deformation begins after reaching the maximum load. This phenomenon is allied with large deformation changes in the area of a slip band. Deformations were calculated using formula (1):

$$\varepsilon_y = \frac{dv}{dy} \quad (1)$$

where ε_y – deformation in longitudinal direction, v – displacement in direction Y (Y = direction of loading).

Deformation was evaluated by non-contact extensometry – videoextensometry. Deformation ε_y was measured between two dots. After the tensile tests the hardness HV 1 were measured in column 2 and column 6 (Fig. 2). Principle of UCI technique for hardness measuring is in Fig. 3. Relation between HV 1 and ε_y of steel IF is in Fig. 4. The relation between the hardness HV 1 and deformation is (2) ref.⁹:

$$HV1 = HV1_p + a\varepsilon^b \quad (2)$$

where $HV1_p$ is the hardness of material before deformation; ε is tensile longitudinal deformation; a , b are coeffi-

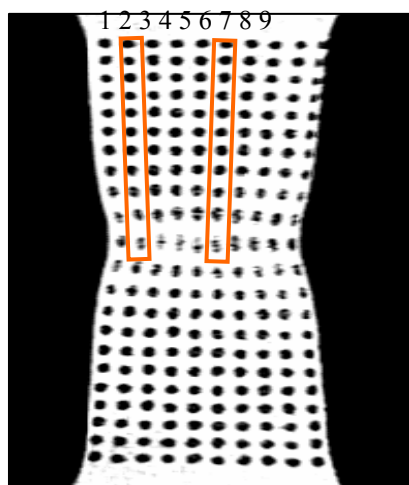


Fig. 2. Position of dots

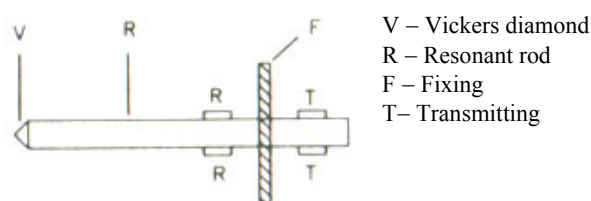


Fig. 3. Principle of UCI

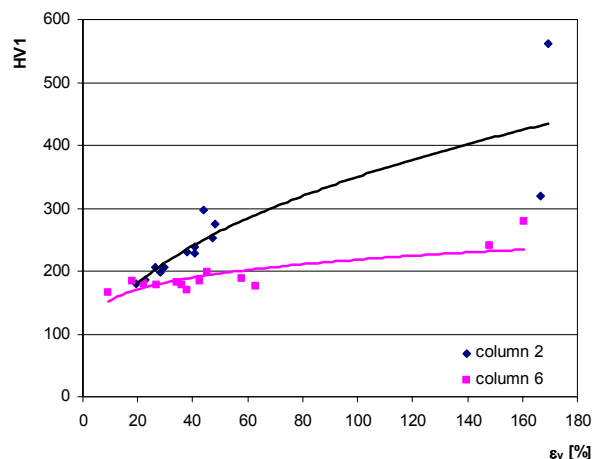


Fig. 4. Relation between HV1 and ε_y of IF steel

icients depending on the properties of the steels. The values of coefficients a are in order of 10^1 – 10^2 . The values of coefficient b are in order of 10^{-1} for all investigated steels. For steel IF the $HV1_p = 110$.

3. Conclusions

Using the videoextensometry and UCI technique enables to characterize the relation between the plastic deformation ε_y and hardness. The power relation between the hardness HV 1 and longitudinal deformation was applied. UCI is practical, portable experimental technique, appropriate to satisfactory determination of state of materials.

Measured values HV 1 are higher in column 2 near the edge of specimen. The stress conditions at the specimen edge and around the notch affect the hardening effect.

This study was supported by the Grant Agency of Slovak Republic; grant project VEGA No. 1/4149/07 and APVV No. 0326-07.

REFERENCES

1. Lowe K.: Mater. World 2, 557 (1994).
2. Lis J., Lis A., Kolan K.: J. Mater. Process. Technol. 162, 350 (2005).
3. Bidulská J., Kvačkaj T., Bidulský R., Grande M.: Kovové materiály 46, 339 (2008).
4. Ohlsson C.: *International Workshop on Video – Controlled Materials Testing and In – situ Micro structural Characterization*, Nancy France, 89 (1999).
5. Pešek L.: *Lokální mechanické vlastnosti 2006*, (O. Bláhová, L. Pešek, ed.), p. 116. Plzeň – Nečtiny 2006.
6. Mihaliková M., Janek J.: Metalurgija 46, 107 (2007).
7. Sinn G., Reiterer A., Stanzl-Tschegg S. E., Tschegg E. K.: *Holz als Roh- und Werkstoff* 59, pp. 177–182. Springer-Verlag 2001.
8. Mihaliková M., Gazdag Š.: Metalurgija 47, 135 (2008).
9. Zubko P., Ambriško L., Pešek L.: *YUCOMAT 2009: Eleventh annual conference: Herceg Novi, Montenegro, August 31 – September 4, 2009*. Belgrade: Serbian Academy of Science & Arts, 2009. in print.

M. Mihaliková, L. Ambriško, and L. Pešek
(*Department of material science, Faculty of metallurgy, Technical university of Košice, Slovakia*): **The Hardness Analysis of The IF Steel Sheet after a Plastic Deformation**

The paper deals with examination of relation between the hardness and deformation ε_y . UCI hardness method was used for hardness measurements. Deformation was evaluated by non-contact extensometry – videoextensometry. The results present existence of the power relation between hardness and plastic deformation: $HV = HV_p + k\varepsilon^a$.

EVALUATION OF CARBON CONTENT IN AUSTENITE BY INDIRECT METHOD

MÁRIA MOLNÁROVÁ^a, TIBOR KVAČKAJ^{b*}, RÓBERT KOČIŠKO^b, and LENKA NĚMETHOVÁ^b

^a Institute of Materials Research, Slovak Academy of Sciences, 043 53 Košice, Slovakia, ^b epartment of Metals Forming, Faculty of Metallurgy, Technical University of Košice, 042 00 Košice, Slovakia
tibor.kvackaj@tuke.sk

Keywords: intercritical annealing, structure, microhardness, carbon content

1. Introduction

In the present time, marked demands for either a reduction of costs or a sensible increase in properties. The increase of properties can be obtained only through new innovation and/or new adapted solutions^{1–3}.

Indirect method is based on fixation of austenite from experimental conditions by quick quenching to martensite. Authors^{4,5} created a scheme of evolution of secondary phases during continuous cooling, see Fig. 1. Three types of hard phases created from austenite exist. Type 1 – hard boundary martensite, Type 2 – soft interior bainite, Type 3 – hard isolated martensite.

The interior austenite areas produce two types of secondary hard phases (Type 2 and 3) depending upon the

austenite grain size. If concentration of soluted carbon is high enough the stability of untransformed austenite increases and can result in formation of residual austenite.

The phase transformation from austenite must provide ferrite formation and saturation of austenite solid solution by carbon without possibility of pearlite and cementite formation. The pearlite formation can be suppressed by rapid cooling rate (cooling rate can not cross pearlite nose or cross pearlite zone in short time) and elements addition like Cr or Mn suppressing austenite transformation to pearlite at temperatures of 600–700 °C. The carbides formation and cementite precipitation formation are suppressed by adding Si, Al and P (ref.^{6–8}). More ferrite content after intercritical annealing, means more retained austenite supersaturated by carbon diffused from bainitic ferrite after austempering. It can be described as a process in which the part of the austenite transforms to bainite, whereas retained austenite may become stabilized by carbon from bainitic ferrite but not transform to martensite during the final quenching to room temperature⁹.

This paper is aimed to evaluation of the carbon content in austenite by so called indirect method using microhardness measurement by Vickers method.

2. Experimental material and methods

Steel based on C-Mn-Si was investigated for the evolution of carbon content in austenite by indirect method based on microhardness measurement of martensite after scheme in Fig. 2, consisting of the controlled rolling and

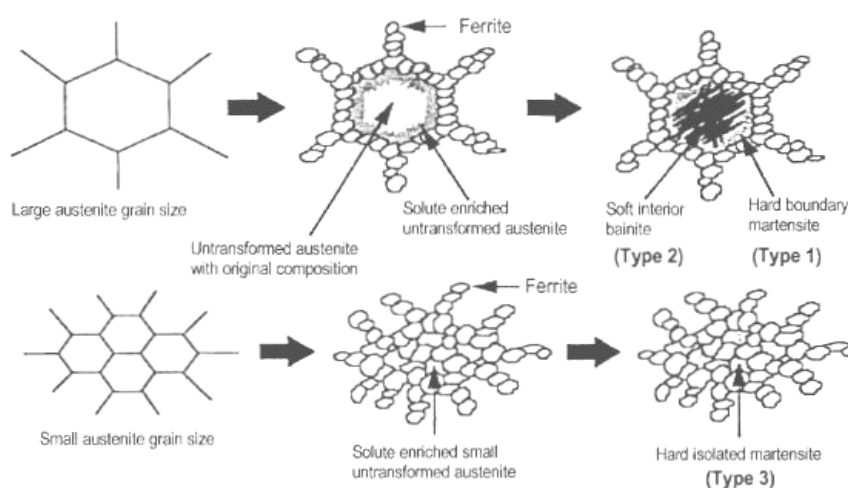


Fig. 1. Classification of hard second phase structures during continuous cooling^{4,5}

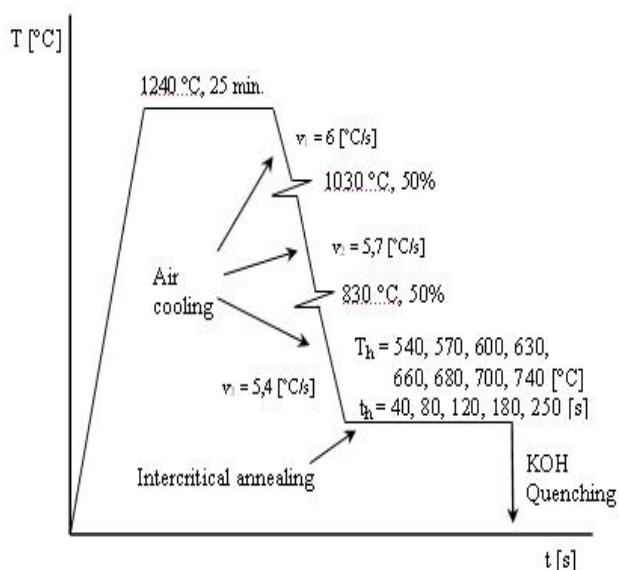


Fig. 2. Scheme for laboratory rolling and controlled cooling

controlled cooling process, included two step deformation (each 50 %). Intercritical annealing was held in temperature interval from 540 °C to 740 °C, with holding times from 40 to 250 s. Local chemical composition of the steel is in Tab. I.

Indirect method is based on fixation of austenite from experimental conditions by quick quenching to martensite. Carbon content was evaluated through the microhardness measurement (HV 0,05) by Vickers method. The data measured were converted into HV hardness values and carbon content in martensite was determined according to the equations published by^{10,11}.

Microhardness was evaluated from about 30 indentations on each from selected samples and average values were used for equations (1–3) (ref.^{10,11}):

$$\text{HV} = 0,75 \text{ HV}0,05 \quad (1)$$

$$\text{HV} = 812 \text{ C} + 293 \quad (2)$$

$$\text{HV} = 930 \text{ C} + 283 \quad (3)$$

where C [wt.%] is the carbon content in martensite and/or in austenite.

3. Results and discussion

The experimental results of carbon content in satu-

Table II
Measured and calculated experimental data

Sample	Intercritical annealing	X_F [%]	HV 0,05	HV	C_{Mart} [wt.%]
1	670 °C / 120 s	24	724	543	0,28
2	620 °C / 120 s	39	810	608	0,35
3	700 °C / 180 s	32	763	572	0,31
4	700 °C / 240 s	32	749	562	0,30
5	740 °C / 180 s	18	637	478	0,21
6	570 °C / 180 s	62 +1%P	795	596	0,34
7	540 °C / 180 s	51 +30%P	700	525	0,26
8	570 °C / 80 s	49	759	569	0,307
9	740 °C / 40 s	7,5	677	508	0,242
10	660 °C / 40 s	1	687	515	0,249

rated austenite are given in Tab. II. Subsequently the experimental data were treated by linear statistics method and a regression equation was derived:

$$\% C_\gamma = -29,2 / (\%F - 132,3) \quad (4)$$

where F [%] is ferrite fraction in microstructure.

Fig. 3 shows the dependences of carbon content on ferrite fraction in saturated austenite for experimental C-Mn-Si steel (TRIP) and comparison with dual phase (DP) steel according to author¹².

As it can be seen in Fig. 3, the experimental results of carbon content in austenite for C-Mn-Si steel (TRIP) refer to the higher values than for compared DP steel. Equilibrium value is 0,18 % C in austenite. Calculated values for carbon content in saturated solid solution of stabilized austenite were C = 0,21–0,35 % with dependence on ferrite fraction.

The curve course of carbon values is the same for the compared steel types, even though values for TRIP are higher for specific ferrite fractions (X_F [%]). Also, the curve course is not so rapid, as for the DP steel.

The presence of silicon in steel 1,8 % Si combined with laboratory rolling and controlled cooling leads to ferrite and austenite formation and caused the carbon dif-

Table I
Local chemical composition of C-Mn-Si steel [wt.%]

Steel	C	Mn	Si	P	S	Cu	Ni	Cr	Al _{tot}	Nb	Sn
C-Mn-Si	0,18	1,47	1,8	0,015	0,007	0,06	0,04	0,06	0,028	0,005	0,007

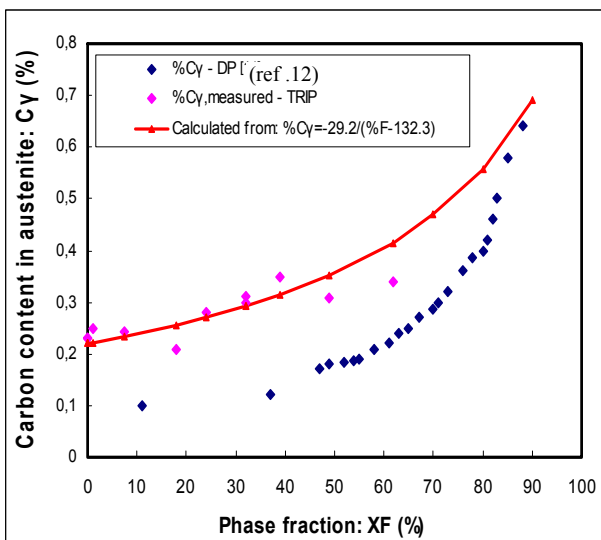


Fig. 3. Dependence of carbon content in austenite on ferrite fraction⁶

fusion from ferrite areas into austenite. Due to this austenite stabilization and saturation by carbon over the equilibrium value occurs.

Mechanical properties were influenced by the final structure, that after intercritical annealing consisted of ferrite, some mixture of bainite / martensite, and in some cases also pearlite. Intercritical annealed samples were quenched into KOH water solution, and mechanical properties were carried out by means of static tensile test. Yield strength $R_{p0.2}$ and tensile strength R_m of air cooled samples reached values from 510 to 898 MPa and from 1052 to 1457 MPa.

4. Conclusions

- The indirect method for evaluation of carbon content in saturated solid solution of stabilized austenite was used based on microhardness measurement of martensite.
- Calculated values of carbon content in austenite were 0,21–0,35 %, whereas the equilibrium value is 0,18 %C.
- Compared with results from author¹² for DP steels, carbon content for investigated TRIP steel refer to higher values for specific ferrite fractions.

This work was supported by the Scientific Grant Agency of Slovak republic as a grant project VEGA No. 2 / 7195 / 27.

REFERENCES

1. Pernis R., Bidulská J.: *Manufact. Eng.* 7, 17 (2008).
2. Bidulská J., Pokorný I.: *Manufact. Eng.* 7, 39 (2008).
3. Bidulský R., Actis Grande M.: *High Temp. Mater. Process.* 27, 249 (2008).
4. Kvačkaj T., Molnarova M., Misicko R., Fujda M.: *14th International Scientific Conference on Plasticity of Materials, Podbanské, Slovakia*, 181 (2007).
5. Park S.H., Choo W.Y., in: *Hot workability of steel and light alloy composites*, p. 493. Montreal, Canada, 1996.
6. Kvačkaj T., Molnárova M., Mišičko R., Kočiško R., Bidulská J.: *15th International Conference on the Strength of Materials, Dresden, Germany*, 136 (2009).
7. Black W.: *International Conference on TRIP aided high strength ferrous alloy, Gent, Belgium*, 13 (2002).
8. Elsner A.: *Advanced hot rolling strategies for IF and TRIP steels*, Delft University Press, The Netherlands, 2005.
9. Jiang H., Wu H., Tang D., Qiang L.: *J. of Univ. of Sci. and Techn. Beijing* 15, 574 (2008).
10. Terasaki T., Akiyama S., Serino M.: *International Conference JOM-2*, 381 (1984).
11. Bernasovký P. et al.: *Náuka o materiáli a zvariteľnosť ocelí*. Weldtech, Bratislava 1996.
12. Waterschoot T., De Cooman B. C., Vanderschueren D., Staelens B.: *Thermomechanical processing of steels*, p. 407. IOM Communications, London 2000.

M. Molnárová^a, T. Kvačkaj^b, R. Kočiško^b, and L. Némethová^b (^aInstitute of materials research, Slovak academy of sciences, Košice, Slovakia, ^bDepartment of Metals Forming, Faculty of Metallurgy, Technical University of Košice, Slovakia): **Evaluation of Carbon Content in Austenite by Indirect Method**

The main aim of this paper was to evaluate the carbon content in austenite by so called indirect method using microhardness measurement by Vickers method. Indirect method is based on fixation of austenite from experimental conditions by quick quenching to martensite. Carbon content in saturated solid solution of stabilized austenite was $C_\gamma = 0,21–0,35$ %, whereas equilibrium value in austenite is 0,18 %. This over-equilibrium carbon value is caused by increased silicon content in steel $Si = 1,8$ %.

EXPERIMENTAL BACKGROUND FOR DIFFUSION MODELS OF Zr1Nb-O SYSTEM

MARTIN NÉGYESI^a, OLGA BLÁHOVÁ^b,
JAROSLAV BURDA^c, and VĚRA
VRTÍLKOVÁ^{d,*}

^a Czech Technical University in Prague, FNSPE, DM Trojanova 13, 120 00 Praha 2, ^b New Technologies Research Centre, University of West Bohemia, Univerzitní 8, 306 14 Plzeň, ^c NRI Řež a.s., Husinec-Řež 130, 250 68 Řež, ^d UJP Praha a.s., Nad Kamínkou 1345, 156 10 Praha – Zbraslav, Czech Republic
vrtilkova@ujp.cz

Keywords: Zr1Nb, oxygen concentration, nanohardness, pseudobinary phase diagram Zr1Nb-O

1. Introduction

The Zr1Nb alloy is used as a material for fabrication of nuclear fuel cladding tubes, which are the first barrier between the nuclear fuel and surroundings in the nuclear reactor. They lose their mechanical properties during operating conditions and especially after the hypothetical LOCA (Loss of Coolant Accident), because of oxidation, the oxygen and hydrogen uptake, a thermal shock and radiation damage. The oxygen and hydrogen uptake have the worst influence on the mechanical properties^{1–3}. It is necessary to ensure that the reactor core integrity and cooling possibility, claddings' thermal shock resistance and the consequential materials handling during transport from the reactor is maintained even after the hypothetical LOCA. Many criteria based on claddings' mechanical properties after the simulated LOCA have been set up so far^{4,5}. It should be noted that those high-temperature tests on unirradiated pre-corroded fuel claddings have the same predictive value as in case of high-temperature tests with long-term in-reactor exposure fuel claddings due to fact that the material damage is annealed during the heating process before the phase transformation α -Zr \rightarrow β -Zr⁶. Nowadays there is an effort to create a universal criterion, applicable to any type of zirconium alloy, a cladding with any wall thickness and any number of fuel cycles (any corrosion thickness and any hydrogen content). That is why it is necessary to know the oxygen distribution (the microstructure) inside the fuel cladding's wall after the thermal transient. There is a picture of the cross section in Fig. 1 with a typical microstructure inside the wall of Zr-alloy fuel cladding after a transient. Upon the transient there is the phase transformation α -Zr \rightarrow β -Zr inside the cladding and at the same time the oxygen stabilized α -Zr(O) layer rises under the oxide layer, because of the oxygen uptake. After

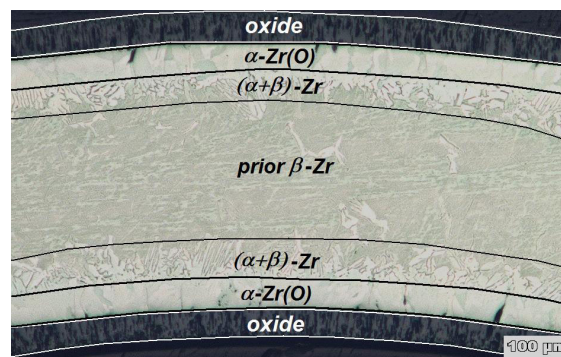


Fig. 1. A typical microstructure inside the wall of Zr1Nb fuel cladding - the 1200 °C/ 9 min sample

the cooling-down the wall microstructure consists of three layers: the oxide layer, the oxygen stabilized α -Zr(O) layer and prior β -Zr layer, which is actually the Zr-alloy α -phase transformed from the high-temperature Zr-alloy β -phase during the cooling⁷. In case of the Zr1Nb alloy there is a mixture of α -Zr(O) and prior β -Zr between the oxygen stabilized α -Zr(O) layer and prior β -Zr layer, because of the β -stabilizing effect of niobium⁸. In this paper the region is marked as $(\alpha+\beta)$ -Zr.

2. Experimental

All specimens used in this study were made from the Zr1Nb alloy (Zr-1.0Nb-0.035Fe-0.135O, all in wt. %). Only as-received specimens were used. 30 mm long tubes (outside diameter 10 mm, wall thickness 686 μ m) were exposed in a steam (0.1 MPa) at high temperatures (900–1200 °C) for variable time intervals in the resistance furnace CLASIC. The specimens' temperature was measured with a thermocouple inside the tube. After the high-temperature steam oxidation the specimens were quenched into water with ice. For nanohardness measurements and X-ray microanalysis polished cross sections were used.

Nanohardness measurements were carried out on a Nano Indenter XP (MTS System Corp. USA) with Berkovich indenter. The force was induced by a 0.8 g weight, so the indentation surface projection was about 0.5–2 μ m² and the indentation depth was < 500 nm.

A wavelength-dispersive spectrometer INCA Wave 700, fully focusing six-crystal spectrometer Johan-Johansson (Oxford Instruments) was used for the oxygen concentration determination. A surface oxide layer was

removed from specimens. Specimens were polished with an OP-S suspension of colloidal silicate (Struers) and aluminized (~ 15 nm). SiO_2 as a standard and LSM80N with the resolution FWHM 17 eV as a crystal were used for oxygen analyses.

3. Results and discussions

Nanohardness measurements were carried out in a few series perpendicular to the oxide/alloy interface leading over the α -Zr(O) layer (showing a linear decrease of measured values) and the region $(\alpha+\beta)$ -Zr (showing an experimental scatter increase and a decrease of the gradient) towards the middle of the cladding's wall – the prior β -Zr region with constant nanohardness values (Fig. 2). A nanohardness increase in the prior β -Zr region corresponds to a α -Zr(O) grain. Distances between each indentation were $5 \mu\text{m}$. The measurement of the oxygen concen-

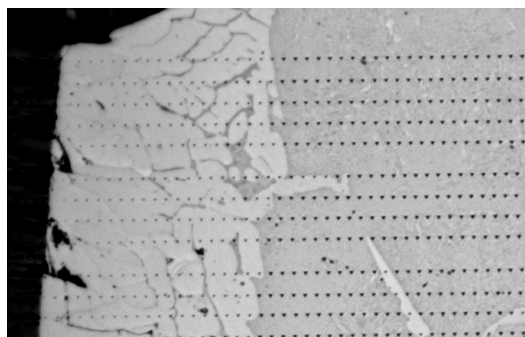
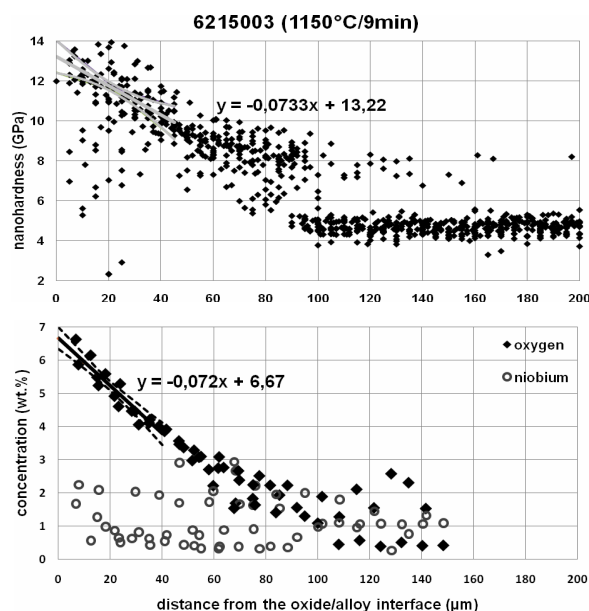


Fig. 2. Nanohardness and oxygen concentration profiles and an image of nanoindentation series - the 1150 °C/ 9 min sample

tration was carried out similarly. In both cases the measured values come from a volume of a few μm^3 . A link between the measured nanohardness and oxygen concentration can be seen in Fig. 2. The nanohardness mainly depends on the oxygen concentration in the alloy. The experimental scatter of nanohardness values is caused mainly by the state of the sample surface.

There are also linear regression lines (a simplification: a linear decrease was supposed) with their equations and 95 % confidence intervals, which defines the area, in which the real regression line lies to 95 %, in Fig. 2. It is difficult to determine the exact values of the nanohardness and oxygen concentration at the $\alpha/\alpha+\beta$ phase boundary, because this boundary is non-uniform in the Zr1Nb alloy. The following rules were used:

- A steep decrease of nanohardness/oxygen concentrations to the values equal to measured prior β -Zr values indicates the two-phase region $(\alpha+\beta)$ -Zr.
- Nanohardness/oxygen concentrations at the $\alpha/\alpha+\beta$ phase boundary must not be lower than values measured in the region $(\alpha+\beta)$ -Zr and prior β -Zr.

In addition, for the determining of oxygen concentrations at the $\alpha/\alpha+\beta$ phase boundary the niobium concentration profiles, which were measured together with the oxygen, could be used. The niobium is β -stabilizer, so there are locations containing more than 1 wt. % (a nominal content) of niobium in front of the α -Zr(O) layer (Fig. 2). These locations can also rise inside the α -Zr(O) layer, because the niobium has low diffusivity in zirconium cell.

The oxygen concentration at the $\alpha/\alpha+\beta$ phase boundary is determined by linear regression methods (come from one specimen only) and the nanohardness at the boundary is a mean value, because of larger amount of experimental results. The nanohardness measurement is less time-consuming compared to WDS, which is great advantage. Nanohardness and oxygen concentrations at the $\alpha/\alpha+\beta$ phase boundary rise with rising exposition temperature (Fig. 3, 4). The whole oxygen concentration profile at the specimen exposed to 950 °C temperature was systematically lower. The nanohardness measurement of the specimens exposed to the 1,050 °C may also have a systematic error (e.g. poorly prepared surface). There are also nanohardness and oxygen concentrations at the $\alpha/\alpha+\beta$ phase boundary in the cladding wall from the Zry-4 alloy (Zr-(1.3–1.5)Sn-0.2Fe-0.1Cr-0.12O, all in wt. %) with various amount of hydrogen, for comparison in Fig. 3 and 4. The results are adopted from earlier work⁹. The hydrogen (β -stabilizer) causes an oxygen concentration and also nanohardness increase at the $\alpha/\alpha+\beta$ phase boundary in the cladding wall from the Zry-4 alloy^{5,9}. It is therefore likely that niobium will have the similar effect. Nanohardness and oxygen concentrations at the $\alpha/\alpha+\beta$ phase boundary in the cladding wall from the Zr1Nb alloy are similar to nanohardness and oxygen concentrations at the $\alpha/\alpha+\beta$ phase boundary in the cladding wall from the Zry-4 alloy with high hydrogen content (> 2000 wppm). Fig. 4 shows the comparison of WDS results with the Zry-4-O pseudobi-

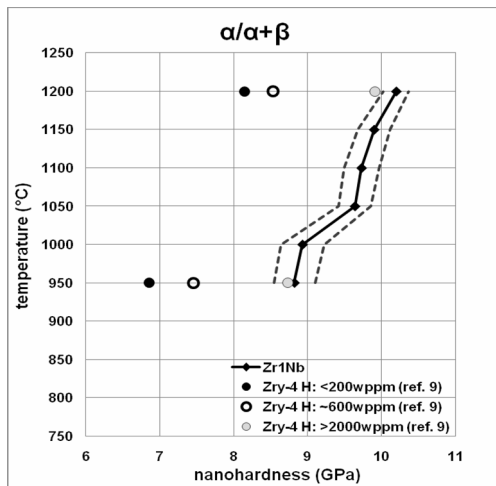


Fig. 3. Nanohardness at the $\alpha/\alpha+\beta$ phase boundary in the cladding's wall from the Zr1Nb and Zry-4 alloys with various hydrogen content

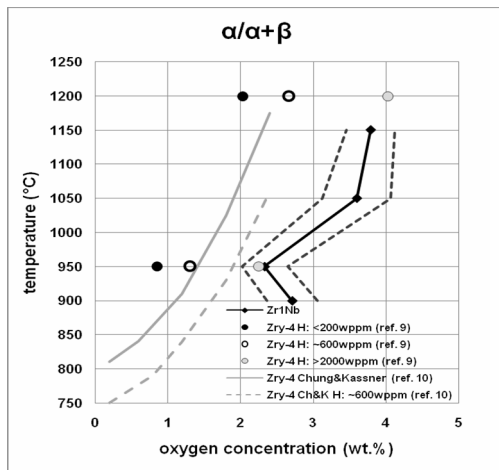


Fig. 4. Oxygen concentrations at the $\alpha/\alpha+\beta$ phase boundary in the cladding's wall from the Zr1Nb and Zry-4 alloys with various hydrogen content

nary phase diagram¹⁰. The present results for the Zry-4 alloy are systematically lower. Dashed curves in both graphs are constructed using the 95 % confidence intervals. They define the region, in which the real boundary line $\alpha/\alpha+\beta$ lies to 95 % (without any consideration of measurement errors).

In an earlier work⁹ a relation between the nanohardness and oxygen concentration at the $\alpha/\alpha+\beta$ phase boundary in the cladding wall from the Zry-4 alloy was determined. The results come from the alloy Zr1Nb confirm this relation (Fig. 5). The relation is extended to the point [6.82:12.5] – the oxygen concentration and nanohardness at the oxide/alloy phase boundary. The nanohardness value (12.5 GPa) is the average value of all measured samples

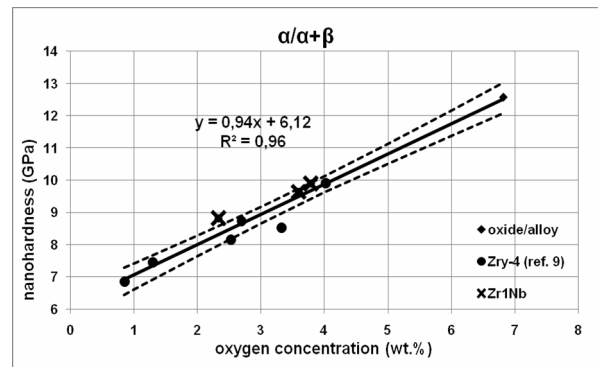


Fig. 5. The relation between the nanohardness and oxygen concentration at the $\alpha/\alpha+\beta$ phase boundary

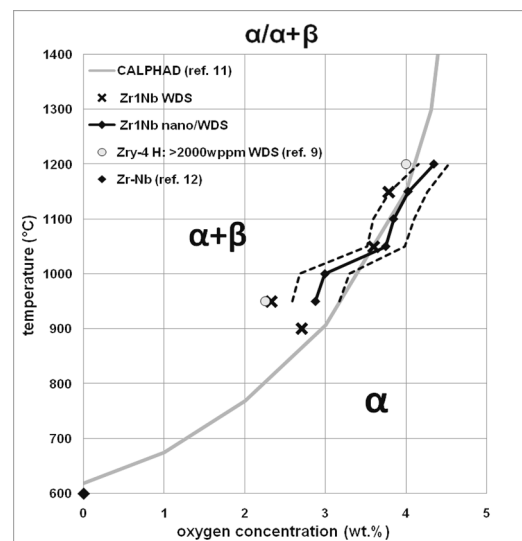


Fig. 6. A part of the Zr1Nb-O pseudobinary phase diagram determined by nanoindentation and WDS methods and computed by the method CALPHAD

and the oxygen concentration (6.82 wt. %) is the average value of oxygen concentrations at the temperatures 950 and 1200 °C come from the Zr-O equilibrium phase diagram. There is also the linear regression line with its equation and 95 % confidence interval in Fig. 5. The relation is equally valid for both alloys.

Using the relation above oxygen concentrations at the $\alpha/\alpha+\beta$ phase boundary can be determined indirectly from nanohardness values. Such determined oxygen concentrations are together with oxygen concentrations determined by WDS are shown in Fig. 6. Dashed curves define the region, in which the real boundary line $\alpha/\alpha+\beta$ lies to 95 % (without any consideration of measurement errors). Assuming local equilibrium conditions at the phase boundaries in the exposed cladding, the oxygen concentrations at the phase boundaries can be considered equilibrium. So

the oxygen concentrations measured at the $\alpha/\alpha+\beta$ phase boundary can be used to construct a part of the Zr1Nb-O pseudobinary phase diagram. There are also oxygen concentrations at the $\alpha/\alpha+\beta$ phase boundary in the cladding wall from the Zry-4 alloy with high hydrogen content ($> 2,000$ wppm) for a comparison in Fig. 6. Very good agreement with the calculation CALPHAD¹¹ has been obtained. The point corresponding to the zero oxygen concentration comes from the Zr-Nb equilibrium phase diagram¹².

A part of the Zr1Nb-O pseudobinary phase diagram (the interface $\alpha/\alpha+\beta$) has been estimated using exposed fuel claddings by methods WDS and nanohardness measurements. Such way a pseudobinary phase diagram of the Zr-alloy-O system up to a few units wt. % could be constructed. This is unavailable by conventional methods such as dilatometry, calorimetry, etc., because specimens are very brittle.

4. Conclusions

The aim of this work was to determine the nanohardness and oxygen concentration at the $\alpha/\alpha+\beta$ phase boundary in the cladding wall of exposed specimen from the Zr1Nb alloy by nanoindentation and WDS methods and to try to use these results to the construction of the Zr1Nb-O pseudobinary phase diagram. The conclusions:

- Oxygen concentrations and also nanohardness at the $\alpha/\alpha+\beta$ phase boundary in the cladding from the Zr1Nb alloy rise with rising exposition temperature and are similar to oxygen concentrations and nanohardness at the $\alpha/\alpha+\beta$ phase boundary in the cladding from the Zry-4 alloy with hydrogen content $> 2,000$ wppm.
- The relation between the nanohardness and oxygen concentration at the $\alpha/\alpha+\beta$ phase boundary in the phase α -Zr(O) for the temperature range 950–1200 °C has been assessed. The relation is equally valid for both alloys.
- The part of the Zr1Nb-O pseudobinary phase diagram (the interface $\alpha/\alpha+\beta$) has been estimated by WDS methods and nanohardness measurement using exposed fuel claddings.

For more exact determination of the Zr1Nb-O pseudobinary phase diagram it is required to have more experimental results, especially results of time-consuming WDS measurements. Using the relation between the nanohardness and oxygen concentration at the $\alpha/\alpha+\beta$ phase boundary the oxygen concentrations can be determined indirectly from the nanohardness values.

Authors wish to thank Mr. L. Novotný, J. Šustr and A. Příbyl for the samples and metallographic scratch patterns and S. Linhart for English correction. This work was supported by "PROJEKT MPO 2A-1TP1/037".

REFERENCES

1. Billone M., Yan Y., Burtseva T., Daum R.: Research report NUREG/CR-6967. ANL, Argonne 2008.
2. Grandjean C., Hache G.: Research report DPAM/SEMCA 2008-093. IRSN, 2008.
3. Stern A. et al.: J. ASTM Int. 4, 1 (2007).
4. Chung H. M., Kassner T. F.: Research report NUREG/CR-1344 ANL-79-48. ANL, Argonne 1980.
5. Chung H. M.: Nucl. Eng. Tech. 37, 327 (2005).
6. Portier L. et al.: J. ASTM Int. 2, 103 (2005).
7. Brachet J.C. et al.: Research report DEN/DMN/SRMA 91191. CEA, Saclay.
8. Vrtílková V. aj.: Research report UJP 1313. UJP, Praha 2008.
9. Négyesi M.: Research report. ČVUT-FJFI-KMAT, Praha 2008.
10. Chung H. M., Kassner T. F.: J. Nucl. Mat. 84, 327 (1979).
11. Sopoušek J.: Research report. MU PF, Brno 2009.
12. Okamoto H.: J. Phase Equil. 13, 577 (1992).

M. Négyesi^a, O. Bláhová^b, J. Burda^c, V. Vrtílková^d
^aCzech Technical University in Prague, ^bNew Technologies Research Centre, University of West Bohemia, ^cNRI Řež a.s., ^dUJP Praha a.s., Czech Republik: **Experimental Background for Diffusion Models of Zr1Nb-O System**

A pseudobinary phase diagram of the Zr1Nb-O system, acceptable for diffusion models predicting the behavior of Zr1Nb fuel claddings during transients, has not been still published. This work is the contribution for this problem solving. The determined oxygen concentrations at the phase boundaries in the wall of fuel claddings exposed in a steam have been used for the phase diagram assessment. In this study oxygen concentrations at the $\alpha/\alpha+\beta$ phase boundary in the phase α -Zr(O) have been determined base on results of WDS and nanoindentation measurements. The relation between the nanohardness and oxygen concentration at the $\alpha/\alpha+\beta$ phase boundary in the phase α -Zr(O) has been assessed.

NEW GRID INDENTATION METHOD FOR MULTIPHASE MATERIALS

JIRÍ NOHAVÁ^{a*} and PETR HAUŠILD^b

^a CSM Instruments, Rue de la Gare 4, CH-2034 Pesieux, Switzerland, ^b Czech Technical University in Prague, Faculty of Nuclear Sciences and Physical Engineering, Department of Materials, Trojanova 13, 120 00 Praha 2, Czech Republic
jno@csm-instruments.com

Keywords: Nanoindentation; Stainless steel; Martensitic transformation

1. Introduction

Instrumented indentation or shortly nanoindentation is very powerful technique for characterization of materials in small volumes. Despite its undoubted contribution to the measurements of mechanical properties care must be taken during experiments to correctly understand the obtained results while testing certain types of materials.

Among such materials belong non-homogeneous (multiphase) materials whose indentation testing is complicated especially when the dimensions of the phases are unmatched. Even very high positioning precision is not always sufficient in such cases to differentiate between the phases.

The measurement parameters of indentation on non-homogeneous materials shall not affect the results which is important especially in cases where the cracking or the stress/strain induced phase transformations can occur. On the one hand, the indent should be sufficiently small in order to distinguish the tiny phases. On the other hand, the interaction of the indenter tip with surface becomes complex contact problem especially for low indentation depths when rounding of the indenter tip can play an important role. Moreover, growing popularity of using low loads brings up another problem known as indentation size effect, which affects mainly the hardness values^{1–3}. Consequently the hardness can be used only for comparative purposes in this load range.

Compared to standard indentation using Vickers indenter and measurement of the imprint's diagonals, instrumented indentation is based on recording of the force and indentation depth data. The so obtained curve is then used for calculation of hardness. The hardness calculation is not based on optical observation and can therefore be done automatically. Additionally, important material characteristics such elastic modulus and energy of indentation can be calculated from the indentation data record. Finally, as the calculation of hardness and elastic modulus is calcu-

lated by the indentation software, automated series of measurements can be done. This is particularly useful when large statistical datasets are required which is the case in the grid indentation method⁵. This method is based on several hundreds of indentations and their subsequent statistical evaluation. The grid indentation method is used for calculation of local mechanical properties of multiphase materials in which satisfactory results cannot be obtained by other techniques or single indentations. The application of this method on material with different volume fraction of two phases and its results are subject of this paper.

The low-nickel metastable austenitic stainless steel was chosen as it undergoes the deformation-induced phase transformation of face-centered cubic (fcc) γ austenite to body-centered cubic (bcc) α' -martensite and hexagonal closed packed (hcp) ε -martensite⁶. The ε -martensite forms from randomly spaced overlapping stacking faults while the α' -martensite forms at shear band intersections^{7–9}. During straining, the volume fraction of α' -martensite rapidly prevails over the volume fraction of ε -martensite and the α' -martensite grows at the expense of the ε -martensite. High internal stresses are generated due to an incompatible transformation strain accompanying the martensitic transformation. The good knowledge of local properties of austenitic and martensitic phases is therefore an essential constituent for modeling the material behavior of metastable austenitic steels subjected to plastic strain.

2. Experimental details

The material chosen for this paper was experimental steel provided by the ARCELOR-MITTAL. The chemical composition is given in Tab. I and corresponds to the AISI 301 grade. The low nickel and chromium content situates the steel at the limit of the austenite field in the Schaeffler's diagram¹⁰. The material was supplied as cold rolled sheets of 0.68 mm thickness in the bright annealed state.

The measurements were performed on samples in the initial state and on the tensile pre-deformed specimens. Strain level was chosen $\varepsilon = 0.1$ (10 %) and $\varepsilon = 0.2$ (20 %) of logarithmic (true) deformation in order to obtain the microstructure with predominant austenitic phase

Table I
Chemical composition of AISI 301 steel (in wt. %)

	C	Cr	Ni	Si	Mn	Mo
Nominal	max 0.12	16–18	6.5–9	<1.5	<2	<0.8
Analyzed	0.05	17	7	0.5	1.5	0.1

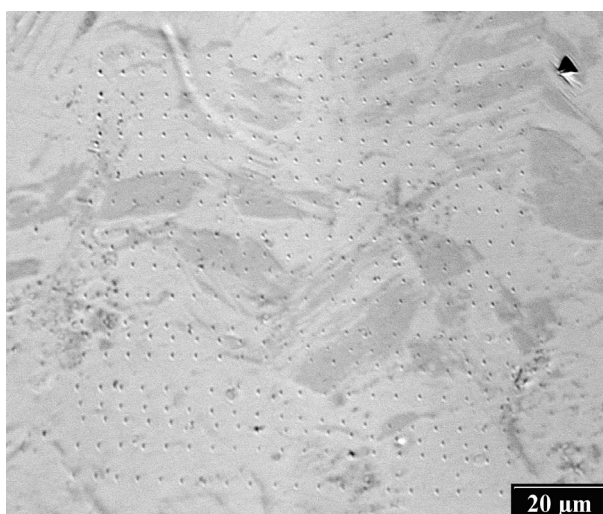


Fig. 1. Indentation grid on 10 % pre-deformed sample: light gray – austenite, dark gray – martensite

($\varepsilon = 10\%$) and α' -martensitic phase ($\varepsilon = 20\%$), in both cases with low fraction of ε -martensite.

Surface of samples was electro-polished in 5 % perchloric acid solution in ethanol at 40 V to avoid the surface layer affected by mechanical grinding and polishing, which can itself produce the deformation induced martensitic transformation.

Nanindentation measurements were performed on CSM Instruments NHT Nano Indentation Tester with Berkovich indenter using instrumented indentation technique. The NHT uses passive top referencing concept which almost entirely eliminates the thermal drift and is therefore ideal for several hours taking grid indentation method. The indentation parameters chosen from preliminary experiments were as follows: maximum load 1 mN, loading rate 6 mN min^{-1} , unloading rate 6 mN min^{-1} , 5 s hold at the maximum load. The grid indentation was performed on predeformed samples with different martensite volume fraction. Several randomly selected rectangular areas in dimensions of $100 \mu\text{m} \times 100 \mu\text{m}$ were tested on each sample. The indentation matrix on each of such areas comprised 20×20 indentations equidistantly spaced by $5 \mu\text{m}$ (Fig. 1).

Electron back scattered diffraction (EBSD) analysis was carried out in scanning electron microscope FEI Quanta 200 FEG equipped with a TSL™ EBSD analyzer. The samples were inspected at a tilt angle of 70° . Acquired data were evaluated by OIM™ software.

3. Results and discussion

Figure 2 shows typical force versus indentation depth record as obtained on stainless steel and fused silica. The areas corresponding to elastic and plastic work of indenta-

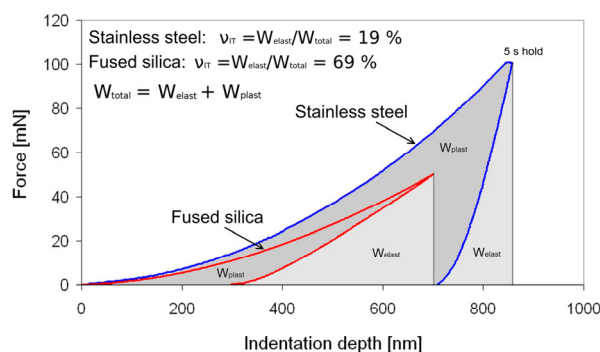


Fig. 2. Typical force versus indentation depth curve

tion are gray shaded. For the samples tested in this study, the maximum indentation depth varied from about 77 nm (in the deformed material) to 90 nm (in the non-deformed material) for maximum load of 1 mN.

The results of grid indentation in form of dataset were treated statistically in order to extract the properties of single phases by fitting the data using appropriate distribution function. The hardness values were selected for the statistical evaluation as the Young's moduli of austenite and martensite are very close. The elastic to total work of indentation ratio v_{IT} was also less correlated with the phase occurrence than hardness and it was therefore not considered for statistical treatment.

The hardness values measured on austenite in non-deformed state matched the Gaussian distribution (see Fig. 3). Bimodal Gaussian distribution function (I) was in the first instance chosen to describe the grid indentation results obtained on pre-deformed (two-phase) samples:

$$f = \frac{1-p}{\sqrt{2\pi}\sigma_1} \exp\left[-\frac{(H_{IT} - \mu_1)^2}{2\sigma_1^2}\right] + \frac{p}{\sqrt{2\pi}\sigma_2} \exp\left[-\frac{(H_{IT} - \mu_2)^2}{2\sigma_2^2}\right] \quad (1)$$

where H_{IT} is the hardness, p is the mixing parameter, and μ_1 , σ_1 , μ_2 , σ_2 are the parameters of distribution.

The parameters of distribution were identified by maximum likelihood method using Generalized Reduced Gradient nonlinear optimization¹¹. The identification is slightly complicated by the fact that the peaks of distribution are overlapping.

It can be seen that with increasing pre-deformation the hardness increases and the distribution changes from right-hand tailed to left-hand tailed as the martensite volume increases (Fig. 3). Further, the deformation of remaining austenite is constrained by the martensite laths and its apparent hardness therefore increases.

In the second step, the area containing the indentation grid was analyzed by EBSD. The martensite volume fraction f_m obtained by EBSD is in fairly good agreement with the mixing parameter p of the fitted bimodal Gaussian

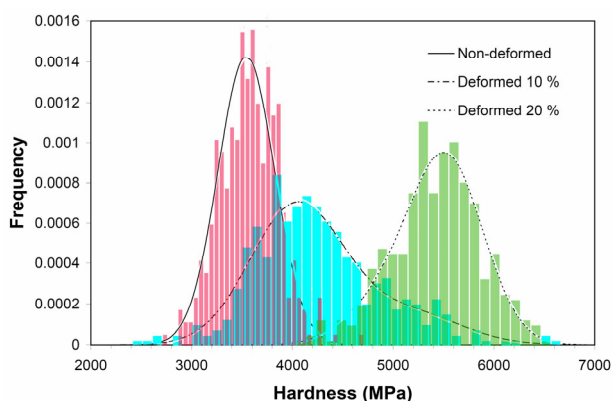


Fig. 3. Comparison of hardness distribution on all three tested samples

distribution function. For both pre-deformation, the predominant phase is slightly overestimated by the fitting parameter of bimodal Gaussian distribution (79 % comparing to 76 % in the case of 10 % predeformation and 81 % comparing to 79 % in the case of 20 % predeformation).

Subsequently the perimeter of $0.5 \mu\text{m}$ was traced around each indent and the measured hardness values were sorted in cases belonging to austenitic (A), austenitic and martensitic (A+B) and martensitic (B) according to occurrence (see Fig. 4 for schematic representation). It should be noted that even if we do not know how far the phases extend under the surface, the indentation depth is fairly low compared to the chosen surrounding area size so one can expect that in the majority of cases this classifying is correct.

The distributions identified separately on austenite and/or martensite indentation cases were compared with the apparent bimodal distribution as obtained by Gaussian fit. The apparent distribution leads to slight over- and un-

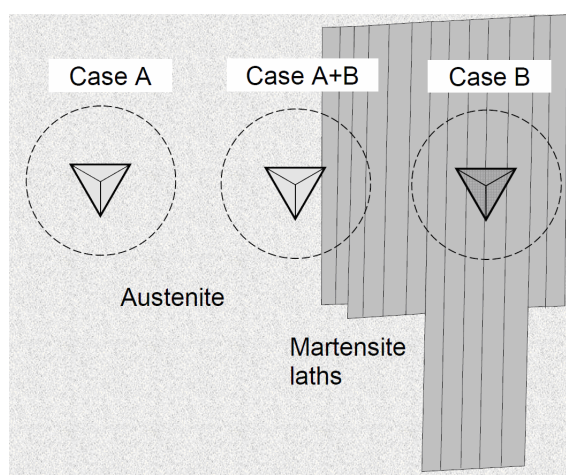


Fig. 4. Three principle cases of indentation: austenitic (A), austenitic and martensitic (A+B) and martensitic (B)

der-estimation of the μ_1 and μ_2 mean hardness values of austenitic and martensitic phases respectively. The scatters of both austenitic and martensitic phases σ_1 , σ_2 are slightly higher for the apparent distribution than for the distributions identified separately.

Nevertheless, the discrepancy between the parameters obtained for the apparent distribution and for the distributions identified separately is relatively low (less than 5 %) so that the parameters obtained by the apparent distribution can be taken as the first approximation of the real behavior.

4. Conclusions

The application of the grid indentation method on austenitic steel with pressure induced transformations is shown in this paper. The results of the experiments confirm that this method can be used for estimation of mechanical properties of materials with two phases even if these are unmatched. The phase volume fractions and the distribution of hardness in each phase at different strain levels were determined by the instrumented indentation and statistical analysis with reasonable accuracy. The EBSD results confirmed the volume fraction of each phase as found by the statistical analysis of the indentation experiments. The grid indentation method can be used on multiphase materials for calculations of single phase properties which are hardly accessible by other measurement techniques. The so obtained results are indispensable for correct modelling of mechanical behaviour of these materials.

This work was carried out in the frame of research project MSM 6840770021. Arcelor-Mittal group is acknowledged for preparing the experimental material.

REFERENCES

- Gane N.: Proc. Royal Society A 317(1530), 367 (1970).
- Kreuzer H.G.M., Pippan R.: Mater. Sci. Eng., A 387–389, 254 (2004).
- Kreuzer H.G.M., Pippan R.: Mater. Sci. Eng., A 400–401, 460 (2005).
- Randall N.X., Vandamme M., Ulm F.-J.: J. Mater. Res. 24, 679 (2009).
- Mangonon Jr. L., Thomas G.: Metall. Trans. 1, 1577 (1970).
- Suzuki T., Kojima H., Suzuki K., Hashimoto T., Ichihara M.: Acta Met. 25, 1151 (1977).
- Brooks J.W., Loretto M.H., Smallman R.E.: Acta Met. 27, 1839 (1979).
- Humbert M., Petit B., Bolle B., Gey N.: Mater. Sci. Eng., A 454–455, 508 (2007).
- Schaeffler A.L.: Metal Progr. 56, 680 (1949).
- Fylstra D., Lasdon L., Warren A., Watson J.: Interfaces 28, 29 (1998).

J. Nohava^a and P. Haušild^b (^a *CSM Instruments, Czech Technical University in Prague, Faculty of Nuclear Sciences and Physical Engineering, Department of Materials*): **New Grid Indentation Method for Multiphase Materials**

Mechanical properties of metastable austenitic steel were investigated using a novel grid indentation method. Under deformation martensitic laths are formed in this steel. As the martensite laths are of submicrometric dimen-

sions, single spot nanoindentation failed and the grid indentation method had to be used. The method was applied on samples with three levels of predeformation. A matrix of 800 indentations was done on each sample. The results were plotted in form of a histogram and statistically evaluated using bimodal Gaussian distribution. The results allowed estimation of the hardness of the martensite laths and the austenite matrix. The volume fraction of martensite was also calculated and it corresponded well to the results obtained by the EBSD.

MECHANICAL PROPERTIES AND STRUCTURE OF Zr-Nb ALLOY AFTER HIGH-TEMPERATURE TRANSFORMATIONS

JAN ŘÍHA*, OLGA BLÁHOVÁ,
and PAVOL ŠUTTA

New Technologies – Research Centre, University of West Bohemia, Univerzitní 8, 306 14, Plzeň, Czech Republic
janriha@ntc.zcu.cz

Keywords: Zirconium alloys, In situ X-ray diffraction analysis, Phase transformations, Indentation hardness

1. Introduction

Zirconium alloys are indispensable part of materials used in nuclear reactors already 50 years. With regard to their excellent corrosion resistance in water at high temperatures and having very low effective cross-section capture of thermal neutrons, zirconium alloys are used as protective layers of nuclear fuel rods¹.

Presently the development is focused on behaviour of Zr-alloys during Loss - Of - Coolant - Accident. In this case integrity and dimension stability of the components are the key parameters. During the rapid heating up to 1000 °C the accelerated oxidation takes place and subsequent fast quenching leads to deterioration of their mechanical properties. Mainly the hardness is growing up whereas the ductility is falling down^{1,2}.

At high temperatures proceeds also the phase transformation of zirconium from α -phase (hexagonal close - packed lattice) to β -phase (body centered cubic lattice). Current temperature of transformation strongly depends on impurity elements presence in zirconium. Niobium causes

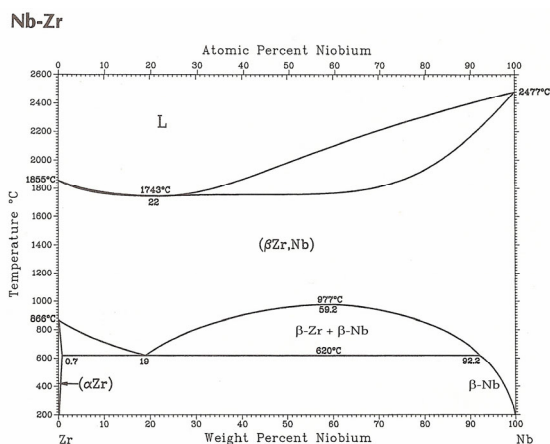


Fig. 1. Binary phase diagram of Zr – Nb system (ref.⁴)

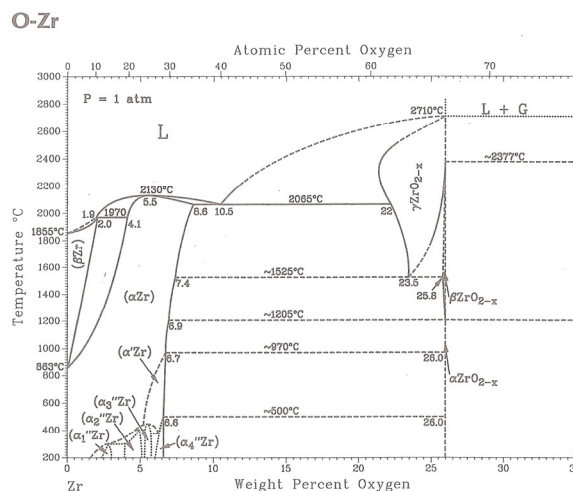


Fig. 2. Binary phase diagram of Zr – O system (ref.⁴)

a movement of transformation to lower temperatures whereas the oxygen to higher temperatures² (Fig. 1, 2).

This paper is focused on an interpretation of phase transformations and mechanical properties changes after high temperature processing.

2. Experiment

For the experiment the E110G Zr alloy was used. Initial semiproducts were in form of weldless tubes with outer diameter 9 mm and 0.7 mm wall thickness. These tubes were cut up into 11 mm wide rings. The rings were halved and mechanically compressed into a plane. Their surface was grinded and polished and then etched by an acid mixture of HNO₃, HCl and HF. The influence of plastic deformation caused by mechanical flattening was removed during the high-temperature exposition. The chemical composition of alloys is presented in Tab. I.

The *in situ* X-ray diffraction phase analysis was carried out on a Panalytical X'Pert Pro automatic powder diffractometer. This machine is equipped with a copper X-ray tube with K α radiation ($\lambda_{K\alpha} = 0.154$ nm) and high-temperature chamber Anton Paar HTK 1200 N. This device enables an equable heating up to 1200 °C and can be

Table I
Chemical composition of experimental material

Nb [wt.%]	H [ppm]	N [ppm]	C [ppm]	O [ppm]
1,0 ÷ 1,1	3	20	100	840

filled by an inert gas or evacuated. In this case a rotary oil pump with liquid nitrogen trap was used. For comparison one sample was measured also under vacuum created by a turbomolecular pump.

For the illustration of crystalline state an automatic powder diffractometer AXS Bruker D8 Discover was used analysing the lateral profile of the (002) line. This diffractometer is equipped with a cobalt X-ray tube ($\lambda_{K\alpha} = 0.179$ nm) and an area detector HI – STAR.

With a view to previous measurements published in³, the samples were exposed to the temperature 1000 °C. The deaeration of the sample surface during the heating was a very serious problem. That is why the temperature had to be increased very slowly for complete deaeration, which markedly influenced the size of crystallites.

For investigated samples, different deaeration temperatures were used. The first one was without deaeration, the temperature for the second one was 100 °C and 250 °C for the third one. Summary of the investigated samples and conditions is in Tab. II. The heating courses of some samples are in Fig. 3 and 4.

Measuring range for *in situ* measurements was from 25° to 75° 2 θ scale. The diffraction patterns were collected in initial state at room temperature, during the deaeration, at the exposition temperature and after the cooling at the

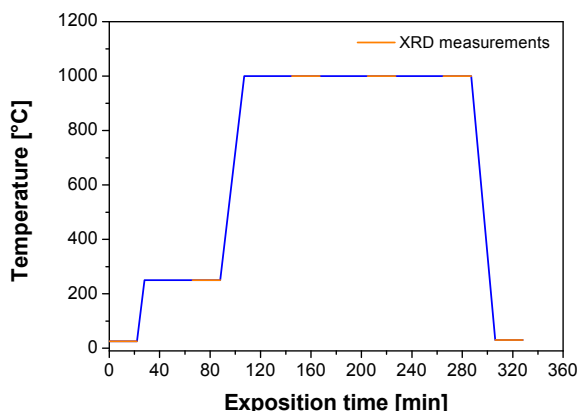


Fig. 3. Heating course for rotary pump

Table II
Experimental samples and conditions

Sample	Vacuum pump	Exposition temperature [°C]	Deaeration temperature [°C]
0201	Rotary	1000	0
0202	Rotary	1000	100
0203	Rotary	1000	250
0207	Turbo-molecular	1000	250

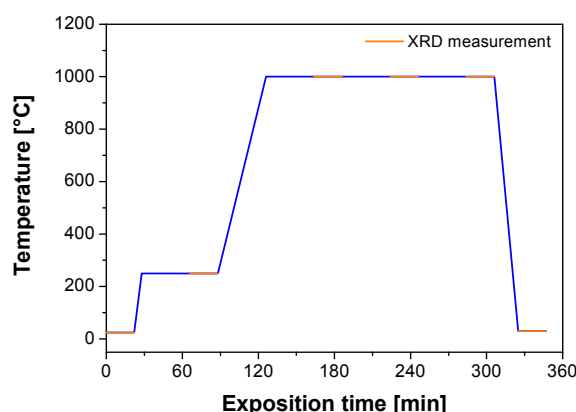


Fig. 4. Heating course for turbomolecular pump

temperature 30 °C. During the high-temperature exposition the samples were measured three times for better examination of the phase transformations. The pressure created by a rotary pump during the measurements was about $6 \cdot 10^{-1}$ Pa.

Measurements performed on AXS Bruker D8 diffractometer were collected in the range $25^\circ \pm 103^\circ$ 2 θ .

The indentation hardness measurements were carried out on a NanoIndenter XP with Berkovich indenter as a value in depth of 2 μm . Sixty-five indents were created on the sample surface and the resulting values of indentation hardness and modulus of elasticity were obtained as mean values.

3. Results and discussion

Results of diffraction phase analysis show that the structure of all samples was in initial state created by α -phase of zirconium and with a trace amount of zirconium hydride ZrH. The ZrH phase was possible to identify according to a single diffraction line (111) with 100 %

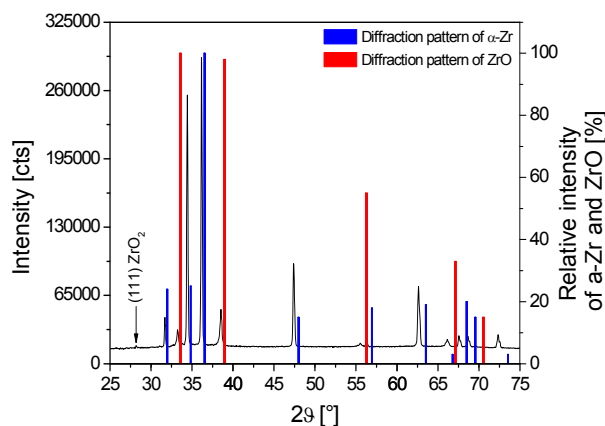


Fig. 5. The first diffraction pattern of sample 0203 at 1000 °C with referential diffraction patterns of α -Zr and ZrO

relative intensity. At high temperatures the ZrH phase disintegrated and the free gaseous hydrogen escaped from the samples. The first diffraction patterns of sample 0201 showed an influence of deaeration step absence, Fig. 6. There is a corrosion layer markedly seen on the surface.

This layer was composed of monoclinic oxide ZrO_2 and non-stoichiometric tetragonal oxide $\text{ZrO}_{1.99}$. A cubic oxide ZrO was also identified in the structure. A decreasing amount of surface oxides is seen in the second diffraction patterns of the same sample as a consequence of its transformation. A surface oxide layer represented only by a trace amount of ZrO_2 is seen in the third diffraction pattern.

The same phase composition was identified in diffraction patterns of samples 0202 and 0203 during the whole high-temperature exposition and also after the cooling, Fig. 7, 8. The measurements carried out at 1000 °C also showed that the transformation of α -Zr to β -Zr did not proceed. In all diffraction patterns only lines of α -phase of zirconium were identified.

This is probably caused by higher free oxygen amount in interstitial places of Zr matrix, which markedly increased the $\alpha \rightarrow \beta$ transformation temperature. The diffraction lines shift observed in all diffraction patterns is caused by thermal dilativity and partially also by crystallographic lattice expansion due to interstitial oxygen, Fig. 5.

Diffraction patterns of sample 0207 measured under vacuum $2 \cdot 10^{-3}$ Pa indicate that even here the phase transformation did not take place. Except of α -phase zirconium the ZrO and a trace amount of ZrO_2 were identified. In diffraction patterns of all samples measured at 1000 °C it is evident a growth in amount of ZrO phase, Fig. 6–8. This indicates that ZrO is not a part of surface corrosion layer but that it is in inner alloy volume.

The results from AXS Bruker D8 show an expressive influence of heating course on size of the crystallites, Fig. 9. All samples in initial state were rather finegrained – their lines are smooth and continuous.

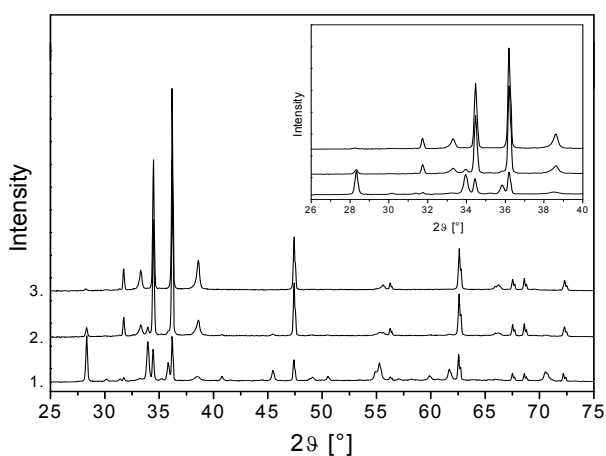


Fig. 6. Diffraction patterns of sample 0201 at 1000 °C

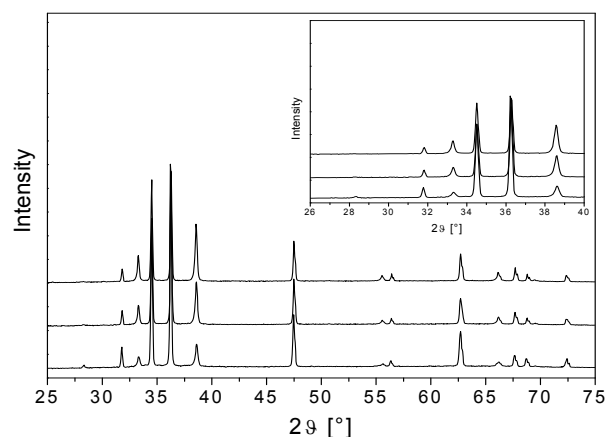


Fig. 7. Diffraction patterns of sample 0202 at 1000 °C

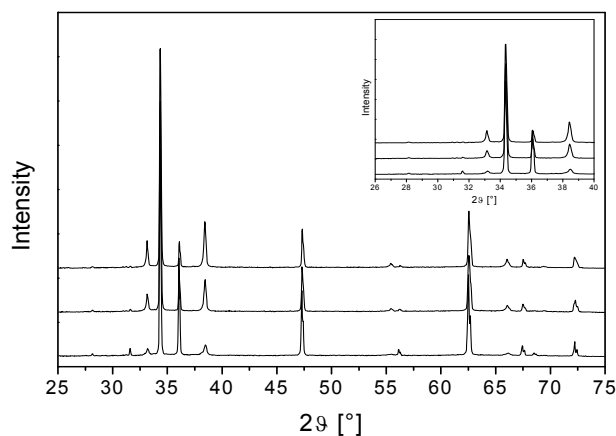


Fig. 8. Diffraction patterns of sample 0207 at 1000 °C

After the exposition the structure of α -Zr phase become considerably coarse. The structure of sample 0201 is homogeneously coarse-grained due to relatively fast heating without the deaeration step.

The α -Zr lines of samples 0202 and 0203 are created by single points with high intensity.

These points represent coherently diffracting large crystallites. The diffraction patterns are similar because there was relatively small difference in delivered energy. The α -Zr structure of the sample 0207 was very coarse-grained because the energy delivered during the heating was much higher than that in case of previous samples. The smooth continuous lines in all diffraction patterns belong to ZrO phase.

The amount of ZrO phase was growing with an energy delivered during the exposition, which directly influenced the course of indentation hardness and modulus of elasticity, Fig. 10. During the high-temperature heating at first the corrosion layer is growing up. After that this layer is disintegrated and the free oxygen diffused to inner volume of material where the ZrO phase is created, Fig. 6.

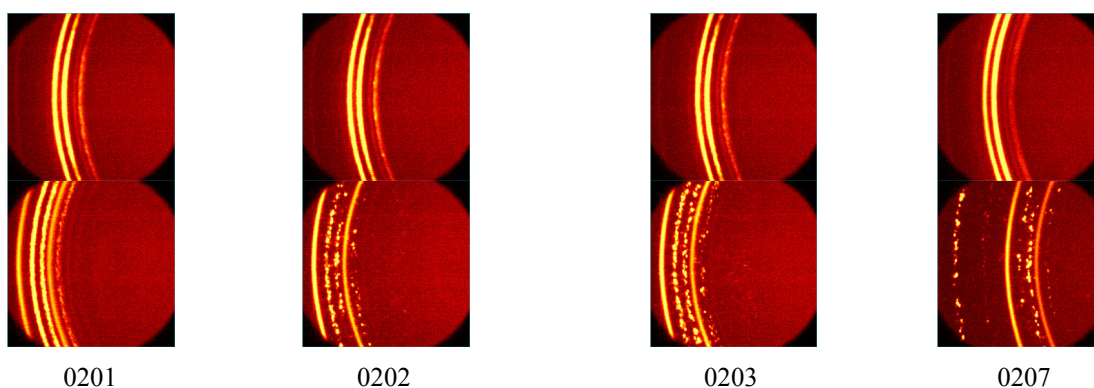


Fig. 9. Partial diffraction patterns measured by Bruker D8, upper pictures - initial state, bottom pictures – state after the exposition

Fig. 11 shows a dependence of indentation hardness on displacement into the surface. Apparently the hardness values of all samples in depth 2 μm are practically stable. That is why these values were taken as conclusive.

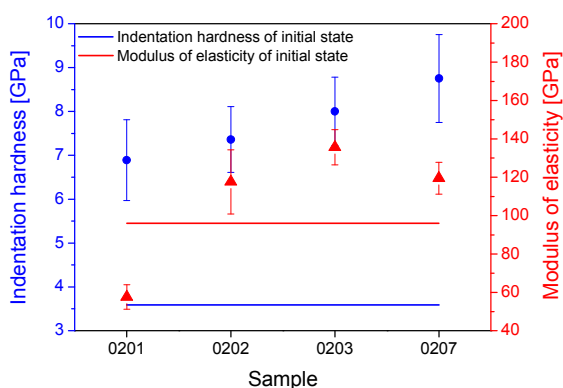


Fig. 10. Course of Indentation hardness and Modulus of elasticity

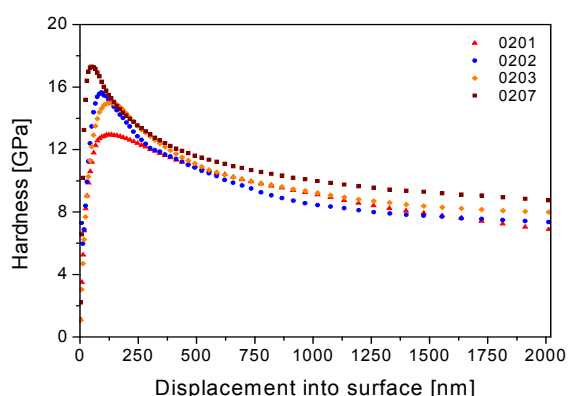


Fig. 11. Course of measured values of indentation hardness in dependence on displacement into surface

4. Conclusions

The results of XRD analysis and indentation hardness measurements presented that oxygen is probably the most important element influencing properties of Zr alloys. The XRD analysis demonstrated that corrosion layer formed during the heating, subsequently desintegrated and the free oxygen caused creation of ZrO phase. The amount of this phase grew with an exposition time at high temperature and caused the alloy hardness increasing. XRD analysis also indicated that vacuum value had only insignificant influence on properties of this type of alloy.

The work is supported by the MPO CR project 2A – ITP1/037.

REFERENCES

1. Koutský J., Kočík J.: *Radiation damage of structural materials*. Academia, Praha 1994.
2. Pétigny N., Barberis P., Lemaignan C., Valot Ch., Lallemand M.: *J. Nuclear Mater.* 280, 318 (2000).
3. Říha J., Bláhová O., Šutta P.: *Chem. Listy*, v tisku.
4. Baker H. (ed.): *ASM Handbook*, vol. 3, Alloy Phase Diagrams, ASM International, Materials Park, Ohio 1992.

J. Říha, O. Bláhová, and P. Šutta (*New Technologies – Research Centre, University of West Bohemia, Plzeň, Czech Republic*): **Mechanical Properties and Structure of Zr-Nb Alloy after High-Temperature Transformations**

The paper deals with study of phase transformations of Zr-Nb alloy and its influence on mechanical properties. For the experiment *in-situ* XRD analysis and indentation hardness measurements were used. The XRD measurements proceeded in evacuated high-temperature chamber with different heating process for each sample.

NANOINDENTATION AS A NEW TOOL FOR EVALUATION OF HEN'S EGGSHELL LOCAL MECHANICAL PROPERTIES

**LIBOR SEVERA^{a*}, JAROSLAV
BUCHAR^a, JIŘÍ NĚMEČEK^b,
and ŠÁRKA NEDOMOVÁ^a**

^a Mendel University of Agriculture and Forestry in Brno, Faculty of Agronomy, Zemědělská 1, 613 00 Brno, Czech Republic, ^b Czech Technical University in Prague, Faculty of Civil Engineering, Thákurova 7, 166 29 Praha 6, Czech Republic
severa@mendelu.cz

Keywords: eggshell, micro-mechanical properties, nanoindentation, elastic constants

1. Introduction

Elastic properties belong to the key engineering properties of an eggshell material. Their knowledge enables us to evaluate material stiffness that is further related also to the eggshell strength which is an important parameter of the eggs' quality¹⁻⁴. There are many techniques for the evaluation of main elastic properties, namely the Young's modulus E . Generally, they include static loading (mainly quasi-static compression)⁵⁻⁷ and different kinds of dynamic loading^{5,8-10}. The evaluation of the elastic properties is mainly based on the assumption of the homogeneous and isotropic behavior of the eggshell. The eggshell is a bioceramic material constructed of columnar calcite crystals preferentially oriented with their c-axis perpendicular to the shell surface. The detail analysis revealed the microstructure varies through the thickness of the eggshell, so that the elastic properties must be expected to differ from the in-plane directions. However there is a little evidence to expect directional variations in properties in the plane of the eggshell. In order to examine these changes new techniques are needed. Nanoindentation seems to be a very promising procedure. The method is based on the direct measurement of the load-displacement relationship using a very small tip pressed into the material surface. The depth of penetration starts from the nanometer scale. Nanoindentation was originally developed and used mainly for studying of homogenous materials such as metals, coatings, glass and crystal materials. Successive evolution of the method led to testing of less conventional materials, some of which are of biological nature.

The objective of the present study was to investigate the potential utilization of nanoindentation as a tool for determination of eggshell's micro-mechanical properties

and to compare the experimental results with results obtained from conventional tests.

Finally it must be mentioned that, as it results from findings documented in literature, mechanical properties of hen's eggshell are strongly affected by many factors such as diet¹²⁻¹⁴, breeding conditions^{15,16}, hen breed^{17,18}, egg shape^{6,19,20} and other parameters under both static and dynamic loading. Thus single variable evaluation must be considered carefully and with respect to the previous facts.

2. Materials and Methods

2.1. Eggshells

Eggs (*Hisex Brown* strain) were collected from a commercial breeding farm in the Czech Republic. Hens were kept in cage technology. Eggs were collected when the hens were 75 weeks old. Double-yolked eggs, rough shelled eggs and abnormally shaped eggs were not included in the experiment.

2.2. Preparation of specimens

The eggshell chips from equatorial position on the egg were embedded into metacrylate tablet. The specimens were cold-prepared (the structure was not thermally affected). Commercially available two-component resin was used for metacrylate mixture preparation and the specimens were left to dry and cure for 8 hours. The tablets were polished in order to achieve flat surface with maximum roughness of 10-20 nm.

2.3. Experimental set-up and loading conditions

Nanohardness tester CSM was used to perform the experiments. Standard Berkovich tip was brought to the sample surface producing a series of imprints. Load versus depth of penetration was measured through the whole procedure of loading, holding, and unloading (see Fig. 2 for an example). Loading and holding parts of the diagram contain elastic, plastic and viscous deformations, whereas the unloading part is usually supposed to be elastic. Elastic constants were extracted from this unloading part using semi-analytical elastic solutions¹¹.

The eggshell chips (from equatorial position of the egg) were loaded in both radial (i.e. perpendicular to the surface) and tangential (i.e. parallel with the surface) directions. The set-up is shown in Fig. 1. Standardly used trapezoidal loading diagram with linear loading, unloading and intermediate holding period was performed.

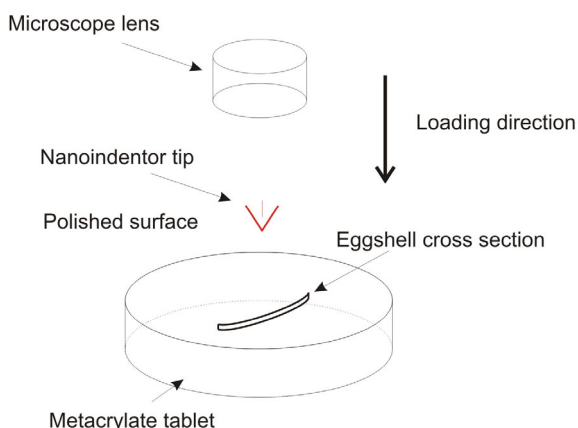


Fig. 1. Experimental set-up and loading in tangential direction

3. Results and discussion

Series of experiments containing around 25 measuring points on several cross sectional locations in two loading directions (radial and tangential) described above has been performed. For illustration, the overall view (200 \times magnification) on the eggshell cross section is shown in Fig. 3. The beads or little circles in the picture represent undissolved particles of metacrylate. The detailed view of an individual imprint of the indenter tip is depicted in Fig. 4.

An example of a typical loading diagram is shown in Fig. 2. Loading parameters with the main results are summarized in Tab. I.

Evaluation of the Young's modulus¹¹ includes the choice of Poisson's ratio ν . The value $\nu=0.345$ has been adopted from measurement described in Nedomová et al.⁶, where the similar eggshells were used (the research was conducted in parallel with this one and the same eggs were used). Other authors report similar values of ν , e.g. 0.307

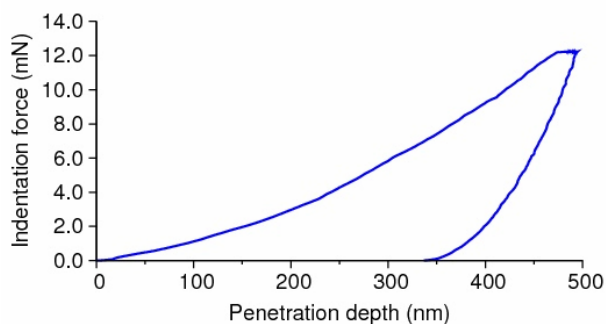


Fig. 2. Typical nanoindentation loading diagram (load vs. depth of penetration)

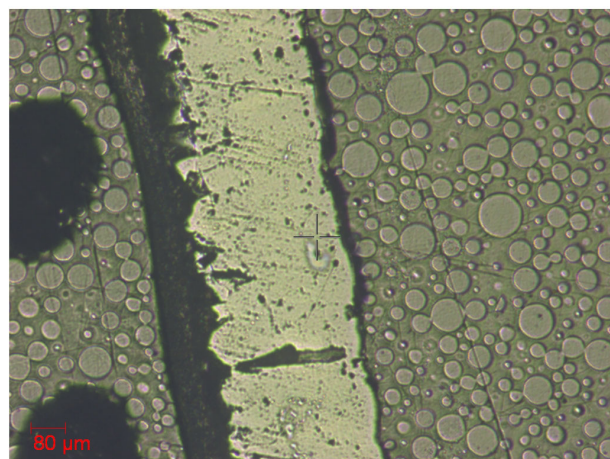


Fig. 3. Overall view on the eggshell cross section

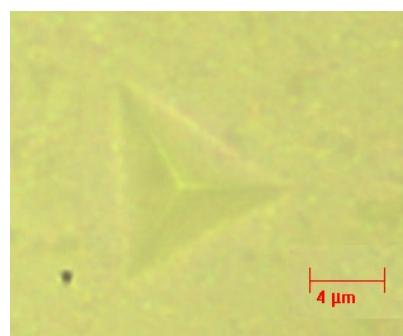


Fig. 4. Individual indenter imprint as seen in optical microscope (4000 \times magnification)

Table I
Experimental parameters and results

Peak load	10–12 mN
Loading rate	20 mN min ⁻¹
Unloading rate	20 mN min ⁻¹
Holding period	10.0 s
Young's modulus – radial loading	41 \pm 3.9 GPa
Young's modulus – tangential loading	43 \pm 4.1 GPa

(ref.²¹) or 0.300 (ref.⁸) but in these cases different eggs (hen strain, age etc.) were used.

The values of E obtained from radial and tangential directions did not vary significantly (41 \pm 3.9 GPa and 43 \pm 4.1 GPa, respectively). This scatter indicates isotropic nature of the eggshell structure. Due to small number of tests, this conclusion has to be confirmed by further and more detailed experiments, but it already shows on the general trend.

The E values did not significantly vary when testing different locations over the cross section which again shows on homogenous nature of the tested material. The possible edges, membrane, inhomogeneities and pores were avoided in the measurements. As can be seen in Fig. 4, the surface structure appears to be fairly homogenous, which supports the micromechanical measurements.

Young's moduli obtained from nanoindentation are in general agreement with values reported by Nedomová et al.⁶. Nedomová et al. found that elastic constants are independent on the egg shape as well as loading force orientation (egg loaded either on equator strip and/or egg-tip). The conclusions were supported also by numerical simulations.

4. Conclusions

The results obtained from nanoindentation in both radial and tangential directions of the eggshell equator revealed homogeneous nature of the material. Based on the limited number of experiments, it is assumed that local variation in the stiffness is not direction dependent and the tested material appears to be more or less isotropic.

It follows from macroscopic measurements that mechanical properties show certain degree of variability when measured at different locations on the same egg¹. Therefore, the use of nanoindentation for creating of a more detailed „map“ of eggshell's micromechanical properties from various locations seems to be a promising and probably one of very few applicable approaches. The research in this area is planned as a future goal.

Presented results approved that nanoindentation, as a novel testing method used for determining of eggshell micromechanical properties, offers a precise tool for describing material characteristics on eggshell micro-scale and thus offers precise and valuable data for mapping of material parameters, modeling, numerical simulations and procedures used for upgrading of the current state of knowledge at this particular field.

The research has been supported by the Grant Agency of the Czech Academy of Sciences under Contract No. IAA201990701 and Ministry of Education of the Czech Republic (Research Plan MSM 6840770003).

REFERENCES

- Lin J., Puri V. M., Anantheswaran R. C.: *Transaction of the ASAE* 38, 1769 (1995).
- Carnarius K. M., Conrad K. M., Mast M. G., Mac Neill J. H.: *Poultry Sci.* 75, 656 (1996).
- Nirasawa K., Takahashi H., Takeda H., Furukawa T., Takeda T., Nagamine Y.: *J. Anim. Breed. Genet.* 115, 375 (1998).
- Picman J., Pribil S.: *J. Ornithology* 138, 531 (2002).
- De Ketelaere B., Govaerts T., Coucke P., Dewil E., Visscher J., Decuypere E., De Baerdemaeker J.: *Br. Poult. Sci.* 43, 238 (2002).
- Nedomová Š., Severa L., Buchar J.: *Int. Agrophysics* 23, 249 (2009).
- Buchar J., Simeonovová J.: 19th CAD – FEM USERS MEETING 2001, *International Congress on FEM Technology, 17-19.October 2001, Potsdam, Berlin.*
- Coucke P.: *PhD Thesis*, KU Leuven 1998.
- Severa L.: *Acta of Mendel University of agriculture and forestry Brno = Acta Universitatis agriculturae et silviculturae Mendelianae Brunensis* 55, 137 (2007).
- Nedomová Š., Trnka J., Dvořáková P., Buchar J., Severa L.: *J. Food Eng.* 94, 350 (2009).
- Oliver W. C., Pharr G. M.: *J. Mater. Res.* 7, 1564 (1992).
- De Andrade A. N., Rogler J. C., Featherston W. R., Alliston C. W.: *Poult. Sci.* 56, 1178 (1977).
- Grizzle J., Iheanacho M., Saxton A., Broaden J.: *Br. Poult. Sci.* 33, 781 (1992).
- Lichovníková M., Zeman L., Jandásek J.: *Czech J. Anim. Sci.* 53, 7 (2008).
- Emery D. A., Vohra P., Ernst P. A., Morrison S. R.: *Poult. Sci.* 63, 2027 (1984).
- Lichovníková M., Zeman L.: *Czech J. Anim. Sci.* 53, 162 (2008).
- Máchal L., Jeřábek S., Zatloukal M., Straková E.: *Czech J. Anim. Sci.* 49, 51 (2004).
- Máchal L., Simeonovová, J. – *Archiv fur Tierzucht* 45, 287 (2002).
- Anderson K. E., Tharrington J. B., Curtis P. A., Jones F.T.: *Int. J. Poult. Sci.* 3, 17 (2004).
- Havlíček M., Nedomová Š., Simeonovová, J., Severa L., Křivánek I.: *Acta Universitatis agriculturae et silviculturae Mendelianae Brunensis* 56, 69 (2008).
- Lin H., Mertens K., Kemps B., Govaerts T., De Ketelaere B., De Baerdemaeker J., Decuypere E., Buyse J.: *Br. Poult. Sci.* 45, 476 (2004).

L. Severa^a, J. Buchar^a, J. Němeček^b, and Š. Nedomová^a (^aMUAF in Brno, ^bCTU in Prague): **Different Methods of Evaluation of Hen Eggshell Mechanical Properties**

The paper studies suitability and applicability of nanoindentation as a method used for assessment of hen's eggshell local micromechanical properties. The eggshells were tested in the area surrounding equator line. The values of Young's modulus E obtained from radial and tangential directions did not vary significantly (41 ± 3.9 GPa and 43 ± 4.1 GPa, respectively). This fact shows on isotropic nature of eggshell structure. It was found that values of E does not significantly change across the cross sectional area. The values obtained within this research correspond to values reported in literature and obtained on macroscopic samples. Nanoindentation was found to be a precise and powerful tool, suitable for determining local variations of mechanical properties of eggshells.

EFFECT OF TEMPERATURE AND GASEOUS MEDIUM ON THE STRUCTURE AND MICROHARDNESS OF THE COBALT BASE CLAD LAYERS

HANNA SMOLENSKA*

*Gdansk University of Technology, Faculty of Mechanical Engineering, Department of Materials Science and Engineering, 11/12 Narutowicza str., 80-233 Gdańsk, Poland
hsmolens@pg.gda.pl*

Keywords: cobalt alloy, oxidation, hardness

1. Introduction

The engines, gas turbine or industrial applications like for example: moulds for glass and ceramics, automotive valves, chemical and petrol-chemical valves need special material. For such a severe service conditions materials must have high strength and adequate resistance to gaseous corrosion at elevated temperatures. There are a wide range of compositions based on nickel, cobalt and nickel-iron. Their various applications are based largely on their suitability at higher temperatures to a particular environment. During recent decades, the high-temperature oxidation of structural materials, such as Fe-, Co-, and Ni-base alloys, for which high-temperature oxidation resistance is an important parameter, has been investigated intensively. In general, these alloys, developed good resistance to hot corrosion gases by possessing proper amounts of Al, Cr, and Si and are called as alumina, chromia, and silica formers. For chromia formers, maximum protection against oxidation is obtained only if a continuous and coherent Cr_2O_3 scale layer is formed and maintained. That alloys must have a sufficient chromium content to initially form a chromium oxide and supply of chromium by diffusion within the underlying alloy in order to continuous growth of the protective scale¹⁻³. In spite of the long history of the investigation of oxidation and oxide scales, there are still many aspects of this phenomenon that are not well understood. Our incomplete understanding of scale formation and evolution is due to both the extraordinary complexity of the process and the limited availability of tools that allow a complete characterization of the scales themselves⁴⁻⁶. The growing of the protective oxide scale must cause different processes which involve selective oxidation of alloy elements and lead to changing of the alloy composition in the subsurface region and even phase transformation may occur. Typically it is scale formation and subsurface degradation. As the time passed the scale may change its chemical composition. The degradation of the alloy may be a result of phase formation or dissolution and formation of voids⁷⁻⁹. Not only corrosion resistance is desirable but also the mechanical properties like: high temperature

strength, fatigue strength, hardness, creep and wear resistance.

2. Experimental

In this work the cobalt base clad layers were examined. They were produced on the face of the exhaust valve head of the marine diesel engine in order to prolong service time of this part. The substrate material was A-R-H10S2M (X40CrSiMo10-2) steel. The equipment used for the plasma transferred arc (PTA) cladding was a CASTOLIN EUTRONIC GAP 200. The layer consisted of three sublayers with three tracks for each one. The subsequent tracks were overlapped by 30–40 %. The powder was delivered straight to the melt pool. The chemical composition of the powder was as follow: C – 1,32 %, Si – 1,25 %, Cr – 29 %, W – 5,3 %, Ni – 2,1 %, Mo – < 0,1 %, Fe – 1,9 %, and Co as balance. After cladding the layer underwent turning in order to obtain proper geometry. The prepared base materials – exhaust valve – covered with clad layers was cut into pieces and then heat-treated under different conditions. The conditions were as follow: isothermal oxidation at 750 °C for 200 hours, isothermal oxidation at 850 °C for 200 hours, cyclic oxidation at 1100 °C for 100 hours (100 cycles) and cyclic corrosion in exhaust gases at 750 °C for 200 hours. The response of the coating to the elevated temperature was illustrated by the microstructural changes and microhardness profiles of the cross-section of the specimens. After metallographic preparation, the cross-sections were examined. The analytical techniques used to characterize the samples included optical microscopy, scanning electron microscopy (SEM), energy dispersive spectroscopy (EDS) and X-ray powder diffraction (XRD). SEM was conducted at accelerating voltages ranging from 15–30 kV in backscattered and secondary electron imaging modes. Mechanical properties were represented by hardness measurement on the cross-section.

3. Results and discussion

3.1. Microstructure investigation

The cross-section of the hardened layer on the valve presented typical welding solidification structures for as-deposited state. This microstructure can be described as a Co rich matrix with a network of carbides and eutectics in the interdendritic regions¹⁰⁻¹² (Fig. 1). Cross-section EDAX analysis of the clad layers revealed that the matrix was enriched in chromium and tungsten. Eutectics were

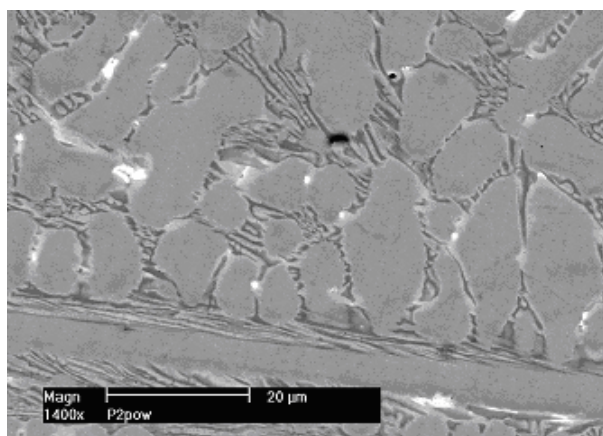


Fig. 1. SEM - Cross-section of the cobalt base layer as clad

enriched in chromium, tungsten and silicon¹³. After oxidation the changes in microstructure were dependent on oxidation temperature and distance from the surface.

After 750 °C oxidation treatment the oxide scale was very thin and almost difficult to observe on the cross section of the sample. The higher temperatures, 850 and 1100 °C, caused forming thicker oxide scales and also internal oxidation region was observed after 1100 °C processes. In the bulk of the layer not visible changes were noticed. Cross-section EDAX analysis of oxidized laser clad revealed that the uppermost part of the scale has relatively high concentration of Cr and O while the amount of Co remained unchanged¹³. It suggested the formation of Cr-rich outer oxide scale and relatively less Cr amount just under the scale. The other elements did not indicate any changes. After heating at 850 °C, the scale was dense, an approximately 6 μm thick (Fig. 2).

For this case under the dense scale layer the negligible traces of internal oxidation were noticed only on the boundaries of some dendrites. The degradation of clad

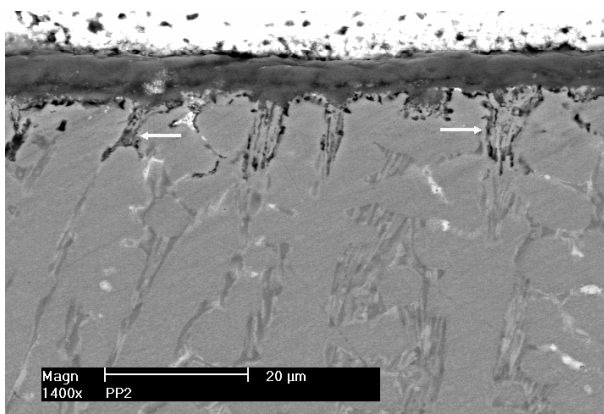


Fig. 2. SEM - Cross-section of the clad layer after oxidation at 850 °C. The arrows indicate the internal oxidation traces

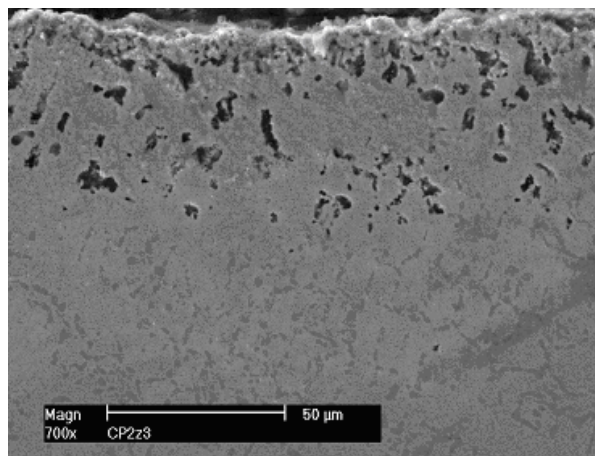


Fig. 3. SEM - Cross-section of the clad layer after oxidation at 1100 °C

material reached no more than 34 μm. The XRD analysis revealed generally Cr₂O₃ (ref.¹³) presence in the scales. The scale and the degradation of the clad after oxidation at 1100 °C (Fig. 3) were more critical. The scale was thicker, uniform and partially showed tendency to spalling. This led to disappearance of the carbides and degradation of the interdendritic regions in the cobalt alloy under the scale. The degradation of clad material reached about 60 μm.

After corrosion in exhaust gases the scale on the surface of the clad was so thin that it was difficult to notice on the samples' cross-section because during the metallographic preparation it was difficult to get sharp edge. However the observation of the top of the valve face confirmed the presence of the oxide layers. In the case of corrosion in exhaust gases scale composition appeared different. The scale was much thinner and consisted of chromium and iron oxides and possible small amount of sulfides. The chromium decrease under the scale was less noticeable.

3.2. Microhardness measurement

For hardness measurement the GOST 7865–86 manual microhardness tester was used. The test was carried out on the finely polished transversally sectioned surface perpendicular to the surface of the layer, at the load of 200 g for a loading time of 20 s. This load produced clear indentation, easy for optical measurement and small enough for proceeding hardness measurements within the space 0,2 and even 0,05 mm. The first measured point was placed at the distance 0,05 mm from the clad surface. For the next points the distances between them were 0,2 mm. On the clad-steel interface the points were situated at 0,05 mm distance on both sides of the fusion line. Because of hardness variation across the layer the 3 series of measurement were made. Fig. 4 presents the hardness profile of the clad and steel base just after cladding.

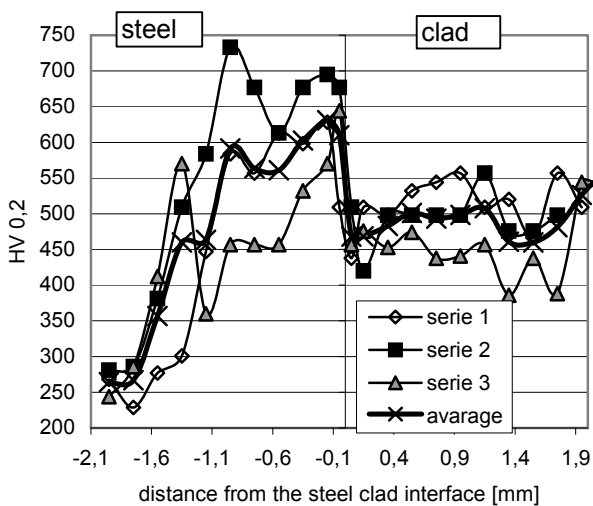


Fig. 4. Microhardness measurement for as-clad layer and steel base

The non-uniform hardness across the coating was a result of multilayer producing process and structure of this layer. The heat affected zone (HAZ) was observed in the steel under the clad layer. From the morphological point of view, the measured differences in hardness were affected by the dendrite structure and can also be attributed to the morphology of the carbides^{11,12}. This phenomenon is related to the multiple heating and cooling during the multi layer cladding process. The heat treatment in different temperatures and atmospheres led to the changes in the hardness especially in the upper part of the clad.

Even for the low temperature (750 °C) heat treatment, when changes in microstructure were negligible the hardness decrease was observed (Fig. 5, 6).

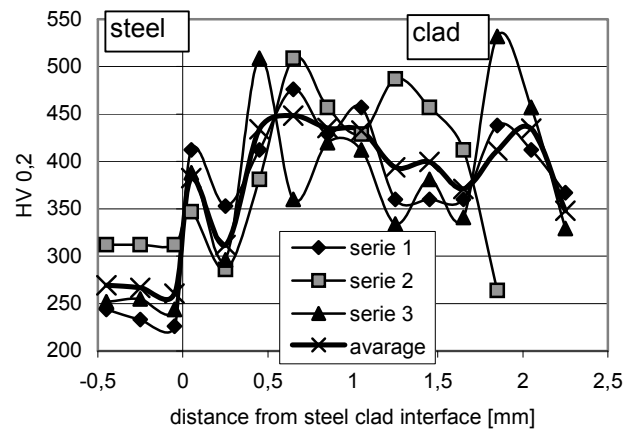


Fig. 6. Microhardness measurement after corrosion in exhaust gases at 750 °C

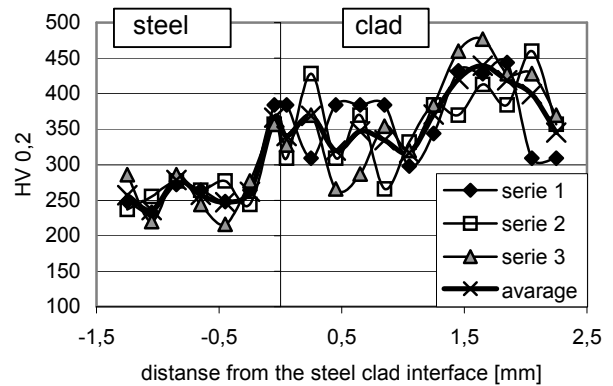


Fig. 7. Microhardness measurement after oxidation at 850 °C

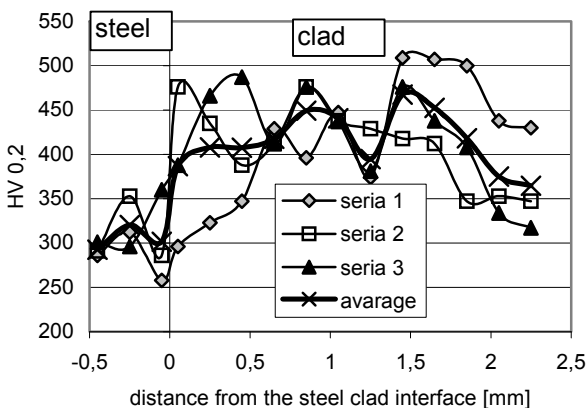


Fig. 5. Microhardness measurement after oxidation at 750 °C

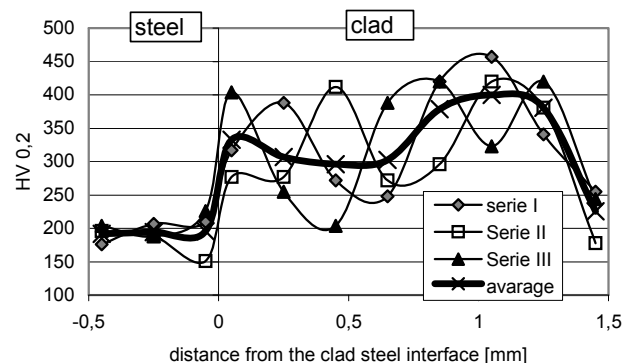


Fig. 8. Microhardness measurement after oxidation at 1100 °C

After treatment at higher temperatures the hardness decreases were obvious and corresponded with the microstructure changes (Fig. 7, 8).

For all temperatures the hardness decreased in the HAZ. It was a result of the temperature influence. The oxidation treatment acted as annealing process and removed microstructural changes typical for HAZ. As a result the HAZ zone disappeared.

4. Conclusion

For the conditions tested the results led to some important conclusions:

- The oxidation reaction in investigated alloy was initiated by the formation of the outer scale of chromia which was nucleated and subsequently grew in thickness by diffusion and caused depletion the underlying alloy of chromium. The high chromium content carbides situated on the dendrite boundaries were the main source of the chromium. The decomposition of the carbides led to degradation of the dendrite boundaries and caused the voids formation. The increase of the oxidation temperature strongly influences the thickness of the material which underwent the degradation process.
- In the outer surface sublayer with thickness of about 0,3 mm, a significant decrease of hardness was found. This observation correlated with the microstructural changes that are the disappearance of carbides in the interdendritic region and their replacement by Cr-oxide.
- The correlation between hardness and microstructure of clad layers was proved for as –clad and after oxidation state.
- The microhardness measurement is more sensitive on material changes due to the heat treatment than microstructural analyzes.

REFERENCES

1. Gleeson B., Harper M. A.: *Oxid. Metals* 49 (3/4), 1998.
2. Gleeson B., Harpe M. A.: *Oxid. Metals* 49 (3/4), 1998.
3. Yuan F., Sun X., Guan H., Hu Z.: *J. Chinese Society of Corrosion and Protection* 22 (2), 2002.
4. Uran S., Veal B., Grimsditch M., Pearson J., Berger A.: *Oxid. Metals* 54 (1/2), 2000.
5. Yang F. M., Sun X. F., Guan H. R., Hu Z. Q.: *Metall. Mater. Trans. A* 34, 979 (2003).
6. Berthod P., Michon S., Aranda L., Mathieu S., Gachon J.C.: *Comput. Coupling Phase Diagrams Thermochem.* 27, 353 (2003).
7. David J. Young, Brian Gleeson: *Corros. Sci.* 44, 345 (2002).
8. Douglass D. L., Armijo J. S.: *Oxid. Metals* 3 (2), 1971.
9. Jones D. E., Stringer J.: *Oxid. Metals* 9 (5), 1975.
10. Liu P.S., Liang K.M.: *Oxid. Metals* 53, 351 (2000).
11. Hou P. Y., Stringer J.: *Oxid. Metals* 33 (5/6), 1990.
12. Li B., Gleeson B.: *Oxid. Metals* 65, 101 (2006).
13. Smolenska H.: *Adv. Mater. Sci.* 7, 254 (2007).

H. Smolenska (*Gdansk University of Technology, Poland*): **Effect of Temperature and Gaseous Medium on the Structure and Microhardness of the Cobalt Base Clad Layers**

The influence of oxidation temperature on the hardness and microstructure of Co-base alloy coatings were investigated. Coatings were manufactured by PTA cladding on a valve steel X40CrSiMo10-2 substrate. The cobalt alloy was exposed to high temperatures in air from 750 °C to 1100 °C and in exhaust gases at 750 °C. As a result of oxidation treatment the changes in microhardness for cobalt layers were observed. In the outer surface sublayer with thickness of about 0,3 mm a significant decrease of hardness was found. The higher temperature was applied, the bigger decrease of hardness was observed. The hardness measurement presents more sensitive reaction on material changes during the heat treatment than microstructural analyzes.

COULD HUMIDITY AFFECT THE MECHANICAL PROPERTIES OF CARBON BASED COATINGS?

JAROSLAV SOBOTA^{a*}, JAN GROSSMAN^a, JIŘÍ VYSKOČIL^b, RUDOLF NOVÁK^c, TOMÁŠ FORT^a, TOMÁŠ VÍTU^d, and LIBOR DUPÁK^a

^aInstitute of Scientific Instruments, Academy of Sciences of the Czech Republic, Královopolská 147/62, 612 64 Brno,

^bHVM Plasma Ltd. Na Hutmance 2, 158 00 Praha 5,

^cFaculty of Mechanical Engineering, Czech Technical University, Technická 4, 166 07, Praha 6, ^dFaculty of Transportation Sciences, Czech Technical University, Na Florenci 25, 110 00, Praha 1, Czech Republic

sobota@isibrno.cz

Keywords: coatings, carbon, mechanical properties, humidity, fracture toughness

1. Introduction

We evaluated the effect of humidity on tribological behaviour¹ and impact resistance at elevated temperatures of carbon-based hard composite coatings deposited by PACVD with an interface metallic layer prepared by unbalanced planar magnetron sputtering. These layered systems are intended to be used as a protective coatings in car engine components exposed to a dynamic load. To evaluate the impact resistance of thin hard composite coatings in dynamic loading wear applications an impact test was used. Impact testing of coatings was proposed by Knotek et al. in the 1990's (ref.²). During this testing, the specimen was cyclically loaded by a tungsten carbide ball that impacted against the coating-substrate surface. Both impact tests and wear test with linear reciprocating movement were made in dry and humid air.

2. Experimental Details

Carbon-based composite coatings were prepared in industrial equipment by a combined PVD/PACVD (physical vapour activated deposition) process. An interface metallic layer prepared by unbalanced planar magnetron sputtering and DLC (diamond like carbon) coating was deposited by PACVD with pulsed bias from hydrocarbon gases. HSS (high speed steel) was used as a substrate material and polished to Ra of about 0.05 μm . Total thickness of the coating determined by the calotest method was about 2.5 μm .

The impact tester developed at the Institute of Scientific Instruments ASCR, Brno was modified for measurements in controlled environment, to evaluate the possible influence of humidity on the impact resistance of coating-substrate system, Fig. 1.



Fig. 1. Impact tester developed at the Institute of Scientific Instruments ASCR, Brno for measurement in controlled environment

A reciprocal tribometer with controlled humidity was used to study friction/wear properties of coatings, Fig. 2. Normal and tangential loads measured by tensiometers are recorded every 10–50 ms. Typical parameters include a normal load of 5–30 N.

A high temperature tribometer (CSM Instruments) was used to measure friction and wear characteristics of



Fig. 2. Reciprocal tribometer developed at HVM Plasma Ltd

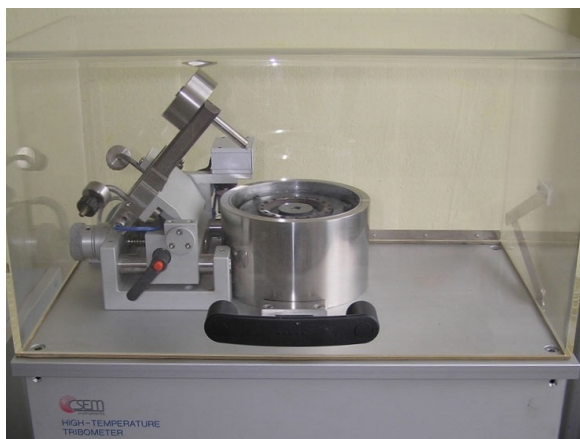


Fig. 3. High temperature CSM tribometer

coatings at an elevated temperature, Fig. 3. The principle of measurement is the pin-on-disc method with rotating disc and this measurement is considered as a “standard”.

The pin is mounted on a stiff lever designed as a frictionless force transducer. As the sample is rotating, the effect resulting friction forces between the pin and the sample is measured through very small deflection of the lever. This device allows to carry out precisely calibrated friction and wear measurement at temperatures ranging from the room temperature (RT) up to 800 °C with these main specifications: rotational speed 1 to 500 rpm, forces up to 10 N and maximum disc dimensions: Ø 60 mm × 15 mm.

3. Results

3.1. Impact Tests

In Fig. 4 we can see the dependence of the crater volume created during impact testing of the coated sample on the number of impacts^{2,3}.

The tests were carried out at the relative humidity (RH) levels of 2.5 % and 95 % at an impact force of 600 N.

Mean values are indicated with marked error bars. As a ratio of the number of impacts and volume of the crater, the dynamic impact resistance was calculated. At the relative humidity of 2.5 %, the dynamic impact resistance was $2.17 \cdot 10^4$, but at RH 95 % it reached $9.09 \cdot 10^4$. That means that the value of dynamic impact resistance increased more than four times.

Upon comparing measured of crater volumes, we can see, that the relative humidity substantially influences dynamic resistance of the coating-substrate system, in particular in the region of mechanical erosion of the coating

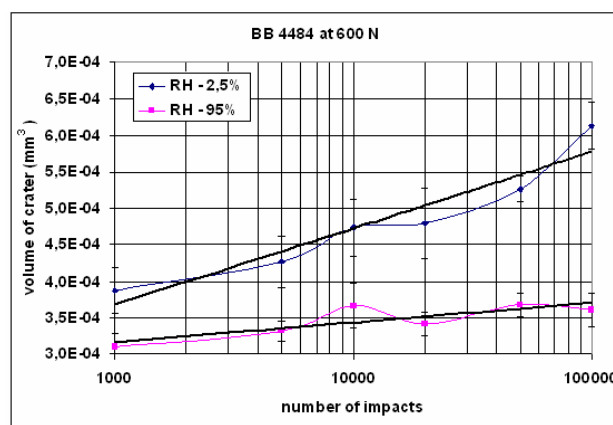


Fig. 4. The dependences of the crater volume created during impact testing of the coated sample on the number of impacts obtained at an impact force of 600 N measured at the relative humidity levels of 2.5 % and 95 %

3.2. Reciprocal Tribometer

In Fig. 5, the enormous influence of humidity on the coefficient of friction and wear rate of the coating can be observed. By increasing the RH from 0 % to 80 %, the wear rate of the coated part increases by more than four orders of magnitude. The effect of humidity on the coefficient of friction cannot be neglected either.

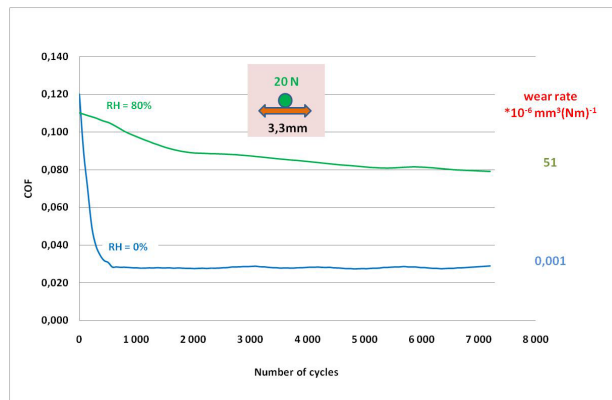


Fig. 5. Coefficient of friction (COF) and wear rate measured on the reciprocal tribometer at the relative humidity levels of 0 % and 80 %

3.3. High Temperature CSM Tribometer

The typical friction curves of a hard coating sliding against a 100Cr6 ball at room temperature, 120 °C and 200 °C are given in Fig. 6. All measurements were performed at the load of 15 N and a linear speed of 4 cm s^{-1} , with the relative air humidity of $25 \pm 5 \%$. The first part of the curve, the run-in stage, was represented by a strong

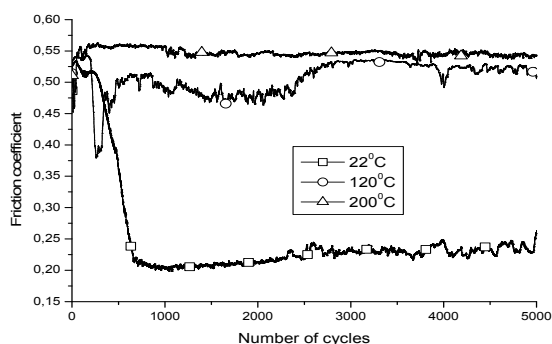


Fig. 6. Friction curves of the hard coating sliding against a 100Cr6 ball measured on a high temperature CSM tribometer at the room temperature, 120 °C, and 200 °C

increase in the coefficient of friction during the first cycles to a high value of 0.53.

In the next 700 cycles, the coefficient of friction dropped to a lower level. The following part, in which the coefficient of friction remained constant until destruction of the coating, was determined as the steady-state wear. The coefficient of friction during the steady-state wear stage depended essentially on temperature. At RT the reactions of the ball surface with oxygen and water played a significant role resulting in a low value of coefficient of friction. Drying of the coating and ball surfaces at a temperature above 100 °C resulted in an increase of the coefficient of friction. By additionally elevating the temperature, the formation of oxides species was expected and it took effect in a substantial increase of the coefficient of friction.

4. Conclusion

Humidity can significantly influence not only the tribological behaviour of carbon-based coatings¹, but unexpectedly, as we discovered, also their impact resistance.

By increasing the relative humidity, the dynamic impact resistance increases more than four times. Simultaneously, the wear rate of the coated part increases by more than four orders of magnitude. The coefficient of friction during the steady-state wear stage depends essentially on temperature. At RT, the coefficient of friction has a low value. Drying of the coating and ball surfaces at temperatures above 100 °C results in an increase in the coefficient of friction.

In optimising the coated car engine components exposed to dynamic loads, we must take into account not only the temperature, roughness of surfaces, and contact pressure but also the influence of the relative humidity at which the component runs.

This work has been supported by a grant from the Czech Ministry of Industry and Trade MPO 2A-ITP1/031.

REFERENCES

1. Svahn F., Kassman-Rudolphi A., Hogmark S.: *Wear* 261, 1273 (2006).
2. Knotek O., Bosserhoff B., Schrey A., Leyendecker T., Lemmer O., Esser S.: *Surf. Coat. Technol.* 54/55, 102 (1992).
3. Engel P. A., Yang Q.: *Wear* 181-183, 730 (1995).

J. Sobota^{a*}, J. Grossman^a, J. Vyskočil^b, R. Novák^c, T. Fořt^a, T. Vítů^d, and L. Dupák^a (^a *Institute of Scientific Instruments, Academy of Sciences of the Czech Republic, Brno*, ^b *HVM Plasma Ltd., Praha 5*, ^c *Faculty of Mechanical Engineering, Czech Technical University, Praha 6*, ^d *Faculty of Transportation Sciences, Czech Technical University, Praha 1, Czech Republic*): **Could Humidity Affect the Mechanical Properties of Carbon Based Coatings?**

We evaluated the influence of humidity on tribological behaviour, impact resistance and tribological behaviour at elevated temperatures of carbon-based hard composite coatings deposited by PACVD with an interface metallic layer prepared by unbalanced magnetron sputtering.

Impact tests were carried out at a relative humidity of 2.5 % and 95 % at an impact force of 600 N. Comparing measured values of crater volumes we can see, that the relative humidity substantially influences dynamic resistance of the coating – substrate system, in particular in the region of mechanical erosion of the coating.

It is well known for years, that humidity can significantly influence the tribological behaviour of carbon-based coatings. However, unexpectedly, humidity also influences the impact resistance of this type of films. By increasing the relative humidity, the value of dynamic impact resistance significantly increases. Simultaneously the wear rate of the coated part increases by many orders of magnitude. By optimising components coated by carbon-based coatings exposed to dynamical load, we must take into account not only temperature and, roughness of surfaces, but also the influence of the relative humidity at which the coating – substrate system runs.

CHARACTERISTICS OF DUPLEX COATED STEELS

**MARIE VÁLOVÁ^{a,*}, JAN SUCHÁNEK^a,
and OLGA BLÁHOVÁ^b**

^a Czech Technical University, Technická 4, 166 07 Praha 6, ^b University of West Bohemia, Univerzitní 22, 306 17 Plzeň, Czech Republic
marie.valova@fs.cvut.cz

Keywords: duplex coating, nanohardness, tribological properties, PVD

1. Introduction

The requirements for materials used in the machine parts production, especially their functional characteristics and service life are currently increasing. The need strength, ductility and toughness on the one hand and low weight, corrosion and wear resistance on the other hand, are often contradictory and with standard materials hardly realizable¹. One suitable solution of this formidable situation appears to be a surface treatment, which can create a coating with special properties mentioned above. The example is a die, which keeps the basic material's characteristics and, thanks to the coating, the functional properties of its surface are improved. In this case, there is a problem of cracking of the coating when overloaded. Very hard and abrasion-resistant coating is applied on the softer base material. The substrate is able to deform in an elastic or plastic manner under the load, but the brittle coating cracks. That leads to an intensive wear of the coating and subsequently of the die, too.

The strengthening of substrate surface layers, e.g. by plasma nitriding, appears to be a suitable solution of the low strength of the substrate. On the nitrided surface a suitable PVD coating with required properties is deposited².

2. Experimental

The material used for nitriding is low-alloyed steel 31CrMoV9 (ČSN 41 5330). The specimens (Fig. 1) prepared from this steel were quenched, tempered, pulse plasma nitrided and subsequently lapped. Nitriding was carried out at the temperature of 540 °C for a period of 20 hours in an atmosphere containing $N_2 : H_2 = 3 : 1$. Heat-treated and plasma nitrided specimens were PVD coated in a HAUSER coating equipment (low-voltage arc). There were several PVD coatings deposited: TiN (Fig. 2), CrN, TiAlN, $3 \times (\text{CrN} - \text{TiN})$. Specimen's roughness were $Ra = 0.19 \mu\text{m}$.



Fig. 1. Specimen with wear marks (TiN coating)

The coating's thickness was measured with calotest. The diameter of polished steel ball is 15 mm. The measurement was checked by evaluation on light microscope Axio Observer D1m.

The adhesion to the substrate was classified by a scratch test. There were evaluated critical loads L_c .

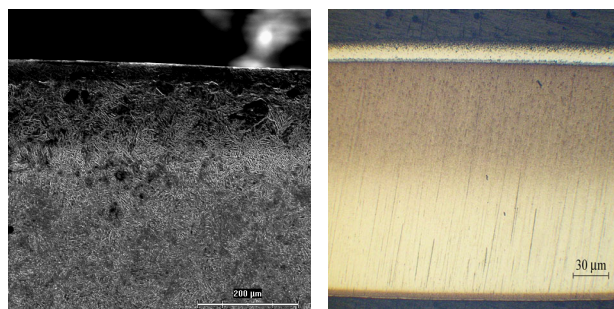


Fig. 2. TiN coating on nitrided surface (chamfer cut) – SEM and light microscope

Both microhardness (load of 200 gf) and nanohardness (indentation hardness³) were measured (in cooperation with UWB in Plzeň) on all the samples.

Nanoindentation measurements were carried out by Nanoindenter XP with CSM module. This additional device allows reading the contact stiffness during whole process of indentation. Principle of this measurement is oscillation along primary load with frequency of 0.05–200 Hz and amplitude of 60 nN – 300 mN. Instrument analyses dynamic response of tested material and it is possible to estimate material parameters like hardness and modulus, by this way.

The contact depth h_c was determined:

$$h_c = h - \varepsilon \frac{P_{\max}}{S} \quad (1)$$

where h is the total indenter displacement corresponding to the load P_{\max} , ε is a correction factor for non-circular shape of the indenter ($\varepsilon = 0.75$ for Berkovich indenter), and S is the contact stiffness.

The formulas quoted above allowed determining a reduced elastic modulus of E_r from the dependence:

$$E_r = \frac{\sqrt{\pi} \cdot S}{2 \cdot \beta \cdot \sqrt{A_p}(h_c)} \quad (2)$$

where S – contact stiffness, A_p – contact area, with taking account of permanent deformation, β – correction constant for the indenter tip shape (for Berkovich indenter, $\beta \approx 1.034$).

The reduced modulus E_r is used to account for the fact that elastic displacements occur in both the indenter and the sample. The elastic modulus of the test material E is calculated from E_r using:

$$\frac{1}{E_r} = \frac{1 - \nu^2}{E} + \frac{1 - \nu_i^2}{E_i} \quad (3)$$

where E , ν – elastic modulus and Poisson's ratio for the investigated material, E_i , ν_i – elastic modulus and Poisson's ratio for the material of the indenter (for diamond $E = 1141$ GPa, $\nu = 0.07$).

The hardness was determined as a ratio of the maximum load P_{\max} imposed on the indenter and the projection contact area A , the latter being a function of the indenter shape at the contact depth h_c :

$$H = \frac{P_{\max}}{A_p} \quad (4)$$

Hardness was measured by CSM method up to maximum load $P_{\max} = 670$ mN according to EN ISO 14577-1 (ref.³).

The samples were subsequently tested on a pin - on - disc tribometer. The tests were carried out at temperatures of 22 °C and 250 °C, under the load of 1, 2 and 5 N. Others parameters of measurement is in Tab. I.

The samples were tested in dry conditions. The recorded friction coefficient values were processed using the program OriginLab®.

Table I
Parameters of measurement with pin - on - disc tribometer

Diameter of pin [mm]	Material of pin	Diameter of distance [mm]	Speed [cm s ⁻¹]	Distance [m]
7.94	HSS	15.00	10	100
7.94	HSS	16.00	10	100
7.94	HSS	17.00	10	100

3. Results and Discussion

Values reading from Calotest marks was difficult. Measured values are only approximate and they are differ from values measured by microscope. All of values measured by calotest are about 0.5 μm lesser (Tab. II.). The thickness of nitrided layer are 400 μm .

Table II
Values of coating's thickness

Coating	t [μm] (calotest)	t [μm] (light microscope)
TiN	1.1	1.6
CrN	1.6	2.1
TiAlN	1.9	2.4
3 × (TiN - CrN)	1.6	2.2

Results of scratch test are shown in Tab. III. It was measured values of critical loads L_c according to specification EN 1071-3 (ref.⁴). The highest adhesion to the basic material was detected in the TiN coating and the lowest adhesion in the CrN coating, as in Fig. 3. The adhesion of all tested PVD coatings was sufficient.

Table III
Values of critical loads L_{C2} and L_{C3} measured with scratch test

Coating	L_{C2} [N]	L_{C3} [N]
TiN	78	87
CrN	34	52
TiAlN	52	61
3 × (TiN - CrN)	52	61

Hardnes was measured on chamfer cut and cross-cut (Fig. 2). Measured data on following graph clearly shows that the nitrided layers increased the hardness of the substrate subsurface layer. The hardness gradually drops from the values near 850 HV to the values common for a heat-treated steel (cca 575 HV) as in Fig. 4.

The dependence of the nanohardness on distance from surface (Fig. 5) shows that the nitride hardening process could be much more favourable with regard to coating break than with common treatment without plasma nitriding.

The most favourable nanohardness curve was measured on TiN coating. The hardness curves of TiAlN and multilayer 3 × (TiN - CrN) shows good valuable as well (Tab. IV).

The most suitable wear resistant coating for dies in term of service life at the temperature of 22 °C was the TiN coating. This coating had the lowest values of friction coefficient and the smallest wear.

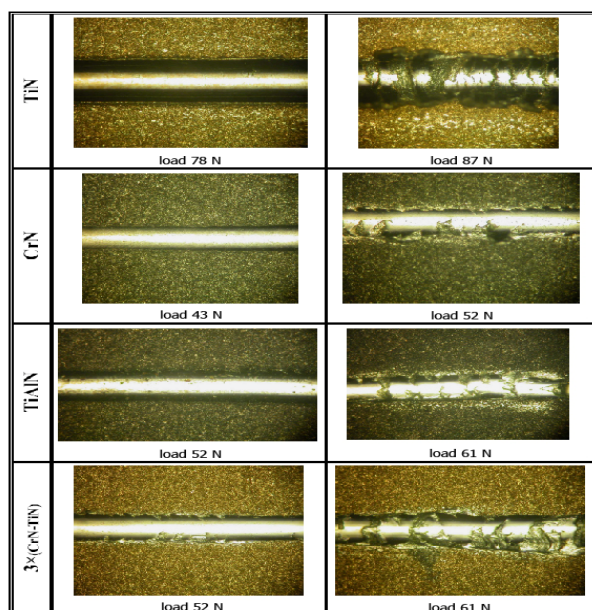


Fig. 3. Check measurement of the coating adhesion by a scratch test (indicated forces are maximum loads in given locations), magnification is $50\times$

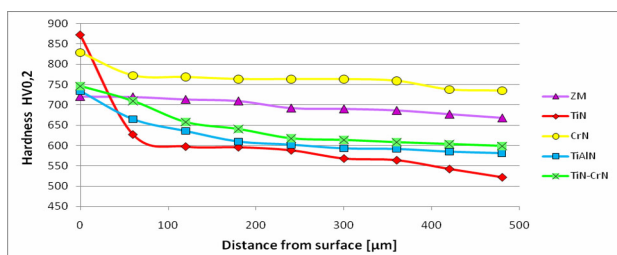


Fig. 4. Hardness of nitride layer on measured samples (hardness of coatings wasn't measured)

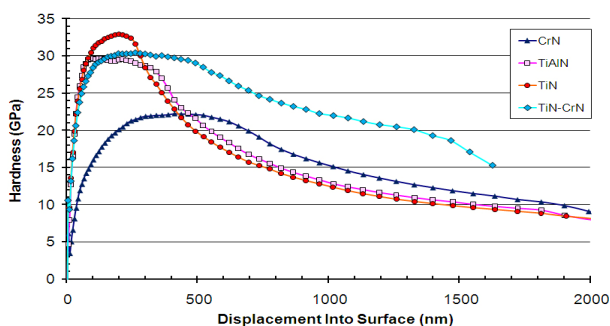


Fig. 5. Nanohardness of the coatings

Table IV
Modulus and hardness of coatings

	H [GPa]	E [GPa]
TiN	35.8 ± 4.6	504 ± 80
CrN	26.9 ± 3.4	327 ± 43
TiAlN	32.9 ± 5.8	497 ± 98
TiN - CrN	34.2 ± 8.1	566 ± 83

The most unfavourable results were obtained for TiAlN coating at the temperature of $22\text{ }^\circ\text{C}$. The same results were achieved at the load of 1, 2 and 5 N (Tab. V).

During tests at the temperature of $250\text{ }^\circ\text{C}$, the coating $3\times(\text{CrN} - \text{TiN})$ turned out the under lower load. TiN coating became the optimal one for lower loads. TiAlN showed the poorest performance of all tested coatings, as shown in Tab. V. Experimental results showed that during testing of the duplex treated steel with different PVD coatings the friction coefficients increased.

The mechanism of deterioration of the duplex coated steel is a combination of adhesive and abrasive wear. The adhesive wear took place on the disk during experiment while the ball was worn down in an abrasive manner. The evidence of abrasive wear can be seen on the grooves formed on the ball during experiment.

4. Conclusion

The conclusions drawn from the experiment, indicate that duplex treatment is a useful way to increase the die

Table V
Friction coefficient for all coatings at the load of 1, 2 and 5 N and temperature of $22\text{ }^\circ\text{C}$ and $250\text{ }^\circ\text{C}$ after 100 m of wearing

$L = 1\text{ N}$	$22\text{ }^\circ\text{C}$	$250\text{ }^\circ\text{C}$
TiN	0.38	0.74
CrN	0.48	0.79
TiAlN	0.46	0.76
TiN - CrN	0.41	0.8
$L = 2\text{ N}$	$22\text{ }^\circ\text{C}$	$250\text{ }^\circ\text{C}$
TiN	0.52	0.8
CrN	0.64	0.7
TiAlN	0.62	0.8
TiN - CrN	0.57	0.72
$L = 5\text{ N}$	$22\text{ }^\circ\text{C}$	$250\text{ }^\circ\text{C}$
TiN	0.74	0.81
CrN	0.74	0.8
TiAlN	0.76	0.82
TiN - CrN	0.71	0.81

service life and that the most suitable coating is the PVD coating TiN. This coating in combination with a nitrided substrate, had a low friction coefficient and a small wear.

As far as the coating hardness is concerned, the most favourable is the coating TiN, in terms of nanohardness – depth profile.

In respect to results of measurement of the friction coefficient and wear, we can see, that hardness course on nitride surface is slow enough and it shouldn't reach a coating cracking also when coatings TiN and TiAlN are used. On the contrary, these coatings exhibit better service life and friction coefficient.

Current thin abrasion-resistant surface layers and coatings bring remarkable extension of service life and reliability to machine parts and dies. Most technologies have not managed to reach the limits of their possibilities so far.

The research was carried out within the framework of research programmes COST 532 with the financial support of the Czech Ministry of Education, Youth and Sport.

REFERENCES

1. Liscano S., Gil L., Leon O., Cruz M., Staia M.: *Coat. Surf. & Coat. Tech.* 201, 4419 (2006).
2. Válová M., Suchánek J., Bláhová O.: Vliv povlakování na zvyšování životnosti tvářecích nástrojů. In: *Vrstvy a povlaky 2009*, DIGITAL GRAPHIC, Trenčín, s. 153–158 (2009).
3. EN ISO 14577 - 1 *Metallic materials - Instrumented indentation test for hardness and materials parameters - Part 1: Test method.*
4. EN 1071 - 3 *Advanced technical ceramics - Methods of test for ceramic coating - Part 3: Determination of adhesion and other mechanical failure modes by a scratch test.*

M. Válová^{a*}, J. Suchánek^a, and O. Bláhová^b
(^aCTU in Prague, Praha 6; ^bUWB in Plzeň, Plzeň): **Characteristics of Duplex Coated Steels**

This paper presents results of tribological testing of duplex coated low-alloyed steel 31CrMoV9. Plasma nitrided low-alloyed steel was coated with TiN, TiAlN, CrN and 3 × (CrN - TiN). After duplex treatment all coatings were tested by calotest, scratch test, nanoindenter, hardness tester and CSM tribometer.

ESTIMATION OF FRACTURE PROCESS ZONE EXTENT IN CEMENTITIOUS COMPOSITES

VÁCLAV VESELÝ^{a*}, ZBYNĚK
KERŠNER^a, JIŘÍ NĚMEČEK^b, PETR
FRANTÍK^a, LADISLAV ŘOUTIL^a,
BARBARA KUCHARCZYKOVÁ^a

^aBrno University of Technology, Faculty of Civil Engineering, Veveří 331/95, 602 00 Brno, ^bCzech Technical University in Prague, Faculty of Civil Engineering, Thákurova 7, 166 29 Praha 6, Czech Republic
vesely.vl@fce.vutbr.cz

Keywords: fracture process zone, quasi-brittle fracture, cementitious composites, nanoindentation

1. Introduction

Cementitious composites are materials extensively utilized in the building industry. Concretes, mortars and plaster mixes are the most common examples of such materials; however, a wide range of other silicate-based composites are also broadly used. Cementitious composites are microscopically highly heterogeneous materials, which results in their tensile failure being quasi-brittle in nature. Quasi-brittle fracture can be generally characterized by a fracture process zone (FPZ) evolving around the tip of a propagating (macroscopic) crack; in this zone, the material behaves non-linearly, which is referred to as tension softening for this type of material^{1–3}. ‘Concealed’ behind such a macroscopic description of this phenomenon are several types of failure mechanisms which take place on several ‘hidden’ material levels (mezo-, micro-, nano-)^{2,3}.

This paper refers to an attempt to determine the width of the FPZ by means of nano/micro-indentation tests. The proposed utilization of nanoindentation aims to evaluate a change in material properties measured by indents positioned on side surfaces of a test specimen close to a crack incurred in the specimen during a preceding fracture test. The indentation should disclose the spatial (surface) distribution of mechanical properties from which the extent of the material damage zone accumulated during the fracture process can be estimated.

Various sophisticated experimental techniques for the determination of either the propagating crack tip or rather the entire FPZ extent have been reported in the literature (summarized e.g. in ref.^{2,3}). For the latter case, holographic interferometry technique in combination with digital image analysis was used to determine the FPZ extent from specimen surface strain fields^{2,3}. Other reported successful techniques utilize such phenomena as acoustic emission^{2–5}, X-ray radiation^{3,4}, or infrared thermography³. All these techniques are rather demanding, especially from the point

of view of the experimental devices and equipment needed. Therefore, a rather simple nanoindentation method has been tried out.

The experimental work was conducted in order to validate an analytical method for estimation of the FPZ’s size and shape proposed in (ref.^{6,7}). The technique is being developed to refine methods for determination of the fracture mechanics parameters of quasi-brittle cementitious materials. It should provide real material parameters describing the tensile failure of such materials, in contrast to the existing methods (e.g. ref.⁸) that suffer e.g. from the influence of the test specimen size, geometry or boundary effect. The method is based on specification of the energy dissipated in the FPZ by the volume of this zone. Therefore, the estimation of the damage zone extent is essential for the verification of this analytical method.

In this work, the estimation of the FPZ width during fracture is performed for a single-edge notched beam subjected to a loading test in three-point bending configuration (SEN-TPB geometry, see Fig. 1b). Theoretical predictions are compared to the damage zone width evaluated from the data obtained from the pilot experimental study.

2. Theoretical estimation of the FPZ extent

The procedure exploits a general description of the stress field in cracked bodies using Williams’ power series⁹ in combination with the philosophy and selected features of the classical non-linear fracture models for concrete (i.e. the effective crack model¹⁰ and the fictitious crack model¹¹). The basic approaches of linear elastic fracture mechanics (LEFM) and plasticity theory are also employed. A detailed description of FPZ extent estimation is performed in (ref.^{6,7}). Here we only sketch out the fundamental ideas behind the procedure, which provides the boundary of the zone of damaged material that is later compared to the experimental results.

The method is utilized within the processing of fracture test records; typically, load–displacement diagrams (P – d diagrams, see Fig. 1c). For individual stages of the fracture process, the length of the equivalent elastic crack is estimated by means of the effective crack model¹¹. Then, the stress state in the body with the effective crack is approximated through the Williams’ power series⁹, whereby the number of terms in the series must be chosen with respect to the mutual relation between the assumed FPZ size/shape and the size/shape of the body (with respect to the distance of the FPZ from the free boundaries of the body). Subsequently, the extent of the zone where the until-now elastic material starts to fail is determined by comparing the tensile strength f_t of the material to a relevant characteristic of the stress state around the crack tip (some sort of equivalent stress, σ_{eq} , for cementitious com-

posites e.g. the Rankine¹² failure criterion can be employed). The zone is denoted here as Ω_{PZ} (index PZ stands for ‘Plastic’ Zone). Then, in agreement with the cohesive crack approach^{11,12}, the FPZ (its boundary marked as Ω_{FPZ}) is supposed to extend from the Ω_{PZ} around the current crack tip up to a Ω_{PZ} corresponding to the prior crack tip (i.e. currently a point at the crack faces), where the value of crack opening displacement w reaches its critical value (i.e. the value of cohesive stress $\sigma(w)$ drops to zero here). Finally, the envelope of the Ω_{PZ} zones for each stage of fracture represents a region in which some sort of damage has taken place during the fracture process throughout the entire specimen ligament. It is denoted here as Ω_{WRAP} .

The construction of the boundaries of the zones of current and cumulative material damage (Ω_{FPZ} and Ω_{WRAP} , respectively) evolving during fracture in a SEN-TPB quasi-brittle specimen is illustrated in Fig. 1a. The thick solid lines in the graph indicate the initial crack face, and the front and back boundaries of the beam. The other lines correspond to the boundaries of the zones described above. An example of FPZ size and shape together with an indication of the intensity of the cohesive stress within it for three stages of the fracture process (corresponding to the three points emphasized in the P – d diagram in Fig. 1c) in a particular SEN-TPB specimen are displayed in Fig. 1d and 1e, respectively.

3. Experimental validation

For experimental validation of the theoretical procedure an experimental program was carried out consisting of fracture and nanoindentation tests.

Specimen preparation and fracture tests

A set of 6 notched beams of a nominal size of $40 \times 40 \times 160$ mm was prepared from cement paste with a water to cement ratio equal to 0.41 and cement type 42.5 R. The specimens were demoulded after 24 h of casting and placed into a temperature-controlled water bath set at 22 ± 2 °C. After two months of curing the specimens were provided with a notch of up to 1/3 of the width W by means of a diamond saw. The following day, the SEN-TPB tests were performed at the Brno University of Technology. P – d diagrams that were recorded are drawn in Fig. 2. Responses with considerable variation in their ultimate load can be observed. Although the tests were performed under displacement control in a very stiff testing machine, only the very initial part of the descending branch of the P – d curve was typically recorded. After that the test proceeded unstably.

Fracture parameters of the cement pastes were evaluated from the P – d diagrams, particularly the Young’s modulus, the effective fracture toughness and the critical effective crack extension, and the estimation of the specific fracture energy. The compressive strength was determined from compressive tests on (selected) specimen fragments from the SEN-TPB tests. Visual examination of the specimen surfaces was also performed after the bending tests by an illuminated magnifier (Fig. 3a). A net of hair (shrinkage) cracks was observed at various locations on the specimen’s surfaces (Fig. 3b) and caused the zigzagging and bending of the major crack into directions unfavourable by the stress state from mechanical loading (Fig. 3c), which most likely resulted in the rather uneven ascending branch of the recorded P – d curves and finally in the unstable fracture.

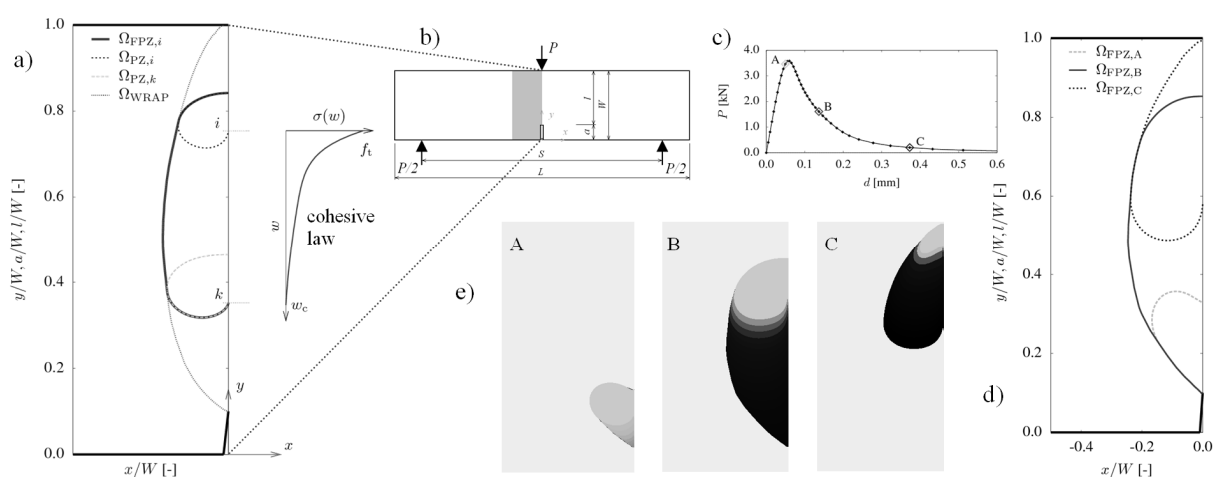


Fig. 1. **Brief overview of the theoretical estimation of current FPZ extent:** a) FPZ size and shape (Ω_{FPZ} , a union of plastic zones Ω_{PZ} for the current crack tip position i and the past crack tips within the range of action of the cohesive law – up to position k), the zone of damaged material (Ω_{WRAP} , a union of Ω_{PZ} for all crack tip positions during the fracture process along the entire specimen ligament); b) SEN-TPB test configuration; c) P – d diagram for a particular SEN-TPB test; d) and e) extent of the FPZ for three stages of the fracture process (corresponding to the highlighted points in the P – d diagram), the boundary of the FPZ and the intensity of the cohesive stress within it (grey: $\sigma(w) = f_t$, black: $\sigma(w) = 0$), respectively

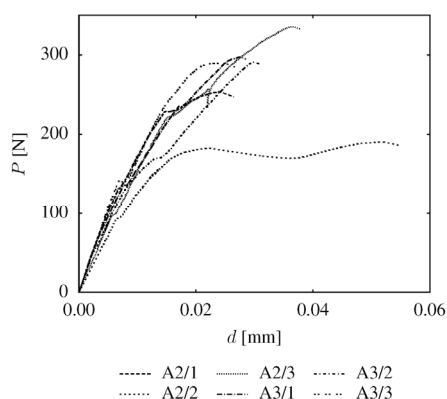


Fig. 2. Load–deflection curves recorded during SEN-TPB tests

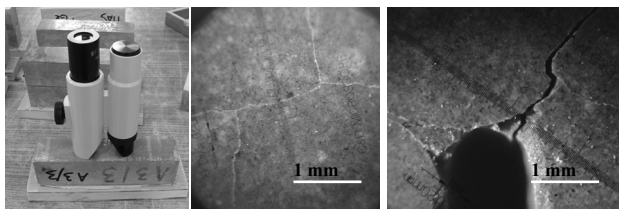


Fig. 3. Visual examination of cracks on the specimens' surfaces

Indentation tests

The indentation tests were performed on selected specimens at the Czech Technical University in Prague using a CSM Nanohardness tester. The Young's modulus of the lateral surface layer (polished) in the vicinity of the major crack was evaluated by standard Oliver and Pharr procedure¹³ (assumption of Poisson's ratio value $\nu = 0.2$).

First, a 'large' matrix of $20 \times 25 = 500$ large indents covering a rectangular area of 23.75×4.8 mm was implemented in order to assess average material behaviour around the crack. The mutual distance between individual indents was 1.25 mm in the longitudinal and 0.2 mm in the transversal direction with regards to the crack. The indents reached an average maximum depth of about $4.7 \mu\text{m}$ and thus the volume influenced by the indentation was relatively large, around $14 \mu\text{m}^3$. It implies that homogenized (average) material properties from the main material phases such as hydrates, unhydrated clinkers and some pores were included in the results from such a large volume. A high maximal load of 400 mN was applied and a trapezoidal loading diagram (loading 5 s, pause 15 s, unloading 5 s; loading/unloading rate 4800 mN min^{-1}) was used for all indents in the matrix. The distribution of the values of Young's modulus within the large matrix of indents is plotted in Fig. 4 (left). Only some fluctuation in the values around the mean was found with no significant trend in the values farther from the crack.

These results brought us to the conclusion that the FPZ extent is located much closer to the crack. Therefore, the vicinity of the crack face was covered by 'small' matrices of smaller indents at two positions along the crack length approximately in the first third of the initial ligament length. The 'small' matrices consisted of 200 indents (10×20 , distance $6 \times 6 \mu\text{m}$, covered area $54 \times 114 \text{ mm}^2$) with an average maximal indent depth of around 200 nm (influenced volume ca. 600 nm^3) induced by a maximal load equal to 2.1 mN (trapezoidal loading diagram: loading 10 s, pause 20 s, unloading 10 s, loading/unloading rate 12 mN min^{-1}). Local properties of cement paste (hydrated, unhydrated) were expected to be obtained. Fig. 4 (right) shows the measured distributions of Young's modulus values within the two 'small' indentation matrices. In the bulk material, the fluctuation of low/high properties should be more or less randomly distributed. In Fig. 4 (right), the concentration of low Young's modulus values in a band of approximately $50\text{--}70 \mu\text{m}$ is noticeable, regardless of the phase that was indented.

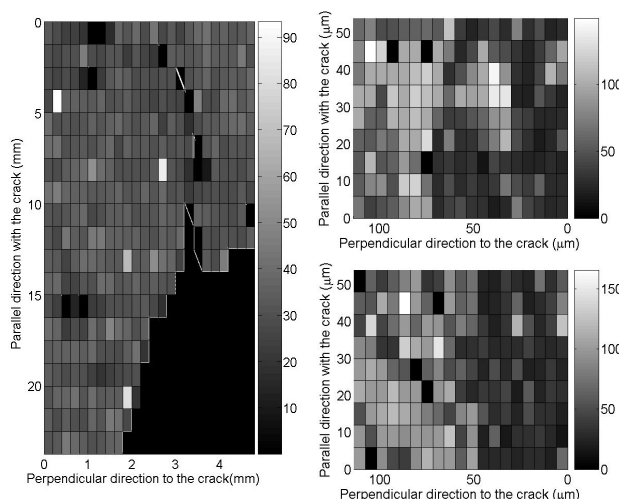


Fig. 4. Distribution of Young's modulus E (GPa): large matrix (left) and small matrices (right)

4. Discussion of results and conclusions

The extent of the material damage due to bending was identified by changes in mechanical parameters determined by nanoindentation tests, particularly by the decrease in the Young's modulus. The surface fluctuation of this mechanical parameter was evaluated, and from it the boundary of the damaged material zone was assessed. Meanwhile, parameters of the cohesive crack model serving as inputs in the theoretical procedure for FPZ extent determination were identified by an inverse analysis from the results of fracture and compressive tests. Then, the FPZ extent for the tested material was computed. A comparison of the theoretical prediction of the damaged zone width (for two estimates of tensile strength f_t) with the experimental results is depicted in Fig. 5.

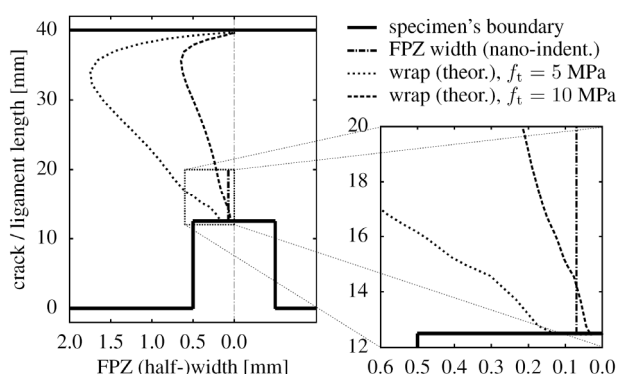


Fig. 5. Comparison of the theoretical and experimental data: experimentally determined damaged zone width and theoretically predicted boundary of damaged material (wrap) for two estimates of f_t

It was proved that the performed nanoindentation experiment can answer the question regarding the width of the zone of material failure at the end of the fracture process based on the measured decrease in local micromechanical properties across the crack. Large scale measurements from the 'large' indentation matrix did not reveal any substantial information on the FPZ extent in the case of the tested material. It was found that the damaged zone is located in the close vicinity of the crack and must be analyzed by means of nanoindentation focused on this small area. The half-width of the damaged zone for the tested cement paste lies in the range of 50–70 μm (in the first quarter of the initial specimen ligament, in the case of the SEN-TPB test). The theoretically predicted FPZ width reached considerably higher values. Revision of the theoretical procedure as well as its validation by other experimental methods is being considered for the future.

This pilot indentation experiment demonstrated the feasibility of the method, although a lot of uncertainties were introduced to the experiment through the high variation in the fracture behaviour of the chosen material, particularly due to its massive shrinkage. Continuing indentation tests on other types of silicate-based building materials in combination with more complex experiments are planned in order to evaluate the size and shape of the fracture process zone during various stages of the fracture process.

This outcome has been achieved with the financial support of Research Plan MSM 6840770003. The support of the Czech Scientific Agency (GAČR 103/07/1276 and 103/09/1748) and the Czech Academy of Sciences (GA AV IAA200710801) is also gratefully acknowledged.

REFERENCES

1. Bažant Z.P., Planas J.: *Fracture and size effect in concrete* ... CRC Press, Boca Raton 1998.
2. Shah S.P., Swartz S.E., Ouyang C.: *Fracture mechanics of structural concrete*... J. Wiley, New York 1995.
3. van Mier J.G.M.: *Fracture Processes of Concrete*... CRC Press, Inc., Boca Raton 1997.
4. Otsuka K., Date H.: *Eng. Fract. Mech.* 65, 111 (2000).
5. Muralidhara S., Raghu Prasad B.K., Eskadri H., Karihaloo B.L.: *Constr. Build. Mater.*, article in press, 2009.
6. Veselý, V., Frantík, P.: *Proc. of IM 2009, Svratka. J. Náprstek, C. Fischer (eds.), ITAM AS CR, 288–289 + 12 p. CD (in Czech).*
7. Veselý V., Frantík P., Keršner Z.: *Proc. of conf. CC 2009, Funchal, Portugal.* (B.H.V. Topping, L.F. Costa Neves, R.C. Barros, ed.), Civil-Comp Press, Stirlingshire, UK, paper 194 (16 p.), 2009. doi:10.4203/ccp.91.194.
8. RILEM Committee FMT 50: *Mater. Struct.* 18, 285 (1985).
9. Williams M.L.: *ASME J. Appl. Mech.* 24, 109 (1957).
10. Nallathambi P., Karihaloo B.L.: *Mag. Concr. Res.* 38, 67 (1986).
11. Hillerborg A., Modéer M., Petersson P.-E.: *Cem. Concr. Res.* 6, 773 (1976).
12. Jirásek M., Zeman J.: *Inelastic deformation and failure of materials...* (in Czech), Czech Technical University in Prague, 2008.
13. Oliver W.C., Pharr J.: *J. Mater. Res.* 7, 1564 (1992).

V. Veselý^a, Z. Keršner^a, J. Němeček^b, P. Frantík^a, L. Řoutil^a, and B. Kucharčzyková^a (^a Brno University of Technology, Faculty of Civil Engineering, Brno, ^b Czech Technical University in Prague, Faculty of Civil Engineering, Praha 6): **Estimation of Fracture Process Zone Extent in Cementitious Composites**

The paper proposes a method for determination of the fracture process zone (FPZ) width in cementitious composites by means of nano/micro-indentation tests. The FPZ width was assessed from changes in (micro-) mechanical parameters on side surfaces of a test specimen close to a crack propagated in the specimen during the fracture test (three point bending). The experimental work was conducted in order to validate a suggested analytical method for estimation of the FPZ's size and shape. The pilot indentation experiment demonstrated the feasibility of the proposed experimental method.

TESTING OF SMALL LOCAL ZONES BY MEANS OF SMALL PUNCH TEST AT ROOM AND CREEP TEMPERATURES

J. VOLÁK* and **V. MENTL**

ŠKODA VÝZKUM Ltd., Tylova 1/57, 316 00 Plzeň, Czech Republic
josef.volak@skodavyzkum.cz

Keywords: small punch test, correlation, creep, temperatures, specimen

1. Introduction

In many industrial applications, materials are subjected to degradation of mechanical properties as a result of real service conditions, temperature, cyclic loading, humidity or other corrosive media, irradiation, their combination etc..

The assessment of the remaining lifetime of components and structures is commonly based on correlated procedures including numerous destructive, non-destructive and mathematical techniques that should guarantee reasonably precise assessment of the current damage extent of materials in question and the remaining lifetime evaluation of the component under consideration.

The answers to demands of customers to extend the lifetime of existing components beyond their original design life must be based on detailed assessment of the current degradation extent, what can be rarely realized by means of traditional mechanical (standardized) tests that need relatively large volumes of representative material for the test specimen manufacturing. This fact accelerated the research of miniaturized test specimen that can be sampled non-invasively from the component.

The miniaturized test specimens include e.g. miniature Charpy bars or compression test samples; interesting results can be obtained also by means of instrumented hardness testing („Ball Indentation Test“). Among these, a technique called the Small Punch Test (SPT) test has emerged as a promising candidate. It is an efficient and cost-effective technique and has the potential to enable measurement of the realistic material properties.

The Code of Practice¹ gives guidance on the procedure to be followed when carrying out Small Punch Creep tests. The objectives of such tests are to evaluate the creep behavior of materials exposed in operating plant components in order to provide data needed for plant life and integrity assessment. The Code of Practice primarily addresses metallic materials tested under creep loading but can also be used for other materials. Determination of tensile test data can also be realized using this methodology.

Test pieces are discs of specified dimensions procured

from components or any other source. A major benefit of the small punch (SP) test is that it often enables mechanical characterization of material from in-service components in a minimally invasive, virtually nondestructive manner; i.e., component material is removed for testing without necessarily a requirement for repair.

The SP test provides a direct means of mechanical testing material from a localized region of a component or structure, such as the heat-affected zone of a weld, a coating, etc. The test potentially provides a more reliable means of characterization than indirect methods based on laboratory simulations of the localized region or analytical predictions based on general models (Ref.¹).

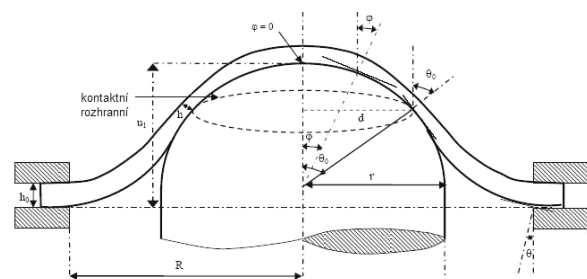


Fig. 1. Geometry of small punch test specimen deformation¹

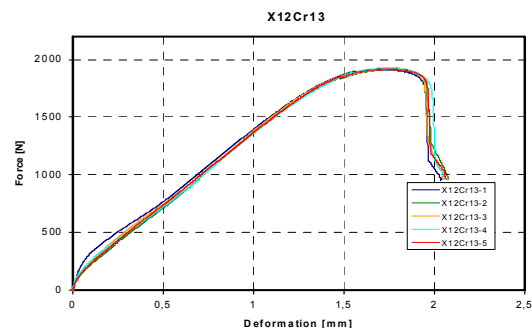
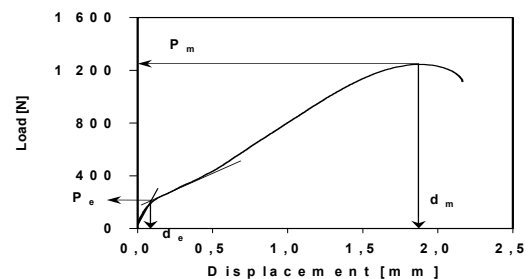


Fig. 2. Schematic and real view of the quasi-static small punch test curves at room temperature

P_c [N]	load characterizing the transition from linearity to the stage associated with the spread of the yield zone through the specimen thickness (plastic bending stage)
P_m [N]	maximum load recorded during punch test
d_m [mm]	displacement corresponding to P_m
SP [J]	fracture energy – energy obtained from the area under the load displacement curve up to the fracture load or maximum displacement
ε_f	effective fracture strain, $\varepsilon_f = \ln(h_0/h_f)$ where h_0 is the initial thickness of the specimen and h_f is the minimum thickness of the fractured specimen

The small punch tests are used for:

- assessment of yield point and ultimate strength of steels with strength within 500–1700 MPa,
- estimate of transition temperature,
- creep characteristics at elevated temperatures,
- estimate of fracture toughness.

2. The tensile test and small punch test correlation

The tensile test were performed for several steels, see Table I. The correlation was based on the following expression:

$$\frac{F}{\sigma} = 3.33 k_{sp} R^{-0.2} r^{1.2} h_0$$

F	maximum force during the small punch test [N],
R	diameter of the test fixture [mm],
r	diameter of the loading ball [mm],
h_0	original test specimen thickness [0,500±0,005 mm],
k_{sp}	proposed coefficient [1,385],
$\sigma (R_m)$	maximum stress at SP test [MPa]

Weld metal (ESAB OK Autrod 13.43 + OK Flux 10.62) of a high temperature turbine rotor tensile properties (yield

Table I
Steels used for tensile test and small punch test correlation

Material	F_{max} [N] SP test	R_m [MPa] from tensile test	R_{msp} [MPa] SP after correlation
CSN 16537	2331	902.8	905.5
X12Cr13	1919	733.4	745.4
X14CrMoVNbN10-2	1928	824.0	748.9
22CrMoNiWV8-8	2085	820.2	809.9
Steel „7“	1729	688.2	671.6
Steel „8“	1801	700.9	699.6
Steel „6“	1804	719.3	700.8

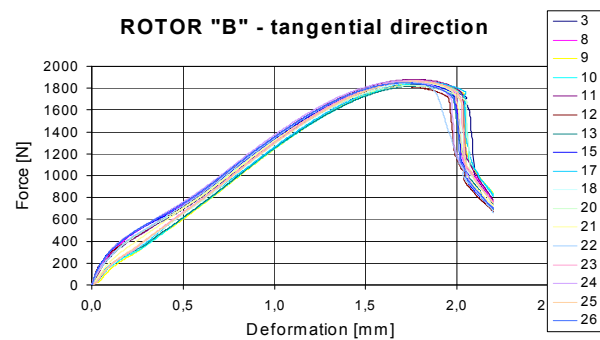


Fig. 3. Small punch test records in tangential direction

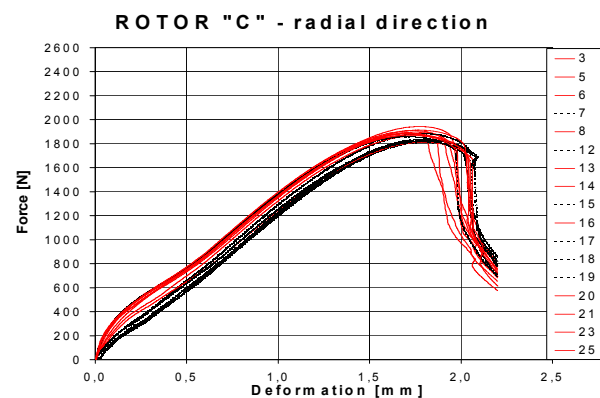


Fig. 4. Small punch test records in radial direction

Table II
Tensile to rupture properties – weld metal

Designation	S_0 [mm ²]	l_0 [mm]	A [%]	$R_{p0.2}$ [MPa]	R_m [MPa]
ROTOR “B” – Z9	28.27	30,00	21,9	636	713
ROTOR “B” – Z10	28.27	30,00	23,0	628	708
ROTOR “C” – Z1	28.27	30,00	18,3	622	703
ROTOR “C” – Z2	28.27	30,00	19,4	629	699

point and ultimate strength) in tangential and radial direction were measured by means of classical tensile to rupture tests and small punch tests. The small punch test curves are presented in Fig. 3 and 4.

The mutual relationship between F_{max}/σ_{max} and $F_{p0.2}/\sigma_{p0.2}$ was determined as follows:

1. Tangential direction

$$\frac{F_{max}}{\sigma_{max}} = 2,61 \quad \text{for} \quad \frac{[N]}{[MPa]} \quad \text{the ultimate strength, and}$$

$$\frac{F_{p0,2}}{\sigma_{p0,2}} = 2,05 \quad \text{for} \quad \frac{[N]}{[MPa]} \quad \text{the yield point}$$

2. Radial direction

$$\frac{F_{\max}}{\sigma_{\max}} = 2,67 \quad \frac{[N]}{[MPa]} \quad \text{for the ultimate strength, and}$$

$$\frac{F_{p0,2}}{\sigma_{p0,2}} = 1,92 \quad \text{for} \quad \frac{[N]}{[MPa]} \quad \text{the yield point}$$

F_{\max} maximum force during the small punch test [N],
 $F_{p0,2}$ force at yield limit [N],
 σ_{\max} maximum stress at tensile test [MPa],
 $\sigma_{p0,2}$ yield point in tension [MPa].

For the determination of the mutual relationship, only metallographically prepared samples were used, because, as it is seen from the curves in Fig. 3 and 4 (in Fig. 4 distinguished by color), the rough samples give lower unrealistic values.

3. Fracture toughness determination

The J-integral in the elastic-plastic region can be correlated with the fracture deformation ε_f by means of the following equation:

$$J_{IC} = K \cdot \varepsilon_f - J_0$$

For the case of low-alloyed steel, the constants K and J_0 were proved to be material independent, $K = 280 \text{ N mm}^{-1}$ a $J_0 = 50 \text{ N mm}^{-1}$.

The effective fracture deformation ε_f can be measured on metallographic sample, or determined from displacement at rupture d^* by means of the empiric expression

$$\varepsilon_f = \ln(h_o/h_f) = \beta \cdot (d^*/h_o)^x$$

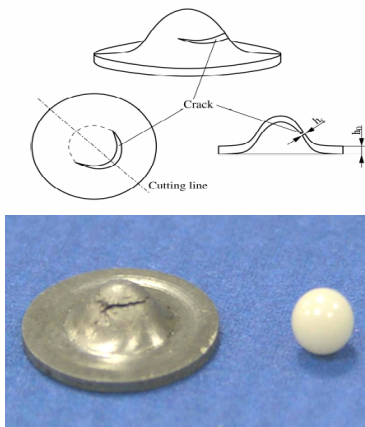


Fig. 5. Small punch test specimen after test

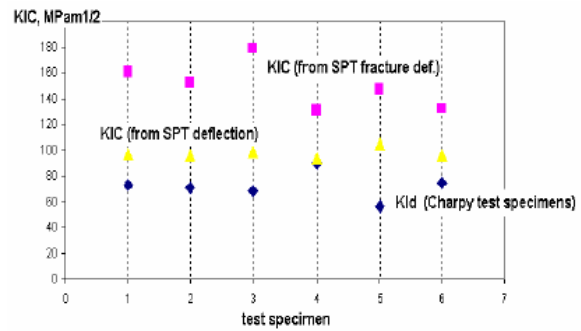


Fig. 6. Fracture toughness values comparison for Al-Alloy EN AW-2017A T4

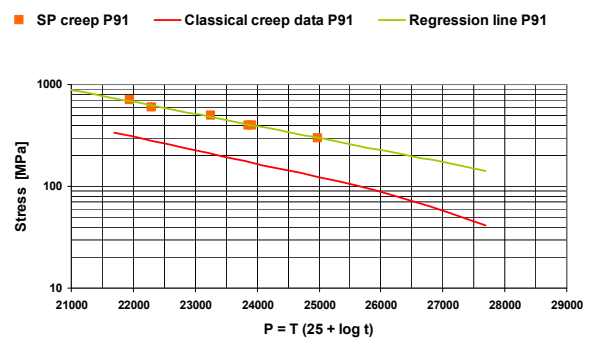


Fig. 7. Diagram Larson – Miller, steel X10CrMoVnB 91

4. Summary

The small punch test proved to be a useful tool for the mechanical properties determination during service in cases where the possibility of sufficient amount of representative material is limited.

The both tensile and creep to rupture data can be well correlated and also fracture toughness values determined by means of the small punch testing. The reliability of the small punch test data and the correlation coefficients should be based on more experimental data making it possible to use mathematical statistics.

We would also recommend a wide round-robin testing among numerous laboratories all over the world.

This work was supported by the project of the Ministry of Education, Youth and Sports, No. VZ/MSM 4771868401.

REFERENCES

1. Bicego V. et al.: Small Punch Test Method for Metallic Materials, Code of Practice CEN_WS_21, 2006

2. Volák J., Mentl V.: Korelace výsledků zkoušky tahem se zkouškami Small Punch Test za pokojové teploty, Srní 2008, 254–257.
3. Mentl V., Volák J., Sobol O., Chvostová E.: “SMALL PUNCH TEST” – Hodnocení lomové houževnatosti, Internal document ŠKODA VÝZKUM Ltd. No. VYZ 1127/08.

J. Volák and V. Mentl (*ŠKODA VÝZKUM Ltd., Plzeň, Czech. Rep.*): **Testing of Small Local Zones by means of Small Punch Test at Room and Creep Temperatures**

Small Punch Test (SPT) is a relatively new and promising test method making it possible to determine basic mechanical properties of metallic structural materials at room as well as low and elevated (e.g. creep) temperatures. The most important advantage of the method is the nearly non-destructive withdrawal of the test material and

small size of test specimen, which is interesting in cases of remaining lifetime assessment when a sufficient volume of the representative material cannot be withdrawn of the component in question.

On the other hand, the most important disadvantage of the method stems from the necessity to correlate SPT results with the results of classical test procedures and to build up a database of material data in service. The database should comprise not only original (virgin) basic materials and weld metals data, but also material properties degraded by service conditions. The correlations between the SPT results and the results of tensile tests, fracture toughness values and time to rupture characteristics at creep temperatures etc. are necessary for the remaining lifetime assessment of structure in long-time service.

The paper describes the results of Small Punch Test for basic materials and weld metals in correlation with the classic mechanical tests for several steels applied in power producing industry.

MECHANICAL PROPERTIES OF THERMOPLASTIC COMPOSITES

PAVOL ZUBKO*^a, **LADISLAV PEŠEK**^a,
IVANA ZAJACOVÁ^a, and **OLGA**
BLÁHOVÁ^b

^a Department of Materials Science, Faculty of Metallurgy, Technical University of Košice, Letná 9, 042 00 Košice, Slovakia, ^b New Technologies Research Center, West Bohemian University, Universitní 8, Píslen, Czech republic
pavol.zubko@tuke.sk

Keywords: Composite, polymer, polyamide, depth sensing indentation, videoextensometry, montmorillonite

1. Introduction

Nanocomposites are new developing branch of composites materials, where one of the components has one dimension in nano scale. Changing dimension from micro to nanoscale changes the ratio surface/volume three time^{1,2}. This cause that nanostructured materials have markedly different properties in comparison to the same materials stiffened by nano scaled filler. The physical properties, heat conductivity, shape endurance, surface roughness are improved by good dispersed nanofiller. The MMT positive effects some mechanical properties like modulus of elasticity, stiffness. The positive improvements of physical properties consequence decrease of toughness of composite matrix. This is strongly affected by character of interface interaction between the matrix and nanofiller²⁻⁴.

The influence of nanofiller on mechanical properties will be investigated in following article on two types of thermoplastics in local, meso and global scale.

2. Experimental materials

Experiments were performed on commercial type of nanocomposite SCANCOMP PP CN30, which matrix is composed of thermoplastic PP. The organic modified clay base on montmorillonite (MMT) was used as filler. The amount of filler is aprox. 5 wt.%. The second experimental material was chosen commercial type SCANCOMP PA B40 A6, with PA matrix. The same MMT filler was used as for PP. To describe the influence of nanofiller to mechanical properties were used not filled materials too.

3. Experimental methods and procedures

Two new experimental methods were used for experiments – depth sensing indentation technique (DSI) and videoextensometry.

Depth sensing indentation is a useful technique to assess the mechanical behaviour of coatings, small devices and local phases, particles and to study the tribological behaviour of materials, among others. Today, there are well-established straightforward methods to determine the elastic⁵ and plastic^{6,7} properties of solids by indentation. As for time-dependent mechanical properties, and especially creep behaviour several efforts have also been made^{8,9}.

NanoindenterXP equipped by Berkovich tip was used for experiments. The loading procedure consists of penetration to depth of 12 μm with 10 dwells, see Fig. 1. The dwell time was 200s for each step. The indentation hardness (H_{IT}), Young modulus (E_{IT}), creep -curves and -rates were determined during the dwell. Twenty measurements on each sample were performed.

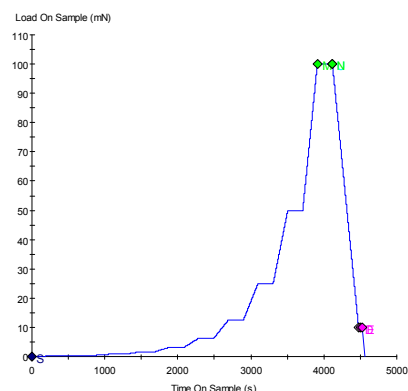


Fig. 1. The loading procedure

The tensile tests were performed to describe the mechanical properties in global and meso scale in comparison to properties in nanoscale determined by DSI. In order to determine the deformation in two directions (in the loading direction and perpendicular to it) in a contact free way¹⁰ an optical system (videoextensometer ME 46) was used during the tensile test. A regular array of black dots (15×12) was plotted on the specimen surface and images of the loaded specimen were recorded subsequently by a CCD camera during deformation (see Fig. 2). The double-edged notched tension specimen were used to localize deformation in scanned area. The dimensions of specimens were 10×4 mm and notches were bothsided with depth of 1 mm.

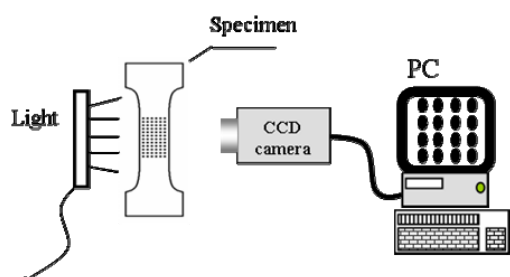


Fig. 2. The principle of videoextensometry

4. Results and discussion

Measured hardness (H_{IT}) values for all investigated materials (PA, PP, PP+MMT, PA+MMT) were summarized in the Fig. 3. The influence of MMT addition on hardness values was evaluated. The average values of hardness decrease with the indentation depth in the case of PP. Opposite behaviour was observed in the case of PA. There was no evident difference found between the matrix and composite material hardness values. Due to addition of MMT increased the scatter of hardness values.

The same evaluation was made in the case of Young modulus (E_{IT}), Fig. 4. The average values of both composites are influenced by MMT. The average modulus values of PP and PA composite increase of 12 % and 20 % in comparison to clear PP matrix, respectively. The scatter of modulus values increase too, but it is no high like in the case of hardness values.

During the dwell was indentation depth monitored in relation to dwell time. The indentation creep behavior at room temperature was evaluated on both investigated type of materials. The influence of MMT on creep curve of PA is evident. The addition of MMT causes the decrease of the indentation creep depth up to 25 % for the load of 100 mN, Fig. 5. The influence of MMT on indentation

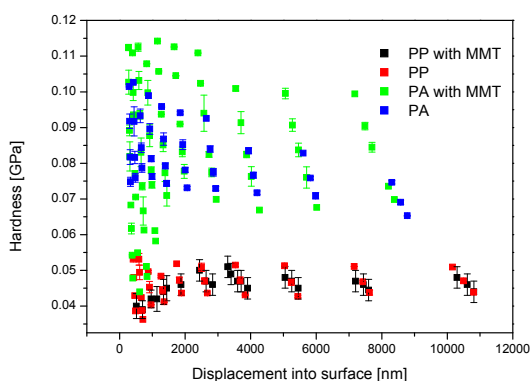
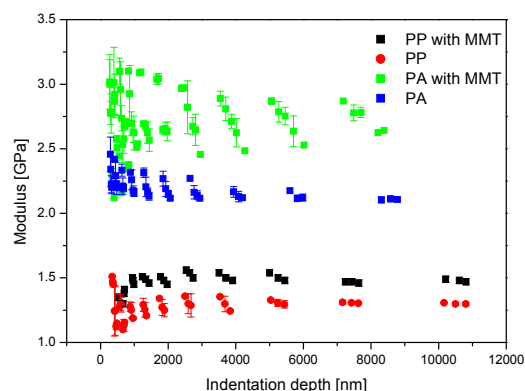
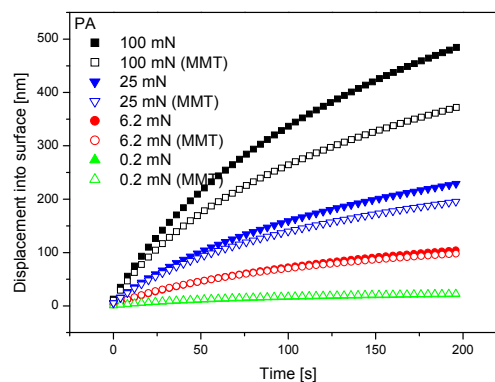
Fig. 3. Dependence of hardness (H_{IT}) on the indentation depthFig. 4. Dependence of Young modulus (E_{IT}) on the indentation depth

Fig. 5. The creep behaviour of PA (full marks) and PA composite (empty marks) for chosen loads

Table I

Creep rate (nm s^{-1}) of investigated plastics after 200 s dwell time for chosen dwell forces

Force [mN]	PA		PP	
		+MMT		+MMT
100	1.243	0.89	1.92	1.79
25	0.59	0.45	0.88	0.86
6.2	0.28	0.21	0.43	0.39
0.2	0.07	0.05	0.15	0.09

creep behavior of PP composite at room temperature is negligible, Fig. 6.

The indentation creep rates deps/dt at maximal time for four different dwell forces are presented in the Tab. I. The creep rates are higher for the PP than PA, but the dif-

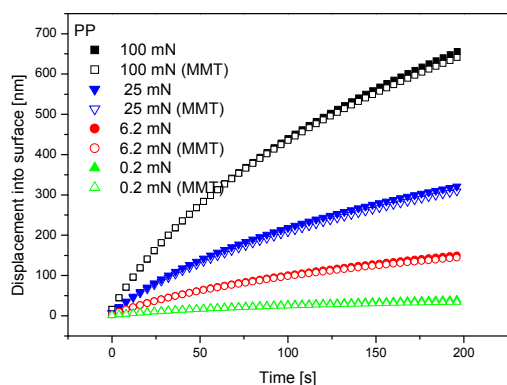


Fig. 6. The creep behaviour of PP (full marks) and PP composite (empty marks) for chosen loads

ference between matrix and composite material is lower than 8 %. In the case of PA the difference between the matrix and composite material is 29 %.

The results of tensile tests are summarised in the Tab. II. The MMT increased the values of $R_{e1\%}$ and R_m of PA composite. The influence of MMT on PP composite properties is not important.

Table II
Results of tensile test

Material	$R_{e1\%}$ [MPa]	R_m [MPa]
PP	17.5	20.6
PP+MMT	17.2	21.0
PA	24.1	44.6
PA+MMT	47.5	56.3

The strain distribution map in transversal direction of PP were determined by the method¹⁰ and is presented in the Fig. 7. The strain is concentrated in the left notch and develops in transversal direction. The same strain distribu-

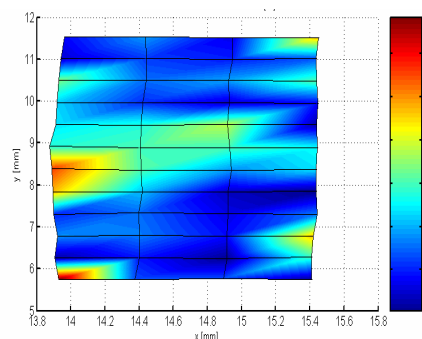


Fig. 7. The strain distribution of PP in transversal direction at R_m

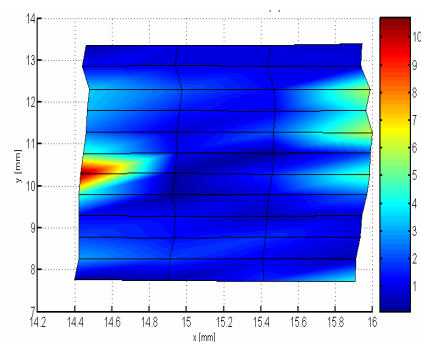


Fig. 8. The strain distribution of PP+MMT in transversal direction at R_m

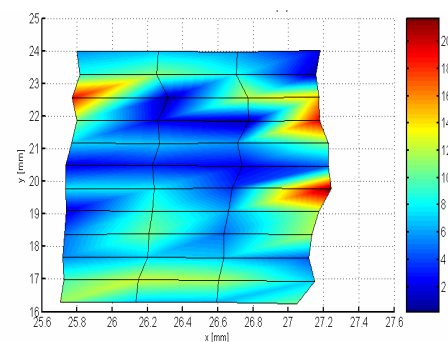


Fig. 9. The strain distribution of PA in transversal direction at R_m

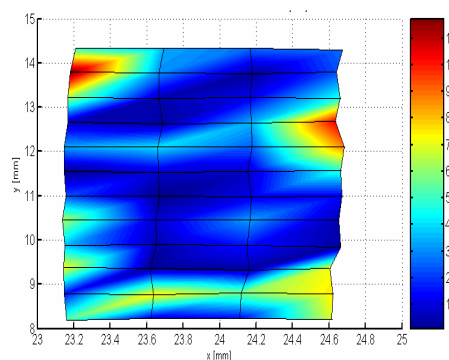


Fig. 10. The strain distribution of PA+MMT in transversal direction at R_m

tion was observed in the case of PP composite, Fig. 8. The strain is developing in transversal direction of PA and PA+MMT homogeneously from both notches, Fig. 9.

5. Conclusions

The following conclusions can be drawn from the analysis and test results:

The addition of MMT causes increase of elastic properties of both investigated materials as well the strength and hardness of PA composite. The MMT cause decrease of plastic properties of both investigated materials. The plastic properties of PA composite are affected by MMT strongly then in the case of PP composite. The effect of MMT on reological properties is higher for PA then for PP. The scatter of measured values of hardness and modulus increase by addition of MMT.

This work was supported by the grants VEGA 1/4149/07, APVV SK-CZ-0108-07, APVV-0326-07.

REFERENCES

- Hell J., Válek R., Čižmárová E.: *Nano07, Plzeň, 2007*.
- Bareš R., in book: *Kompozitní materiály*. STNL, Praha 1998.
- Čižmárová E., Pešek L., Gazdag Š., Horniak L.: *Metallography 2007, Stará Lesná, 2007*.
- Hidvégy J., Dusza, J. in book: *Nekovové konstrukčné materiály, Konštrukčná keramika*. Košice 1998.
- Oliver W.C., Pharr G.M.: *J. Mater. Res.* 7, 1564 (1992).
- Chollacoop N, Dao M, Suresh S.: *Acta Mater.* 51, 3713 (2003).
- Cao YP, Lu J.: *Acta Mater* 52, 4023 (2004).
- Huang G., Wang B., Lu H.: *Mech. Time-Depend Mater.* 8, 345 (2004).
- Seltzer R., Mai Y.-W.: *Eng. Fracture Mech.* 75, 4852 (2008).
- Pešek L.: *Plzeň-Nečtiny, KNoM ZČU v Plzni*.

P. Zubko^a, L. Pešek^a, I. Zajacová^a, and O. Bláhová^b (^a *Technical University of Košice, Faculty of Metallurgy, Department of Materials Science*, ^b *New Technology Center University of West Bohemia, Plzeň, Czech Republic*): **Mechanical Properties of Thermoplastic Composites**

The contribution deals with influence of montmorillonite (MMT) nanoparticles on strength, hardness and deformation properties of composites with PP and PA matrix. The mechanical properties were determined (H_{IT} , E_{IT}) using the depth sensing indentation technique (DSI) and creep behavior of investigated materials was monitored in the means of DSI. Non contact videoextensometric method of strain measurement was used to determine distribution of local deformations during the static tensile loading. MMT increased the tensile strength about 1.5 % in PP and about 26 % in PA matrix. Tensile strength in PA nanocomposite is about 174 % higher then that in PP nanocomposite. PA matrix is stronger about 121 % then that of PP matrix. PA+MMT is resistant to creep much more than PA and PP nanocomposite, but PP+MMT crepted nearly as PP.

Author Index

- Ambriško E. s287, s350
- Bacsó J. s330
Barylski A. s342
Beneš P. s334
Bláhová O. s271, s291, s310, s318, s346, s356, s364, s378, s390
Bohac P. s295
Bradna P. s307
Brumek J. s299
Buchar J. s368
Burda J. s356
- Ctvrtlik R. s295
Cybo J. s342
- Dlouhý I. s299
Dupák s375
Ďurišin J. s330
Dvořáková R. s303
- Eichlerová R. s307
- Fořt T. s375
Frantík P. s382
- Garbiak M. s267
Gavendová P. s310
Gaydarov V. s283
Grossman J. s375
- Haušild P. s360
Hlebová S. s287
Holáň L. s314
Houdková Š. s318, s326
- Joska Z. s322
- Kadlec J. s322
Kašparová M. s326
Keršner Z. s382
Kočiško R. s330, s353
Konvičková S. s307
Kováčová A. s330
Kříž A. s334
Kucharczyková B. s382
Kvačkaj M. s330
Kvačkaj T. s353
- Lofaj F. s271
Lukeš J. s279, s307, s338
- Mañas K. s303
Maszybrocka J. s342
Medlín R. s346
Menčík J. s275
Mentl V. s386
Mihaliková M. s350
Molnárová M. s330, s353
- Nedomová Š. s368
Négyesi M. s356
Němeček J. s271, s279, s338, s368, s382
Némethová L. s353
Nohava J. s360
Novák R. s375
- Pešek L. s287, s310, s350, s390
Pokluda J. s314
Pospíchal M. s322
- Říha J. s364
Řoutil L. s382
- Severa L. s368
Silva L.G.A. s283
Slámečka K. s314
Smolenska H. s371
Sobota J. s375
Stranyanek M. s295
Strnadel B. s299
Suchánek J. s378
Sukáč J. s322
Svoboda E. s303
- Šepitka J. s338
Šimeček J. s334
Šutta P. s364
Švorčík V. s346
- Válová M. s378
Veselý V. s382
Vítů T. s375
Volák J. s386
Vrtílková V. s356
Vyskočil J. s375
- Zahálka F. s318, s326
Zaharescu T. s283
Zajacová I. s390
Zamfirova G. s283
Zubko P. s310, s330, s390